DETECTION AND REMOVAL APPROACHES FOR FOOD MYCOTOXINS

Vicente Antonio Mirón Mérida

Submitted in accordance with the requirements for the degree of

Doctor of Philosophy

The University of Leeds

School of Food Science and Nutrition

October 2021

The candidate confirms that the work submitted is his/her own, except where work which has formed part of jointly-authored publications has been included. The contribution of the candidate and the other authors to this work has been explicitly indicated below. The candidate confirms that appropriate credit has been given within the thesis where reference has been made to the work of others.

Details of any jointly authored publication and its contributions are outlined as follows:

Chapter 2

Mirón-Mérida, V. A., Gong, Y. Y., & Goycoolea, F. M. 2021. Aptamer-based detection of fumonisin B1: A critical review. *Analytica Chimica Acta*, **1160**, p.338395.

Chapter 3

Mirón-Mérida, V.A., Wu, M., Gong, Y.Y., Guo, Y., Holmes, M., Ettelaie, R. and Goycoolea, F.M., 2021. Mathematical characterization of ink diffusion and imbibition processes in chromatography paper as a biosensing platform. *Sensing and Bio-Sensing Research*, **32**, 100421.

Chapter 4

Mirón-Mérida, V.A., Wu, M., Gong, Y.Y., Guo, Y., Holmes, M., Ettelaie, R. and Goycoolea, F.M., 2020. Genipin cross-linked chitosan for signal enhancement in the colorimetric detection of aflatoxin B1 on 3MM chromatography paper. *Sensing and Bio-Sensing Research*, **29**, p.100339.

Chapter 5

Mirón-Mérida, V.A., Gonzalez-Espinosa, Y., Collado-González, M., Gong, Y.Y., Guo, Y. and Goycoolea, F.M., 2020. Aptamer-target-gold nanoparticle conjugates for the quantification of fumonisin B1. *Biosensors, **11***(1), p.18.

Authorship contributions

Vicente Antonio Mirón-Mérida: designed the literature review and research questions, planned the experimental steps, analysed the data, summarized findings, performed their mathematical analysis and discussion, drafted the manuscripts and replied to the comments from the reviewers, when pertinent.

Mengqi Wu: Conducted experiments for crosslinked chitosan in the colorimetric detection of AFB1 in bulk and paper.

Yadira Gonzalez-Espinosa: developed the AF4 method for the analysis of AuNPs and the method for the preparation of β-chitin scaffolds, collaborated on the isolation of chitin and provided supervision, training and feedback on this technique.

Mar Collado-González: developed the method for gel electrophoresis, collaborated on the isolation of chitin and provided feedback and discussion on the assays with gold nanoparticles.

Mel Holmes and Rammile Ettelaie: provided supervision and feedback on the research with crosslinked genipin and mathematical diffusion.

Yuan Guo: provided the stocks of gold nanoparticles and supervision on their related research

Yunduo Lu: carried out the incubation of polymeric structures in milk and beer

Paul Moisey: performed the analysis of L-phenylalanine by HPLC

Lei Xia: conducted the analysis of FB1 by LC-MS

Yun Yun Gong and Francisco M. Goycoolea: provided supervision and detailed feedback on the conducted research, literature review and research manuscripts proofreading and editing.

List of accepted conference abstracts

Poster presentations:

- **Mirón-Mérida, V.A.**, Wu, M., Gong, Y.Y., Guo, Y., & Goycoolea, F.M., Efficiency of chitosan on a paper-based model colorimetric assay. (June 2019). 6th International Conference on Bio-Sensing Technology-Kuala Lumpur, Malaysia.

- **Mirón-Mérida, V.A.**, González-Espinosa, Y., Gong, Y.Y., Guo, Y., & Goycoolea, F.M. Comparison of the performance of two aptamers on a colorimetric assay for the quantification of fumonisin B1. (November 2020). The 1st International Electronic Conference on Biosensors-Online.

Oral presentations:

- **Mirón-Mérida, V.A.**, Gong, Y.Y., Guo, Y., Holmes, M., Ettelaie, R. & Goycoolea, F.M. Characterisation of diffusion performance for paper-based biosensors. (June 2019). 6th International Conference on Bio-Sensing Technology-Kuala Lumpur, Malaysia.

- **Mirón-Mérida, V.A.**, Lu. Y., Xia, L., González-Espinosa, Y., Collado-González, M., Gong, Y. Y., & Goycoolea, F.M. Comparison between chitin scaffolds and chitosan hydrogels as potential decontaminants in food. (September 2019). 4th UK Hydrocolloids Conference - Leeds, United Kingdom.

- **Mirón-Mérida, V.A.**, Wu, M., Holmes, M., Ettelaie, R., Collado-González, M., González-Espinosa, Y., Guo, Y., Gong, Y.Y., & Goycoolea, F.M. Mycotoxin detection through biosensors. (November 2020). Congreso Internacional de Ingenierías 2020 “Smart Cities: Una aproximación emergente hacia el Desarrollo sustentable” -Misantla, Mexico.

- **Mirón-Mérida, V.A.**, Wu, M., Holmes, M., Ettelaie, R., Collado-González, M., González-Espinosa, Y., Guo, Y., Gong, Y.Y., & Goycoolea, F.M. Paper-based biosensors for the quantification of mycotoxins. (November 2020). Segundo congreso Internacional de Multidisciplinario #ESCUESTIONDEINGENIO-Xalapa, Mexico.

Acknowledgements

First, I would like to thank Professor Francisco Goycoolea, not only for being an excellent supervisor, but a mentor, an example of leadership, a friend, and of course for giving me the opportunity of achieving one of my dreams as part of his research group. His support, guidance, passion, patience, optimism, love for research, and joy for life, are attributes that I will always treasure and hope to develop in my professional and personal future.

I would also like to thank Professor Yun Yun Gong for her kind help and interest in my project, especially for including me in her research group, where I discovered new topics and met fascinating people, her impact as a woman of science is something I will always admire.

I would like to thank Dr Yuan Guo for her advice and help with my project and for always having some time when I approached her with questions and hesitations.

I must thank the “Consejo Nacional de Ciencia y Tecnologia (CONACyT)” for the financial support during the whole length of my studies, which was key for their conclusion.

I would also like to thank my family from Food Science, Dr Yadira Gonzalez, Dr Mar Collado, Dr Gurmeet Kaur, Dr Andrea Araiza, MSc Suvro Saha, Dr Pilar Cabezon, Dr Amelia Torcello, Dr Efren Andablo, and MSc Alberto Rubalcava, for sharing the meals, the drinks, the talks, the stress, the laughs, the pressure, in few words the whole adventure of a PhD.

To the wonderful people I met in or through Leeds, their company, food, talks, calls helped me through this challenging time. Especially, I would like to thank Hiroshi, Alix, Perla, Lorenzo, Alex, Iulian, Kim, Filipe, Samantha, Rafael, Nere, Alejandra, Sara, Sam, Sergio, Chichi and Julia for bringing me joy with their physical and online company through this long journey.

To my small family, I do not have enough words to express my love and how proud I am of your accomplishments, your resilience, and your strength. Eli, Jenny, Carlos, los quiero mucho y gracias por todo su amor y apoyo.

Last, but not least, to my biggest inspiration in life, my mother. Although she left at the beginning of this journey, her words always pushing me to complete all my projects and surpass my limits, were the constant fuel that motivated me to continue through my experiments, and my late nights. Siempre estaré agradecido, te llevo en mi mente y en mi corazón y hasta donde estés te digo que ¡Si se pudo mami!

Abstract

Mycotoxins, secondary metabolites from diverse fungal strains, are relevant compounds whose occurrence affects not only low-income countries, but high-income nations through imported products. Their threatening effects to human health, along with the negative impact on economic, social, and agricultural levels, have established an area of study for the development of better agricultural practices, more sensitive detection techniques and effective detoxification methods. Despite their great sensitivity and selectivity, conventional methods for mycotoxin quantification require long assay times, expensive equipment and instrumentation, specialized operators, and multiple steps of sample pre-treatment. Hence, less complex yet effective techniques are required for such targets. In addition, decontamination is sometimes the last alternative for some agricultural and food products in which the use of waste-based adsorbents results in a cheap, ecological, and affordable solution to this problem, when compared to other utilized materials. In this regard, natural polymers have been explored with promising results over the las years.

This thesis was focused on the development and improvement of bulk and paper-based biosensing techniques for the quantification of mycotoxins, and the exploration of natural polymeric materials as potential adsorbents for food decontamination and biosensing platforms. In order to examine the application of paper as a sensing matrix, five model samples (aqueous ink) were applied on 3MM chromatographic paper for the analysis of their flow-related phenomena by mathematical fitting to diffusion and imbibition equations. The characterized paper matrix was then applied on the colorimetric detection of aflatoxin B1 (AFB1), by exploiting its inhibitory effect towards acetylcholinesterase (AChE) in Ellman's reaction, where the immobilization of AChE was assessed in two types of chitosan (high and low degree of acetylation (DA)/ molecular weight (MW). The application of a high MW/high DA cross-linked chitosan resulted in the linear quantification of AFB1. In addition, an aptamer (ssDNA)-based detection of fumonisin B1 (FB1) was developed with two aptamers (96 and 40 nt) incubated with FB1, followed by another incubation step with gold nanoparticles (AuNPs) and the addition of NaCl. From all the tested conditions, only the 96 nt aptamer was specific to FB1, whose biosensing properties were regulated by the formation of an aptamer-FB1-AuNP conjugate in $MgCl_2$. These conjugates were stable to NaCl-induced aggregation at increasing concentrations of FB1 and characterized by Asymmetric Flow Field-Flow Fractionation (AF4), a technique showing low LODs in the fg/mL level. Finally, preliminary results for the mycotoxin adsorption of β-chitin scaffolds and N-isobutyryl chitosan (NIBC) hydrogels were obtained for FB1-spiked beer and milk. In this regard, although more exploration is necessary, the preliminary results indicated a slightly better performance from NIBC gels, specially at lower pH values. Furthermore, the potential application of NIBC gels as support materials in molecular imprinting, were explores through the use of L-phenylalanine as an analogue of ochratoxin A, in which no interference with the gel formation process and a complete template removal were observed in the selected material. Nevertheless, further optimization is required for the successful completion of both applications in the selected polymeric materials. In general, through this thesis more understanding

on the diffusive and capillary-driven phenomena in a paper matrix was reported with a subsequent improvement of its performance in mycotoxin biosensing, which led to a space for improving other sensing and biosensing techniques through such immobilization method. Besides, the sole application of an aptamer in the sensitive detection of mycotoxins was achieved by denoting the effect of the incubation conditions and the selected sequence, which outlines another route for tackling aptasensing methods depending on the selected supports and sequences, while leaving an open door for its future implementation as a paper-based detection for mycotoxins. Lastly, the exploratory results on the application of chitin and chitosan-based structured materials, left a promising scope for more research and projects dedicated to the exploitation of these materials in similar and multiple applications.

Table of Contents

List of Tables

List of Figures

List of Abbreviations

ACh	Acetylcholine
AChE	Acetylcholinesterase
ACTh	Acetylthiocholine
AF4	Asymmetric Flow Field-Flow Fractionation
AFB1	Aflatoxin B1
AuNPs	Gold nanoparticles
BHQ2	Black hole quencher
BIS	N,N'-methylene-bis-acrylamide
BSA	Bovine serum albumin
CD	Circular dichroism
CE	Capillary electrophoresis
CF	Cross flow
CL	Chemiluminescence
CTN	Citrinin
DA	Degree of acetylation
DLCA	Diffusion-limited cluster aggregation
DLS-NIBS	Dynamic light scattering with non-invasive back scattering
DLVO	Dejarguin, Landau, Verwey and Overbeek
DON	Deoxynivalenol
DRI	Differential refractive index
DTNB	Dithiobis(2-nitrobenzoic acid)
EAS	East African Community
ECL	Electrochemiluminescent
EGMP	Ethylene glycol methacrylate
ELISA	Enzyme-linked immunosorbent assay
EOW	Electrolyzed oxidizing water
EU	European Union
FAM	Fluorescein amidine
FAO	Food and Agriculture Organization
FB1	Fumonisin B1
FMOC-Cl	9-fluorenylmethyl chloroformate
FRET	Förster resonance energy transfer
FSO	Full-scale output
FTIC	Fluorescein isothiocyanate
FTIR	Fourier Transform Infrared
GCE	Glassy carbon electrode
GO	Graphene oxide
GONCs	Graphene oxide nanocolloids
GS-TH	Graphene-thionine
HFB1	Hydrolysed fumonisin
HLB	Hydrophilic-lipophilic balance
HPLC-FLD	High-performance liquid chromatography with fluorescence detection
HRP	Horseradish peroxide
IAC	Immunoaffinity columns
IgG	Immunoglobulin G
IS	Internal standard
IST	Interfacial surface tension

ITO	Iridium tin oxide
LC	Liquid chromatography
LC-MS	Liquid chromatography-mass spectrometry
LOD	Limit of detection
LOQs	Limits of quantification
L-phe	L-phenylalanine
LXR	Liver X receptor
MAA	Methacrylic acid
MALS	Multi-angle light scattering
MB	Molecular beacon
MINIBC	Molecularly imprinted NIBC hydrogels
MIPs	Molecularly imprinted polymers
MGITC	Malachite green isothiocyanate
µPADs	Microfluidics paper-based analytical devices
MW	Molecular weight
NAPMA	N-(3-Aminopropyl) methacrylamide hydrochloride
NIBC	N-isobutyryl chitosan
NIPAM	N-isopropylacrylamide
nt	Nucleotides
OTA	Ochratoxin A
PB	Prussian blue
PBR	Primer binding regions
PBS	Phosphate buffered saline
PCA	Principal component analysis
PMTDI	Maximum tolerable daily intake
PtNPs	Platinum nanoparticles
QD	Quantum dots
RBITC	Rhodamine isothiocyanate
RT	Room temperature
Rt	Retention time
SAX	Strong anion exchange
SELEX	Systematic evolution of ligands by exponential enrichment
SEM	Scanning electron microscopy
SERS	Surface-enhanced Raman scattering
SPCMs	Silica photonic crystal microspheres
SPE	solid phase extraction
SPR	Surface plasmon resonance
ssDNA	Single stranded DNA
TBAm	N-tert-butylacrylamide
TCT	Trichothecenes
TEM	Transmission electron microscope
TNB	2-nitro-5-thiobenzoic acid
UCNPs	Upconversion fluorescent particles
UK	United Kingdom
ZEN	Zearalenone

List of Symbols

A	Absorbance
a	Radius of the cylindrical scaffold
APt	Assay preparation time
$ATmax$	Maximum assay time
ATt	Assay time
A_{650}/A_{520}	Absorbance ratio
$Blank$	Signal exhibited by the blank (sample with no FB1)
C	Solution concentration
C_i	Concentration of the blank sample
C_s	Residual concentration of FB1after adsorption
D	Diffusion coefficient
dm	Diameter of pores
dL	Distance achieved by a fluid in a porous media
dt	Function of time
σ	Shear stress
σ_L	Vectorial equilibrium along the liquid surface
σ_S	Vectorial equilibrium along the solid surface
σ_{SL}	Vectorial equilibrium at the liquid-solid interface
ε	Molar absorptivity
ε	Dielectric constant
Φ	Porosity of material
$f(\kappa a)$	Henry function
γ	Shear strain
$\dot{\gamma}$	Shear rate
γ	Surface tension
$\%I$	Degree of inhibition
ICi	Color intensity with aflatoxin B1
$IC0$	Color intensity without aflatoxin B1
k	Permeability
ka	Debye length ratio
Kd	Dissociation constant
L	Length of the light path
l	Thickness of the plane sheet
$L(t)$	Front ink distance at a time t
l_t	Front ink distance at a time t
l_0	Front ink distance at time 0
l_∞	Front ink distance at the diffusion equilibrium time
LOD	Limit of detection
$LODmax$	Maximum limit of detection
$LODt$	Treated limit of detection
l_{rel}	Relative distance
Λ	Wavelength
M	Amount of adsorbent
M_t	Amount of diffusing substance entering the scaffold at time t
$M\infty$	Amount of diffusing substance at equilibrium
μ	Dynamic viscosity
η	Zero-shear viscosity
Δp	Pressure difference through the fluid interface

p_c	Capillary pressure
Q_{eq}	FB1 adsorbed per gram of adsorbent
R	Retention ratio
r_p	Pore radius
r_s	Initial front radius
r_0	Radius of the initial wetted area
$R1, R2$	Radii of curvature
S	Swelling ratio
t	Time
t_o	Initial time
t_0	Void time
t_r	Retention time
θ	Contact angle
Ue	Electrophoretic mobility
V	Volume
V_c	Cross-flow rate
V_0	Channel void volume
W	Channel thickness
W_h	Mass of hydrated sample
W_s	Mass of the dry sample
ζ	Zeta potential
$3\sigma_{blank}$	Three times the standard deviation of the blank
$\%$	Adsorption efficiency

Chapter 1
General Introduction

Mycotoxins, secondary metabolites produced by different fungal strains as part of their defence mechanism, are classified as food contaminants by means of their negative impact on the health of humans and animals. The co-occurrence of mycotoxins in several crops has prioritized them as a global concern and an economic issue, which affects both producing and importing countries with an estimated occurrence of 60-80% (Eskola et al., 2020). Along with mycotoxicosis and cancer, mycotoxin exposure could also be associated with reproductive, immune, renal and hepatic complications. Hence, the identification and sensitive quantification of mycotoxins at low levels, are important goals that must be guided according to the worldwide scenario, with careful attention on the geographical and economic constrains of some low-income countries and regions (Khaneghah et al., 2019). Nevertheless, high-income countries are not exempt of mycotoxin occurrence, especially those importing different agricultural products. For instance, the United Kingdom has established a surveillance strategy for the prediction of aflatoxin exposure, in which new techniques are required for an adequate estimation in imported products (Food Standards Agency, 2019).

Besides, billionaire losses are estimated as a result of mycotoxin contamination of food and feed. This not only occurs due to an increase in the production costs with a simultaneous reduction in the livestock production and the international market prices, but it also reduces the stability of the production rates, forcing crop producers to implement cost-added controls such as testing and quality programmes (Agriopoulou et al.,2020; Cinar and Onbaşı, 2019). In this regard, conventional methods for mycotoxin detection comprise chromatographic (HPLC, LC-MS, TLC, GC-MS), and enzymatic assays (ELISA), however due to their complexity and limitation, a reduction in mycotoxin contamination is commonly preferred by crop producers as the main strategy (Cinar and Onbaşı, 2019). As already stated, the analytical and biotechnological needs derived from the occurrence of mycotoxins in a broad range of countries was the main motivation behind the different studies in this thesis. Likewise, this is a priority in developed countries such as the United Kingdom, while in developing countries those new developments can be translated into useful applications for tackling the global mycotoxin situation. As an example, my home country Mexico, has been silently affected by the presence of mycotoxins in staple crops including corn and its derived products (Cerón-Bustamante et al., 2018; Molina-Pintor et al., 2021; Wall-Martínez et al., 2019a; Wall-Martínez et al., 2019b), as well as other relevant products such as coffee, cereals, beer (Marin and Ramos, 2001;

Molina-Pintor et al., 2021), in which their negative effect might be related to several diseases already present among the Mexican population (Garcia and Heredia, 2006; Gilbert-Sandoval et al., 2020; Gong et al., 2008; Wall-Martínez et al., 2019b). Hence, innovative detection methods are required for the simplification and quick detection of mycotoxins in outbreak and occurrence zones, where biosensors of many types appeared as an ongoing alternative to conventional methods. Along with novel biosensing techniques, the utilization of different decontamination methods requires further investigation to achieve their applicability and affordability in regions with high mycotoxin incidence. In this regard, many applications have utilized natural materials, precisely waste-based polymers, for the detoxification of many food products; as already reported for chitin and chitosan (Assaf et al., 2018; Mine Kurtbay et al., 2008). Based on the knowledge of our research group regarding the isolation of chitin from the exoskeleton of crustaceans (shrimp, squid), and its subsequent deacetylation into chitosan, several applications can be explored for those polymeric materials and derived structures. The development of hydrogels (Félix et al., 2005) and scaffolds (β-chitin) from both polymers, have stablished an opportunity for exploring their multiple applications, where mycotoxin removal has a promising future based on previous reported findings for non-structured materials. For those reasons, this thesis explores the improvement of the detection conditions of different biosensing techniques for mycotoxins, and the application of waste-based polymeric matrices for the potential detoxification and detection of such hazards.

1.1 Overall research aim

The United Nations (2015) indicated that mycotoxins are responsible for the contamination of 25% of food crops, yet this value has been underestimated (Eskola et al., 2020). For instance, around 4.5 billion people are annually exposed to aflatoxins, which generates premature deaths of women, high rates of liver cancer and childhood stunting. In addition, aflatoxin contamination generated serious food safety and economic implications for the agroindustry around the world, whilst conventional quantification methods of toxigenic molds are expensive and time consuming (Mangal et al., 2016). The development of cheap and rapid biosensors to detect mycotoxins contamination in food, has gained traction, as the availability of such rapid methods is essential to the prompt detection of contaminated food and chronic exposure to these contaminants.

The working hypothesis of this thesis states that the utilization of waste-based biopolymers as immobilization and decontamination matrices could result in materials of enhanced performance, however, this is not a general effect and depends on the

structural properties of the polymeric matrix, the properties of the selected food matrix and the method optimization. This hypothesis was based on the previous reported utilization of chitosan as immobilization support for enzymes, reactions elements, antibodies, and DNA in diverse biosensing techniques, where its role as both immobilizing agent and reaction medium can be exploited on paper-based methods. In addition, the successful application of chitin and chitosan-based materials for the detoxification of food samples might be in close relation to the negative charge of chitosan in acidic conditions and hydrogen bond adsorption, while the detoxifying effect of chitin is expected due to electrostatic interactions. For those reasons, the decontamination approaches were studied in liquid samples (beer and milk), where the physicochemical and incubation parameter were controlled with ease. Similarly, another hypothesis of this work indicates that the successful application of aptamers in biosensing techniques depends on the binding conditions and the selected sensing platform, which could be the main reason for the favoured utilization of specific sequences and the disparity of results among methods for the same aptamer.

Thesis objective: The overall objective of this thesis was to develop simple, sensitive and accurate biosensing techniques for the enhanced and simplified detection of mycotoxins, and to explore potential decontamination methods through the utilization of waste-based polymeric materials, previously developed in our research group.

Specific objectives:

- To explore the effect of chitosan on a paper-based biosensor through a microfluidic device designed for the colorimetric quantification of AFB1 as a model determination.
- To mathematically describe the movement of samples within the selected paper matrix.
- To develop an aptamer-based biosensor for the colorimetric detection of FB1 by comparing the specificity of two aptamers of 40 and 96 nt (Cheng and Bonanni, 2018; McKeague et al., 2010), under different binding conditions, where the application of gold nanoparticles was needed for studying their distinct performance.
- To study the potential application of chitosan and chitin-based materials as FB1 adsorbents,
- To assess the feasibility of utilizing chitosan hydrogels as support materials for molecular imprinting of a non-toxic surrogate, towards a potential mycotoxin quantification and removal approach.

It is worth mentioning that the novelty of this research relied on the application of a simplified method for paper characterization, in combination with the comparison of two types of chitosan to uncover the relation of their properties with their signal enhancement capacity. Likewise, this is the first time that the highly used, label-free 96 nt aptamer specific to FB1, is applied in biosensing as a single probe-based assay. Finally, new modified polymeric structures, developed at our research facilities, were considered for the first time as mycotoxin decontaminants and MIPs platforms.

1.2 General insights on mycotoxins

In this thesis aflatoxin B1 (AFB1), fumonisin B1(FB1) and ochratoxin A (OTA) were selected for the exploration and improvement of different biosensing and decontamination techniques based on the relevance and high co-occurrence in some products (Eskola et al., 2020).

1.2.1 Rational behind the selected mycotoxins

Produced by several fungal strains, mycotoxins are secondary metabolites with hazardous effects to vertebrates when consumed in contaminated food commodities (Marin et al., 2013). Despite the efforts for decreasing contamination throughout the food chain, only a small number of countries have managed to deploy complete regulations for the existing mycotoxin diversity affecting food and feed around the world (Karlovsky et al., 2016). African and Latin-American nations, in addition to often applying inadequate methods for food harvesting, storage and processing; are at high risk of mycotoxin proliferation due to their tropical and subtropical climate (high temperature and humidity) and heavy rain conditions, which favour the growth of mycotoxigenic fungi in crops. Likewise, ideal conditions for proliferation arise from drought stress, heat stress and insect damage, and have been potentiated with the appearance of climate change (Darwish et al., 2014; Gbashi et al., 2018; Misihairabgwi et al., 2019; Pitt et al., 2013). Furthermore, those countries occasionally fail to implement strategies for the effective reduction of mycotoxin contamination and exposure. This represents a heavy burden to health systems in rural regions of many countries. Besides, developed countries in Europe, Asia and North America are not exempt of issues related to mycotoxin contamination, as they commonly rely on imported foods and exhibit vulnerable groups, for instance people with celiac disease or with vegetarian and vegan lifestyles (Bennett and Klich, 2003; FAO, 2003). Approximately 400 mycotoxins are reported in the literature, where aflatoxins, fumonisins, ochratoxins, zearalenone (ZEN), trichothecenes (TCT) and deoxynivalenol (DON) are the more explored (Cinar and Onbaşı, 2019); from these,

AFB1, FB1 and OTA were selected in this thesis, and discussed in the following sections. In addition, more general information and significant data regarding mycotoxins will be presented in chapter 2.

1.2.1.1 Aflatoxins

Aflatoxins have been widely studied and controlled as they set a main issue for food safety and agriculture economy (Mangal *et al*., 2016). These important toxins are secondary compounds produced after the infectious effect of *Aspergillus* species on food matrices such as cereal, oilseeds, coconut and corn kernels, where their occurrence is predominant from tropical and subtropical regions (Cinar and Onbaşı, 2019; Dhakal *et al*., 2016; Eskola et al., 2020). The ideal growth conditions for aflatoxin-producing fungi oscillate between 21 °C and 35 °C but are benefited by drought stress. Additionally, rain not also promotes preharvest fungal growth, but alters the postharvest dry-down process, and modifies the humidity conditions in both stages (Paterson and Lima, 2011). The synthesis of aflatoxins is a genetically co-regulated process, simultaneously occurring with conidiation (Roze et al., 2004). Aflatoxins are hazardous to health, due to their carcinogenic, immunosuppressive, hepatotoxic, renal effects on humans and animals (Cinar and Onbaşı, 2019). Aflatoxins are the most recurrent mycotoxins in number of incidents, where the most representative aflatoxins are AFB1, AFB2, AFG1, AFG2, and AFM1. In this regard, the EU limit for the carcinogenic AFB1 (Figure 1.1a) in cereals is equivalent to 0.02 µg/kg. While early studies have been focused on diminishing aflatoxin accumulation during preharvest (weather, plant stress) and postharvest (storage) of different crops (Agriopoulou et al., 2020), new approaches are guided to develop practical systems for detection and decontamination of aflatoxins, in which polysaccharide-based sensing is a feasible option (Ma et al., 2016; Zhao et al., 2015).

1.2.1.2 Fumonisins

Fumosinins are a group of mycotoxins generated by diverse fungi including *Fusarium verticillioides*, *Alternaria alternata*, *Aspergillus niger*, *Tolypocladium cylindrosporum*, *Tolypocladium geodes* and *Tolypocladium inflatum* (Abbas et al., 1992; Abbas et al., 1995; Frisvad et al., 2007; Gelderblom et al.,1988; Månsson et al., 2010; Mogensen et al., 2011). The presence of warm weather and rain during crop growth increases the development of fusarium species (Patterson and Lima, 2011). The chemical structure of fumonisin consists on an alkylamine with two propane tricarboxylic acids esterified in hydroxyl groups which are linked to adjacent carbons (Lamprecht et al., 1994). The substitution of up to seven side chains in two specific backbone sites, allows the formation of 28 fumonisin analogues, from which group B is the most common in nature (Cinar and Onbaşı, 2019; Rheeder et al., 2002). Due to the

structural similarities between fumonisins and the sphingoid base backbone from sphingolipids, the acetate incorporation into the backbone occurs through the head-to-tail condensation of acetyl CoA from the biosynthesis of lipids and polyketides (ApSimon, 2001). The importance of fumonisins emerged because of their known hepatotoxicity, brain damage and pulmonary affections to animals (Bouhet et al., 2006; Colvin and Harrison, 1992; Gelderblom et al 1991; Kellerman et al., 1990), and their relation with oesophageal cancer in humans (Marasas et al., 1988). Hence, they are classified as group 2B hazard (Ostry et al., 2017) and are also related to immunotoxicity (Cinar and Onbaşı, 2019). Therefore, monitoring and controlling fumonisin contamination in food commodities such as corn products and seedlings, rice, tomato leaves and seedlings, dried coffee and vine fruits (Bartók et al., 2006; Lamprecht et al., 1994; Bezuidenhout et al., 1988; Noonim et al., 2009; Savi et al., 2016; Varga et al., 2010), is relevant for protecting the health worldwide. The structure of FB1 is indicated in Figure 1.1b, and more information regarding its regulation, structure, impact and quantification methods will be presented in **Chapter 2**.

1.2.1.3 Ochratoxins

Ochratoxins, produced in tropical and subtropical environments by *Apergillus* and *Penicillium*, are polyketides that have been disclaimed as carcinogenic, hepatotoxic, immunotoxic, nephrotoxic, and teratogenic. Ochratoxins are biosynthesized by the combination of phenylalanine from the shikimic acid pathway, with an isocoumarin moiety from the head-to-tail condensation of five acetate units, as denoted in the structure of ochratoxin A (OTA) from Figure 1.1c (Ciegler, 1972). From the different groups (A, B, C), ochratoxin A is the most relevant polyketide due to its ingestion through cereals, herbs, seeds, fruits and wine. In addition, dermal and respiratory exposure along with water, food supplements and food colorant contamination also represent a risk (Cinar and Onbaşı, 2019). The occurrence of OTA is mainly favoured by high temperatures (~30 °C), humidity and drought stress (Paterson and Lima, 2011). Prior to food storage, contamination with OTA commonly occurs during harvesting and handling, yet it could be reduced by some processing steps, as in the case of the 69% reduction in roasted coffee (Napolitano et al., 2007). A value of 5 µg/kg has been stablished as the maximum residue limit (Luan et al., 2015), which also regulates the limit of detection and decontamination target of some approaches. Due to its co-occurrence with other mycotoxins, OTA has been used as a control for measuring the specificity of certain multiplex detection techniques (Jiang et al., 2020; Niazi et al., 2019; Wei et al., 2020).

a)

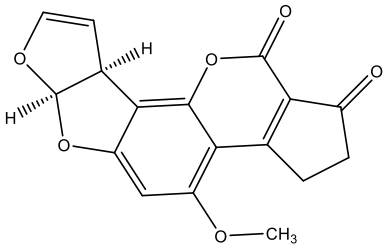

b)

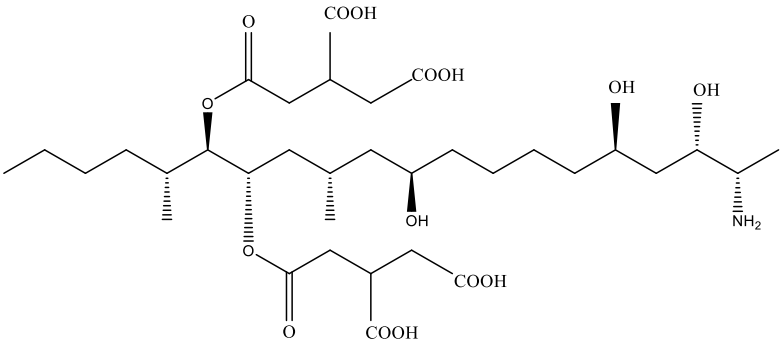

c)

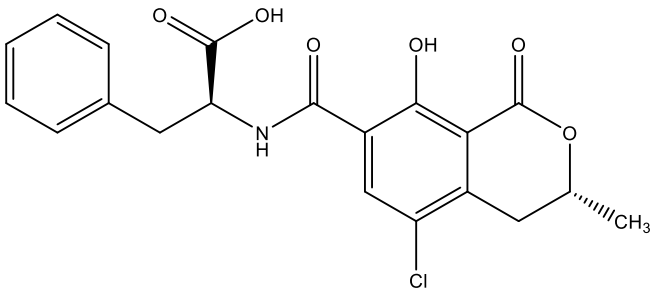

Figure 1.1 Molecular structure of (**a**) aflatoxin A, (**b**) fumonisin B1, and (**c**) ochratoxin A

1.3 Rational behind the selected principles

1.3.1 Biosensors

A sensor can be defined as a device capable to convert a given analyte measurement (input) from a sample into a signal (output). A biosensor consists of three major components: 1) a bioreceptor (e.g. antibodies, aptamers, enzymes, nucleic acids, bacteriophages, whole cells, organelles, etc.); 2) a transducer (optical, electrochemical, thermal, mass, etc.); 3) an actuator that transforms the transducer signal into an action (Harsányi, 1995).

Often, biosensors also incorporate a labelling element (fluorescence, chemiluminescence, etc.) necessary to amplify the signal and increase the detection capacity. As displayed in Figure 1.2, the performance of a biosensor is defined by the relation between the output signal and the analyte. The sensitivity indicates the slope

on the function between these parameters, while in practice denotes the measurement of any target within a given a range, and ideally without preconcentration and precleaning steps. The full-scale output (FSO) is the maximum output signal, while the limit of detection (LOD) is the lowest value of target that can be detected by the sensor. The linearity for the sensor's calibration curve should indicate closeness to a specific straight line, however most cases targeting biological samples exhibit a nonlinear behaviour. The zero-measurand output is the recorded value when no measurand is applied and it is commonly referred as blank sample. Some hysteresis processes might occur due to differences in output at any given measurand value, when increasing and decreasing its concentration within a certain range (Harsányi, 1995; Ahmed et al., 2017).

Other characteristics inherent to a sensor are the repeatability, which is the ability to reproduce output readings at the same measurand value when consecutive applications are carried under the same conditions. The smallest increment in the output is called resolution, while the selectivity and lifetime are crucial properties related to the suppression of environmental interferences and the length of time for sensitivity, respectively. The two critical properties when choosing a specific sensor are the response time, implying that the biosensor has to be quick enough for real-time detection, and the specificity for no cross-reaction with structurally similar compounds (Harsányi, 1995; Ahmed et al., 2017).

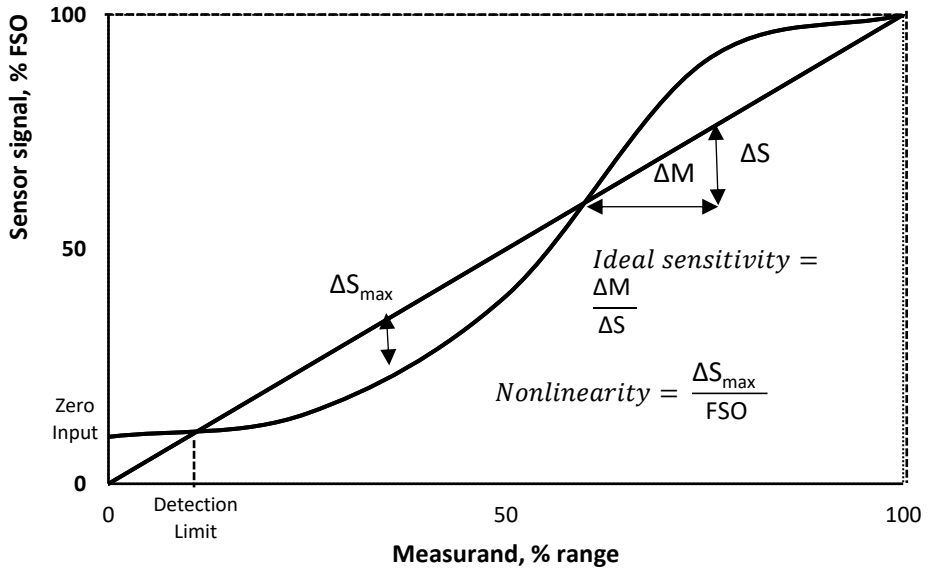

Figure 1.2 Sensor calibration curves and their properties (Harsányi, 1995)

The non-linear behaviour described in Figure 1.2 corresponds to the observe responses in the biosensing techniques reported in the following chapters, mainly due to the biological nature of their bioreceptors, namely enzymes and aptamers (single stranded DNA or RNA). In both cases a dynamic equilibrium governs the molecular biorecognition moment and its limits and is closely related to the previously outlined biosensor qualities necessary for its commercialization (Ahmed et al., 2017). In this work, the utilized enzymatic approach (acetylcholinesterase) for detecting AFB1was previously reported as a reversible inhibition (independent of the enzyme concentration), in which the dynamic equilibrium was translated into a dissociation constant (*Kd*) of the inhibition towards the free enzyme or the substrate-enzyme complex (Arduini et al., 2007). In the case of aptamers a small dissociation constant (*Kd*) value denotes the dynamic equilibrium from the interconversion of inactive states with small amounts of active species (Latham et al., 2009). Identifying the role of dynamic equilibrium in biosensing is important for neglecting background parameters (Jeng et al., 2014), especially through the measurement of a blank sample and the dissociation constant.

1.3.2 Paper as a biosensing platform.

Along with its low cost, paper has attracted the attention due to its capillary action for the passive flow of samples, sample compatibility and its excellent application in on-site and point-of-care analysis (Choi and Choi, 2016; Elizalde et al., 2015). The most common substrates are filter and chromatography paper (made of cellulose fibres) along with nitrocellulose membranes, produced from the nitration of cellulose. In this regard, the physical (porosity, fibre arrangement, optical properties), and chemical (water and solvent insolubility, biodegradability, hydrophilicity) properties of cellulose $(C_6H_{10}O_5)_n$ reflect the versatility of paper as a sensing matrix (Hu et al., 2014). Sample diffusion in paper matrices has been assessed by pulse gradient spin-echo methods (Li et al, 1992), H-NMR (Topgaard and Söderman, 2001), geometrical paper strips, slit microchannels, geometrical porous media (Elizalde et al., 2015; Shou et al., 2014), and capillary imbibition in paper channels (Hong and Kim, 2015); however, many of those methods are complex and required specialized devices and designs, which do not resemble the real procedure in paper-based biosensing. For that reason, a simplified method for assessing the diffusion process in paper will be developed in **Chapter 3**, where the experimental diffusion of 5 model samples in chromatography paper, was mathematically fitted to different equations and validated with a permeability value.

The use of paper as a platform for the quantification of different compounds was reported almost two centuries ago, through the colorimetric detection of uric acid. This concept has evolved from using paper in indicators, dipsticks and chromatography, into what we know as microfluidics paper-based analytical devices (µPADs), were different microchannels are outlined with hydrophobic boundaries (Abadian et al., 2017; Carvalhal et al., 2010). Designing such hydrophobic techniques can be accomplished by precise equipment such as laser cutters, photolithography machines and wax printers (Cardoso et al., 2015). Despite the high resolution obtained with photolithography, inkjet etching, polydimethylsiloxane plotting and wax printing; some of these techniques require expensive and harmful materials (solvents, photoresists, plasma), expensive equipment (photolithography, plotters, wax printers) or specialized personnel, which contrasts with its desired application in low-income countries (Dungchai et al., 2011). Nevertheless, a reduction in manufacturing costs can be achieved by dipping paper templates in wax, applying wax stamps, wax pens, or utilizing permanent markers as hydrophobic materials (Cardoso et al., 2015; Lu et al., 2009). The successful application of permanent markers has been proven as a simple, quick and approachable alternative with no interference in enzymatic reactions (Ghaderinezhad et al., 2017; Gallibu et al., 2016; Nie et al., 2012). Paper-based determination of aflatoxins has been reported in varied designs which mainly include colorimetric lateral flow assays combining gold nanoparticles (AuNPs) (Anfossi et al., 2011; Moon et al., 2012) or magnetic beads with antibodies (Liu et al., 2015), where immunoglobulin G (IgG) worked as a control line and target-BSA as the test line (Shim et al., 2007). Similarly, dipsticks have been applied with biotin modified-aptamers through the competitive binding between AFB1 and a cy5-modified probe, where the two specific zones treated with anti-cy5 antibody or streptavidin indicated a positive or negative result (Shim et al., 2014). In the case of FB1, paper-based developments have been carried out in lateral flow immune assays combined with gold (Anfossi et al., 2010; Molinelli et al, 2009; Venkataramana et al., 2014), which also allowed the multiplex analysis of two (Wang et al., 2013a) and four (Lattanzio et al., 2012) mycotoxins. On the other hand, lateral flow immunoassays have been compatible with multiplex analysis by chemiluminescent signals (Zangheri et al., 2015), fluorescent quantum dots (Anfossi et al., 2018; Hou et al., 2020) and fluorescent nanoparticles (Guo et al., 2020). On that note, more paper-based biosensors will be reported in **Chapter 2** for the specific detectiohallowen of FB1. Likewise, more methods for mycotoxin detection will be discussed in the following sections.

1.3.3 Rational behind the application of acetylcholinesterase (AChE) in the detection of AFB1

Acetylcholinesterase is the enzyme responsible for the catalysis of acetylcholine (ACh) hydrolysis, food and water intake mediation, aggressiveness in sexual behaviour, and sexual development. Its inhibition hence represents a decrement in the hydrolysis rate of ACH. Although dietary FB1 has been reported as inhibitor of the AChE activities in brain an hypophyseal regions (Gbore, 2010), significant effects were observed only through the in vitro incubation of high concentrations of FB1 with AChE (p<0.05), as indicated in Figure 1.3, where the same trend was found for OTA (p=0.003), which in both cases were not suitable for their further application in sensitive biosensing techniques through this mechanism. In the case of FB1, an interference in sphingolipid metabolism takes place through the inhibition of ceramide synthase, which eventually results in disruption of basal membranes and endothelial cells (Gbore et al., 2010). On the contrary, a greater AChE activity was observed in lymphocytes incubated with OTA (Lautert et al., 2014), which explains the absence of significant differences among every concentration in Figure 1.3.

The enzymatic analysis of AFB1 has been carried out trough Ellman's method, where AChE is reversibly inhibited by AFB1, therefore less substrate (Acetylthiocholine: ACTh) is hydrolysed into thiocholine. The measurement of this compound by the addition of dithiobisnitrobenzoate (DTNB), results in the formation of the yellow (λ= 412 nm) 2-nitro-5-thiobenzoic acid (TNB), where less amount is produced at higher AFB1 concentrations (Figure 1.4). From the different enzymatic sources, AChE from electric eel is the most sensitive to AFB1 (Arduini et al., 2010). In fact, instead of binding the active catalytic site in AChE (stearic subsite), the pyrone moiety from AFB1 binds to a peripheral site (tryptophan 86 residue) in AChE, which is close to the active site and is relevant to non-synaptic functions (Cometa et al., 2005; Puiu et al., 2012). In the case of AFB1, this mechanism is independent of the incubation time and the enzyme concentration (allowing short assay times), as well as non-competitive, which allows the use of high substrate concentration. Such inhibitory action is favoured at pH 8 and a maximum methanol concentration of 50%, however, it also portrays cross reaction with AFB2 (Arduini et al., 2007; Arduini et al., 2010).

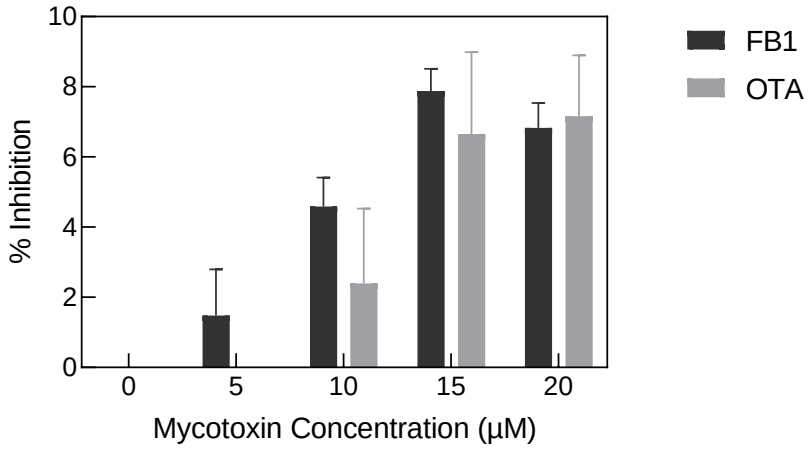

Figure 1.3 Inhibition percentage of different concentrations of FB1 and OTA on the activity of AChE. (Incubation (10 min) of mycotoxin (5 µL), AChE (50 U/mL, 80 µL), DTN (10 µL to a final concentration of 500 µM). Followed by 5 min incubation with ATCh (10 µL to a final concentration of 300 µM). % Inhibition obtained from the absorbance at 412 nm (TECAN plate reader) in comparison to the blank; n=3)

As an alternative to bulk experiments, µPADs are suitable for the conduction of enzymatic methods with colorimetric read outs. Nonetheless, some shortcomings are indicated by the lack of colour homogeneity at the detection zones, due to colour washing and enzyme mobility (Gabriel et al., 2016). In this regard, the application of Ellman's method has been improved by immobilizing AChE with gelatine (Pohanka, 2013), sandwiching AChE in sol-gel materials, which preserved its enzymatic activity and allowed reproducibility (Hossain et al., 2009), or applying materials such as Prussian-blue and polyvinylalcohol, yet more immobilization methods should be explored for the determination of AFB1 through this enzymatic method (Arduini et al., 2010). The effect of the application of chitosan on µPAD test zones for uric acid and glucose detection, denoted is role as microenvironment in enzymatic reactions (Gabriel et al., 2016), however little has been explored about the influence of chitosan properties on the final biosensing performance. The aforementioned will be explored in **Chapter 4**, through Ellman's determination of AFB1 as a model reaction in µPADs designed with permanent markers.

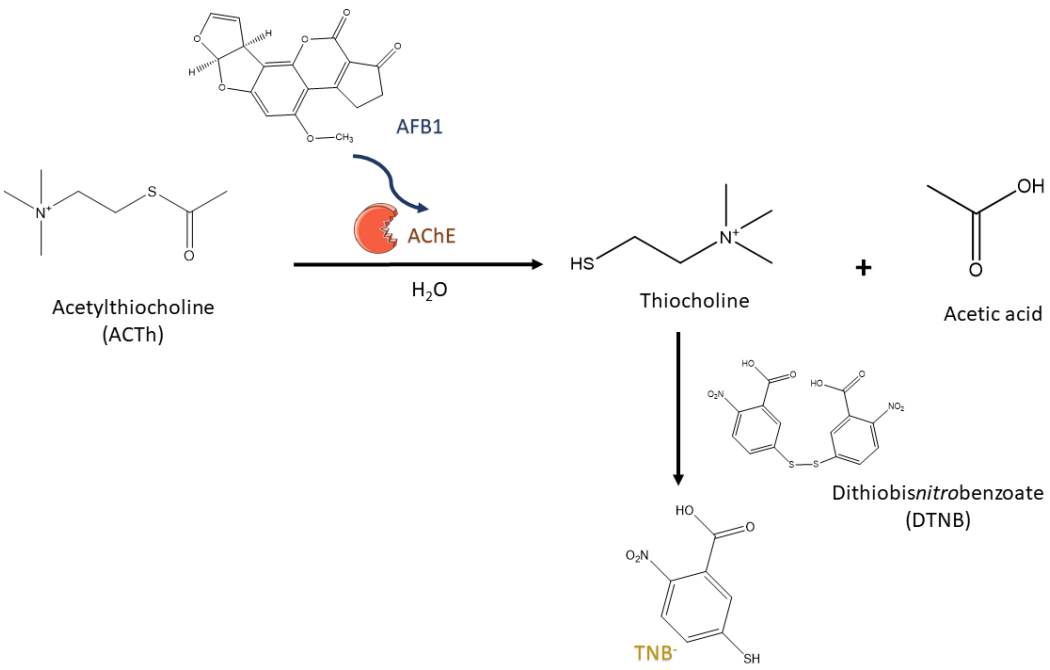

Figure 1.4 Detection reaction in Ellman's assay

1.3.4 Rational behind the application of gold nanoparticles functionalized with aptamers.

1.3.4.1 Gold nanoparticles (AuNPs)

Gold nanoparticles (AuNPs) have gained immense traction over the recent two decades or so. This is due to a wealth of applications because of their optical properties induced by their particle size, which can be conveniently modified. The surface plasmon resonance (SPR) of the surface electrons, enables the utilization of AuNP in attempts where the interaction with light is mediated by the particle size and shape (Sonavane et al., 2008). The observable colour of AuNPs originates from localised plasmon resonance (LSPR) in which the negative free conduction electrons move away from the positive particle core by the effect of an incident light, as the oscillation of the electron cloud is produced by the net charge restoring force. LSPR can be explained by Mie theory, which describes the interaction between light and spherical particles by integrating the particle size and dielectric functions of both the medium and the metal. A total extinction value can be obtained from the sum of absorption and scattering cross sections, from which the scattering to absorption ratio of spherical particles increases with bigger particle sizes (Wrigglesworth and Johnston, 2021).

Gold nanoparticles are synthesized through the reduction of gold salts by reducing agents, which trigger the nucleation of Au ions. Such agents also become stabilizers by adsorbing to the particles, thus equally charging the nanoparticles so they become colloidally stable as they repel each other (Sperling et al., 2008). The most studied stabilization methods for AuNP synthesis comprise the reduction with phosphorus in carbon disulphide from Faraday, the Brust-Schiffrin biphasic method for thiolated-AuNPs, and the citrate reduction method improved by Frens in 1973 from the 1951's Turkevich method. The preparation of AuNP can be conducted as either a "top-down" approach, where bulk Au is broken down, or as a "bottom up" method, in which AuNPs formed from single molecules through chemical or biological reduction (Zhao and Astruc, 2013).

The synthesis of AuNPs by citrate reduction starts with boiling a diluted tetrachloroauric acid ($HAuCl_4$), followed by the stirred addition of trisodium citrate until a red solution is formed as described in reaction 1.1, where the concentration of sodium citrate governs the size of AuNPs (Verma et al., 2014).

$$2HAuCl_4 + 3C_6H_8O_7 \text{ (citric acid)} \rightarrow 2Au + 3C_5H_6O_5 \text{ (3-ketoglutaric acid)} + 8HCl + 3CO_2 \quad (1.1)$$

The synthesis of gold nanoparticles with sodium citrate contributes to the formation of electrostatic repulsive forces, and therefore with their own stability. Charge screening is caused by salt and other cationic compounds that, by allowing London forces, head particles to aggregation (Pandey et al., 2016). Particle aggregation is visually detected by the colour change from a red to a blue solution after salt addition (Figure 1.5), while single-strand DNA oligomers can stabilize AuNPs, impeding the salt-aggregation process (Rosi et al., 2005). Based on the Dejarguin, Landau, Verwey and Overbeek (DLVO) theory, a diffusion-limited cluster aggregation (DLCA) is most plausible to occur in the interaction of NaCl 0.2M with gold nanoparticles in Figure 1.5, as there is faster aggregation kinetics produced by a lower energy barrier than the thermal energy in convergent particles, whose effect rapidly maintains them adhered (Meakin, 1983; Pamies et al., 2014).

a)

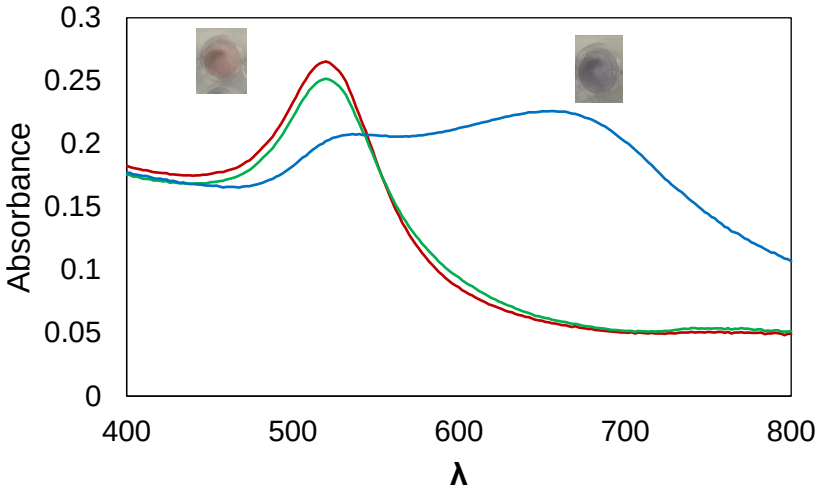

b)

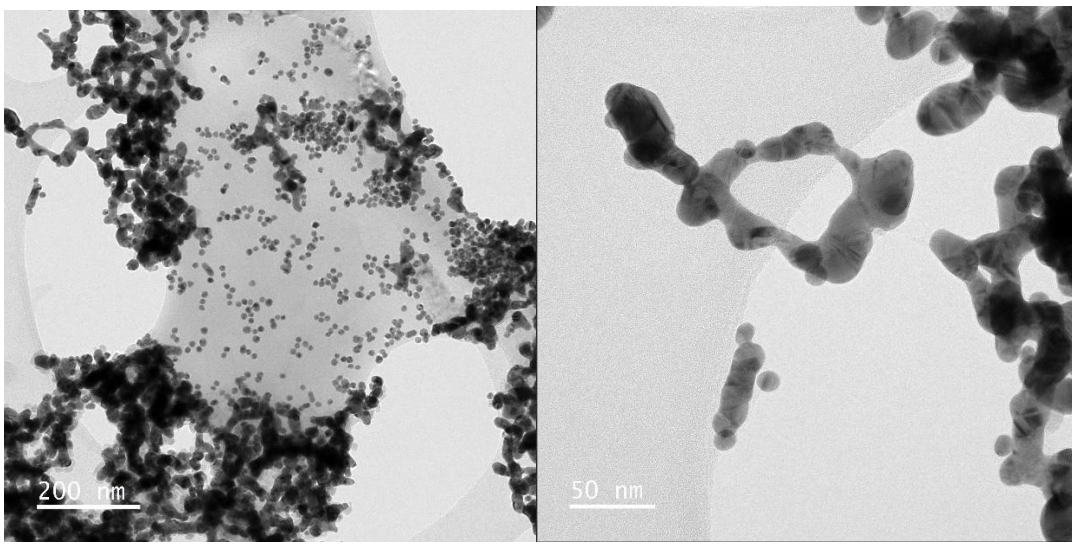

Figure 1.5 (**a**) UV/Vis absorbance spectra of a stock of AuNPs (—), and upon addition of NaCl 0.1 M (—) and 0.2 M (—). (**b**) TEM images of AuNPs aggregated with NaCl 0.4 M (Stock concentration: 2.4 nM particle size: 21.53±0.3 nm, polydispersity index: 0.08±0.01)

1.3.4.2 Aptamers

Aptamers are single-stranded(ss) molecules of either DNA or RNA with high binding affinity for the molecular recognition of specific molecules (Yang et al., 2017). Linear aptamers can adopt 3D conformations, for the selective and sensitive interaction with their target, which makes them comparable to antibodies (Yang et al., 2011). Such biorecognition is modulated/by hydrogen bonds, van der Waals, stacking and electrostatic interactions. The high affinity of aptamers makes them ideal components for the development of biosensing techniques. Aptamers are generated by a selection process called systematic evolution of ligands by exponential enrichment (SELEX), which involves the interaction of a DNA library with a target molecule for certain time

and the amplification of bound oligonucleotides sequences (McKeague et al., 2010; Yang et al., 2011). Due to the somehow recent exploration and development of aptamers specific for mycotoxins, especially FB1, the interested of this thesis was focused on the exploration, simplification, and optimization of novel biosensing approaches incorporating the reported sequences. Extensive information regarding aptamers and their applications will be found in **Chapter 2** and **Chapter 5**.

1.3.4.3 Adsorption and desorption of aptamers on AuNPs for mycotoxin detection

The scattering properties and the change in the surface plasmon peak from citrate coated and aggregated particles, can be applied for biosensing based on the desorption ability of aptamers immobilized on gold nanoparticles, upon the addition of target molecules by means of their specific binding. The presence of non-specific interactions between DNA and gold nanoparticles was explored through some preliminary experiments regarding the effect of aptamer adsorption on the zeta potential of AuNPs, as indicated in Figures 1.6a and 1.6b. The selected aptamer specific to OTA (OTAap: 5'-CTG GGA GGG AGG GAG GGA TCG GGT GTG GGT GGC GTA AAG GGA GCA TCG GAC ACC CGA TCC C-3') has been successfully reported in the quantification of this mycotoxin (Luan et al., 2015), and as already displayed in Figure 1.6b, AuNPs stabilized with this aptamer acquired a more negative Z potential in comparison to the blank samples (AuNP stock). A more negative charge is caused by the aptamer adsorption on the particle surface, which leads to a charge redistribution on the conjugate (Li and Rothberg, 2004a), and the subsequent stabilization of colloidal gold (Figure 1.6a), whose effect cause the addition of negative charges and the enhancement of repulsive forces (Pamies et al., 2014). In its natural conformation, ssDNA maintains a coil structure with an exposed phosphate backbone, whose negative charge determines the interactions in aqueous solutions (Li and Rothberg, 2004a). However, in the appropriate ssDNA:AuNP molar ratio, AuNPs are stabilized by ssDNA due to exposition of its bases when uncoiled. Additionally, the backbone's negative charge is remote enough to allow the attachment of the aptamer bases to the AuNP, by van der Waals attractive forces (Li and Rothberg, 2004b), as lustrated in Figure 1.7. During such interaction, both the AuNPs and the aptamer molecules attract counterions from the media by forming double layers (Li and Rothberg, 2004a). Even though the aptamer bases are the mean aspect for its immobilization on citrate-capped AuNP, the hydrophobicity of the sugar residues and their modifications also play an important role in the physi-sorption of DNA on AuNPs (Derbyshire et al., 2012).

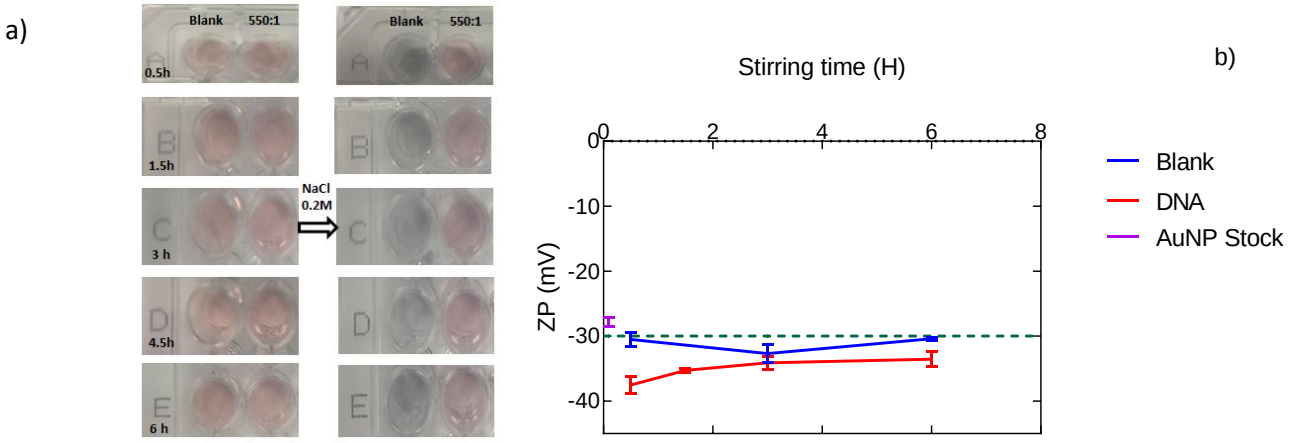

Figure 1.6 (**a**) Aggregation profile and (**b**) zeta potential of AuNPs functionalized with OTAap at different stirring times. (OTAap:AuNP ratio= 550:1, incubation at room temperature)

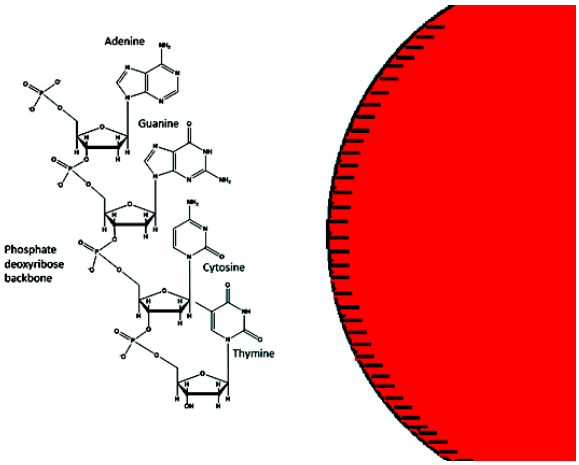

Figure 1.7 Representation of the interaction between an uncoiled DNA structure and negative AuNPs

The stabilization of AuNP with the minimum amount of aptamer, is essential for improving the sensitivity of any mycotoxin quantification assay based on the preservation from salt aggregation (Derbyshire et al., 2012). The most common and simple colorimetric aptasensing techniques combining AuNPs and aptamers, comprise the functionalization of AuNPs with aptamers, followed by target incubation, which promotes aptamer releasing and allows aggregation from salt (Dalirirad and Steckl, 2019). This procedure has been performed for OTA detection (Yang et al., 2011), where the presence of OTA results in aptamer desorptiont, target binding and further particle aggregation, as outlined in Figure 1.8. Based on a length-dependent adsorption and desorption of ssDNA on AuNP, as the length of the chain increases,

there is a trend for keeping a coil structure that needs more transitory variations to be uncoiled. Those structural fluctuations are more dominant in short DNA sequences, as they contain less segments imposed to a coiled arrangement, hence short ss-aptamers adsorb and desorb more rapidly (Li and Rothberg, 2004b). Improvements to the aforementioned design, include the performance of aptamers on paper strips, reported for the detection of ochratoxin A, in which gold nanoparticles (Wang et al., 2011a) and quantum dots (Wang et al., 2011b) were functionalized with two DNA probes coupled to streptavidin for a competitive reaction or as a control probe.

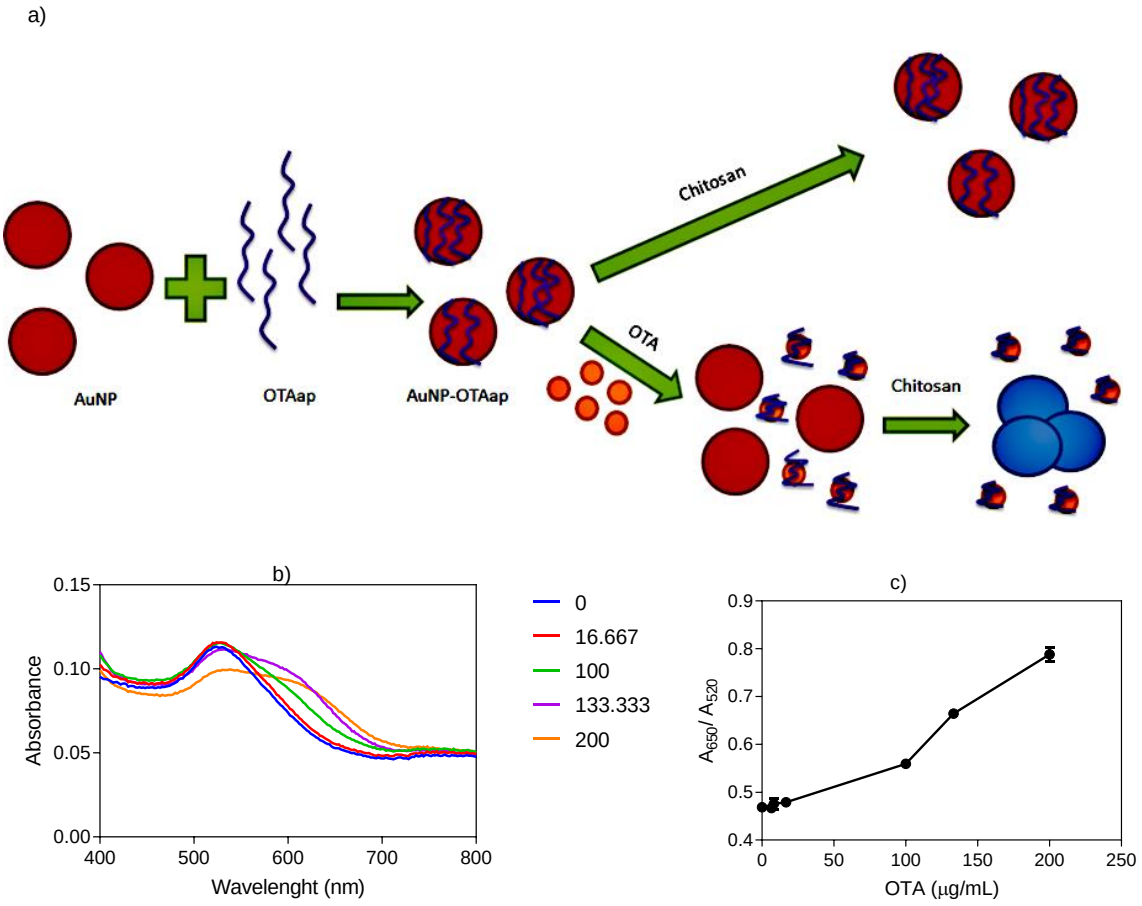

Figure 1.8 (**a**) Colorimetric assay for OTA detection using and an aptamer (OTAap) and citrate-capped AuNPs. (**b**) OTA biosensing assay based on the OTAap-AuNP behaviour at varying target concentrations (as shown in label); and (**c**) its corresponding $A_{650/A520}$ ratio

Aptamers could be hybridized by electrostatic interactions with cationic polymers such as poly(diallyldimethylammonium chloride), which also aggregates AuNPs as proven in the detection of OTA with OTAap (Luan et al., 2015). Besides, quantum dots were also conjugated with aptamers specific to AFB1, where AuNPs served as quenchers, with a fluorescence recovery upon target binding (Sabet et al., 2017). A comparison of two aptamers specific to FB1, through a colorimetric detection with AuNP will be presented in **Chapter 5**, where two different mechanisms will be reported, with an

important role from the binding conditions and the read out signals, on the final selectivity, linearity, specificity and sensitivity of the biosensing technique.

1.4 Rational behind the selected methodology

To characterize the model samples in diffusion experiments, as well as paper matrices, AuNPs, and aptamers in biosensing techniques, multiple analytical instruments were utilized during the length of this PhD. Therefore, some theoretical and experimental aspects of these techniques, that are not detailed in the following chapters, will be explained in the next sections.

1.4.1 Rheological properties

Viscosity describes the resistance to flow that a liquid displays due to its internal friction. In viscosity determinations, a layered flow, also known as shear flow, is produced by the action of a shearing force, denoted as shear stress. The force in shear stress acts over a unit area, which generates a gradient of velocities (shear rate) throughout the sample width. The ratio between shear stress and shear rate determine the dynamic viscosity value, often indicated as shear viscosity (Malvern Panalytical), as summarized in Figure 1.9:

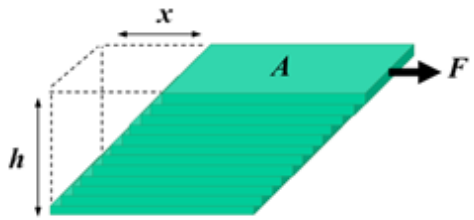

Shear stress (Pa): $\sigma = F / A$

Shear strain: $\gamma = x / h$

Shear rate (s^{-1}): $\dot{\gamma} = d\gamma / dt$

Shear viscosity (Pa s): $\sigma / \dot{\gamma}$

Figure 1.9 Representation of the dynamic viscosity profile and its equations, figure from Malvern Panalytical

The dynamic performance of a liquid, whose equilibrium has been disturbed by a mechanical stress is defined as dynamic viscosity. Depending on the type of liquid, when the relaxation time is shorter to the time of shear stress a viscous flow is expected. On the other hand, if the deformation time is shorter than the time to achieve molecular equilibrium, an elastic performance occurs. Viscoelastic samples are observed when both behaviours take place (Harrison and Barlow, 1981). The aforementioned is key to determine the measuring system for assessing the dynamic viscosity of samples. In the case of the ink models from **Chapter 3**, a Kinexus

rotational rheometer was used for the analysis of their viscosity, where a double gap cell was used due to its suitability to highly fluid-like samples.

1.4.2 Scanning, particle size and z potential analysis.

As indicated in **Chapter 5**, a UV/Vis spectroscopy wavelength scan of AuNPs is performed from 400-800 nm in spectrophotometer, from which the concentration of the AuNP stock solution can be calculated according to Lambert-Beer equation:

$$A = C * \varepsilon * L \tag{1.2}$$

Where A, C, ε, and L represent the sample absorbance, solution concentration, molar absorptivity and the length of the light path (cm) respectively. This equation can be applied for the characterization of AuNPs by means of the specific wavelength, in which light extinction (absorption and scattering) occurs due to SPR. As the particle size increases, the maxim absorption shifts to greater wavelength values from 500 to the near-infrared region. When transversal and longitudinal SPR take place, a broad peak is observed, indicating sizes above 100 nm (Cytodiagnostics).

The particle size distribution (nm) of AuNPs in **Chapter 5** was determined by dynamic light scattering with non-invasive back scattering (DLS-NIBS) with a measurement angle of 173°, as indicated in Figure 1.9a. Whereas, the zeta potential was measured by mixed laser Doppler elocimetry and phase analysis light scattering (M3-PALS). A Malvern Zetasizer NanoZS (Malvern, UK) fitted with a red laser (λ=632.8 nm) was used for both determinations. The principle of operation of the DLS determination is illustrated in Figure 1.10. The general light scattering detection involves a light passing from a laser through a polarizer, from which its incidence trespasses a scattering medium. Once scattered, the light goes to an analyser at a given polarization, continuing its way to a detector, whose position determine the scattering angle (Berne and Pecora, 2000). Size determination in Zetasizer Nano is carried out by measuring the Brownian motion of particles, through the incidence of a laser on particles for the analysis of the scattering intensity fluctuations (Malvern). The concept of Brownian motion implies the movement of particles in a suspension, motivated by random forces from the collision with solvent molecules (Stetefeld et al., 2016). According to DLS theory, small particles move faster while bigger particles exhibit a slower motion. In this regard, the Stokes-Einstein equation relates the friction of particles to their radius and viscosity, associating the size of a particle to its speed. This particle movement will create dark and bright areas of scattered light, known as scattering intensity fluctuations, which can be digitally correlated by comparing two signals within a small-time frame, where large particles portray slow fluctuations and vice versa. The

application of this correlation function derives in a size distribution graph (Malvern; Stetefeld et al., 2016).

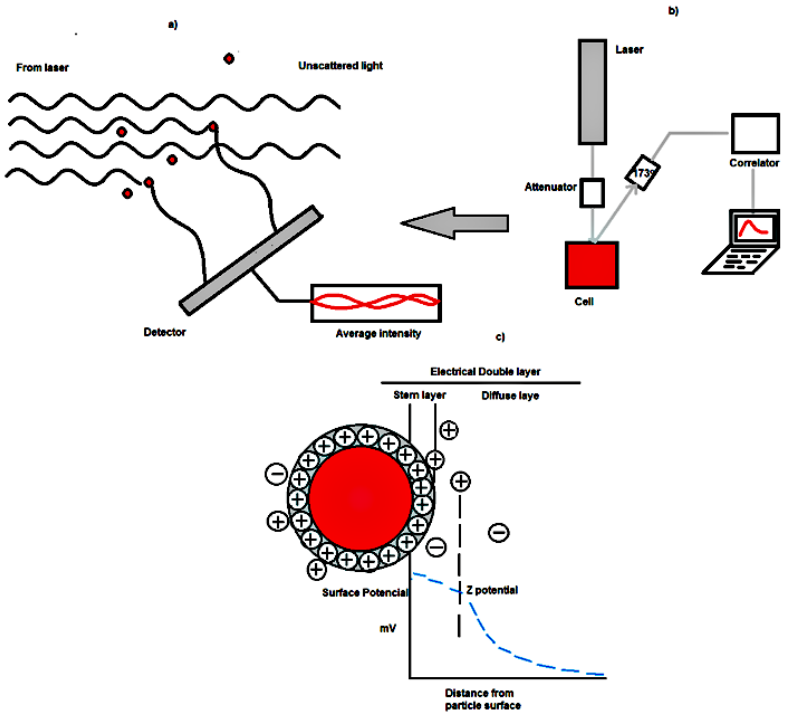

Figure 1.10 Representation of the dynamic light scattering principle (**a**); schematic layout of the ZetaSizer NanoZS instrument fitted with non-invasive back scattering (DLS-NIBS) (**b**), and fundamentals of the calculation of the zeta-potential (**c**), adapted from Malvern

On the other hand, the zeta potential determination of nanoparticles in ionic solution is completed by the formation of two layers around each particle, due to arrangement triggered by the surface charge. The layer bound to the particle surface, known as the Stern layer, is formed by ions with opposite charge to that from the particles. A second layer, named Diffusive layer, contains untied ions which differentiate from the ions in the Stern layer during the Brownian motion of the particle and its shell-like outer layer (Figure 1.9b). The boundary between both layers is known as the slipping plane, whose electrostatic potential is what we call zeta potential, and is in close relation to the charge of the surface. Henry equation (1.3) is utilized for converting the signal obtained after the application of an electrical field on the sample, where the electrophoretic mobility is reported by laser doppler velocimetry (Clogston and Patri, 2011; Salopek et al., 1992).

$$Ue = \frac{2\varepsilon z f(\kappa a)}{3\eta} \qquad (1.3)$$

Where the electrophoretic mobility (Ue) is given by the product of the dielectric constant (ε), zeta potential (z), and Henry function ($f(\kappa a)$: 1.5 or 1.0) for the particle radius to Debye length ratio (ka), divided by the medium absolute zero-shear viscosity (η). The zeta potential values indicate if nanoparticles are neutral (-10 to +10 mV), cationic (>+30 mV) or anionic (<-30 mV). In addition, particles with zeta potential values between -30 mV to +30 mV are considered unstable, while values beyond this region indicate stable particles (Clogston and Patri, 2011; Malvern).

1.4.3 Microscopy analysis

To bear with the limitations of optical microscopes, an acceleration of electrons (2 to 1000 keV) could be generated to interact as a high energy beam with the atoms within a sample. In scanning electron microscopy (SEM) the broad sample thickness allows imaging by transmitting particles from its surface (electrons, photons, x-rays). On the other hand, in transmission electron microscope (TEM), the sample is thin enough for the transmission of unabsorbed electrons from which the image is formed. SEM is suitable for reporting the topographic, crystalline, chemical and electrical profile of different samples. Its general procedure applies an electron beam (2-40keV) from a thermal gun (tungsten, lanthanum hexaboride) or a field emission gun (cold cathode), which is demagnified to a fine probe by a condenser. This probe is focused over a specific sample area by the scan coils. A tear-drop penetration occurs producing more electrons (secondary, backscatter, Auger electrons, X-rays), which are detected along with the electron beam into a monitor to form the image (Vernon-Parry, 2000).

The electron-specimen interaction occurs as either elastic or inelastic. In elastic interactions the electron beam is deflected by the specimen atoms (nucleus) or by same-energy shell electrons, in which no energy is lost, and backscattered electrons are used for imaging. Opposite to the aforementioned, during inelastic interactions the electron beam transfers energy to the atoms, and results in secondary electrons (<50 eV) suitable for imaging and analysis. Prior to their analysis many samples only need to be loaded on a carbon tape, however some nonconductive materials require a metal coating step (Zhou et al., 2006).

TEM also explores the advantages of focusing the electron beam, where its high energy produces electron excitation in the atoms from the specimen. The chemical characterization in TEM is carried out by either energy-dispersive x ray spectrometry in which a spectrum is obtained from localized specimen regions, or electron energy-loss spectrometry, where energy losses from the electron beam passing through the specimen. In TEM, the diffraction profile and phase contrast from the specimen are using during imaging (Fultz and Howe, 2012). In this thesis SEM analysis were carried

for the characterization of paper matrices with different treatments (**Chapter 4**) and the exploration of the microstructure in natural polymeric materials (**Chapter 6**).

1.4.4 Asymmetric Flow Field-Flow Fractionation (AF4)

Originated in the 60s, asymmetric flow field-flow fractionation (AF4) is a separation method based on the hydrodynamic diameter of a sample. Such separation occurs through the diffusion of particles (1 nm to µm); with low sample alteration and the capacity to analyse the molecular weight, size, stability and composition of a range of polymer, nanomaterials and biological samples (bacteria, viruses, DNA) (Cho and Hackley, 2010; Hagendorfer et al., 2011), as well as the analysis of their chemistry, concentration and size by UV/Vis, fluorescence and differential refractive index (DRI) (Hagendorfer et al., 2011). The procedure for AF4 is displayed in Figure 1.11, where a parabolic laminar flow transports different particles in a long thin channel, at different velocities, due to their layer arrangement caused by a perpendicular cross-flow. Unlike larger particles, the smaller particles will have a greater diffusivity due to their Brownian motion. Therefore, they will diffuse to an upper layer from the accumulation wall (membrane) and migrate first, producing a fractionated separation with different elution times. From these fractions, a relation between particle size and retention time can be incorporated for further measurements, as indicate in Equation 1.4 and 1.5 (Cho and Hackley, 2010; Mudalige et al., 2015).

$$R = \frac{t_0}{t_r} \tag{1.4}$$

Where R, t_0 and t_r are the retention ratio, void time, and retention time, respectively.

$$t_r = \frac{t_0 V_c w^2}{6 D V_0} \tag{1.5}$$

Where the retention time (t_r) is given by the void time (t_0), cross-flow rate (V_c), channel thickness (W), diffusion coefficient (D) and the channel void volume (V_0) (Cho and Hackley, 2010). The void peak is closely related to the dead volume in the channel as well as any unretained sample, and normally appears at the beginning of each run, referred as void time (Engel et al., 2014).

Once the eluted fractions move towards the detectors, the retention times can be related to specific particle sizes. Additionally, the radius of gyration can be obtained from multi-angle light scattering (MALS), while the hydrodynamic diameter is calculated from dynamic light scattering (DLS) results. In some cases, the molecular weight is determined through refractive index or viscometry measurements (Cho and Hackley, 2010). AF4 analysis of aptamer-FB1-AuNPs will be presented in **Chapter 5**, where this technique revealed a promising biosensing technique when analysing multiple signals (MALS, DLS, UV/Vis).

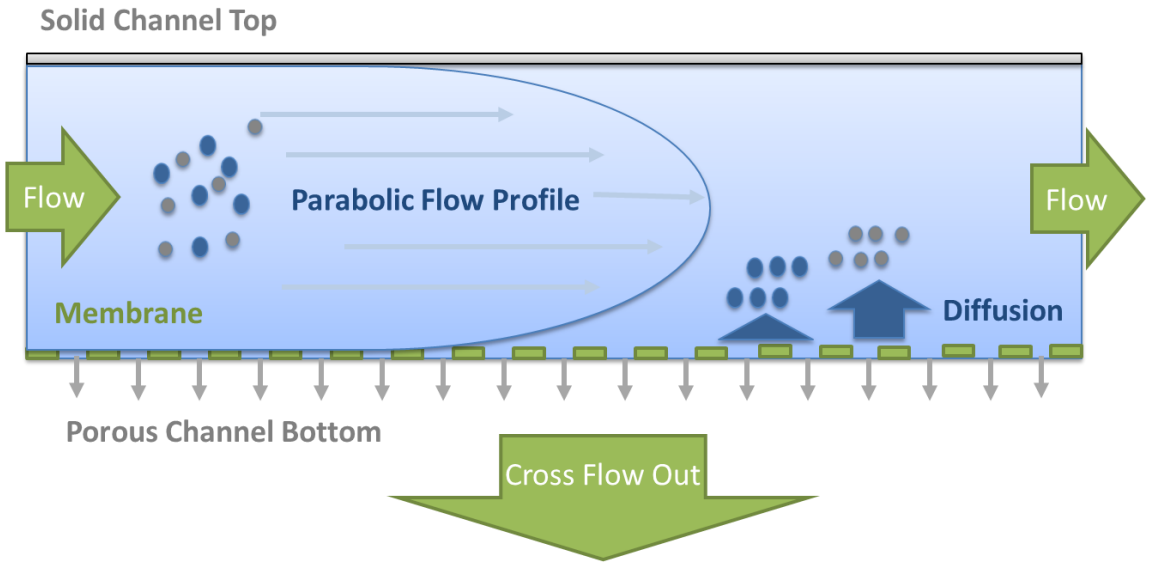

Figure 1.11 Asymmetric Flow Field-Flow Fractionation principle from Postnova

1.4.5 Folded DNA structure prediction by Mfold

Although the Mfold software was launched for RNA folding, DNA structures can be predicted since 1996. This tool integrates stacking, single mismatch, dangling end, terminal stacking and loop parameters, along with Na^{+} and Mg^{++} corrections. This web server needs to be fed with a formatted DNA sequence and its relevant constrains such as structural nature (linear, circular), folding temperature (0 to 100 °C), and the ionic conditions [Na^{+}] and [Mg^{++}]. The main obtained results are the energy dot plot, from which the algorithm favours the structure with the minimum free energy (ΔG), and minimum folding free energies in base pairs (Zuker, 2003). A 2D DNA structure is mapped based on the energy dot plot, here, as shown in Figure 1.12, each dot represents a base pair, where each colour is specific to one of the predicted structures, from which red is associated to the lower free energies. The whole folded structure is predicted by matching a base pair according to the crossing line (diagonal), whenever a coloured dot is indicated.

a) b)

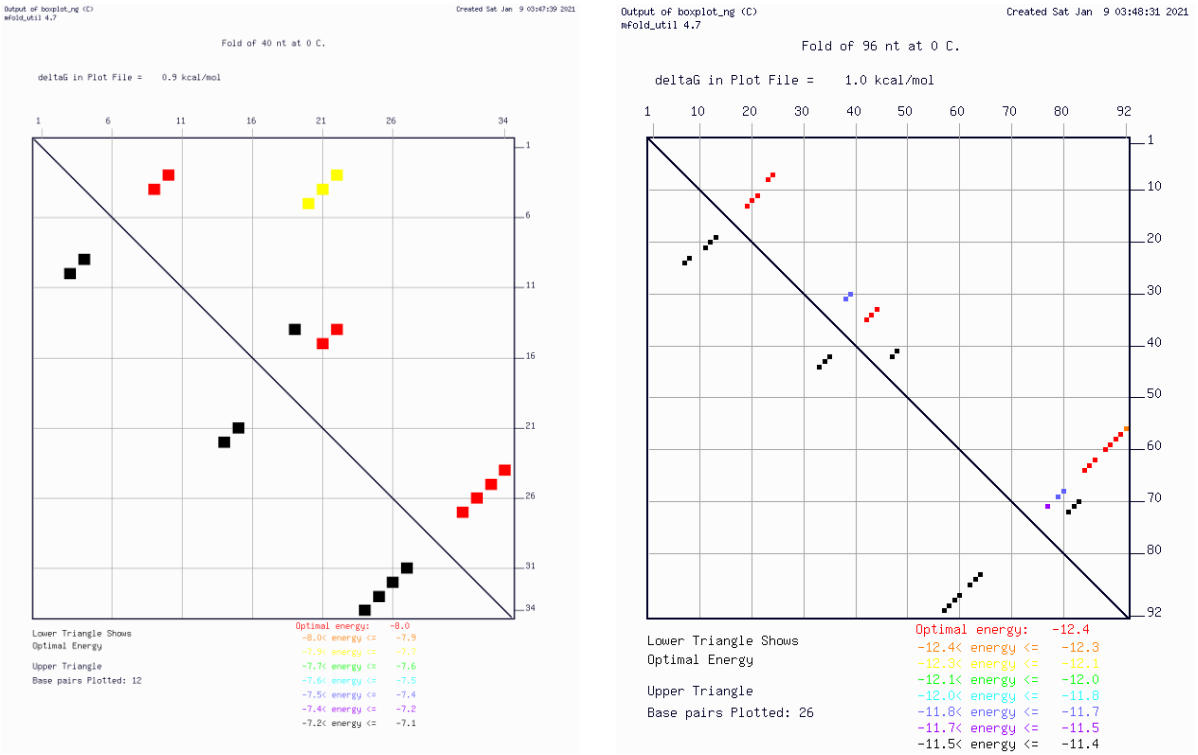

Figure 1.12 Energy dot plots for a (**a**) 40 nt and (**b**) 96 nt aptamer utilized in **Chapter 5**. (Folding constrains 40 nt: 0°C, [Na^+]=85 mM, [Mg^{++}]=2 mM; Folding constrains 96 nt: 0°C, [Mg^{++}]=1 mM)

1.4.6 High-Performance Liquid Chromatography with Fluorescence Detection (HPLC-FLD) and Liquid Chromatography-Tandem Mass Spectrometry (LC-MS)

Novel methods for mycotoxin detection, require a validation step by commercial ELISA (Masikini et al., 2015; Wu et al., 2013), LC-MS/MS (Di Nardo et al., 2017), or HPLC (Quan et al., 2006). Similarly, decontamination processes need the analysis of mycotoxins by conventional methods, in order to quantify the amount of toxin that was removed. In **Chapter 6**, FB1 removal was measured by LC-MS, however FB1 can be also quantified by HPLC-FLD. Liquid chromatography (LC) is based in the interaction of a stationary and a mobile phase with the sample molecules. The general liquid chromatography setting consists in a reusable column with a packing material, sample injection elements (syringe, valve), and high-pressure pumps to control the solvent flow through the column and to the detectors. A good chromatographic separation requires the optimization of the conditions in the aforementioned elements and takes place through the differential migration of solutes as either liquid-liquid (partition), liquid-solid (adsorption), ion-exchange (ionic groups) and size exclusion separation

(porous material). The detectors can account for general (bulk) properties such as refractive index of both the solute in the mobile phase, or a selective approach focused on the solute, as in UV absorption. UV/Vis detection is the most used, due to its measurement of light absorption, followed by differential refractometers, where the refractive index is compared between mobile phase and the eluted phase. Other detection methods include infrared photometers for transparent molecules, amperometric detection for compounds with redox properties, radioactive detectors when solutes are radio-labelled, and conductivity detectors for ionic compounds. Nevertheless, fluorometers are widely used in mycotoxin detection, as they can measure the energy emitted by mycotoxins or their derivatives exposed to UV radiation (Snyder et al., 2011). Fluorescence is a type of luminescence generally observed in aromatic molecules, meaning that a substance emits light from electronically excited singlet states. Fluorescence occurs in approximately 10 ns, through pairing of opposite spin electrons in the excited orbital with electrons in the ground-state orbital, followed by photon emission (~10^8 s^{-1}) from the quick return to the ground state (Lakowicz, 1999). Some molecules such as aflatoxin B1 are naturally fluorescent depending on the state, while many compounds are non-fluorescent and require the addition of labels and probes. The attachment of fluorescent labels takes place by covalent interactions with amino, carboxyl, hydroxyl, or sulfhydryl groups in the targeted molecule (Sharma et al., 2018).

Current HPLC methods for fumonisin B1 utilize a reverse phase system with fluorescence detection, with a pre-column derivatization step (pH 7.5, RT) of FB1 with 9-fluorenylmethyl chloroformate (FMOC-Cl) to obtain the fluorescent reaction product indicated in Figure 1.13, where FMOC-Cl reacts under mild conditions with the non-sterically hindered amino moiety in FB1 (Smith et al., 2017). This derivative is stable for 72 h and commonly used in the determination of amino acids, where the derivatization reaction of primary amines occurs in approximately one minute. Fluorescence detection of FMOC-derivatized products is carried out at 263 and 313 nm of excitation and emission wavelengths, respectively (Smith et al., 2017).

Notwithstanding, some difficulties such as low sensitivity to fluorophore-labelled fumonisin and matrix interference on the instrument response, are possible to occur. For a good performance during HPLC-FLD, controlled pH and temperature must be maintained during the derivatization step, this can be accomplished by adding boric acid to the sample extracts and controlling the temperature with digital instruments (air-condition) (Smith et al., 2017). Besides, matrix effects can be avoided by passing FB1 extracts through an immunoaffinity solid phase extraction (SPE) column, which is an imperative step to prevent response changes produced by residual matrix

components in the sample (Smith et al., 2017). More information regarding the chromatographic detection of FB1 will be illustrated in **Chapter 2**.

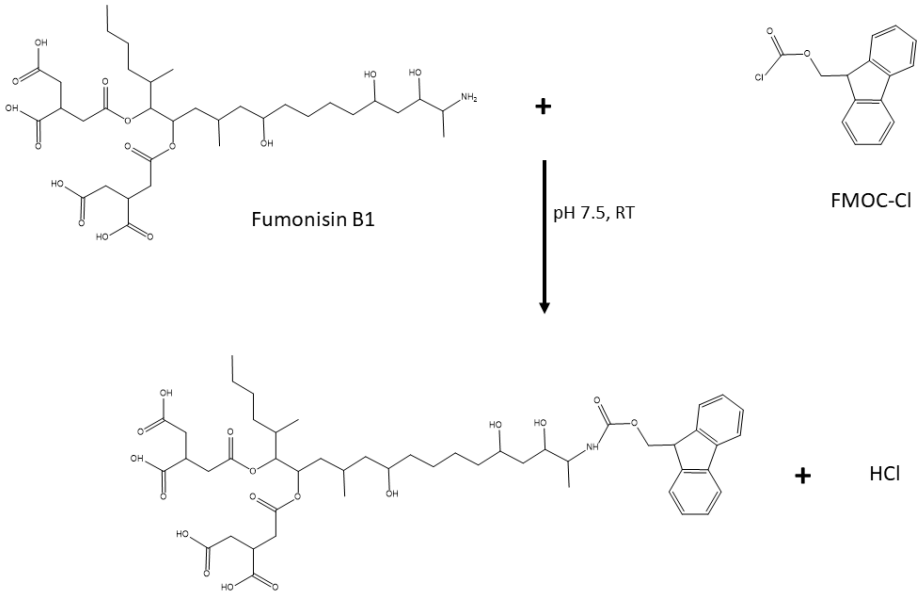

Figure 1.13 Synthesis of the highly fluorescent reaction product between fumonisin B1 and FMOC-Cl, at RT and pH 7.5 (Smith et al., 2017).

On other hand, in order to avoid the time consuming and sometimes inefficient derivatization step for FB1, liquid chromatography can be coupled with mass spectrometry. In this instrumental setting a ion source produces gas ions that are separated by a mass analyser based on the mass to charge ratio (*m*/*z*), whose ions intensities are counted by the detector and converted into a mass spectrum (De Hoffmann, 2005). The quantification of FB1 in **Chapter 6** will be performed by LC-MS, while L-phenylalanine will be quantified by HPLC-UV.

1.4.7 Fourier Transform Infrared (FTIR) spectroscopy

FTIR is a non-invasive vibrational spectroscopic method with high reproducibility, simplicity and capacity for small amounts of non-aqueous samples. FTIR is suitable for analysing the functional groups, bonds, and molecular structure of several materials, by means of the vibrational spectra in which thin peaks are associated to the chemical composition of the sample. In this technique, infrared absorption principally influences dipole and ionic bands (O-H, N-H, C=O) (Movasaghi et al., 2008). Most of the peaks in chitin and chitosan analysis can be interpreted into specific functional groups or vibrations such as hydroxyl groups (3450 cm^{-1}), NH stretching (3360 cm^{-1}), CH_2 in the pyranose ring (2920, 2880,1430, 1320, 1275, 1245 cm^{-1}),

carbonyl groups (1730 cm^{-1}), the amide I group C=O (1660 cm^{-1}) and its NH bending (1560 cm^{-1}), amino groups NH_2 (1590 cm^{-1}), OH and CH in the ring (1415, 1320 cm^{-1}), CH_3 in amide groups (1380 cm^{-1}), C-O groups (1255 cm^{-1}), glycosidic linkages -C-O-C- (1150-1040 cm^{-1}), and CH_3COH groups (850, 838 cm^{-1}) (Pawlak and Mucha, 2003). In fact, because of such characteristic bands, FTIR spectroscopy could be used as method for determining the acetylation degree in chitin and chitosan (Duarte et al., 2002). This type of analysis was necessary for the characterization of β-chitin scaffolds and N-isobutyryl chitosan (NIBC) hydrogels in **Chapter 6**, in which a confirmation of the synthesis of these materials as well as an estimation of possible mycotoxin binding, could be obtained from FTIR. However, a consideration should be made from the analysis in **Chapter 6**. As a portable FTIR spectrometer was utilized, no sample preparation was necessary (KBr discs), hence an unknown quantity was analysed per run.

1.5 Outline of the thesis

The structure of this thesis is composed by a literature review of different methods for the determination of FB1, where a systematic comparison between conventional and aptamer-based techniques was made. This review is followed by the exploration of the diffusion of samples in paper matrices, the application of a colorimetric method for assessing different treatments on paper, the establishment of novel methodologies and mechanisms for detecting FB1 with aptamers and gold nanoparticles, and the decontamination of samples with natural polymers and their structured materials. The general thesis outlined is displayed in Figure 1.14 where it follows three investigation lines.

Chapter 2 covers a literature review to state the development of aptasensing techniques for the detection of FB1. An exploration of immunologic, chromatographic and other methods was simultaneously made in order to compare them with aptamer-based biosensors, through statistical analysis, namely, principal components analysis. This is the first review that covered all the biosensing techniques applying different aptamer sequences specific for FB1, where it was clear that no label-free single probe assay was developed for ssDNA-AuNPs, prior to our research in Chapter 5. This literature review was submitted to the peer-reviewed journal, “Analytica Chimica Acta “.

Chapter 3 explores the diffusion of five model samples in a paper matrix (3MM chromatography paper). A mobile phone was employed for recording the diffusion of a known sample volume, and specific frames were analysed in Image J. The diffusion coefficient or pertinent constants were calculated by fitting the experimental data

(radial growth over time) to different mathematical equations. In addition, the physico-chemical properties of the ink models (density, viscosity, interfacial surface tension, contact angle) were combined with the fitted diffusion values, and the analysis of paper porosity, for the calculation of the permeability in each case. The selection of the best mathematical model was carried out by comparing the experimental and theoretical permeabilities. The innovative aspect of this determination is the simplified approach achieved by the sole application of samples without the aid of complex settings, expensive devices, or controlled conditions, which in fact allowed the investigation of diffusion and imbibition processes in regular biosensing conditions. The results of this chapter were submitted to the peer-reviewed journal, “Sensing and Biosensing Research”.

Chapter 4 studies the signal enhancement effect from applying two chitosan samples with different acetylation degrees (DA) and molecular weights (MW), on the test zone of a paper-based colorimetric biosensor for aflatoxin detection. For that reason, the inhibition effect of AFB1 on an enzymatic reaction (Ellman’s Assay) was selected for the comparison of both treatments, with special attention on the enzyme immobilization step by simple combination with chitosan or through cross-linking. As many papers describing the use of chitosan forget to include important parameters such as the DA and MW, the contribution of this paper relies on the examination of those properties for a differentiated signal, and the exploration of different immobilization mechanism in the same polymeric material. The implementation of low manufacturing costs by means of the integration of paper as a biosensing platform, permanent markers as design tools, and chitosan as the waste-based immobilizing agent, allows the potential application of its benefits for point-of-care and on-site analysis, as well as an expected increment of its profitability towards its possible commercialization. The results of this chapter were published in the peer-reviewed journal, “Sensing and Biosensing Research”.

Chapter 5 compares the performance of two aptamers in the quantification of FB1. To this purpose, different binding conditions (temperature, binding buffer) were tested. A different mechanism was proposed for each aptamer, where the limit of detection and specificity were assessed. Furthermore, size fractionation of aptamer-FB1-AuNPs conjugates was performed by AF4 and analysed by UV/Vis, MALS and DLS, which in addition to work as a characterization method indicated promising detection limits for the establishment of a novel technique. The interaction taking place during the formation of conjugates was explored by circular dichroism and DNA folding, and the analysis of different signals was compared for the selection of an optimal detection method. The formation of a conjugate with a ssDNA aptamer-FB1-AuNPs as presented in this chapter has been never reported, and this is the first time that such

conjugates are related to the quantification of FB1. Likewise, this is the first time AF4 is utilized for exploring those aptamer-target interactions under the presence of AuNPs. The results of this chapter were published in the peer-reviewed journal “Biosensors”.

Chapter 6 explores the preparation of β-chitin scaffolds and N-isobutyryl chitosan (NIBC) as potential mycotoxin adsorbents. The swelling kinetics and apparent diffusion coefficient were estimated in PBS (pH 7.4), while the structural properties were obtained by SEM and FTIR analysis. Adsorption experiments were carried out in both materials through their incubation at low and high amounts of adsorbent per volume of spiked sample (beer, milk). A better swelling performance was observed from conventionally frozen materials and the overall swelling and adsorption properties were more promising in NIBC. Nevertheless, those results should be regarded as preliminary due to the low adsorption efficiencies in both samples. Likewise, molecularly imprinted NIBC were produced with L-phenylalanine as template molecule, where no interference effect was found for the selected template. Despite the preliminary status of chapter 6, this was the first attempt to use NIBC as a mycotoxin adsorbent and a molecular imprinting platform for its future application in different approaches.

Chapter 7 is the final chapter, in which a summary of main results along with a discussion of such are included. Additionally, the areas of future studies are included at the end of this chapter.

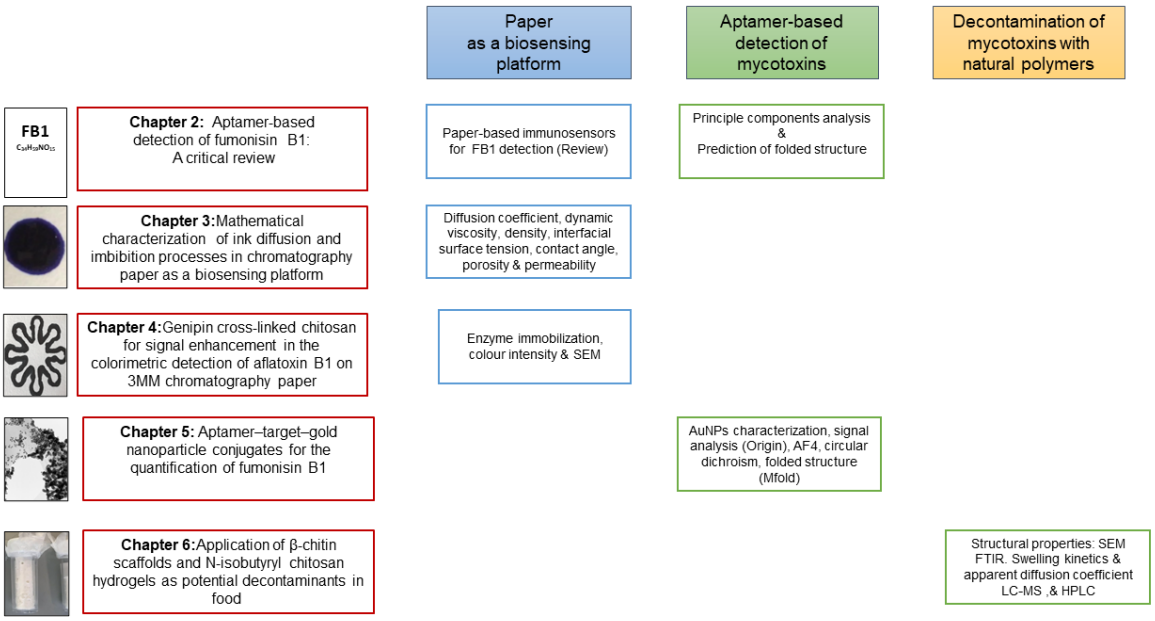

Figure 1.14 Schematic representation of the thesis

Chapter 2
Aptamer-based detection of fumonisin B1: A critical review

Abstract

Mycotoxin contamination is a current issue affecting several crops and processed products worldwide. Among the diverse mycotoxin group, fumonisin B1 (FB1) has become a relevant compound because of its adverse effects in the food chain. Conventional analytical methods previously proposed to quantify FB1 comprise LC-MS, HPLC-FLD and ELISA, while novel approaches integrate different sensing platforms and fluorescently labelled agents in combination with antibodies. Nevertheless, such methods could be expensive, time-consuming and require experience. Aptamers (ssDNA) are promising alternatives to overcome some of the drawbacks of conventional analytical methods, their high affinity through specific aptamer-target binding has been exploited in various designs attaining favorable limits of detection (LOD). So far, two aptamers specific to FB1 have been reported, and their modified and shortened sequences have been explored for a successful target quantification. In this critical review spanning the last eight years, we have conducted a systematic comparison based on principal component analysis of the aptamer-based techniques for FB1, compared with chromatographic, immunological and other analytical methods. We have also conducted an *in-silico* prediction of the folded structure of both aptamers under their reported conditions. The potential of aptasensors for the future development of highly sensitive FB1 testing methods is emphasized.

2.1 Introduction

Mycotoxins are thermoresistant low molecular weight (300-700 Da) secondary metabolites, mainly produced by fungi such as *Alternaria*, *Aspergillus*, *Claviceps*, *Fusarium* and *Penicillium*, as part of their defense mechanism (Eskola et al., 2020; Khaneghah et al., 2019). These biotic compounds act as hazards towards vertebrates, causing diseases when ingested, inhaled, or through skin contact. Some infectious processes, for instance, mycotoxicosis, take place after metabolization and accumulation of mycotoxins in several organs and tissues, due to immediate and progressive consumption of different contaminated food commodities (Marin et al., 2013), namely cereals, cocoa, coffee, fruit juices, milk and dairy, vegetable oils, beer, dried fruits, nuts, spices and their derived products. The presence of mycotoxins in

[1] Published as: Mirón-Mérida, V.A., Gong, Y.Y. and Goycoolea, F.M. 2021. Aptamer-based detection of fumonisin B1: A critical review. *Analytical Chimica Acta*, **1160**, p. 338395.

feed affects the livestock industry by negatively impacting not only the animal health, but also the human health through the consumption of contaminated by-products (eggs, meat, milk) (Magnoli et al., 2019). Similarly, the presence of mycotoxins in cereals, fruits, and nuts could prevail after beverage processing, which corresponds to their manifestation in wine, beer, fruit and vegetable juice, drinks and spirits, as well as cocoa, coffee and liquorice (Quintela, 2020). Initially, the production of mycotoxins is determined by environmental and ecological conditions (temperature, type of substrate, moisture and humidity, water activity, physical damage, insects, fungicides) (Kebede et al., 2020). However, multiple food matrices have been considered for the mitigation of toxin contamination (Karlovsky et al., 2016), as mycotoxin occurrence takes place at different stages of the food chain, including field handling, storage and subsequent steps. Although the WHO estimated that 25% of the food crops worldwide were contaminated with mycotoxins, recent estimations have revealed that as high as 60 to 80% of occurrence can be detected in many food products (Eskola et al., 2020).

Among the nearly 300 different mycotoxins that have been documented, the most relevant from a food safety perspective comprise aflatoxins (AFB1, AFB2, AFG1, AFG2, AFM1), citrinin, deoxynivalenol, ergot alkaloids, fumonisins (FB1, FB2), HT-2 toxin, ochratoxin A, patulin, T-2 toxin and zearalenone, whose co-occurrence in food products could reach more than 40% incidences, which might derived in multiple toxicological effects via co-exposure (BIOMIN, 2015; Eskola et al., 2020; Khaneghah et al., 2019; Liu et al., 2020a). In addition to mycotoxicosis, mycotoxins are related to carcinogenic and mutagenic effects along with reproductive, immune, renal, fetal and hepatic complications (Khaneghah et al., 2019).

Exposure to mycotoxins is more likely to arise in regions with scarce methods for manipulation and storage of food products and can be related to other conditions such as malnutrition, limited regulations, and lack of protection for exposed groups (Bennett and Klich, 2003). These metabolites affect staple foods widely consumed in the poorest and most vulnerable areas of Africa, Asia and Latin America (Pitt et al., 2012). Likewise, high-income countries are not exempt from mycotoxin occurrence, especially those importing agricultural and processed products from developing economies. North America and Europe encounter the highest mycotoxin risk in livestock (BIOMIN, 2015). As shown in Figure 2.1, there has been an increasing number of mycotoxin notifications in the last five years for the European Union (EU), whereas the United Kingdom (UK) has maintained a regular number of incidences, mostly identified through alerts, and border rejections of food and feed from EU member and non-member countries. To date, products such as peanuts, pistachios, hazelnuts, groundnuts, almonds, nutmeg, chilies, maize and dried figs are the most recurrent commodities exhibiting mycotoxin contamination; with a greater incidence in

goods from Africa, South Asia, South America, China, USA and the Middle East (European Commission, 2018).

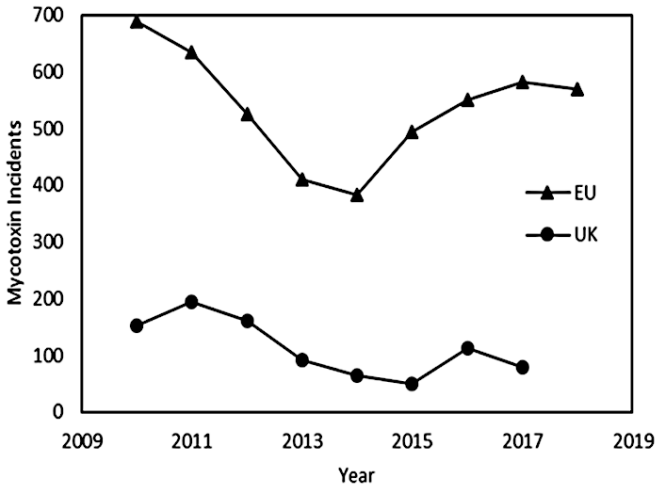

Figure 2.1 Number of mycotoxin notifications per year in the EU and the UK. Data based on the available Rapid Alert System for Food and Feed 2010-2018 by the European Commission (2018) and the Incidents Annual Report 2010-2017 by the Food Standards Agency (FAO, 2019)

Mycotoxin contamination negatively impacts a public health and food safety level, as denoted by the economic losses in the food sector, mainly generated by a reduction on crop yields, product trade profit and livestock production. Such impact is estimated in billions of dollars and it is heightened by additional costs related to the application of control strategies and mycotoxin analysis, mostly imposed to the producers by several regulations (Agriopoulou et al., 2020; Cinar and Onbaşı, 2019; Magnoli et al., 2019; Quintela, 2020). Likewise, prohibitions placed on contaminated products from African countries represent millionaire loses (Kebede et al., 2020). The occurrence of mycotoxins in crops modifies the fluctuations of market supply and demands, the costs in local, regional and international markets and generates public health-related costs due to interventions on medical services and support to people with mycotoxin-related disabilities (Pitt et al., 2012). For those reasons, the identification and sensitive quantification of low mycotoxin levels is a necessity for the worldwide panorama (Khaneghah et al., 2019). In fact, current estimations of a higher mycotoxin occurrence in food products are not only related to the effect of climate change, but also to the development of more sensitive analytical methods (Eskola et al., 2020). This was especially achieved through the advent of highly sensitive LC-MS methods, where a 200-fold improvement has allowed the analysis of multiple metabolites within the same run (BIOMIN, 2015).

In developed countries such as the United Kingdom, ongoing surveillance strategies are planned for the prediction and satisfactory estimation of mycotoxins in imported goods (FAO, 2019). The analytical methods utilized, namely HPLC-MS, and rapid screening methods (quantitative enzyme-linked immunosorbent assay (ELISA), fluorometric and lateral flow methods), require advanced infrastructure, electricity supply, availability of reagents, experienced technicians, instrument maintenance and validated tools. Consequently, developing countries commonly tend to utilize less complex techniques such as thin-layer chromatography (TLC) and immunological methods with semi-automated detections and minimal sample purification. TLC integrates expensive standards which are converted into perishable solutions requiring freezing and refrigeration. Similarly, antibody-based kits still present constrains regarding their refrigeration and shelf-life (Pitt et al., 2012). In this regard, even when conventional methods for mycotoxin detection, including chromatographic (HPLC, LC-MS, TLC, GC-MS) and immunological (ELISA) techniques, exhibit excellent sensitivities, their performance requires long times, expensive instrumentation and specialized operators, which limits their utilization for point-of-care and on-site analysis, and leads to the prioritization of decontamination methods (Cinar and Onbaşı, 2019; Lee et al., 2013). ELISA is a sensitive, accurate, selective and reproducible technique, which depending on its detection strategy, could be arranged in low cost, portable, and multiplex methods. This method's main disadvantages are the long incubations and its required multi-step washings, which are not suitable for its desired automatization (Lin and Guo, 2016; Majdinasab et al., 2020).

Furthermore, methods such as GC-MS and two-dimensional liquid chromatography difficult the analysis of polar metabolites, while small-sized compounds and the absence of specific biomarkers also produce analytical limitations (Tittlemier et al., 2019; Tittlemier et al., 2020). The application of chemometrics in infrared spectroscopy is still a time-consuming method due to its calibration stage (Tittlemier et al., 2019). Analytical methods in rural areas should be rapid, easy to implement whilst involving little transportation and a wide analytical scope (Pitt et al., 2012). Despite the indicated challenges, mycotoxin detection needs to be carried out in places with geographical and economic constrains, especially low-income countries with high mycotoxin exposure and outbreak risk (Agriopoulou et al., 2020; Khaneghah et al., 2019).

This goal can be achieved with advanced analytical methods, including novel biosensing techniques, which could be developed as quick yet accurate assays, with significant cost reductions. Novel methods include the innovation of previously used concepts, the development of original mechanisms and the resourceful integration of specific technology. For instance, displacement immunosensing reactions for

mycotoxin detection have been studied through the role of versatile materials as pseudo haptens and nanocontainers. Particles such as mesoporous silica were loaded with glucose, whose design was scaled to a portable analysis, where the indirect measurement of the target molecule (AFB1) corresponded to the concentration of free glucose measured with a personal glucometer. Although this type of designs have been disclosed as quick, portable and low-cost detection methods comparable to commercial ELISA kits, cross reactivity was reported under the presence of analogue molecules (AFB2), while some issues related to the generation of nanomaterials included the long synthesis time, and the lack of repeatability when a different batch was used (Tang et al., 2014).

Electrochemical methods can be coupled with competitive immunoreactions and aptamer-based detections, in which different particles and platforms (gold nanoparticles, magnetic nanoparticles, microplates) are functionalized with monoclonal antibodies (mAb) or aptamers for the achievement of low limits of detection (LODs) (Castillo et al., 2015; Lin et al., 2015). As the use of one competitive immunoassay might not be enough for small mycotoxins, occasionally, two different reactions can be coupled within the same approach (Lin et al., 2015). This strategy involves an initial competitive immunoreaction between the specific mycotoxin and its labeled/loaded mycotoxin conjugate, which depending on the nature of the labeling/loading agent (dopamine, L-cysteine, glucose oxide, silver nanoparticles, invertase) and the interacting nanoparticles (liposomes, magnetic beads, silica), can be followed by hydrolytic reactions (Lin et al., 2015), redox reactions (Lin et al., 2017b), lysis (Lin et al., 2017a; Lin et al., 2018), and acid dissolution (Lin et al., 2016), with an indirect photoelectrochemical determination of the target concentration.

Photoelectrochemical detections portray the advantages of both electrochemical and optical assays, including high sensitivity, ease for miniaturization, and low background signals, cost and power needs (Lin et al., 2017a). However, some photoelectrochemical approaches require laborious steps, which make the determination a complex procedure (Lin et al., 2018). In addition, the sample purity required for electrochemical biosensors increases the assay time, especially in complex food matrices (Tittlemier et al., 2019). Mycotoxins' enzyme-based detection can be an affordable, simple and yet a sensitive and selective option when utilized. Nevertheless, its long incubation and detection times might represent a disadvantage for a large-scale application (Majdinasab et al., 2020). Besides, although the use of nanomaterials results in cost-effective, rapid testing where different nanostructures (e.g. sheets, particles) increase the sensitivity, in addition to the long synthesis and modification procedures, some nanomaterial-based designs also indicate cross-

reactivity (low selectivity), color interference and higher detection limits when used in colorimetric methods (Majdinasab et al., 2020).

Fluorescent and chemiluminescent dyes and nanoparticles have been applied in bulk and paper-based detections (Sabet et al., 2017; Shim et al., 2014), which, even when sensitive in real samples, require specialized electronic and optic equipment (Tittlemier et al., 2021). Antibody-based tests for mycotoxin detection have been commercially developed as dipsticks in different kits (Pitt et al., 2012). Moreover, innovative biosensors have integrated the help of antibodies and colloidal gold (Moon et al., 2012), with the improved integration of smartphone-based readings (Lee et al., 2013). Although many reported lateral flow and microfluidic-based assays, applying aptamers, enzymes or antibodies, are simple, quick, sensitive, and low-cost, in-situ arrangements, they occasionally provide qualitative results, higher LODs, and their reproducibility and stability remain undetermined (Lin and Guo, 2016; Majdinasab et al., 2020).

Other important challenges associated with detecting mycotoxins in food samples appear during sample pretreatment, where mycotoxins are commonly extracted from the food matrix with organic solvents or acidified water, followed by filtration, centrifugation and sometimes more clean-up steps. Although some solvents can affect the performance of certain bioreceptors (*e.g*. enzymes, antibodies), interfering food compounds including lipids, proteins, sugars and salts must be removed before the analysis in order to avoid peak overlap, fluorescence quenching or signal suppression in different detection methods (Majdinasab et al., 2020, Tittlemier et al., 2020). Likewise, multi-detection methods require sample cleaning within the minimum pretreatment steps and sample loss (Tittlemier et al., 2019). Another issue is caused by masked mycotoxins, which form through the conjugation with polar compounds (sugars), resulting in a less detectable metabolite (Kamle et al., 2019). Apart from conjugation, modified mycotoxins can also undergo hydrolysis, degradation, covalent and non-covalent binding to food matrices, which also derive in analytical underestimation (Knutsen et al., 2018). In the case of fumonisins, a strong matrix interaction has been observed, in which the extraction yield is influenced by the matrix constituents and the extraction conditions, resulting in matrix dependent recoveries (Knutsen et al., 2018). In this critical review an exploration of the aptamer-based detection methods of FB1 was carried out by their graphical and principal component analysis comparison with different conventional and novel techniques. Additionally, different aptamers specific for FB1 were identified and separately presented according to their detection signal (fluorescence, electrochemical, colorimetric, others), with a further in-silico prediction of their folded structure.

2.1.1 Fumonisin B1

Fumonisins are usually small alkyl amines containing two hydroxyl esterified propane tricarboxylic acids (tricarballylic acid), which are linked to adjacent carbons (Figure 2.2) (Lamprecht et al., 1994). When substituted in up to seven “R” side chains, the fumonisin aliphatic backbone serves as the basic structural unit for the conformation of different analogues. Existing fumonisin analogues can be classified in series A, B, C and P, where group B is the most abundant in nature (Rheeder et al., 2002). Understanding the structure of fumonisins is critical when selecting and refining some quantification methods. For instance, group B fumonisins are soluble in water and polar solvents, therefore, they can be extracted from the food matrix with binary mixtures of water and methanol or acetonitrile (Knutsen et al., 2018).

a)

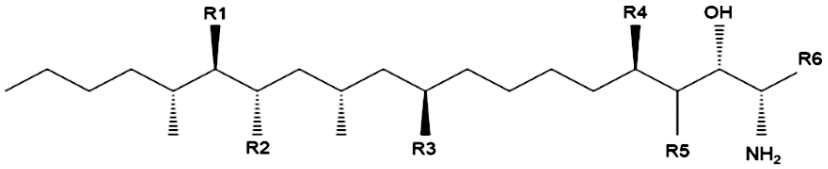

b)

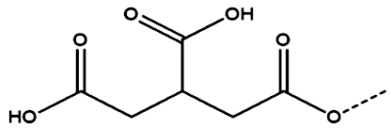

c)

Fumonisin	R1	R2	R3	R4	R5	R6
FB1	TCA	TCA	OH	OH	H	CH_3
FB2	TCA	TCA	H	OH	H	CH_3
FB3	TCA	TCA	OH	H	H	CH_3
FB4	TCA	TCA	H	H	H	CH_3
Iso-FB1	TCA	TCA	OH	H	OH	CH_3
FBK1	=O	TCA	OH	OH	H	CH_3
PHFB1a	TCA	OH	OH	OH	H	CH_3
PHFB1b	OH	TCA	OH	OH	H	CH_3
HFB1	OH	OH	OH	OH	H	CH_3
FC1	TCA	TCA	OH	OH	H	H
FC3	TCA	TCA	OH	H	H	H
FC4	TCA	TCA	H	H	H	H
IsoFC1	TCA	TCA	OH	H	OH	H
OH-FC1	TCA	TCA	OH	OH	OH	H

Figure 2.2 Structure representation of (**a**) the general fumonisin backbone, (**b**) tricarballylic acid (TCA) and (**c**) a list of alkyl amine fumonisins (c) (Rheeder et al., 2002)

Fumonisins B1 and B2 were initially studied and isolated from *Fusarium verticillioides*, formerly known as *Fusarium monoliforme*. They were discovered during the investigation of compounds responsible for leukoencephalomalacia, toxicity and hepatocarcinogenicity in some animal species (Rheeder et al., 2002). Early studies reported the main role of F. verticillioides in the production of FB1, FB2, FB3 (iso-FB2), FB4, FA1, FA2 and FC1 (Abbas et al., 1992; Bezuidenhout et al., 1988; Branham and Plattner, 1993; Gelderblom et al., 1988), when cultivated in liquid cultures and solid matrices (maize). However, depending on the host crop and growth media, fumonisins can be generated by other fungal species such as *Alternaria alternata* on potato

dextrose agar (Abbas and Riley, 1995), stationary cultures of *Aspergillus niger* producing FB6 and FB2 (Frisvad et al., 2007; Månsson et al., 2010) and some strains of *Tolypocladium cylindrosporum*, T. *geodes* and T. *inflatum* which developed fumonisins in high sugar media, when incubated at 25-30 ^{o}C (Mogensen et al., 2011).

2.1.2 Effects of fumonisin B1 on health

Classified as group 2B hazard, fumonisins B1 and B2, are possible carcinogenic to humans (Ostry et al., 2017). Fumonisin B1 causes multiple effects on different species, its toxicity was first related to the disruption of sphingolipid metabolism, as this mycotoxin inhibits ceramide synthase, which leads to both an increase in sphinganine and a decrease in complex sphingolipids, and further cell death observed in pig kidney cells (Gutleb et al., 2002; Riley and Merrill, 2019). Notwithstanding this frequent assumption, studies on the protective role of liver X receptor (LXR) on FB1-caused hepatotoxicity implied the presence of different pathways (Régnier et al., 2019).

Another mechanism triggered by FB1 is oxidative stress, where FB1 reduces mitochondrial and cellular respiration and increases the production of reactive oxygen species, as observed in rat astrocytes and human neuroblastoma cells (Liu et al., 2019). In the same way, FB1 reduced growth of pig iliac endothelial cells and their barrier functions, while decreased the activities of some enzymes with antioxidant effects and enhanced the formation of lipid peroxidation compounds (Yuan et al., 2019). Exposure to fumonisin could also induce epigenetic changes such as DNA methylation and hypomethylation in rat glioma cells and human intestinal and hepatoma cells (Liu et al., 2019). Apart from neurotoxicity, hepatotoxicity, nephrotoxicity, and carcinogenicity, FB1 has also been studied in corneal infections, due to its ability to form Langmuir monolayers on liquid surfaces (Sharma et al., 2019). Besides, some geographical studies have correlated the prevalence of esophageal cancer in humans with the presence of FB1 and FB2 in regional crops (Marasas et al., 1988; Yoshizawa et al., 1994).

In addition, adverse effects from fumonisins in human health were reported for Mexican American women living in the border region between Mexico and Texas, where fumonisin exposure was associated with neural tube defects (Missmer et al., 2006). Fumonisin B1 occurrence in Tanzania was reported in breastfeeding with contaminated milk as a current issue among children under six months of age (Magoha et al., 2014); elevated levels of dietary fumonisin were likewise related to inhibition of ceramide synthase in women from Guatemala (Riley et al., 2015), whose consumption of contaminated maize was detected in their high urinary fumonisin levels (Torres et al., 2014). Other studies conducted in Tanzania have demonstrated the

main role of fumonisin in underweight children due to breastfeeding and weaning within the first 36 months of age (Chen et al., 2018b) as well as the high impact of substituting breastfeeding on the infant mycotoxin exposure (Magoha et al., 2014). Even though fumonisin B1 is not as prioritized as other mycotoxins, single exposure to it and its combination with other mycotoxins such as aflatoxins, represent an issue that needs to be addressed in deep, due to its common occurrence.

2.1.3 Fumonisin occurrence in food commodities and its worldwide regulation

The Food and Agriculture Organization (FAO) of the United Nations trough the worldwide regulations for mycotoxins in food and feed, indicated that by 2003 only 99 countries had regulations in place focused on mycotoxins. Additionally, the extent of those actions covered a brief group of different toxins among continents. As it can be noticed from Figure 2.3, the regulations for fumonisins in food and feed are established on either the sum of fumonisins type B1+B2+B3, B1+B2, or as total content of FB1 (FAO, 2004).

The maximum allowable contamination limit for the sum of FB1 and FB2 is commonly established as 2000 µg/kg and 4000 µg/kg for maize meal and raw maize, respectively, based on the Codex Alimentarius Commission (Kamle et al., 2019). However, as indicated in Table 1, this value has been lowered to 1000 µg/kg in different countries including Iran, France, Bulgaria, Switzerland, Cuba, and Brazil, not only for maize but other cereals and their derived products (Cinar and Onbaşı, 2019; Quintela, 2020). Furthermore, more rigorous regulations have been placed for maize-based breakfast cereals, snacks (800 µg/kg) and food for infants (200 µg/kg) (Table 1). Moreover, a maximum tolerable daily intake of 2 µg/kg has been indicated, while the occurrence of FB1 in cereals (e.g., corn, wheat, rye) oscillates between 40-6000 µg/kg in Europe, 11-30000 µg/kg in Africa, 0.30-18800 µg/kg in Asia and 5-15050 µg/kg in America (Kamle et al., 2019).

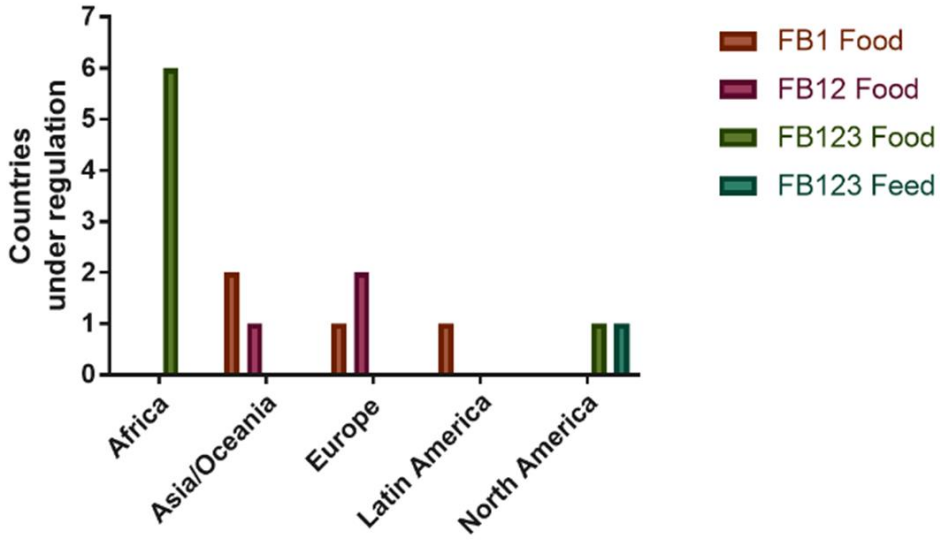

Figure 2.3 Countries regulating fumonisin in food and feed worldwide (FAO, 2004)

The number of countries under fumonisin regulations is equivalent for Europe and Asia/Oceania. On the other hand, the North America region has a noticeable approach by the United States, where limits for mycotoxins are targeted not only in food, but in feed. Based on the FAO controls, Africa was overall the less active region in enforcing mycotoxin regulations, particularly for any type of fumonisin. Paradoxically, though perhaps not surprising, the highest incidence of mycotoxins in food and feed occurs in Africa (Udomkun et al., 2017), however since 2011 a control for aflatoxin and fumonisin was established by the East African Community (EAS), whose scope included the six member countries, with a potential application on the trade activities by the twenty COMESA member states (Table 2.1). Furthermore, Latin America possesses a gap in recognizing fumonisins as an important group of hazardous compounds (FAO, 2004).

The growth of fumonisin producing fungal species has been reported on corn seedlings, grits, meal and flour, tomato leaves, seedlings and rice (Bartók et al., 2006; Bezuidenhout et al., 1988; Lamprecht et al., 1994; Savi et al., 2016; Yamagishi et al., 2006) as well as some dried samples comprising coffee beans and vine fruits (Noonim et al., 2009; Varge et al., 2010). Some Fusarium species can produce fumonisins in media based on rice, oat, carrots and malt. In contrast, A. *niger* requires low water activity media and products with high sugar content (Frisvad et al., 2007; Varga et al., 2010). Maximum levels of fumonisins in both food and feed are shown in Table 2.1.

Table 2.1 Maximum permitted levels (µg/kg) of fumonisins in food and feed set by different organizations[1]

Commodity	Maximum Level (µg/kg)	Type	Authority	Regulatory Framework	Country
Raw maize grain	4 000	B1, B2	FAO, WHO	CODEX STAN 193-1995	International trade
Maize flour and maize meal	2 000	B1, B2	FAO, WHO	CODEX STAN 193-1995	International trade
Unprocessed maize (not for milling)	4 000	B1, B2	CEC	(EC) No 1126/2007	EU
Maize, maize-based foods for direct human consumption	1 000	B1, B2	CEC	(EC) No 1126/2007	EU
Maize-based breakfast cereals and snacks	800	B1, B2	CEC	(EC) No 1126/2007	EU
Processed maize-based foods and baby foods (Infants and young children)	200	B1, B2	CEC	(EC) No 1126/2007	EU
Milling fractions according to size (500 micron) and CN code 19041010	1 400 - 2 000	B1, B2	CEC	(EC) No 1126/2007	EU
Maize and processed products	1 000	B1, B2	MH	BG1	Bulgaria
Maize, rice	1 000	B1	MPH/INHA	CU1	Cuba
Cereals & cereal products	1 000	B1	DGCCRF	FR1	France
Maize	1 000	B1, B2	ISIRI, MOH	IR1	Iran
Corn & corn products	Not given	B1	SG1	AVA	Singapore
Maize	1 000	B1, B2	CH1	OFCACS	Switzerland
Maize products	According to the result of risk assessment	B1	-	-	Taiwan
Degermed dry milled corn products (e.g. flaking grits, corn grits, corn meal, corn flour with fat content of <2.25%, dry weight basis)	2 000	B1, B2, B3	US4, US5	FDA	USA
Cleaned corn intended for popcorn	3 000	B1, B2, B3	US4, US5	FDA	USA
Whole of partially degermed dry milled corn products (e.g. flaking grits, corn grits, corn meal, corn flour with fat content of ≥2.25%, dry weight basis); dry milled corn bran; cleaned corn intended for masa production	4 000	B1, B2, B3	US4, US5	FDA	USA
Corn and corn by-products intended for equids and rabbits	5 000	B1, B2, B3	US4, US5	FDA	USA
Corn and corn by-products intended for swine and catfish	20 000	B1, B2, B3	US4, US5	FDA	USA
Corn and corn by-products intended for breeding ruminants, breeding poultry and breeding mink (includes lactating dairy cattle and hens laying eggs for human consumption)	30 000	B1, B2, B3	US4, US5	FDA	USA
Ruminants ≥ 3 months old being raised for slaughter and mink being raised for pelt production	60 000	B1, B2, B3	US4, US5	FDA	USA
Poultry being raised for slaughter	100 000	B1, B2, B3	US4, US5	FDA	USA
All other species or classes of livestock and pet animals	10 000	B1, B2, B3	US4, US5	FDA	USA
Maize grains/ Millet flour	2 000	Fumonisin	EAC	EAS	Burundi, Kenya, Rwanda, South Sudan, Tanzania, Uganda.

[1] Abbreviations: **AVA:** Agri-Food and Veterinary Authority; **BG1:** Ministry of Health in coordination with the Ministry of Agriculture and Forestry, the Ministry of Industry and the State Standardization Agency (2000). Regulation No.11/2000 of 11 July 2000 laying down the maximum levels of mycotoxins in foodstuffs. Official Newspaper of the Republic of Bulgaria No. 58: 18-24.; **CEC:** Commission of the European Communities; **CH1:** Verordnuung uber Fremd-und Inhaltsstoffe in Lebensmitteln. SR817.021.23; **CN:** Combined nomenclature; **CU1:** Ministerio de Salud Pública (1999). Manual de indicadores empleados en la evaluación sanitaria de alimentos. Instituto de Nutrición e Higiene de los Alimentos (INHA), Diciembre de 1999; **DGCCRF:** Direction Generale de la Concurrence, de la Consommation de la Repression des Fraudes, Ministere de l'Economie, des Finances et de l'Industrie; **EAC:** East African Community, **EAS:** East African Standard 89: 2011, ICS 67.060; **EC:** Commission Regulations**; FAO:** Food and Agriculture Organization of the United Nations: **FDA:** Food and Drug Administration; **FR1:** Avis du Conseil Superieur d'Hygiene Publique de France du 8/12/1998; **IR1:** National standard of Institute of Standard and Industrial Research of the Islamic Republic of Iran (ISIRI) [2002]. Maximum tolerated levels of mycotoxins in food and feeds. No.5925; **ISIRI:** Institute of Standard and Industrial Research of the Islamic Republic of Iran; **MH:** Ministry of health; **MOH:** Ministry of Health and Medical Education; **MPH/INHA:** Ministry of Public Health/Instituto de Nutrición e Higiene de los Alimentos; **OFCACS:** Official Food Control Authorities of the Cantons of Switzerland; **SG1:** Regulation 34 of the Singapore Food Regulations; **US4:** FDA (2001). Guidance for industry: Fumonisin Levels in Human Foods and Animal Feeds, November 9, 200; **US5:** FDA; **WHO:** World Health Organization

As previously mentioned, cereals, rice and maize food and feed products are the most common targeted commodities for possible fumonisin outbreaks. Understanding the maximum values established by regulation, along with the expected contamination levels for distinct samples, is crucial during the design of conventional and novel quantification methods. Also, it is necessary to know the scope and applicability of each technique. The focus of this systematic comparison centers in these aspects by reflecting the state of the art in the field since 2012. In this regard, a 2016 review, focused on fusarium mycotoxins, reported 8 aptasensors from the 9 disclosed until

2015 (Lin et al., 2016). Some articles considered the existence of a single aptamer specific to FB1 (Nguyen et al., 2017; Song et al., 2019; Schmitz et al., 2020; Yüce et al., 2015), despite the disclosure of two sequences selected through SELEX (Chen et al., 2014; McKeague et al., 2010), while other cases reported minimers (shortened sequences) as individual aptamers (Ruscito et al., 2016). More recent articles have overlooked the total number of publications about aptamer-based biosensors for FB1 (Berthiller et al., 2018; Evtugyn et al., 2020; Majdinasab et al., 2020; Pfeiffer and Mayer, 2016; Tittlemier et al., 2020; Zhang et al., 2020a), likewise some other reviews only focused in one specific type of signal (*e.g.*,electrochemical, colorimetric, photoelectrochemical) for the identification of different mycotoxins, which also limited the number of reported techniques for FB1 (Goud et al., 2020; Majdinasab et al., 2020; Zhou and Tang, 2020). Therefore, this review was necessary as the majority of aptamer applications (23 biosensors) for FB1, were reported after 2016. Additionally, this is the first review specialized in addressing all the reported aptamer sequences for detecting FB1 since the first FB1 aptamer publication in 2010 (McKeague et al., 2010), with the novelty of a statistical comparison among different read-outs, and with other novel and conventional techniques. Hence, this work not only enlists existing aptamer-based biosensing techniques for FB1, but also discusses the best approaches in terms of the limit of detection, assay times and assay preparation times, with a thorough exploration of different developments, improvements and new discoveries that occurred throughout this decade of aptasensing research for this important mycotoxin.

2.2 Methods

2.2.1 Systematic comparison

For this systematic comparison a screening was made from results obtained after searching the words “fumonisin + aptamer” and “FB1 + aptamer” in Scopus (28, 12), Web of science (28, 14), and Google Scholar (4, 32); as well as papers containing the specific DNA sequences. As indicated in Scheme 2.1, from the 35 relevant papers, 32 biosensors were identified and compared with other conventional methods for FB1 detection in terms of their limit of detection (LOD), assay time, and assay preparation time. The data were plotted in GraphPad Prism 7 to show the evolution and relation of such parameters throughout the years.

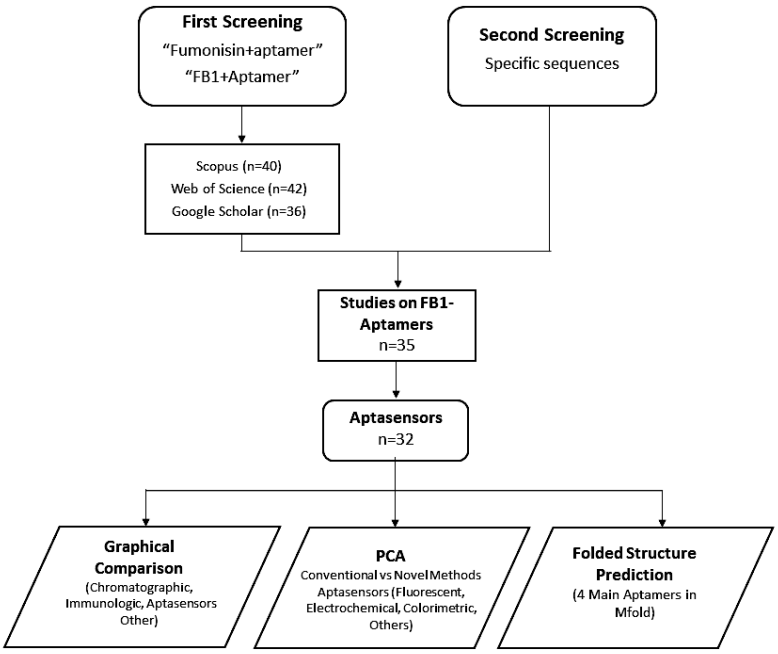

Scheme 2.1 Flow chart of the screening strategy

2.2.2 Principal component analysis

Aptamers are single-stranded DNA (ssDNA) or RNA, commonly formed by 20 to 220 random nucleotides. From the 10^{15} existing random sequences specific to different molecules, aptamers specific to fumonisin have been reported as ssDNA sequences. Aptamer-based sensors, also known as aptasensors, exploit the advantages of such oligonucleotides, including their great affinity, specificity, and applicability, which are promoted by the folded 3D structures generated by means of their complementary base pairs. Aptamer recognition occurs through hydrogen bonds, van der Waals forces, stacking and electrostatic interactions, which enable the recognition between chiral enantiomers, changes in one functional group (hydroxyl, methyl) and slight structural modifications. This is a mechanism observed as either the encapsulation of small molecules (e.g., nucleotides, mycotoxins) or the insertion of large targets (e.g., proteins, cells) (Lin and Guo, 2016; Ruscito et al., 2016; Song et al., 2019). Biosensors utilizing aptamers as bioreceptors, portray excellent sensitivity, selectivity and allow in-field detections with multifunctional, robust, modular and price competitive designs (Yoo et al., 2020). In some cases, aptasensors portray better results to those with other bioreceptors, for instance biosensing techniques applying surface plasmon resonance of AuNPs have been broadened and improved when aptamers were integrated, in comparison to the immunological developments of this principle (Majdinasab et al., 2020). To confirm the existence of such advantages from aptasensors over different methods, all the aptamer-based biosensors for FB1 detection and several conventional and novel methods published since 2012

(publication year of the first aptasensor), were combined in a principal component analysis, performed in Minitab 15 Statistical Software. Before the application of the correlation matrix, all data were treated according to the following equations:

$$LODt = \frac{LOD\ max}{LOD} \qquad ATt = \frac{AT\ max}{AT} \qquad APt = \frac{AP\ max}{AP}$$

Where LODt , ATt and APt are the treated limit of detection, assay time and assay preparation time, respectively; LODmax and ATmax are the maximum limit of detection and maximum assay time for all the data in this comparison (since 2012), equal to 3200 μg/L (Kadir et al., 2010) and 720 min (Liu et al., 2018) respectively. The assay preparation time was calculated by adding the reported times for sample extraction, synthesis of nanoparticles, support treatment, and array assembling. The maximum preparation time per assay was calculated as 12900 min (Wu et al., 2012). This mathematical treatment allowed to determine the correlation of the maximum values to the most sensitive, fast and therefore, effective methods.

2.2.3 DNA folding

The DNA folding forms of the four existing aptamers were predicted with mfold Web Server according to their reported folding conditions.

2.3 Conventional and novel methods for mycotoxin identification

Typical methods for the identification of mycotoxins in food samples incorporate compound separation principles for quantification through TLC, HPLC, and LC-MS (Ghali et al., 2009; Pitt et al., 2012; Zhang et al., 2020a). Simultaneously, some commercial immunoassays optimized the use of antibodies for mycotoxin quantification. However, most of them utilize expensive and sophisticated equipment for time-consuming assays that are required to be performed by skilled operators, as they utilize complex elements and instruments (Hossain et al., 2009; Lee et al., 2013). Novel approaches including optical (Huang et al., 2020; Ren et al., 2015), electromagnetic (Munawar et al., 20210), electrochemical and surface-sensitive techniques (e.g., surface plasmon resonance, ion-selective field-effect transistors, surfaced-enhanced Raman spectroscopy) along with aptamer-based techniques (Cheng et al., 2018; Gui et al., 2015 ; He et al., 2020; Mirón-Mérida et al., 2021; Wu et al., 2020), have been developed and found to exhibit comparable and even higher sensitivities than those of conventional procedures (Da Silva et al., 2019; Souto et al., 2017).

Based on Tables 2.2-2.5, the LODs of different reported methods were plotted against their total assay times, as reflected on Figure 2.4a. The assay time was calculated from either the divulged times at either the injection step in chromatography, or the incubation between the antibody/aptamer/recognition region with its corresponding target molecule. This consideration excluded any pre-treatment, extraction steps and particle fabrication, as those phases were part of the assay preparation time (Figure 2.4b). The shortest response time for the analysis of extracted samples was achieved in seconds to minutes, when using Surface-enhanced Raman spectroscopy (Lee and Herrman, 2016). Nevertheless, some sensors qualified as fast required overnight steps and long incubation times for the whole system arrangement, especially when the synthesis of nanoparticles and drying phases were required. Assay times below ten minutes were achieved through chromatographic, immunoassays, and some innovative methods, nonetheless the more sensitive assays were secured with aptamer-based biosensors (He et al., 2020a; Mirón-Mérida et al., 2021; Niazi et al., 2019), immunosensors with carbon nanotubes (Masikini et al., 2015; Masikini et al., 2016), and molecularly imprinted polymer nanoparticles (MIPs) (Munawar et al., 2020), as indicated in Figures 2.4a and 2.4c.

In addition to high specificity, the combination of minimum assay times with low limit of detections is ideal for an appropriate quantification technique. Nonetheless, an increase in the assay preparation time can complicate the achievement of on-site/point of care analysis and compromise the reproducibility. Even though there is high sensitivity achieved through aptasensors, such DNA-based techniques along with some immunoassays, entail long assay times with extended preparation times, due to incubation and platform arrangement, respectively (Figure 2.4b). In those cases, the final response was normally measured as either a fluorescent or a colorimetric signal. Figure 2.4c portrays the LODs accomplished per year, where it can be noted that ongoing research is still focused on developing chromatographic techniques and immunoassays.

Although, over the last five years there has been an improvement on the detection limits of some protocols, especially for immunoassays whose LODs have reached the picogram scale, most of the new chromatographic and antibody-based methods still quantify values comparable to earlier findings. Conventional assays with the highest sensitivity have included electrochemical designs, electrochemiluminescent quantifications, and MS detection (Table 2.2-2.3). Of note, fluorescent, colorimetric and electrochemical aptamer-based sensors reported over the last three years, accomplished relevant LODs with a promising tendency (Figure 2.4).

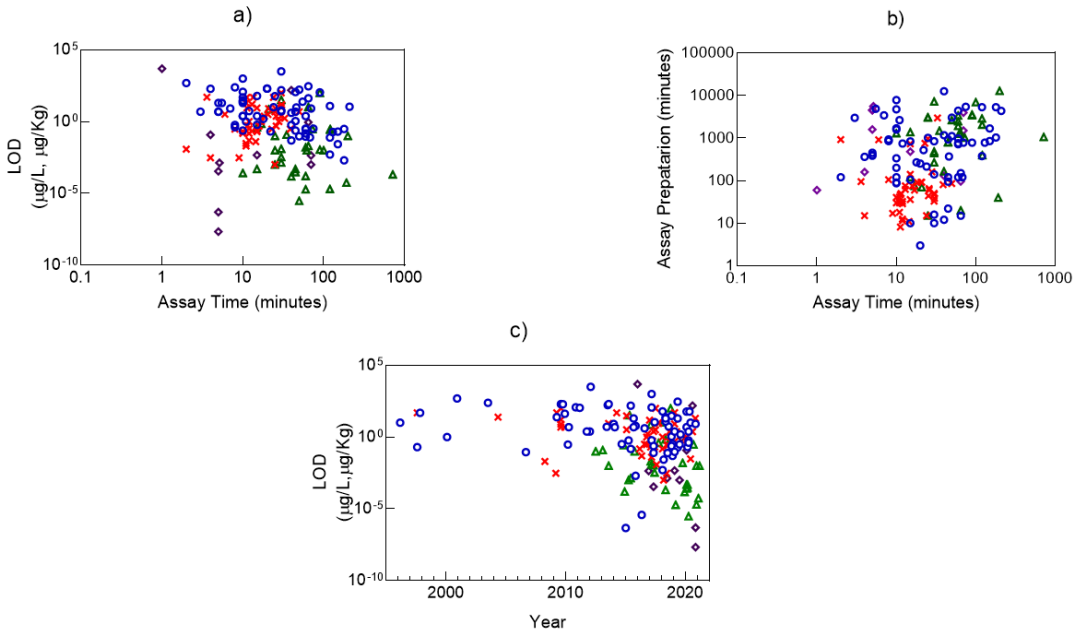

Figure 2.4 Relation of the assay time with (**a**) the limit of detection (LOD) and (**b**) assay preparation time for the approaches reported since 2012, (c) and LODs achieved over time through different methods (**O**: Immunologic, **X**:Chromatographic, **Δ**: Aptamer-based, **◊**: Other)

Despite the fact that the use of antibodies with electrochemical readouts was advantageous for achieving some of the lowest LODs for fumonisin B1, equivalent to $4.6x10^{-7}$ and $3.7x10^{-6}$ µg/L (Masikini et al., 2015; Masikini et al., 2016), these immunosensors were not included in the principal component analysis (PCA), as no assay time was reported in either case. Hence, as indicated in Figure 2.5, LC-MS (Da Silva et al., 2019; Souto et al., 2017), immunoassays with optical (Huang et al., 2020; Ren et al., 2015; Venkataramana et al., 2014), Raman (due to its quick procedure) (Lee and Herrman, 2016), fluorescent readouts (Li et al., 2020) and electrochemical MIPs (Munawar et al., 2020) were correlated to the combination of low LODs with short assay times. However, such statistical analysis did not show the advantages of aptamer-based methods, which was also observed on the correlation of short assay preparation times with LC-MS, immunologic and only three aptasensors (Cheng and Bonanni, 2018; Gui et al., 2015; Mirón-Mérida et al., 2021). This was shown by PCA, where the main drawbacks from aptamer-based sensors for FB1 was their long assay and assay preparation times denoted by its absence of correlation in both components when compared to other methods.

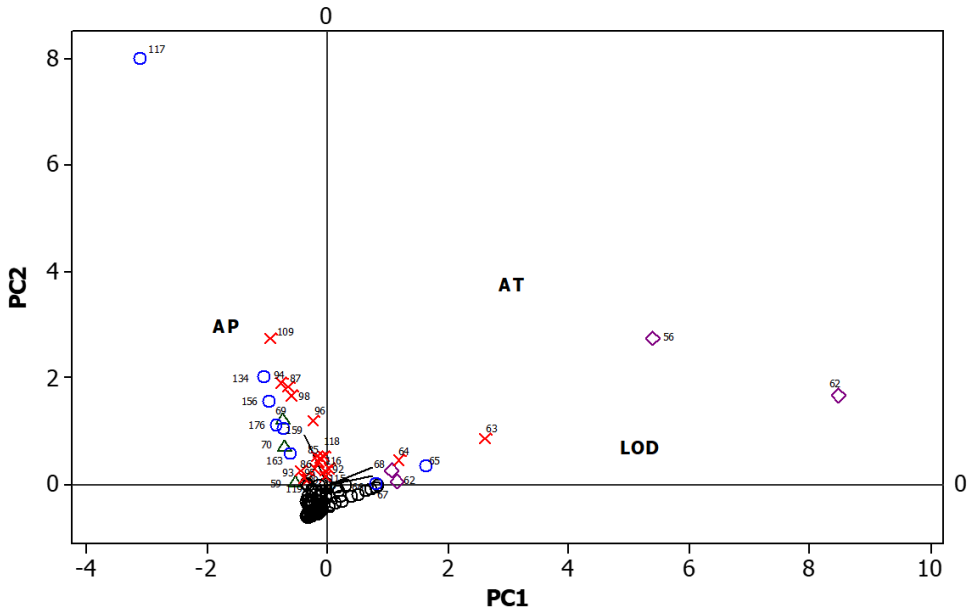

Figure 2.5 Principle component analysis for the correlation of aptasensors and conventional methods reported from 2012 to the lowest detection limits (LOD), assay time (AT) and assay preparation time (AP). (**O**: Immunologic, **X**: Chromatographic, **Δ**: Aptamer, **◊**: Other). The numbers correspond to the correlated references from Table A1

2.3.1 Chromatographic detection of fumonisin B1

Together with immunoassays, chromatographic methods for the quantification of mycotoxins, have been widely studied and optimized for the analysis of several food products as indicated in Table 2.2. Initial chromatographic techniques were focused on the exclusive quantification of fumonisin in corn, through the analysis of either MS/MS or fluorescence signals. Following analysis confirmed the good correlation of maize-based products expenditure with FB1 levels in human urine (Gong et al., 2008); which consolidated its utilization as a relevant biomarker, as a portion of ingested FB1 is excreted in urine (Silva et al., 2010).

The detection of fumonisins is limited by its absence of fluorescence; therefore, the introduction of a chromophore for the derivatization of the amino groups within fumonisin is always required (Siler et al, 1982). Initial derivatization procedures utilized maleic anhydride derivatives and fluorescamine (Gelderblom et al., 1988; Sydenham et al., 1990). Nevertheless, more sensitive detection procedures introduced but still utilize pre-column derivatization with o-phthaldialdehyde (Bordin et al., 2014; Campa et al., 2004; Ghali et al., 2009; Petrarca et al., 2014; Shepard et al., 1990), naphthalene-2,3-dicarboxaldehyde (Dall'Asta et al., 2009), and the quick and stable (9-fluorenylmethyl) chloroformate (FMOC) (Holcomb et al., 1993; Smith et al., 2017).

Table 2.2. Chromatographic determination of FB1[1]

Support	Method	Eluent	Measurement	Assay Time (min)	Limit of Detection	Sample	Fumonisin Type	Ref
Wakosil 5C18 column	HPLC	Acidified methanol and disodium phosphate (80:20 pH 3.3)	Fluorescence	24	50 &100 µg/Kg	Corn	FB1, FB2, FB3	Nguyen et al.,2017
Synergi Max-RP (80 Å, 5 µm, 250 × 4.60 mm) HPLC column	HPLC	Methanol/0.1 M phosphate buffer (77:23, v/v) adjusted to pH 3.35 with concentrated orthophosphoric acid.	Fluorescence	-	25 µg/Kg	Corn kernels, tortillas and masa	FB1	Song et al., 2019
Luna C18 column (50 × 4.6 mm ID, 5 µm Phenomenex)	LC-MS	Water/acetonitrile/formic acid at	MS detection	11	0.02 µg/L	Urine (Tortilla consumption)	FB1	Schmitz et al., 2020
Column C18 XTerra Waters narrow bore with a C18 precolumn cartridge;	LC	Acidified water & methanol	MS/MS analysis	50	5 µg/kg	Corn	FBs,HFBs	Dall'Asta et al., 2009
Column, C18 Hypersil	LC	Acidified water & acetonitrile	MS/MS analysis	13	16 µg/kg	Corn	HFBs	Dall'Asta et al., 2009
Gemini® C18 column	HPLC	Methanol/water/acetic acid with ammonium acetate	MS/MS analysis	21	8 µg/kg	Corn	HFBs	Dall'Asta et al., 2009
Column Brownlee C18	HPLC	Water–acetonitrile–acetic acid	Fluorescence	-	100 µg/kg	Corn	FBs	Dall'Asta et al., 2009
Symmetry Spherisorb ODS2 C18 Column	HPLC	Methanol& sodium dihydrogen phosphate	Fluorescence	11.20	50 µg/kg, 70 µg/kg	Tunisian foods and feed	FB1, FB2	Ghali et al., 2009
XTerra MS C18 column	LC-MS-MS	Acidified water:acetonitrile & acetonitrile	MS-MS detection	<4 min (LC-ESI-MS/MS signal)	0.003 µg/kg	Bovine Milk	FB1	Gazzotti et al., 2009
Luna C18 column	LC-MS-MS	Acidified water & methanol	MS-MS detection	25	5 µg/L	Urine	FB1,FB2	Silva et al., 2010
Agilent Zorbax Eclipse XDB C- 18 column	LC-MS/MS	Acidified water & methanol	MS	15	9, 6 µg/kg	Maize	FB1,FB2	Tansakul et al., 2013
Hypersil™ ODS C18 Columns	HPLC	Acetonitrile & sodium phosphate buffer	Fluorescence	~13.5 (retention time)	50 µg/kg	Rice	FB1	Petrarca et al., 2014
Shimadzu C18 column	HPLC	Water/acetonitrile/acetic acid	Fluorescence	-	30 µg /kg	Corn	FB1	Bordin et al., 2015
Thermo Hypersil GOLD column	LC-MS	Acidified water & acetonitrile	MS detection	6	3.3 µg /kg	Human hair	FB1	Bordin et al., 2015
SHISEIDO Capcell core C18 column	UFLC	Acetonitrile -water (0.1% formic acid)	MS/MS	12	0.15 µg/kg	*Areca catechu*	FB1, FB2	Liu et al., 2016
SHISEIO Capcell coreC18 column	UFLC	0.1% formic acid in acetonitrile and water	MS/MS	12	0.05 µg/L 0.15 µg/L	Yam	FB1, FB2	Li et al., 2016
ACQUITY UPLC BEH C18 column	UHPLC	Water containing 0.1% formic acid (ESI+) or 0.1% ammonia (ESI-) and acetonitrile	MS	12	0.32 µg/kg, 0.08 µg/kg	Radix Paeoniae Alba	FB1, FB2	Xing et al., 2016
ZIC-pHILIC (SeQuant)	LC	Aqueous ammonium formate	MS	23	0.3, 1.3, 1.3, 0.8, 0.9, 2.6 µg/kg	Apples, apricots, lettuce, onion, wheat flour, chickpeas	FB1	Danezis et al., 2016
Poroshell 120 PFP column	UHPLC	Ammonium formate and formic acid in Milli-Q water and methanol (ESI+), and Milli-Q water and acetonitrile (ESI−).	MS/MS	17	1, 1, 3 µg/kg	*Pheretima*	FB1, FB2, FB3	Zhang et al., 2016
Kinetex C18 column	LC	Water-methanol with ammonium formate and formic acid	MS/MS	33	1.7, 3.9 µg/L	Maize	FB1, FB2	Dagnac et al., 2016
CORTECS C18 column	UPLC	Methanol-water with 0.5% (v/v) formic acid	MS/MS	30.3	15 µg/kg	Cereals (Wheat, corn, and rice)	FB1,FB2,FB3	Sun et al., 2016
Acclaim 120 C18 analytical column	HPLC	Acidified acetonitrile	Fluorescence	30	30 µg/kg 2.5 µg/L	Corn based feed	FB_1,FB_2	Smith et al., 2017
BEH C18 column	LC-MS-MS	Acidified water & acetonitrile	MS-MS detection	2, 4 (only hair)	0.014, 0.040, 0.012, ND µg/L	Pig plasma, urine, feces, hair	FB_1	Souto et al., 2017
Nucleodur C18 Gravity SB column	LC	Acetonitrile (2% acetic acid)- water (0.1% acetic acid)	MS	11.5	0.521 µg/L	Human blood	FB1	Osteresch et al., 2017
Ascentis Express C18	LC	Aqueous ammonium formate (0.1% formic acid)-aqueous methanol solution (ammonium formate, + formic acid, 0.1%)	MS/MS	30.1	10.14, 2.5, 0.625 µg/L	Milk	FB1, FB2, FB3	Flores-Flores and González-Peñas, 2017
MNPs + Acquity UPLC®BEH C18 column	UPLC	MeOH/H_2O (60:40) with ammonium acetate and formic acid	MS/MS	10	0.210 µg/kg	Vegetable oil	FB1	Zhao et al., 2017b
Kinetex XB-C18 100 Å column	HPLC	Methanol- water (with ammonium formiate+ formic acid)	MS/MS	30	100 µg/kg	Cereal-derived products	FB1, FB2	Annunziata et al., 2017
Cortecs UHPLC C18 column	LC	Water-MeOH (with NH_4HCOO+ HCOOH)	MS/MS	14.5	0.04 µg/L	Soy, oat and rice beverages	FB1,FB2	Miró-Abella et al., 2017
Gemini® C18 column	LC	Methanol/water/acetic acid 10:89:1 (v/v/v) -97:2:1 (with ammonium acetate)	MS/MS	20.5	3.2 (FB1), 2.4 µg/kg	Maize-*fufu*	FB1,FB2, FB3, FB4, FA1	Abia et al., 2017

C18 column	UHPLC	Water- MeOH with formic acid and ammonium formate	MS/MS	11.25	17.3,12.4,10.7, 9 µg/L (FB1), 11.8,17.2, 9, 10 µg/L (FB2)	Oat, soy,rice and bird seed milk	FB1,FB2	Hamed et al., 2017
Acquity BEH C18 column	UPLC	Water (ammonium acetate)- MeOH (formic acid)	MS/MS	15	0.20, 0.15 µg/kg	*Alpinia oxyphylla*	FB1,FB2	Zhao et al., 2017a
Eclipse Plus C8 RRHD column	MA-D- µ-SPE with UHPLC-Q-TOF/MS	Water containing 0.1% formic acid-acetonitrile	MS	9	0.0068, 0.013, 0.0074, 0.0030 µg//kg	Peach seed, milk powder, corn flour	FB1	Du et al., 2018
C18 column Phenomenex Kinetex	UPLC-MS/MS	Water containing 0.5 mM NH_4Ac - MeOH with 0.1% formic acid	MS/MS	15	0.25 & 0.1 (FB2) µg//kg	Lotus seed	FB1, FB2	Huang et al., 2018
ZORBAX RRHD Eclipse Plus C18	UHPLC	0.1% formic acid solution - acetonitrile (formic acid)	MS	12	1 µg/L	Grape and wines	FB1	Zhang et al., 2018a
Gemini® C18-column	LC	Methanol/water (with acetic acid and ammonium acetate	MS/MS	-	1 µg/kg	Dried date palm fruits	FB2	Abdallah et al., 2018
Acquity UPLC HSS T3 column	UPLC	(Formic acid & ammonium formate) water-acetonitrile	MS/MS	10	0.15, 0.09, 0.04, 0.03, 0.17 µg/L	Broiler chicken plasma	FB1, FB2, pHFB1a, pHFB1b, HFB1	De Baere et al., 2018
Silica based particles bonded with C18-penta fluorophenyl functions	LC-HRMS	Water- acetonitrile (both with formic acid) - MeOH	MS	26	0.5 µg/L	Tea	FB1, FB2	Cladière et al., 2018
Gemini-NX LC-column	LC	Water - methanol acidified (both with ammonium formate +formic acid)	MS/MS	39	1.5, 0.3 (vegetables) µg/kg	Ready-to-eat food (cereals, fish, legumes, vegetables, meat)	FB1, FB2	Carballo et al., 2018
Scherzo Sm-C18 column	HPLC	Acetonitrile (ammonium acetate) - acetonitrile (formic acid)	MS/MS	26	2.4, 2.3 µg/kg	Corn derived products	FB1, FB2	Park et al., 2018
Acquity HSS T3 column	LC	Water-ACN (both acidified with HAc)	MS/MS	25	0.001 µg/L	Human urine	FB1	Šarkanj et al., 2018
Waters ACQUITY HSS T3 column	UPLC	0.1% formic acid and 5 mM ammonium formate (phase A) -methanol (phase B).	MS/MS	13	0.22 µg/L	Beer	FB1, FB1	González-Jartín et al., 2019
Zorbax CX	UHPLC	Methanol/water (1:1 v/v) with 0.1% acetic acid	MS/MS	3.6 (chromatogram time)	51.5, 45.3 µg/kg	Rice	FB1, FB2	Da Silva et al., 2018
Kinetex Core-shell C18	LC	Water- methanol (both with ammonium formate and formic acid)	MS/MS	25.5	8.3 µg/kg	Green coffee	FB1, FB2	Bessaire et al., 2019
Kinetex Biphenyl column	LC	0.01 M ammonium acetate + 0.1% of acetic acid in water/ MeOH - 0.01 M ammonium acetate+ 0.1% of acetic acid in water/MeOH	MS/MS	16	0.50, 1.56 µg/kg	Animal feed	FB1, FB2	Jedziniak et al., 2019
UPLC HSS T3	LC	Aqueous ammonium formate 1mM and formic acid 1% (phase A)-Ammonium formate 1mM and formic acid 1% in methanol:water(95:3.9)	MS/MS	11	20 µg/kg	Nixtamalized Maize	FB1, FB2	Gilbert-Sandoval et al., 2020
Kinetex 2.6 µm C18 100A	UHPLC	Aqueous acetic acid 0.5% (phase A)-Acetic acid 0.5% and isopropanol 99.5% (phase B)	MS/MS	11	0.03, 0.01 µg/L	Kankankan	FB1, FB2	Yapo et al., 2020
Gemini C18-column	LC-ESI	Ammonium acetate 5 mM with methanol/water/acetic acid 10:89:1 (phase A) and 97:2:1 (phase B)	MS/MS	18.5	2.39, 1.68, 8.55 µg/kg	Dried Turkish figs	FB1, FB2, FB3	Sulyok et al., 2020

[1] Abbreviations: **HRMS:** High-resolution mass spectrometry; **SPE:** Solid-phase extraction; **UFLC:** Ultra-fast liquid chromatography; **UHPLC:** Ultra-high-performance liquid chromatography

Fluorescence detectors are restricted for the individual quantification of FB1 (Bordin et al., 2015; Petrarca et al., 2014; Ueno et al., 1997), the sum of FB1, FB2, FB3 (Dall'Asta et al., 2009) or the separate determination of up to three group B fumonisins (Ghali et al., 2009; Smith et al., 2017). On the other hand, one of the main advantages of mass spectrometry detectors is the possibility of performing multiplex analysis, not only for different mycotoxins (Abdallah et al., 2020; Annunziata et al., 2017; Carballo et al., 2018; Dagnac et al., 2016; Du et al., 2018; Flores-Flores and González-Peñas, 2017; González-Jartín et al., 2019; Hort et al., 2020; Huang et al., 2018; Jedziniak et al., 2019; Li et al., 2016; Liu et al., 2016; Miró-Abella et al., 2017; Osteresch et al., 2017; Park et al., 2018; Šarkanj et al., 2018; Sulyok et al., 2020; Sun et al., 2016; Xing et al., 2016; Zhang et al., 2018a; Zhao et al., 2017a; Zhao et al., 2017b), but also when combined with varied metabolites. Growth regulators, antibiotics, pesticides (Cladière et al., 2018; Da Silva et al., 2019; Danezis et al., 2016), and other fungal metabolites (Abdallah et al., 2018; Hamed et al., 2017), were simultaneously identified in analysis capable of assessing up to 74 and 90 compounds (Abia et al., 2017; Nafuka et al., 2019). Mass spectrometry has also been used for assessing mycotoxin transfer from feed to organs and tissue in poultry (Hort et al., 2020).

The importance of novel analytical methods relies on the low sensitivities achieved within a relatively short detection time. The speed of mass spectrometry (ESI+) signals, was early proven to reduce the sole determination of FB1 in bovine milk to 4 minutes (Gazzotti et al., 2009), with a half-fold time reduction on more recent assays for pig samples (plasma, urine, feces) (Souto et al., 2017). Its limits of detection have reached 0.003 µg/kg (Du et al., 2018; Gazzotti et al., 2009) for animal (bovine milk) and food samples (corn meal), and 0.001 µg/L in human urine (Šarkanj et al., 2018). Notwithstanding the excellent performance of conventional analytical methods, some disadvantages are related to sample pre-treatment including long extraction steps with further purification protocols, as well as method optimization of the chromatographic separation, derivatization or internal standard addition, along with its corresponding validation method. For instance, a single drying step could add two days to the total assay preparation time (Dagnac et al., 2016).

Sample clean-up is a key step for reducing matrix effect, where strong anion exchange (SAX) columns have been utilized as cheaper clean up cartridges in LC-MS detection, with recoveries of up to 86.6 and 106% for human hair (Bordin et al., 2015) and piglet urine (Souto et al., 2017) respectively. In a similar way, immunoaffinity columns (IAC) have been proven to attain maximum recoveries of 109% for FMOC-derivatized cornmeal samples (Smith et al., 2017), and 90% in rice analyzed by LC-MS (Da Silva et al., 2019). The specificity of antibodies in IAC also allowed the successful LC-MS analysis of FB1 in complex samples, such as milk (Gazzotti et al., 2009), human urine

(Silva et al., 2010) and chicken tissue (Hort et al., 2020) with peak recoveries of 88.4%, 99.1% and 95-102% respectively. Lower recoveries were found for the determination of OPA-derivatized FB1 in maize (68.5%), rice (72.4%), sorghum (75.6%) and wheat (69.4%) extracts (Pfeiffer and Mayer, 2016). Nonetheless, IACs increase the total assay cost, since they could account for double or triple the price of SAX cartridges, with highly comparable performance. Besides, IACs have a limitation on the variability of analytes and could promote interaction with the matrix constituents (Jedziniak et al., 2019). In both cases (SAX and IAC) the total analysis time is enlarged by the conditioning, loading, washing, elution, evaporation, and reconstitution steps.

Some novel developments incorporated magnetic nanoparticles for the sorption and concentration of mycotoxins, promoting a simultaneous clean-up and sensitivity enhancement in the overall method (Zhao et al., 2017b). Nonetheless, even when the performance of patented commercial clean up columns allows their utilization in single (Campa et al., 2004) and multiple mycotoxin analysis, the adsorption procedure of recent products might impede the detection of FB1 and FB2 (Dagnac et al., 2016). As a replacement, novel dispersants such as nano zirconia, have been found with high extraction efficiency of FB1 (Du et al., 2018).

Alternatively, the QuEChERS method, initially developed for pesticides, was subsequently introduced for the dispersive solid-phase extraction (SPE) of FB1 (Petrarca et al., 2014), and further validated for its application in the multi-target analysis due to its lower cost, less time consumption, easy procedure (Gilbert-Sandoval et al., 2020; Hamed et al., 2017; Xing et al., 2016; Yapo et al., 2020; Zhang et al., 2016), as well as its availability in extraction kits (Sun et al., 2016) with satisfactory recoveries (Annunziata et al., 2017). Likewise, sample preparation with a QuEChERS dispersive SPE was useful for minimization of matrix effects from beer, with a preconcentration step producing enhanced LODs (González-Jartín et al., 2019). In spite of being a favorable option for sugar reduction in the quantification of FB1 in oat, soy and rice beverages (extraction recoveries 80, 82, 85%; matrix effect: 76, 63, 75%) (Miró-Abella et al., 2017), a UPLC-MS/MS study of *Alpinia oxyphylla* revealed the unsatisfactory FB1 and FB2 recoveries from QuEChERS (~50 & 55%) and hydrophilic-lipophilic balance (HLB) cartridges (~65 & 55%) in comparison to solid-liquid extraction (~80 & 70%). Nevertheless, the three extraction methods exhibited a signal increase (80-145%) due to matrix effect (Zhao et al., 2017a). By contrast, recent studies in sugarcane juice proposed the use of HLB cartridges as an alternative to QuEChERS, due to its high recoveries of 98% for FB1 (Abdallah et al., 2020).

Despite the expected disadvantages of the dilute and shoot method towards the complexity of some samples, which could affect the detector sensitivity and assay

performance, when optimized, this procedure can be applied in the multi-target analysis of food samples without a clean-up phase (Abdallah et al., 2018; Cladière et al., 2018; Da Silva et al., 2019; Miró-Abella et al., 2017). For instance, a comparison between the efficiency of dilute and IAC methods revealed that, even when lower LODs and limits of quantification (LOQs) were obtained with the clean-up step (0.5 and 1.66 against 2.3 and 4.3 µg/kg), a dilution procedure accomplished improved regression (0.9941), high recoveries (94-106%) and reproducibility for FB1-spiked animal feed (Jedziniak et al., 2019).

A similar situation was confirmed for matrix-match calibration (Cladière et al., 2018; Li et al., 2016; Tansakul et al., 2013), and internal standard (IS) addition (Goud et al., 2020; Huang et al., 2018; Jedziniak et al., 2019) where a clean-up step was not necessary to eliminate matrix effects and run accurate determinations. Yet, the use of specific IS and a validated method for a single matrix, could reduce the scope of the determination, and increase its final cost. Notwithstanding, some approaches proposed the application of the aforementioned procedures combined with clean up techniques and QuEChERS, for a greater method validation (Carballo et al., 2018; De Baere et al., 2018; Flores-Flores et al., 2017; Šarkanj et al., 2018). As previously mentioned, the use of HPLC and LC-MS methods has been widely explored mostly in developed countries, where the infrastructure and resources allow their application for mycotoxin analysis (Pitt et al., 2012). Moreover, drawbacks from chromatographic analysis comprise complex sample pre-treatment in which immunoaffinity columns increase the cost, utilization of organic solvents during sample extraction, clean-up and separation steps, derivatization if UV-Vis detection is utilized, and the need of trained users for their long and laborious procedures (Chen et al., 2015a; Jiang et al., 2020). Therefore, other alternatives should be considered for in-field assays, especially in rural areas and outbreak regions from developing countries.

2.3.2 Immunosensors for the detection of fumonisin B1

The enzyme-linked immunosorbent assay (ELISA) for the determination of FB1 represents the foundation of different approaches. Competitive assays have been commonly employed for biosensing techniques, mostly because of the restriction produced by single epitopes on other types such as sandwich ELISA (Ligler et al., 2003). Some general procedures for a competitive immunoassay include a coating stage of antibody on the selected support, followed by the incubation with a mixture of free FB1 (sample) and functionalized toxin (horseradish peroxide (HRP)-FB1). After washing the unbound FB1 or HRP-FB1, different substrates can be added for the development of either a chemiluminescence or a colorimetric signal (Quan et al.,

2006). Some commercial kits are also based on a competitive scheme, in which capture antibodies, specific to a FB1 antibody, are coated on a well, where free FB1, enzyme-fumonisin and antibody are incubated. The bound HRP-fumonisin is then measured by incubating with a chromogen (Ghali et al., 2009). In some bulk experiments, magnetic nanobeads have been used as a support with a competitive binding role under the presence of FB1 and its biotinylated antibody (Yang et al., 2020). Other modifications suggested the substitution of HRP with compounds such as glucose oxidase to produce hydrogen peroxide, an inducer of AuNP aggregation (Zhan et al., 2019), and the application of genetically engineered antibodies (Ren et al., 2020). A novel technique used a monoclonal antibody-rhodamine isothiocyanate (RBITC)-AuNPs probe for the competitive binding between OVA-FB1 and FB1, where cysteamine worked as a turn-on compound for revealing the degrees of fluorescence from the quenched probe (Zhang et al., 2020b).

This antigen-antibody interaction has been used, optimized and improved over the years; and commercially available ELISA kits and standardized ELISA protocols are still applied for method validation and comparison with novel biosensing developments (Liu et al., 2018; Munawar et al., 2018; Niazi et al., 2019; Shu et al., 2019; Qu et al., 2019). As presented in Figure 2.4, electrochemical immunosensors have portrayed some of the lowest LODs (Masikini et al., 2015; Masikini et al., 2016). For instance, the signal of an impedance sensor was modified by depositing quantum dots- carbon nanotubes on a glassy carbon electrode (GCE) for the immobilization of the corresponding antibody. In this case, the electron transfer resistance was enhanced after target binding, allowing LODs as low as 0.46 pg/L (Masikini et al., 2015). An electrochemical indirect competitive method was also refined by modifying a GCE with nanotubes-chitosan (undefined characteristics) and FB1-Bovine serum albumin (BSA). The remaining antibody after the incubation with free FB1 (sample) was able to bind FB1-BSA, as well as an alkaline phosphate-labelled anti-antibody, whose substrate triggered the electrochemical signal with lower, yet good sensitivity of 2 ng/L (Yang et al., 2015). The reduction of conductivity promoted by the antibody-antigen reaction was again explored for the immobilization of antibodies on nanotube-modified GCE, attaining a LOD of 3.8 pg/L (Masikini et al., 2016). In addition to electrochemical methods, surface-enhanced Raman scattering (SERS) competitive immunoassays were applied by combining FB1-BSA functionalized Au nanopillars with nanotags, consisting in AuNP simultaneously functionalized with anti-antibody and malachite green isothiocyanate (MGITC). The interaction between the primary antibody and high antigen concentrations resulted in a weak SERS signal, due to the absence of complex formation within free primary antibodies, nanopillars and nanotags, with a LOD of 0.00511 pg/L (Wang et al., 2018).

Table 2.3. Immuno-based assays for the determination of FB1[1]

Support	Method	Labelling/Substrate	Measurement	Assay Time (min)	LOD	Sample	Fumonisin	Ref
96-well immunoplates	ELISA	HRP	Optical density	150	0.2 µg/L	Corn	FB1	Ueno et al., 1997
ELISA kit	AgraQuant Total Fumonisin Assay Protocol	Methanol-water	Intensity of colour	20	200 µg/kg	Corn	FBs	Dall'Asta et al., 2009
96-well plate	ELISA (RIDASCREEN ®)	HRP	Optical density	55	25 µg/kg,	Tunisian foods and feed	FB1+FB2	Ghali et al., 2009
Test kit	ELISA	Antigen	OD	20	200 µg/kg	Maize	FB1+FB2	Tansakul et al., 2013
Optical fibre	DC assay	FITC	Fluorescence	24	10 µg/L	Corn	FB1	Thompson and Maragos, 1996
Sample cell	SPR	Gold film	Reflected light intensity	10	50 µg/L	PBS	FB1	Mullett et al., 1998
Protein-A coated capillary column	Liposome-amplified competitive assay	Liposome	Fluorescence	<11	1 µg/L	TBS	FB1	Ho and Durst, 2000
Glass culture tube	Competition of unlabelled fumonisin	Fluorescein	Fluorescence Polarization	2	500 µg /kg	Maize	FB1	Maragos et al., 2011
Borosilicate glass slides	Competitive assay	Biotin	Fluorescence	~8	250 µg/L	PBSTB	FB1	Ligler et al., 2003
96-well microplate	ECL-ELISA	HRP	Fluorescence	60	0.09 µg/L	Cereals	FB1	Quan et al., 2006
DMA-NAS-MAPS treated glass	Competitive immunoassay	Streptavidin-AP/ NBT/BCIP	Colorimetric	65	43 µg/L	Binding buffer	FB1	Lamberti et al., 2009
NC membrane	LFIA	Colloidal Gold	Line intensity	4	199 µg/kg	Maize	FB1	Molinelli et al., 2009
Luminex 100 microspheres	Indirect competitive fluid array	Biotin	Fluorescence cytometry	60	0.3 µg/L	Grain Products	FB1	Anderson et al., 2010
SPGE	DC assay	HRP-TMB	Chronoamperometry	45	5 µg/L	Corn	FB1,FB2	Kadir and Tothill, 2010
NC membrane	LFIA	Colloidal Gold	Line intensity	10	120 µg/L	Maize	FB1	Anfossi et al., 2010
Aldehydelized glass slides	Specific competitive reactions	Ag conjugates	Fluorescence	90	109.06 µg/L	Wheat	FB1	Wang et al., 2011
NC strip	Competitive lateral flow immunoassay	HRP	CL	15	2.5 µg/L	Maize	FB1,FB2	Mirasoli et al., 2012
NC membrane strip	One-step competitive immunochromatographic	AuNP	Colour density	10	2.5 µg/L	Maize	FB1+FB2+FB3	Li et al., 2012
NC membrane	LFIA	Protein A-gold	Line intensity	30	3200 µg/kg	Maize	FB1	Lattanzio et al., 2012
96-well microplate	IC ELISA	HRP	Absorbance	70	8.32 µg/kg	Corn	FB1	Zou et al., 2013
Paramagnetic beads	Inhibition immunoassay	Mycotoxin-R-Phycoerythrin	Dose–response cytometry (Fluorescence)	50	170, 1270 µg/kg	Maize, wheat	FB1+FB2	Peters et al., 2013
NC membrane	LFDIA	Colloidal Gold	Line intensity	30	5.23 µg/L	Corn	FB1	Wang et al., 2013a
NC membrane	Immunochromatographic strip	Colloidal gold	Visual detection	3	5 µg/L	Cereal	FB1	Venkataraman et al., 2014
PrG functionalized magnetic beads SPCEs	DC multi-channel electrochemical immunoassay	HRP	Current	40	0.58 µg/L	Cereals	FB1	Ezquerra et la., 2015
GCE/PT	Impedimetric immunosensor	PDMA-MWCNT	EIS	-	0.00000046 µg/L	Methanol	FB1	Masikini et al., 2015
					14 µg/kg	Corn	FB1	
					11 µg/kg	Corn	FB2+FB3	
NC strip	LFIA	HRP	CL	30	6 µg/kg	Maize	FB1	Zangheri et a., 2015
SWNTs/CS electrode	Indirect competitive binding	Alkaline phosphatase	Electrochemical	180.11	0.002 µg/L	Corn	FB1	Yang et al., 2015
SPCEs-Magnetic beads	Competitive multi- immunoassay	HRP	Amperometric	60	0.33 µg/L	CRM, beer	FB1,FB2,FB3	Jodra et al., 2015
96-well microplate	Biopanning	Ab2β Nb /HRP	OD	~60	0.15 µg/L	PBS	FB1,FB2	Shu et al., 2015
Microplate reader	FPIA	FITC	Fluorescence Polarization	<30	157.4, 290.6 µg/kg	Maize	FB1, $FB2_2$	Li et al., 2015
NC membrane	Competitive small molecule detection	UGNs	Colour intensity	<5	5 µg/L	Grains	FB1	Ren et al., 2015
NC membrane	Competitive small molecule detection	AuNP	Colour intensity	<5	20 µg/L	Grains	FB1	Ren et al., 2015
PPy/ErGO SPE	Label-free electrochemical immunosensing	AuNP	Current	40	4.2 µg/kg	Corn	FB1	Lu et al., 2016
GCE	Electrochemical impedance spectroscopy	PDMA-MWCNT	Electron transfer resistance	-	0.0000038 µg/L	Corn	FB1	Masikini et al., 2016
NC membrane	Immunochromatographic strip test	DR-AuNP	Visual detection	10	1000 µg/kg	Maize flour	FB1	Di Nardo et al., 2017
Hi-Flow Plus membranes	Competitive reaction	AuNP	Coloration	15	0.6 µg/L	Maize	FB1	Urusov et al., 2017

Microbead	Flow immunocytometry	Phycoerythrin	Fluorescence	45	116 µg /kg	Maize	FB1	Bánati et al., 2017
NC strips	Competitive assay	Colloidal gold	Colour intensity	10	0.24 µg/L	Agricultural products	FB1	Tang et al., 2017
Plates	IC ELISA	IgG-HRP	Absorbance	68	0.08 µg/L	Agricultural products	FB1	Tang et al., 2017
Mimotope on ARChip Epoxy slides	Competitive binding inhibition	Alexa Fluor 647- IgG	Fluorescence	210	11.1 µg/L	Maize, wheat	FB1	Peltomaa et al., 2017
NC high-flow plus membranes	Competitive binding inhibition	AuNP/ HRP-labelled IgG	Colour	10	25 µg/L	Corn	FB1	Hao et al., 2018b
Nitrocellulose membrane	LFIA	AuNP/ CdSe/ZnS QD	Fluorescence	15	62.5 µg//kg	Maize flour	FB1, FB2	Anfossi et al., 2018
96-well microplates	Competitive assay	AuNF@FeTPPCl + TMB	Colour	40	0.05 µg/L	Buffer	FB1	Zhou et al., 2018
Mycotoxin-protein conjugates on chip (MZI)	Primary (mycotoxin/protein conjugates - anti-mycotoxin specific mAbs) and secondary immunoreaction (immune adsorbed mAbs- IgG antibody)	Label-free	Phase shift	12	5.6 µg/L	Beer	FB1	Pagkali et al., 2018
96-well plates with protein G-coated AuNPs (bulk)	Competitive immunoassay	YFP-tagged FB1-mimotope	Fluorescence	45	1.1 µg/L	Wheat	FB1, FB2	Peltomaa et al., 2018
NC membrane	Competitive inhibition reaction	Antibody- AuNP conjugates, FB1-BSA, IgG	Visual detection	10	30 µg/L	Corn	FB1	Yu et al., 2018
Anti-FB1 mAbs on plate well	Competitive fluorescence ELISA	CAT-regulated-fluorescence quenching of MPA-QD	Fluorescence	75n	0.33 µg/L	Corn	FB1	Lu et al., 2018
Gold coated magnetic NP	Competitive CLIA	HRP-LUMINOL	Fluorescence	150	0.027 µg/L	Cereals	FB1	Jie et al., 2018
Microplate	IC-ELISA	IgG-HRP	Absorbance	120	0.078 µg/L	Corn	FB1,FB2,FB3	Li et al., 2018
Microplate	DC-pELISA	AuNP	Absorbance	120	12.5 µg/L	Corn	FB1	Chen et al., 2018a
Test column	IATC	HRP	Color intensity	5.5	20 µg/kg	Maize	FB1,FB2,FB3	Sheng et al., 2018
Au nanopillars	Surface-enhanced Raman scattering	Malachite green isothiocyanate-AuNP	Raman intensity	120	0.00511 pg/mL	Standard curve	FB	Wang et al., 2018
NC membrane	Direct competition	Streptavidin-horseradish peroxidase	Enhanced chemiluminescence	45	0.24 µg/L	Corn samples	FB1	Zhang et al., 2018b
Anti- FB1 mAb in microtiter wells	Non-competitive idiometric nanobodies phage ELISA	HRP conjugated anti-M13 antibody-TMB	Absorbance	130	0.19 µg/L	Corn	FB1	Shu et al., 2019
ITO coated glass integrated with PDMS microfluidic channel.	Three-electrode electrochemical sensor	AuNP-Ab	Current	50	0.097 µg/L	Corn	FB1	Lu et al., 2019
Superparamagnetic carboxylated xMAP® microspheres	Quadplex FCIA	R-PE conjugated goat anti-mouse antibody	Fluorescence	60	2.45 µg/L	Milk	FB1	Qu et al., 2019
NC membranes	Multiplex ICr assay	QD nanobeads	Fluorescence	10	20 µg/L	Maize	FB1	Duan et al., 2019
GONC on DEP electrodes	Electroactivity reduction with biorecognition.	Label-free	CV/DPV	65	294 µg/L	PBS-T	FB1	Cheng et al., 2019
96 well plates with protein-G and BSA	Competitive Plasmonic ELISA	Glucose oxidase-FB1	Absorbance	180	0.31 µg/L	Maize	FB1	Zhan et al., 2019
NC membrane	Competitive multiplex ICr Assay	Quantum dot nanobeads-MAb	Fluorescence (test line/ control line)	18	1.58 µg/L	Cereals	FB1	Shao et al., 2019
NC membrane	ICr strip	Flower-like AuNP	Color intensity	5	5 µg/L	Chinese traditional medicine	FB1	Huang et al., 2020
NC membrane	Multiplex ICr test	AuNP	Colour intensity	-	60 µg/L	Wheat and corn	FB1	Hou et al., 2020a
Nanomagnetic beads	Competitive solid-phase assay	Biotin NHS-Streptavidin-HRP	OD	22	0.21 µg/L	Maize	FB1	Yang et al., 2020
NC membrane	Competitive ICr strip	Colloidal gold-scFv	Color Intensity	10	2.5 µg/L	Maize	FB1	Ren et al., 2020
NC membrane	Smartphone-based multiplex LFIA	AuNP and TRFMs	Ratio T/C line color & fluorescence	8	0.59 µg/kg (C) 0.42 µg/kg (F)	Maize, wheat, bran	FB1	Liu et al., 2020b
Microplate-OVA-FB1	Competitive immunoreaction	Cysteamine on mAb-RBITC-AuNPs	Fluorescence	46	0.023 µg/L	Maize	FB1, FB2, FB3	Zhang et al., 2020b
NC membrane	Competitive ICr strip	QDNBs-mAb	Fluorescence	25	60 µg/L	Wheat. corn	FB1	Hou et al., 2020b
NC-membrane	Immunochromatographic assay	Eu-FM-mAB	Time-resolved fluorescence	7	8.26 µg/kg	Corn, corn flour, wheat, rice, brown rice	FB1	Guo et al., 2020

[1] Abbreviations: **Ab2β Nb:** Anti-idiotypic nanobody; **AP/NBT/BCIP:** Alkaline phosphatase/ nitro blue tetrazolium chloride/5-Bromo-4-chloro-3-indolyl phosphate toluidine salt; **AuNP**: Gold nanoparticles(spherical)**; BSA:** Bovine serum albumin; **CAT:** Catalase; **CL:** Chemiluminescence; **CLIA:** Chemiluminescence immunoassay; **CV:** Cyclic voltammetry; **DC:** direct competitive; **DEP:** Disposable electrical printed; **DMA-NAS-MAPS**: Copoplymer (N,Ndimethylacrylamide)- N,N-acryloyloxysuccinimide-[3-(methacryloyl-oxy)propyl] trimethoxysilyl; **DPV:** Differential pulse voltammetry; **DR:** Desert rose-like; **ECL:** Enhanced chemiluminescent; **EIS:** Electrochemical impedane spectroscopy; **ErGO:** Electrochemically reduced graphene oxide; **Eu-FM:** Europium Fluorescent Nanosphere; **FCIA**: Flow cytometric immunoassay; **FeTPPC:** Iron porphyrins; **FITC:** Fluorescein isothiocyanate; **FPIA:** Fluorescence polarization immunoassay; **GCE:** Glassy carbon electrode; **GONC:** Graphene oxide nanocolloids; **HRP:** Horseradish peroxidase; **IATC**: Immunoaffinity test column; **IC:** Indirect competitive; **ICr:** immunochromatographic; **IgG:** Goat anti-mouse immunoglobullin; **ITO:** Indium tin oxide; **LFIA:** Lateral flow immunoassay; **mAb:** Monoclonal antibody; **MPA-QD:** mercaptopropionic acid-modified CdTe quantum dots; **MZI:** Mach-Zehnder interferometers; **NC:** Nitrocellulose; **NHS:** *N*-Hydroxysuccinimide; **NP:** Nanoparticles; **OD:** Optical density; **p:**plasmonic; **PDMA-MWCNT:** Poly(2,5-dimethoxyaniline) multi-walled carbon nanotube composite; **PDMS:** Polydimethylsiloxane**; PPy:** Polypyrrole; **PrG:** Recombinant Protein G; **QD:** Quantum dot; **QDNBs:** Quantum dots nanobeads; **RBITC:** Rhodamine B isothiocyanate; **R-PE:** R-phycoerythrin; **scFv:** single-chain variable fragment; **SPCEs:** Screen -printed carbon electrode; **SPE:** Screen-printed carbon electrode; **SPGE:** Bare gold screen-printed electrode; **SPR:** Surface plasmon resonance; **SWNTs/CS:** Single-walled carbon nanostructure/ Chitosan; **TMB:** 3,3',5,5'-tetramethylbenzidine dihydrochloride; **TRFMs:** Time resolved fluorescence microspheres; **UGNs:** Urchin-like gold nanoparticles; **YFP:** Yellow fluorescent protein

As noted in Table 2.3, immunosensors can be supported on different matrices, including optical fiber, well plates, glass slides, magnetic beads, magnetic nanoparticles, electrodes and chips. Yet another of the main advantages of using antibodies is the feasibility to be incorporated in paper-based biosensors. Paper matrices are presently relevant for the creation of portable, point-of-care, applicable and cheap devices (Hossain et al., 2009). The conjugation of antibodies with colloidal gold (gold nanoparticles) has been widely applied for the colorimetric detection of FB1 on nitrocellulose membranes (Anfossi et al., 2010; Anfossi et al., 2018; Hou et al., 2020a; Lattanzio et al., 2012; Li et al., 2012; Molinelli et al., 2009; Ren et al., 2015; Tang et al., 2017; Venkataramana et al., 2014; Yu et al., 2018; Wang et al., 2013a; Zangheri et al., 2015). Some modifications included the application of urchin-like and flower-like gold nanoparticles (AuNP), which slightly increased the sensitivity when compared to a spherical particle (Huang et al., 2020; Ren et al., 2015).

As an alternative to color intensity measurements, a chemiluminescent substrate could be incubated with HRP for a slight improvement of the LOD (Mirasoli et al., 2012; Zhang et al., 2018b), or the application of quantum dots (QD) in which a radiometric analysis revealed a constant signal from the test line with biotin-BSA, compared to the calibration with anti-mouse IgG (Shao et al., 2019). Nevertheless, the application of fluorescent QDs not always result in an improved sensitivity, as reported for a nitrocellulose strip for the detection of FB1 (LOD: 60 µg/L), ZEN and OTA with a monoclonal antibody-QD probe placed on the conjugate pad, through the competitive interaction with mycotoxin-BSA at the test line (Hou et al., 2020b), and a mAB-Europium fluorescent nanoparticle with FB1 (LOD: 8.26 µg/L) and FB1-BSA (Test line) (Guo et al., 2020). An advantage of paper-based biosensors is the possibility of performing smartphone-based analysis, as already achieved on colorimetric and fluorescent signals (Liu et al., 2020b). Notwithstanding the multiple modifications, most of the differences among paper-based and other types of immunosensors can be explained in terms of the different antibodies selected and employed in each method.

Although ELISA is characterized by its simplicity, speed, reproducibility, and accuracy, its cost, equipment needs, and assay times make it unsuitable for on-site analysis, especially in developing countries (Majdinasab et al., 2020; Song et al., 2019). Compared to other immunoassays (e.g., electrochemical), ELISA requires more reagent consumption, incubation times and portrays limited separation, cleaning and reproducibility (Zhang et al., 2020b). Of note, the exploitation of the efficient conversion rate of HRP (10^7 substrate molecules/min) in sandwich-type and competitive assays results in specific and sensitive approaches. However, the prolonged incubation times along with the cost of the chemicals and matched antibodies, prevents their wider application for the analysis of small mycotoxins, which

might result in semi-quantitative and qualitatively results, mainly observed in immunochromatographic assays (Di Nardo et al., 2017; Duan et al., 2019; Hao et al., 2018b; Hou et al., 2020a; Huang et al., 2020; Lattanzio et al., 2012; Ren et al., 2020; Sheng et al., Venkataramana et al., 2014; Zhang et al., 2020b). In this regard, immunochromatographic multitarget detection could result in misreading and line interference, with the subsequent detection of false positives (Duan et al., 2019). Besides, the frequent non-linear behavior in the calibration curves from immunological assays has been linked to strenuous and long procedures (Jodra et al., 2015). In addition, compared to aptamers, the application of antibodies presents some drawbacks, including cross-reactivity and false positives, leading to mycotoxin underestimation thus affecting the final selectivity (Lin et al., 2015; Lin et al., 2017a; Lin et al., 2017b; Majdinasab et al., 2020). Apart from the reported cross-reactivity (Bánati et al., 2017; Li et al., 2015; Liu et al., 2020b; Pagkali et al., 2018; Peltomaa et al., 2018; Peter et al., 2013; Ren et al., 2015; Tang et al., 2017; Zangheri et al., 2015; Zhang et al., 2020b), which is occasionally not tested in certain designs (Masikini et al., 2016; Yang et al., 2020; Zhou et al., 2018), antibody-based detections are susceptible to pH changes and matrix effects when inappropriately used or if matrix-matched calibrations have been omitted, which influences the observed preference for chromatographic methods, especially as regulatory analysis (Pitt et al., 2012; Tang et al., 2014). Unlike antibodies, aptamers are chemically and pH stable, resist room temperature storage and present reversible denaturation. Furthermore, their non-biological screening allows their easy, high-purity in-vitro synthesis and modification, whose obtained sequences can be successfully combined with nanomaterials (Ruscito et al., 2016; Song et al., 2019). In fact, attempts to replace antibodies with aptamers have originated an alternative method to ELISA, named enzyme-linked apta-sorbent assay or ELASA (Majdinasab et al., 2020).

2.3.3 Other methods

Alternatives to the extensively known immunologic and chromatographic techniques include chemometric, electrochemical and colorimetric analysis, as shown in Table 2.4. In SERS, the spectral variations of extracted samples mixed with Ag dendrites were measured on a quartz plate (Lee and Herrman, 2016), while innovative, promising and more robust techniques incorporated the use of molecularly imprinted polymer nanoparticles (MIPs). Commonly polymerized with monomers such as methacrylic acid (MAA), ethylene glycol methacrylate (EGMP), N-isopropylacrylamide (NIPAM), N,N'-methylene-bis-acrylamide (BIS), N-tert-butylacrylamide (TBAm), and N-(3-Aminopropyl) methacrylamide hydrochloride (NAPMA); MIPs have functioned as

a replacement of primary antibodies; in which the utilization of FB1 as template molecule enhanced the performance, selectivity, thermal stability, and easy manufacturing of this technique. Once the MIPs are synthesized, the general procedure is similar to ELISA, where free FB1 competes with a FB1-HRP conjugate, where the latter reacts with a substrate (TMB: 3,3′,5,5′-tetramethylbenzidine), bearing a colorimetric response. Such mechanism reduces the limit of the detection to 4.4 ng/L (Smolinska-Kempisty et al., 2016) and 1.37 ng/L (Munawar et al., 2018), while an improvement on the silanisation step yielded more MIPSs and allowed the quantification of FB in maize, with a lower LOD equivalent to 1 ng/L (Munawar et al., 2019). Recent alternative methods suggested the chemical modification of FB1 prior to its quantification assay, where alkaline hydrolysis with KOH was proposed to reduce steric hindrance, allowing the formation of hydrogen bonds between hydrolysed fumonisin (HFB1) and the NH_2 groups in cysteamine functionalized AuNP (Chotchuang et al., 2019). Likewise, a derivatization step between FB1 and a fluorescent derivative was necessary for spectra acquisition on a nylon membrane (Li et al., 2020). Besides, as already observed for some immunoassays, electrochemical methods were combined with MIPs, for a reduction on the limit of detection. A GCE modified with AuNPs and Ru@SiO_2 in chitosan (undefined characteristics), was proved as favorable support to produce MIPs generating electrochemiluminescent estimations with a LOD of 0.35 ng/L (Zhang et al., 2017). In a similar approach, an iridium tin oxide (ITO) electrode modified with CdS quantum dots, chitosan (undefined characteristics) and graphene oxide worked as the UV polymerization area, in which the resulting MIPs were used for photoelectrochemical evaluation of FB1 levels as low as 4.7 ng/L (Mao et al., 2019). The application of nanoMIPs in electrochemical measurements (EIS, DPV) allowed the achievement of LODs as low as 21.6 fg/L, which so far is the lowest value reported for FB1 (Munawar et al., 2020).

On the other hand, capillary electrophoresis (CE) was initially reported in 1995 as a different technique with greater capability for the separation of FB1 to that from LC, where either its integration with MS detection or the quantification of fluorescent derivatives were utilized in the analysis of corn (Hines et al., 1995; Holcomb et al., 1995). Subsequent CE approaches explored the performance of fluorescein isothiocyanate for the derivatization of FB1 (Maragos et al., 1995), and its application in the competitive binding of mAb by labeled (derivatized) and unlabeled FB1, for the CE of the remaining fluorescein-FB1 (Maragos et al., 1997). Despite the advantages of CE in terms of the column efficiency, speed, reduction of organic solvents (Holcomb et al., 1995), the high limit of detections restricted any further applications. After two decades only one recent work on the application of coated (C_1) and uncoated capillaries resulted in a relatively high LOD of 156 µg/L for the analysis of rice and

fusarium microconidia by CE-MS (Kecskeméti et al., 2020), which denotes an opportunity for exploring, refining and optimizing more CE options for the determination of FB1 and other analogues.

Table 2.4 Other methods for FB1 determination [1]

Support	Method	Labelling/ Substrate	Bioreceptor	Measurement	Assay Time (min)	LOD	Sample	Fumonisin Type	Ref
Quartz plate	Surface-enhanced Raman spectroscopy	Ag Dendrites	SPR	Raman signal	<1	>5000 µg /kg (not reported as LOD)	Maize	FB1,FB2, FB3	Lee et al., 2016
Polymer-coated microplates	MIP	HRP-conjugate	nanoMIPs	Absorbance	70	0.0044 µg/L	PBS	FB2	Smolinska-Kempistym et al., 2016
GCE-AuNPs-Ru@SiO_2-Chitosan	SEECL	MIP containing FB1 + MAA+ EDMA+AIBN	MIP-Amino group	ECL	5	0.00035 µg/L	Milk, maize	FB1	Zhang et al., 2017
96-well microplates+EGMP,NIPAm, NAPMA, TBAm	Direct competitive assay based on	HRP–FB1 conjugate + TMB	MINA	Color	5.16	0.00137 µg/L	PBS buffer	FB1	Munawar et al., 2018
ITO electrode surface coated with GO/CdS/CS	MIP-Photoelectrochemical sensor	MIP including FB1, MAA, EDMA and AIBN	MIP	Photocurrent	15	0.0047 µg/L	Maize meal and milk	FB1	Mao et al., 2019
Polymer-coated microplates (EGMP,NIPAm,BIS, NAPMA)	MINA	HRP-conjugate + TMB	nanoMIPs	Absorbance	70	0.001 µg/L	Maize	FB1	Munawar et al., 2019
Cys-AuNPs	Aggregation based colorimetric detection	AuNPs	HFB1	Absorbance	65	0.90 µg/kg	Corn	FB1	Chotchuang et al., 2019
Syringe SPE (Nylon membrane)	Solid-phase fluorescence spectrometry	RhB-Cl	Derivatization	Relative Intensity (Fluorescence)	4	0.119 µg/L	Maize	FB1	Li et al., 2020
nanoMIPSs-PPy/ZnP-Pt Electrode	Electrochemical sensor	MIP+FB1+NIPAM+BIS+TBAm+EGMP+NAPMA	MIP	EIS, DPV	5	0.0000000216, 0.0000005 µg/L	Maize	FB1	Munawar et al., 2020
Fused silica capillary	CE	Ammonium formate/ammonia+ ACN 10% (Background electrolyte)	-	MS	40	156 µg/L	Rice, *Fusarium* microconidia	FB1, FB2	Kecskeméti et al., 2020

[1]Abbreviations: **ACN:** Acetonitrile; **AIBN:** Azodiisobutyronitrile; **AuNP:** Gold nanoparticles; **BIS:** N,N'- methylene-bis-acrylamide; **CE:** Capillary electrophoresis; **Cys-AuNPs:** Cysteamine-capped gold nanoparticles**; DPV:** Differential pulse voltammetry; **ECL:** Electrochemiluminescence; **EDMA:** Ethylene glycol dimethacrylate; **EIS:** Electrochemical impedance spectroscopy; **EGMP**: Ethylene glycol methacrylate; **GCE:** Glassy carbon electrode; **GO:** graphene oxide; **HFB1**: Alkaline hydrolysis of FB1; **HRP:** Horseradish peroxidase; **ITO:** Indium tin oxide; **MAA:** Methacrylic acid; **MINA:** Molecularly imprinted polymer nanoparticles; **MIP:** Molecularly imprinted polymer; **NAPMA:** N-(3-Aminopropyl) methacrylamide hydrochloride; **NIPAm:** N-isopropylacrylamide**; PPy/ZnP:** Polypyrrole-zinc porphyrin; **RhB-Cl:** 9-[2-(Chlorocarbonyl)phenyl]-3,6-bis(diethylamino) xanthylium; **SEECL:** Surface-enhanced electrochemiluminescence; **SPE:** Solid Phase Extraction; **SPR:** Surface plasmon resonance; **TBAm:** N-tert-butylacrylamide; **TMB:** 3,3′,5,5′-tetramethylbenzidine

2.4 Aptamer-based determination of FB1

Aptamers are single-stranded DNA or RNA with high molecular recognition towards different types of targets, including nucleic acids, cells, proteins and small molecules. Such probes exhibit diverse binding affinities and target selectivity and can discriminate even slight chiral differences (McKeague et al., 2010; Song et al., 2019). Due to their exceptional affinity and specificity, aptamers are often considered as comparable to antibodies, with certain advantages for in-field detection caused by their chemical synthesis, easy nucleobase and chemical modification, and exponential self-amplification (Song et al., 2019). Contrary to antibodies, aptamers' chemical production is less costly, laborious, more ethical (as they entail no harm to animals), and allows the obtention, modification, and labeling of large aptamer quantities under many experimental conditions without batch variations. Such benefits have allowed aptamers in diagnosis, therapeutics, drug delivery, environmental monitoring, and

food safety (Evtugyn and Hianik, 2020; Yüce et al., 2015). Likewise, aptamers are aimed to substitute antibodies as the gold standard in molecular recognition, where their three-dimensional folding determines their high affinity and binding capability for the development of quick, cost-effective and wide range methods (Ruscito et al., 2016; Yüce et al., 2015). Aptamers are discovered and selected by a technique called Systematic Evolution of Ligands by Exponential enrichment (SELEX) in which a large DNA library is incubated with the target or other relevant molecules, followed by the amplification of potential binders after several selection and discrimination rounds (McKeague et al., 2010). Depending on the analyte, SELEX can be carried out by target immobilization in magnetic-beads by covalent and non-covalent binding, capillary electrophoresis through electric fields on the target charge and hydrodynamic radius, whole cell-SELEX, and optical surface plasmon resonance chips with mass-related refractive index changes (Yüce et al., 2015).

On the other hand, innovative SELEX techniques include robotic/automated procedures, microfluidic-based chips, next-generation sequencing for the acquisition of millions of sequences, graphene oxide-SELEX, quartz crystal microbalance-SELEX for mass changes after binding, human-genome SELEX, and computer-based screening (in silico SELEX) (Yüce et al., 2015). Aptasensors are biosensing devices that utilize aptamers as biorecognition elements for the conversion of different signals into measurable values (Zhang et al., 2020a). The outstanding performance of aptasensors depends on the sequence architecture and the way it is assembled in the biosensing design (Evtugyn and Hianik, 2020). Depending on the nucleotide number and sequencing, aptamers can take different 3D conformations such as loops, triple stranded and G-quadruplex arrangements, pseudoknots and staples (Schmitz et al., 2020). So far, two aptamers composed by 96 and 80 nucleotides, have been reported through SELEX and utilized in different biosensing approaches (McKeague et al., 2010; Chen et al., 2014). The structure, sequencing and molecular docking of aptamers can be analyzed by specific software tools (Ciriaco et al., 2020; Evtugyn and Hianik, 2020; Yüce et al., 2015), from which mfold and RNA structure 4.6 software have been used for predicting the secondary structure of FB1 specific aptamers (Chen et al., 2014; McKeague et al., 2010). The mfold web server is useful for studying aptamer-target reaction sites (Wang et al., 2020), while the determination of nucleic acid folding calculates a minimum free energy (ΔG) (Zuker, 2003). DNA folding in mfold requires a formatted sequence, the inclusion of its optional constrains including forcing or prohibiting specific base pairs and helixes, and its folding parameters. In this regard, the specific parameters for determining a linear (default) or circular sequence include the folding temperatures (0-100 °C), ionic conditions as molar concentration ($[Na^+]$ or $[Mg^{++}]$), the free energy increments, distance between pairs, and maximum

number of foldings, if necessary. Once the required parameters are included, the software generates a structure plot, based on the energy dot plot for the lower ΔG in optimal conditions (Zuker, 2003). The folded structure of all the reported aptamers for FB1 is presented in Figure 2.6, where the 96 nt and 80 nt aptamers (Chen et al., 2014; McKeague et al., 2010) displayed a more complex structure, mostly expressed by the formation of multiple stem loops, in contrast with the simple folded organization of their reduced aptamers and minimers (Cheng and Bonanni. 2018; Frost et al., 2015). In terms of the 3D conformation, a B duplex structure was confirmed for the 96 nt aptamer, through circular dichroism assays. Nevertheless, 3D representations of docking revealed the susceptibility of FB1 to be bound by the backbone of the 96 nt aptamer and its minimer, along with the 80 nt aptamer (Ciriaco et al., 2020). The final structure, predicted in Mfold, relied on the folding temperature, commonly varying from ice to room temperature, along with the ions present in the buffer (Mg^{+2}, Na^{+}).

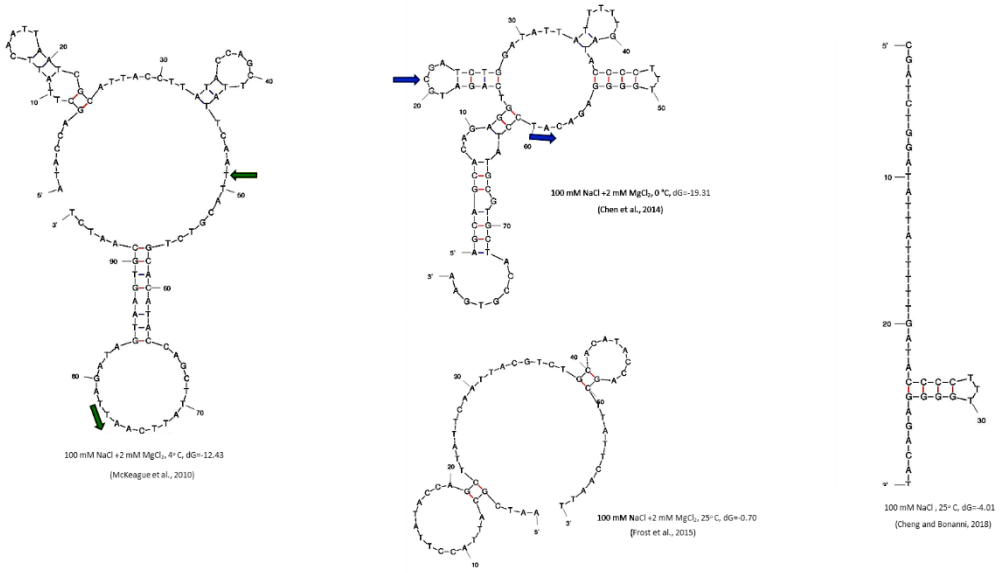

Figure 2.6 Aptamer folding forms obtained in Mfold at the specified conditions in their corresponding references. When reported, target binding regions are indicated by blue and green arrows.

All the aptamer-based sensors are chronologically described in Table 2.5, while the binding and functionalization conditions are illustrated in Table 2.6. From the 32 aptasensors found in the literature, 24 utilized the 96 nt aptamer (McKeague et al., 2010), one method applied a shortened version (60 nt) from this first sequence (Gui et al., 2015), one platform included the second 80 nt aptamer (Chen et al., 2015b), two biosensors manipulated a condensed version (40 nt) of the second main aptamer (Cheng and Bonanni, 2018; Tian et al., 2017), and three references did not specify their single-stranded (ss) DNA sequence (He et al., 2020a; He et al., 2020b; Wu et al., 2020). From the two patented oligonucleotides, the aptamer with sequence: GCA TCA

CTA CAG TCA TTA CGC ATC GCG AGG GGA CGG GAA CGC GCT GAA GGG AGG CCT AGG ATC GTG TGA AGT GCT GTC CC, has not been applied in any other biosensing technique(吴淑庆 et al., 2012). A similar outcome occurred to the second patent, which reported an 80 nt aptamer with 40 non-specified random nucleotides (Wang et al., 2014), flanked by similar primer binding sites to those reported by Chen and collaborators for their 80 nt sequence (Chen et al., 2014). The schematic representation of each type of aptamer-based biosensor is illustrated in Figures 2.7, 2.8 and 2.9, for the fluorescent, electrochemical, and colorimetric/other aptasensors specific for FB1, respectively. It should be noted that the most recent sequences have not replaced the first reported aptamer, and current biosensing designs still apply the 96 nt ssDNA molecule with high sensitivity and specificity.

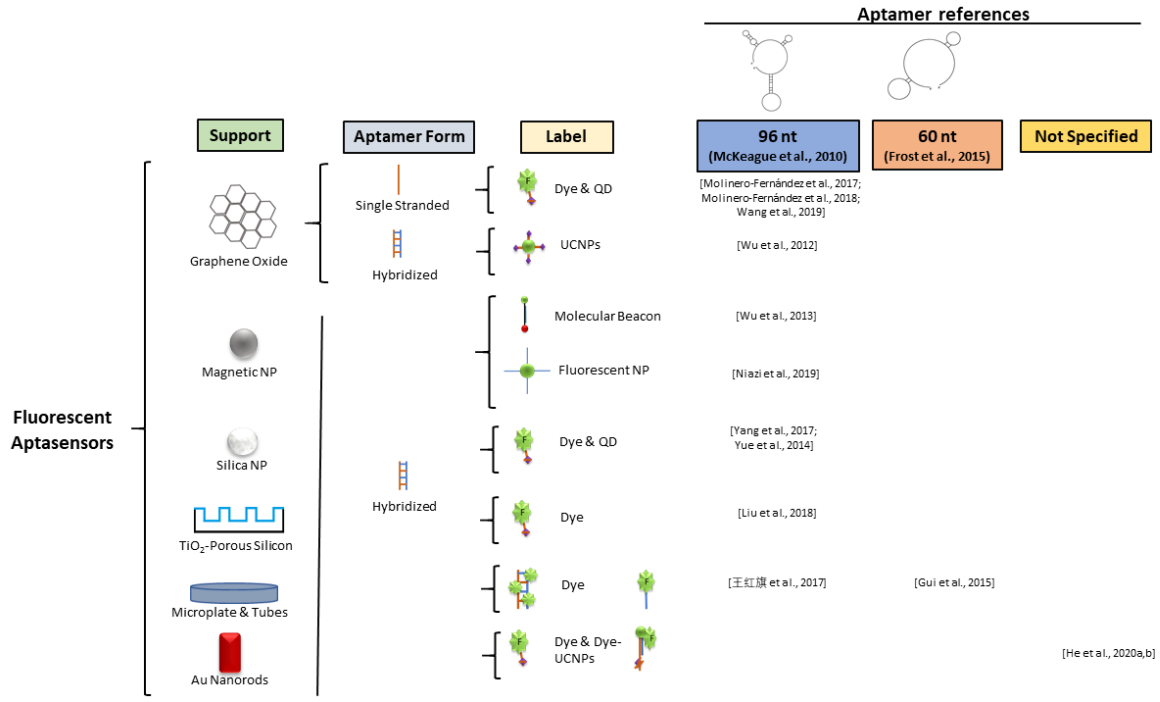

Figure 2.7 Schematic representation of the mechanisms of aptamer-based biosensors for FB1 with fluorescent detections. (Abbreviations: **NP:** Nanoparticles; **QD:** Quantum Dots; **UCNPs:** Upconversion fluorescent nanoparticles)

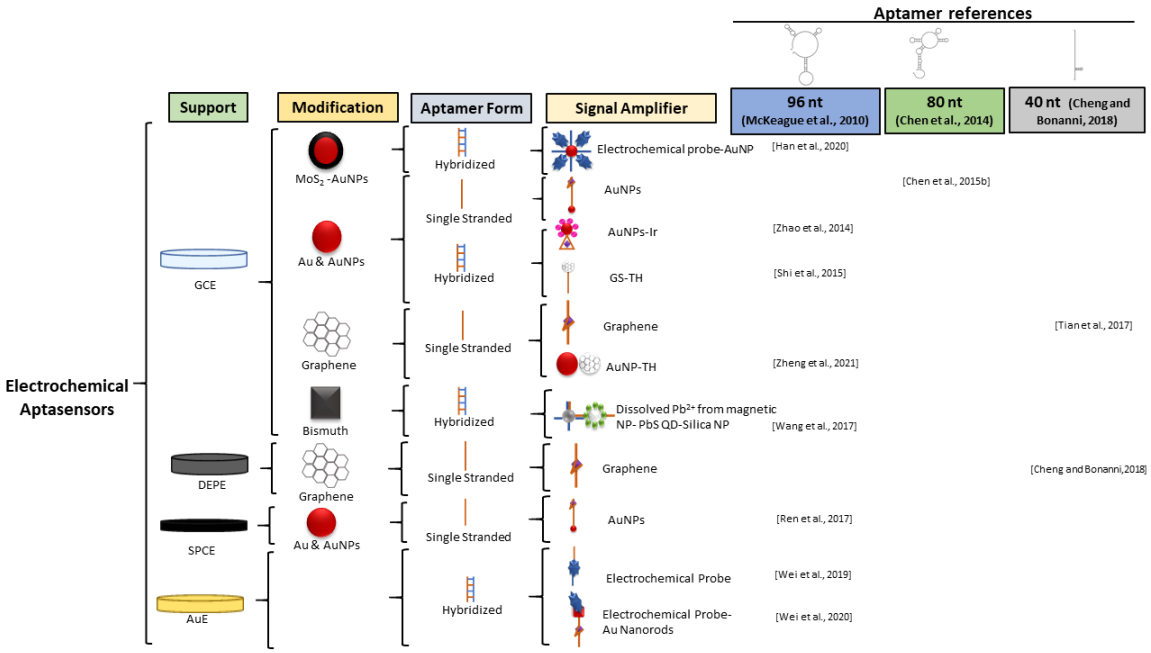

Figure 2.8 Schematic representation of the mechanisms of aptamer-based biosensors for FB1 with electrochemical detections. (Abbreviations: **AuE:** Gold electrode; **AuNPs:** Gold nanoparticles; **DEPE:** Disposable electrical printed electrode; **GCE:** Glassy carbon electrode; **GS:** Graphene sheets; **NP:** Nanoparticle; **SPCE**: Screen-printed carbon electrode; **QD:** Quantum dots; **TH:** Thionine)

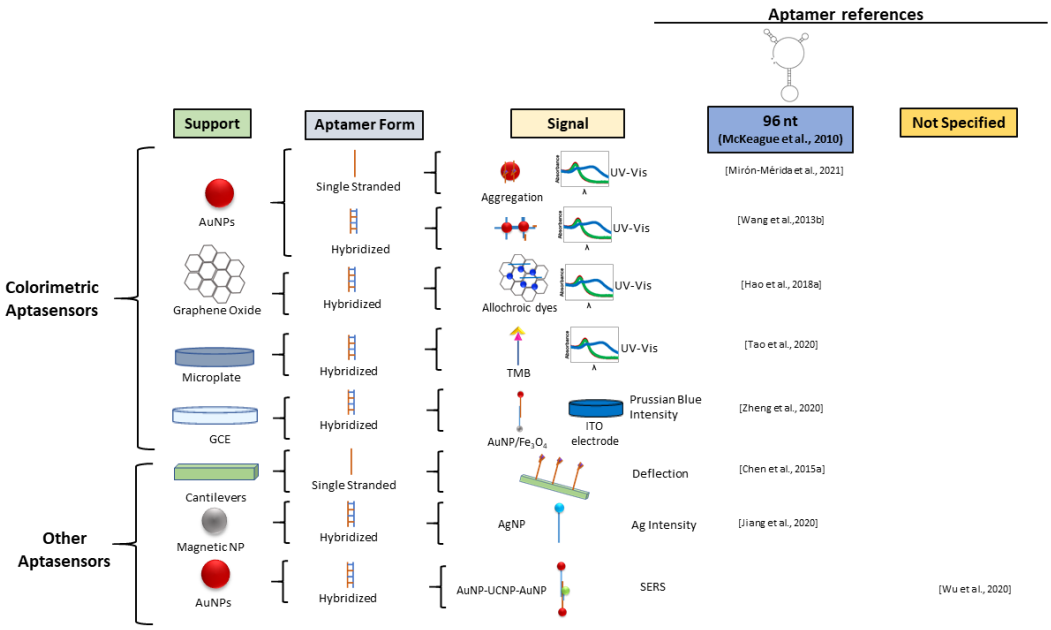

Figure 2.9 Schematic representation of the mechanisms of aptamer-based biosensors for FB1 with colorimetric and other detections. (Abbreviations: **AgNPs:** Silver nanoparticles; **AuNPs:** Gold nanoparticles; **GCE:** Glassy carbon electrode; **ITO:** Indium tin oxide; **NP:** Nanoparticles; **SERS:** Surface enhanced-Raman spectroscopy; **TMB**: 3,3′,5,5′-tetramethylbenzidine; **UCNPs**: Upconversion fluorescent nanoparticles)

Different immobilization mechanisms support the versatility of many aptasensing techniques for FB1. In this regard, aptamer modification with thiol groups allowed Au-S covalent binding with AuNPs (Zheng et al., 2020), gold and AuNPs-modified electrodes (Chen et al., 2015b; Han et al., 2020; Ren et al., 2015; Wei et al., 2019; Wei et al., 2020; Zhao et al., 2014), and gold-coated silicon cantilevers (Chen et al., 2015a). Likewise, biotin modified aptamers have been attached to avidin-conjugated upconversion nanoparticles (UCNPs) (Wu et al., 2012) magnetic nanoparticles (Niazi et al., 2019; Wu et al., 2013), as well as streptavidin-magnetic beads (Jiang et al., 2020), and streptavidin-coated microplates (Tao et al., 2020). Furthermore, amino groups integrated to aptamers promoted binding to glutaraldehyde modified silica photonic crystal microspheres (PHCM) (Yue et al., 2014), isothiocyanate modified PHCM (Yang et al., 2017), GPTMS modified TiO_2-PSi surfaces (Liu et al., 2018), and carboxylic groups in 3-mercaptopropionic acid-capped CdTe quantum dot-coated silica spheres, activated by EDC/NHS (Wang et al., 2017). When no end modification is required in immobilization procedures, aptamers can be adsorbed on graphene oxide and other surfaces. To this end, π-π stacking with their nucleobases (Cheng and Bonanni, 2018; Molinero-Fernández et al., 2017; Molinero-Fernández et al., 2018; Tian et al., 2017; Wang et al., 2019; Wu et al., 2012), electrostatic binding to gold nanoparticles (Mirón-Mérida et al., 2021), or hybridization with complementary sequences fixed to other supports including luminescent nanoparticles (Niazi et al., 2019), electrodes (Shi et al., 2015), magnetic beads (Wang et al., 2017), magnetic nanoparticles (Zheng et al., 2020), quantum dots (Jiang et al., 2020), gold nanoparticles (Wang et al., 2013b; Zheng et al., 2020), gold nanorods (He et al., 2020a; He et al., 2020b) and graphene oxide (Hao et al., 2018a) have been explored.

2.4.1 A 96-mer aptamer for the determination of FB1

The first aptamer specific for FB1 was reported by McKeague (McKeague et al., 2010), after 18 SELEX rounds through negative selections with unmodified and modified (L-homocysteine, L-cysteine, L-methionine and L-glutamic acid) magnetic beads. From the six sequences initially studied, the sequence with the lowest G content (8 %) was selected due to its greatest binding affinity, confirmed by its low dissociation constant (Kd=100 nM). This sequence consisted in 60 random nucleotides (bold letters), surrounded by two primer binding sites: 5'-ATA CCA GCT TAT TCA ATT **AAT CGC ATT ACC TTA TAC CAG CTT ATT CAA TTA CGT CTG CAC ATA CCA GCT TAT TCA ATT** AGA TAG TAA GTG CAA TCT-3' (McKeague et al., 2010). A good binding affinity (Kd= 42.9 pM) was confirm for this aptamer by fluorescent microscale thermophoresis (MST), which differed from the value obtained through magnetic bead

assays (2.11 pM) due to differences in their target and aptamer mobilities (Ciriaco et al., 2020).

Table 2.5. Aptasensors for the determination of FB1[1]

Support	Labelling	Measurement	Detection Time (min)	Extraction Time (min)	Sample Preparation Steps	LOD µg/L	Sample	Specificity Test[2]	Ref
GO	UCNPs with Er and Tm	Fluorescence spectra	200	-	-	0.1	PBS	**OTA**, AFB1, AFB2, AFG1, AFG2, FB2, ZEN	Wu et al., 2012
Carboxilated MNPs/MB	UCNPs	Fluorescence	100	>2	7	0.01	Maize	-	Wu et al., 2013
Centrifuge tubes	AuNP-cDNA	Absorbance	35	30	3	0.125	Beer	-	Wang et al., 2013b
SPCMs	FITC-Complementary DNA	Fluorescence	60	135	3	0.00016	Cereal	AFB1, **OTA**, FB2	Yue et al., 2014
cDNA modified Au electrode	Au NPs–Ir	ECL	120.41	-	5	0.27	Wheat flour	OTA, AFT, L-cystein, BSA	Zhao et al., 2014
GCE-AuNPs	Label free	EIS	30	745	8	0.0014	Maize	AFB1, ZEN, T-2 toxin	Chen et al., 2015a
Au coated silicon cantilever beams	Label Free	Deflection	30	-	-	33	Buffer	OTA, DON	Chen et al., 2015b
GCE-AuNPs-capture DNA	GS-TH	CV	25.11	-	-	0.001	Ultra-pure water	AFB1, OTA, ZEN, DON	Shi et al., 2015
cDNA (Corning® Costar® 96-Well Cell Culture Plates)	PicoGreen	Fluorescence intensity	25	-	2	0.1	Milk	CTN,OTA, AFB1, ZEN	Gui et al., 2015
SPCE- PDMS microcell	AuNPs	Impedance signal	30	735	7	0.0034	Corn	FB2, OTA, AFB1	Ren et al., 2017
SPCM	cy3 modified aptamer	Fluorescence	90	751	7	0.01104	Cereals	AFB1, **OTA**	Yang et al., 2017
SiO_2 spheres/ Fe_3O_4@Au Magnetic Beads-cDNA	PbS QD	SWV (current)	65	15	4	0.02	Maize	**OTA**, OTB, AFB1	Wang et al., 2017
Reduce graphene/Ni/ Pt NPs micromotors	Fluorescein amidine (FAM) labelled aptamer	Fluorescence intensity	15	Maize: 30 Beer: 20 Whine: -	4,1,1	0.4	Maize, Beer	**OTA**	Molinero-Fernández et al., 2017
Graphene modified GCE	Label free	Impedimetric signal	30	-	-	0.0123	Tris buffer	-	Tian et al., 2017
Centrifuge tube	FITC-Complementary DNA	Fluorescence	21	-	-	7.21	Buffer	AFB1, AFB2, OTA, FB2 (response)	王红旗 et al., 2017
TiO_2 modified porous silicon	Cy3 labelled aptamer-BHQ2 labelled anti aptamer	Fluorescence Intensity	720	751	7	0.00021	Cereal (Rice, Wheat, Corn)	**OTA, AFB1**	Liu et al., 2018
GONC on DEP carbon electrodes	GONC	Peak current intensity	65	-	-	10.82	Tris buffer	OTA, Thrombin	Cheng and Bonanni, 2018
Reduced graphene/ Pt NPs micromotors	FAM labelled aptamer	Fluoresecence	17	30, 20	3,2	0.70	Maize. Beer	**OTA**	Molinero-Fernández et al., 2018
GO-cDNA (probe1)& Fe_3O_4/GO-cDNA (probe 2)	Allochroic dyes (thymolphthalein)-alkaline conditions	Absorbance	90	40	7	100 (lowest value explored)	Peanut	**OTA, AFB1, microcystin-LR**	Hao et al., 2018a
Amine funtionalized Fe_3O_4 magnetic particles	$NaYF_4$: Ce/Tb nanoparticles-cDNA	Fluorescence decrease	60	>2	7	0.000019	Maize	**OTA** T-2, AFB1, OTB, ZEN	Niazi et al., 2019
GO/Fe_3O_4 nanocomposites	Aptamer-Red QDs	Fluorescence inensity	60	-	3	0.0162	Peanut	OTA, **AFB1**, OTB. AFM1, AFB2	Wang et al., 2019
cDNA on AuE	Methylene blue	Peak current	40	45 (Corn)	3 (Corn) 1	0.00015	Corn Beer	OTA, ZEN, AFB1	Wei et al., 2019
MoS2-Au modified GCE	FC6S -Au-cDNA	Current difference	15	-	-	0.0005	PBS	**ZEN** α-ZOL, AFB1, DON, T-2, OTA	Han et al., 2020
cDNA on AuE	AuNRs-Fc	DPV	10	-	4	0.00026	Beer	**OTA**, ZEN, AFB1	Wei et al., 2020
cDNA on AuNR	Cy5.5-aptamer	SERS/ Fluorescence	45	735	8	0.0003/ 0.0005	Corn	AFB1, ZEN, PAT, OTA, FB2, FB3	He et al., 2020a
Streptavidin coated microplate	TMB	Absorbance	73	30	11	0.3	Beer Corn	AFB, DON, OTA, ZEN	Tao et al., 2020
cDNA2 on AuNR	UCNPs-Hibridized TAMRA-cDNA1& Aptamer	Fluorescence	50	735	7	0.000003	Corn	**ZEN**, AFB1, OTA, PAT, OTB	He et al., 2020b
Aptamer-Magnetic Beads	cDNA-AgNP	Ag intensity (ICP-MS)	121	42	8	0.3	Wheat Flour	**OTA**, AFB1, DON, ZEN, FB2	Jiang et al., 2020
Aptamer-AuNP-UCNP-AuNP-cDNA	4-MBA	SERS	121	735	9	0.00002	Corn	**ZEN, OTA**, AFB1, PAT, T-2	Wu et al., 2020
ITO electrodes	Silver-Au-Aptamer-cDNA-Fe_3O_4 & Prussian Blue	Color change of ITO (Mobile phone)	62	-	-	0.01	Corn	DON, OTA	Zheng et al., 2020
AuNP	AuNP	UV/Vis	192.2	-	-	0.000056	$MgCl_2$ 1mM Buffer	OTA, AFB1	Mirón-Mérida et al., 2021
GO-Au-Thionine on GCE	Label-Free	CV	25	10 min	4	0.01	Corn	Mycotoxins	Zheng et al., 2021

[1] Abbreviations: **AFB1:** Aflatoxin B1; **AFB2:** Aflatoxin B2; **AFG1:** Aflatoxin G1; **AFG2:** Aflatoxin G2; **AgNP:** Silver nanoparticles; **AuE:** Gold electrode; **AuNP:** Gold nanoparticles; **AuNRs:** Gold nanorods; **BHQ2:** Black hole quencher; **cDNA:** complementary DNA; **CTN:** Citrinin; **Cy:** Cyanine; **DEP:** Disposable electrical printed; **DON:** Deoxynivalenol; **DPV:** Differential pulse voltammetry; **FAM:** Fluorescein amidine; **FB2:** Fumonisin B2; **Fc:** Thiol modified ferrocene; **FC6S:** 6-(Ferrocenyl)hexanethiol; **FITC:** Fluorescein isothiocyanate; **GCE:** Glassy carbon electrode; **GO:** Graphene oxide; **GONC:** Graphene oxide nanocolloids; **GS:** Graphenes; **ICP-MS:** Inductively coupled plasma mass spectrometry; **ITO:** Indium Tin Oxide; **MB:** Molecular beacon; **MBA:** Mercaptobenzoic acid ; **MNP:** Magnetic nanoparticles; **MoS_2:** Molybdenum disulfide; **NP:** Nanoparticles; **PDMS:** Polydimethylsiloxane; **OTA:** Ochratoxin A; **OTB:** Ochratoxin B; **QD:** Quantum dots; **SERS:** Surface-enhanced Raman spectroscopy; **SPCE:** Screen-printed carbon electrode; **SPCM:** Silica photonic crystal microsphere; **TAMRA:** Carboxytetramethylrhodamine; **TH:** Thionine; **TMB:** 3,3′,5,5′-tetramethylbenzidine; **UCNPs:** Upconversion fluorescent nanoparticles; **ZEN:** Zearalenone; **ZOL:** Zearalenol; **PAT:** Patulin

[2] Mycotoxins highlighted in bold indicate a multiplex assay

Table 2.6 DNA sequences utilized for different aptasensors and their binding conditions[1]

Aptamer Modification	cDNA	Other	Binding Buffer	Incubation	Ref
5'-ATA CCA GCT TAT TCA ATT AAT CGC ATT ACC TTA TAC CAG CTT ATT CAA TTA CGT CTG CAC ATA CCA GCT TAT TCA ATT AGA TAG TAA GTG CAA TCT-3'					McKeague et al., 2010
5′-Biotin-(CH2)6-	-	-	Tris-HCl buffer (10 mM containing 100 mM NaCl, pH 7.4)	37 °C Overnight (conjugation in BB) 37 °C, 2 h (Binding) 37 °C, 80 min (Incubation with GO)	Wu et al., 2012
5′-Biotin-(CH2)6-	5′-AAT TGA ATA AGC TGG-3	Molecular Beacon 5′-SH-(CH2)6-GCT CG CCA GCT TAT TCA ATT CGA GC-(CH2)6-H2N-3′	10 mM PBS	37 °C 12 h (immobilization on MNPs) 37 °C, 30 min (hibridization aptamer-cDNA) 37 °C, 30–40 min (incubation) 37 °C, 30 min (hibridization cDNA-MB)	Wu et al., 2013
None	5' -SH-AAT TGA ATA AGC TGG TA-3'	5'-SH TAC CAG CTT ATT CAA TT-3'	10 mM PB containing 1% SDS by mass pH 7.4 (DNA dilution) 500 Mm NaCl cDNA1 300 mM NaCl cDNA2 1 x PCR amplification buffer (Conjugate dilution) 20 mM NaCl + 10 mM PB	37 °C, shaking for 12 h (funtionalization) RT, overnight salt aging 95 °C, 5 min (hibridization cDNA1-cDNA2) Cool down RT	Wang et al., 2013b
-(CH2)6-NH2-3′	5′-FITC-AAT TGA ATA AGC TGG TA-3′	-	TE solution (100 mM Tris-HCl + 10 mM EDTA) 5× saline sodium citrate (hibridization) 10mM Tris-HCl (pH 8.0), 120 mM NaCl, 20 mM CaCl2, 5 mM KCl, 20 mM $MgCl_2$ (binding)	4 °C, 12 h. (Immobilization on SPCMs in TE solution) 37 °C, 1 h. (blocking with 1B% BSA PBS) 37 °C, 2 h. (hibridization) 37 °C, 1 h (binding)	Yue et al., 2014
5′-SH-(CH2)6-	-SH-(CH2)6-AAT TGA ATA AGC TGG TAT	-	Methanol 50%	80 °C, 5 min (hibridization) Cooled to RT 37 °C, 2 h (binding)	Zhao et al., 2014
5′-SH-(CH)6-	-	-	10 mM Tris–HCl, 100 mM NaCl, 100 mM TCEP, pH 7.4 (immobilization) 10 mM Tris–HCl, 100 mM NaCl pH 7.4. (binding)	3 h, 25 °C (Functionalization) 1 h, 25 °C with MCH (blocking) 10 min, 25 °C, (Incubation)	Chen et al., 2015a
None	5′-SH-(CH2)6-AAT TGA ATA AGC TGG TA-3′	-	10 mM Tris-HCl buffer pH 7.4 (hibridization) PBS (pH 7.4). (binding)	24 h, RT (cDNA immobilization) 37 °C, 2 h. (hibridization) Room temperature, 25 min (binding)	Shi et al., 2015
5′-AAT CGC ATT ACC TTA TAC CAG CTT ATT CAA TTA CGT CTG CAC ATA CCA GCT TAT TCA ATT-3'	5′-AAT TGA ATA AGC TGG TAT GTG CAG ACG TAA TTG AAT AAG CTG GTA TAA GGT AAT GCG ATT-3'	-	10 mmol/L Tris, 120 mmol/L NaCl, 5 mmol/L KCl、20 mmol/L $CaCl_2$ (pH 8.5)	95 ℃, 5 min (denaturation) 10 min on ice 25 ℃, 20 min (Incubation) 25 ℃, 5 min (hibridization)	Gui et al., 2015
FB139t3: F- ATA CCA GCT TAT TCA ATT AAT CGC ATT ACC TTA TAC CAG CTT ATT CAA TTA CGT CTG CAC ATA CCA GCT TAT TCA ATT FB139t3-5: F- AAT CGC ATT ACC TTA TAC CAG CTT ATT CAA TTA CGT CTG CAC ATA CCA GCT TAT TCA ATT	-	-	100 mM NaCl, 20 mM Tris, 2 mM $MgCl_2$, 5 mM KCl, 1 mM $CaCl_2$, pH 7.6 (selection buffer)	DNase I assay: 30 min, RT (Incubation with FB1) Magnetic beads assay: 90 °C, 10 min (pre-heating) RT, 30 min RT, 60 min (Incubation)	Frost et al., 2015
5′-SH-(CH2)6-	-	-	Aptamer stock: 50 mM Tris-HCl buffer (ph 7.4, 0.1M NaCl, 0.2M KCl, 5 mM $MgCl_2$ and 1 mM EDTA) Activation Buffer: 50 mM Tris-HCl with 100 mM TCEP Activated aptamer: 50 mM Tris-HCl pH 7.4 with 1.0 mM EDTA) PBS 0.1M, pH 7.4 Binding buffer: TE buffer containing 0.1 M NaCl, 0.2 M KCl, and 5.0 mM $MgCl_2$	Room temperature, 1 h (activation) 6 h and 4 °C (SPCE modification with activated aptamer) 1 h, RT (Blocking with MCH) Room temperature, 30 min h (binding)	Ren et al., 2017
5′-NH2-(CH2)6-reverse sequence-Cy3-*3'	5'-BHQ2-TAT GGT CGA ATA AGT TAA-3'	-	Binding buffer: Tris-HCl, 0.01 M, pH 8.0, NaCl 120 mM, $CaCl_2$ 20 mM, KCl, 5 mM, $MgCl_2$ 20 mM	60 min and 37 °C (hibridization) Room Temperature 12 h (Immobilization on microspheres) 90 min and 45 °C (binding)	Yang et al., 2017
–NH2–3′	5′-TTG AAT AAG CTG GTA TAA GGT AAT GCG ATT AAT TGA ATA AGC TGG TAT–SH–3′	-	10 mM Tris-HCl, 1 mM EDC, 1 mM NHS (aptamer conjugation) 10 mM Tris-HCl with 100 mM TCEP (cDNA activation)	37 °C, overnight (aptamer conjugation) 37 °C, 1 h. (cDNA activation) 37 °C, 30 min (cDNA incubation with MBs) RT, 1 h (blocking with MCH) 37 °C, 2 h. (hibridization) 37 °C, 1 h (binding)	Wang et al., 2017

5′-FAM-		-	Tris-HCl pH 7.5; 10 mM PBST: 100 mM PBS (pH 7.5) with 0.01% Tween (Aptamer dilution)	25 ℃, 15 min (Incubation)	Molinero-Fernández et al., 2017
None	FAM- AATAAGCTGGTATGT	-	20 mM Tris, 0.1 M NaCl, 2 mM $MgCl_2$, 5 mM KCl, 1 mM $CaCl_2$ pH 7.6 (Binding buffer)	95 ℃, 5 min (Heating) 5 min on ice 37 °C, 1 h. (hibridization)	王红旗 et al., 2017
5′-NH2−(CH2)6- reverse sequence-Cy3-3’	5′-BHQ2-TAT GGT CGA ATA AGT TAA-3′	-	Binding buffer: Tris-HCl 10 mM (pH 8.0), NaCl 120 mM, $CaCl_2$ 20 mM, KCl 5 mM,$MgCl_2$ 20 mM)	88 ℃, 5 min (Heating in BB) 25 ℃, 2 h (aptamer-antiaptamer mixture and incubation) 37 ℃, 12 h (hibridization-immobilization) 37 ℃, 12 h (Binding)	Liu et al., 2018
5′-FAM-	-	-	10 mM Tris-HCl pH 7.5 (aptamer reconstitution/ incubation) SDS 1% v/v (aptamer capture) PBS 100 mM pH 7.5 with Milli-Q water and 0.01% of Tween (PBS-T) (Aptamer dilution)	25 ℃, 15 min (Incubation) RT, 2 min (Aptamer capture)	Molinero-Fernández et al., 2018
None	5’-GTG TGT GTG TGT GTG TGT GTG TGT GTG TGT AGA TTG CAC TTA CTA TCT AAT TGA ATA AGC TGG TAT GTG CAG ACG TAA-3’	5’-TTG AAT AAG CTG GTA TAA GGT AAT GCG ATT AAT TGA ATA AGC TGG TAT GTG TGT GTG TGT GTG TGT GTG TGT-3’	PBS, (Na_2HPO_4−NaH_2PO_4, 0.1 M)	RT, 2 h (DNA1 binding on GO) RT, 24 h (DNA2 immobilization on Fe3O4/GO) RT, 12 h (hibridization) 37 ℃, 1.5 h (Incubation)	Hao et al., 2018a
5′-biotin-(CH2)6-	5′-biotin-(CH2)6-TCT AAT TGA ATA AGC TGG TAT GTG CAG ACG-3′	-	PBS (10 mM Na_2HPO_4, 137 mM NaCl, 2.7 mM KCl, 2 mM KH_2PO_4, pH 7.4)	37 ℃, 1 h (Incubation)	Niazi et al., 2019
–NH2–3′	-	-	PBS 0.1M (pH 7.4)	RT, overnight (bio-probe) RT, overnight (Immobilization) 37 ℃, 1 h (Incubation)	Wang et al., 2019
None	5′-SH-GAG GGG TGG GCG GGA GGG AGA TTG CAC GGA CTA TCT AAT TGA ATA AGC-3′		Tris–HCl buffer (containing 0.05 M Tris, 0.2 M NaCl and 0.001 M EDTA)	37 ℃ (cDNA Immobilization) 37 ℃, 2 h (hibridization) 37 ℃, 10 min (Incubation FB1) 37 ℃, 30 min (Incubation Exo-I)	Wei et al., 2019
5′-SH-(CH2)6	5′-SH-(CH2)6-AATTGAATAAGCTGG 3′		TE Buffer (solutions, washing) PBS (0.1 M, ph 6.0)	95 ℃, 5 min (Heating) RT 1h (Cooling) 37 ℃, 2 h (Ap conjugation to electrode) 37 ℃, 2 h (hibridization) 15 min (Incubation)	Han et al., 2020
5′-SH-	5′-SH-GAG GGG TGG AGA TTG CAC TTA CTA TCT AAT TGA GGG GGG TGT CCG ATG CTC-3′		50 mM Tris-HCl	2 h (Conjugation to AuNRs) 37 ℃ , 2 h (cDNA Immobilization on electrode) 37 ℃, 2 h (hibridization) 37 ℃, 10 min (Incubation)	Wei et al., 2020
5’-biotin	5’-biotin- AGA TTG CAC TTA CTA TCT AAT TGA ATA AGC TGG TAT GTG CAG ACG TAA TTG AAT AAG CTG GTA TAA GGT AAT GCG ATT AAT TGA ATA AGC TGG TAT -30.		PBS buffer (10 mmol/L Na_2HPO_4, 2 mmol/L KH_2PO_4, 2.7 mmol/L KCl, 137 mmol/L NaCl, pH 7.4) PBS-T (Washing)	37 ℃, 30 min (Immobilization) 25 ℃, 60 min (Immobilization)	Tao et al., 2020
5’-biotin	5’-biotin-GAT AGG AGT CGT GTG GGA TAG TGT GGG AGA TTG CAC TTA CTA TCT AAT TGA ATA AGC TGG TAT GTG CAG ACG TAA-3’		Tris-HCl buffer 20 mmol/L with 0.5 mol/L NaCl,1 mmol/L EDTA (Washing) 20 mM Tris-HCl pH 7.4 (Dissolving/Target Incubation) 100 mM Tris-HCl pH 7.4 (Re-dispersion)	37 ℃, 120 min (Functionalization of magnetic beads) 37 ℃, 90 min (Labelling of Ag NPs) 37 ℃, 120 min (Hibridization) 37 ℃, 120 min (Target Incubation)	Jiang et al., 2020
5′-SH-C6-	5-NH2-C6-AAT TGA ATA AGC TGG TA-3’	5-SH-C6-GTTGGTGAGTCCAACCACACCA-3’ (Control DNA)	PBS, pH 7.4, 1× (Washing, redispersion, AuNP stability) Tris-HCl buffer 0.01 M, pH 7.4 (Hibridization, target incubation)	37 ℃, 120 min (Functionalization of Fe_3O_4) 37 ℃, 30 min (Hibridization) 37 ℃, 30 min (Target Incubation)	Zheng et al., 2020
None	-	-	$MgCl_2$ 1mM	37 ℃, 30 min (Target Incubation) RT, 60 min (Functionalization of AuNP)	Mirón-Mérida et al., 2021
5′-SH-	-	-	PBS pH 7.4 (Eletrochemical measurements/Sample dilution) Tris-HCl buffer(Washing)	RT, 25 min (Incubation)	Zheng et al., 2021
5’-AGC AGC ACA GAG GTC AGA TGC GAT CTG GAT ATT ATT TTT GAT ACC CCT TTG GGG AGA CAT CCT ATG CGT GCT ACC GTG AA-3’					Chen et al., 2014
5′-SH-(CH2)6-	-	-	pH 7.4, 100 mM NaCl, 20 mM Tris–HCl, 2 mM $MgCl_2$, 5 mM KCl, 1 mM CaCl2	37 °C, 6 h (electrode modification) 94 °C, 5 min followed by 15 min cooling with ice (folding) Room temperature, 30 min (binding)	Chen et al., 2015b
5’-C GAT CTG GAT ATT ATT TTT GAT ACC CCT TTG GGG AGA CAT- 3’	-	-	PBS pH 7.0 (aptamer solution) Tris buffer pH 8.2(FB1 solution)	60 °C, 15 min (aptamer dropcasting) 37 °C, 30 min (Incubation)	Tian et al., 2017

5'-C GAT CTG GAT ATT ATT TTT GAT ACC CCT TTG GGG AGA CAT- 3'	-	-	Aptamer dilution: PBS (10 mM Na_2HPO_4; 100 mM NaCl; pH 7.2) FB1 dilution: Tris (25 mM Tris; 300 mM NaCl; pH 8.2).	60 ℃, 10 min (cast on GONC) 25 ℃, 5 min (washing in PBS) 37 ℃, 1 h (Incubation)	Cheng and Bonanni, 2018
NOT SPECIFIED SEQUENCES					
Cy5.5	cDNA	-	10 mM Tris-HCl, 100 mM NaCl, 1 mM EDTA, pH 8.0 (hibridization buffer) 50 mM TE buffer pH 7.4 (Extract adjustment)	37 ℃, 1 h (Hibridization) 37 ℃, 45 min (Incubation/Hibridization)	He et al., 2020b
None	cDNA1	cDNA2	PBS containing 0.9% NaCl (Hybridization buffer)	RT, 12 h (cDNA2 attachment on AuNR) RT, 12 h (UCNPs funtionalization with aptamers) RT, 12 h (Addition of cDNA1 to aptamer-UCNPs) 60 ℃, 50 min (Hibridization with cDNA2-AuNR) 37 ℃, 50 min (Cooling) 37 ℃, 50 min (Incubation)	He et al., 2020a
NS	cDNA		Hybridization buffer (not specified) PBS buffer(redispersion) 50 mM TE buffer pH 7.4 (pH adjustement)	37 ℃, 12 h (Hibridization) 37 ℃, 2 h (Target Incubation)	Wu et al., 2020

[1] Abbreviations: **AuNRs:** Gold nanorods; **BB:** Binding buffer; **BSA:** Bovine serum albumin; **cDNA:** Complementary DNA; **GO:** Graphene oxide; **GONC:** Graphene oxide nanocolloids; **MCH:** 6-mercapto-1-hexanol; **NS:** Not specified; **RT:** Room temperature; **SPCE:** Screen-printed carbon electrode; **SPCM:** Silica photonic crystal microsphere; **UCNPs:** Upconversion fluorescent nanoparticles

2.4.1.1 Fluorescent detection with the 96 nt aptamer

From all the biosensing designs applying the 96 nt aptamer (Figure 2.7), the most sensitive were those transduced into fluorescent (Liu et al., 2018; Niazi et al., 2019; Yue et al., 2014), and electrochemical (Han et al., 2020; Wei et al., 2019; Wei et al., 2020) signals. The first fluorescent method described the application of avidin-modified fluorescent nanoparticles and graphene oxide (GO), as donor/acceptor pair in Förster resonance energy transfer (FRET). A biotin modified aptamer was attached to upconversion fluorescent particles (UCNPs); under the presence of an increasing fumonisin concentration, the particles were not quenched by GO, thus exhibiting a linear increment on the fluorescence intensity (Wu et al., 2012). A very simple bulk fluorometric method was developed through the hybridization of aptamers with a FAM-labelled complementary DNA, and its displacement upon FB1 binding (王红旗 et al., 2017). The surface of reduced GO/platinum nanoparticles (PtNPs) and RGO/Ni/PtNPs micromotors were also used as a quencher of fluorescein amidine (FAM)-aptamers, with a direct increase on its fluorescence intensity produced by target biding (Molinero-Fernández et al., 2017; Molinero-Fernández et al., 2018). A similar mechanism was developed by immobilization of red CdTe quantum dots-NH_2-modified aptamers on GO/Fe_3O_4 nanocomposites (energy acceptor), where the quenched fluorescence was restored after target binding with a reduction of the background interference by magnetic separation (Wang et al., 2019). Another procedure was proposed for the FRET-quenching effect between AuNP and UCNPs attached to a molecular beacon (MB), although the measured signal intensity was an indirect analysis of the fumonisin content. To this end, a biotinylated aptamer (linked to avidin modified magnetic particles), was hybridized with its complementary DNA, which was also able to hybridize and open the MB, thus forming a fluorescent double-stranded DNA arrangement (Wu et al., 2013).

In the most sensitive development with this long sequence (LOD: 1.9×10^{-5} µg/L), the functionalization of magnetic nanoparticles with aptamers and time-resolved fluorescent nanoparticles with complementary DNA, resulted in the formation of capture and signal probes, respectively. The DNA hybridization step derived to a magnetic/fluorescent biocomplex, whose magnetic separation at rising concentrations of FB reported a reduction in fluorescence intensity (Niazi et al., 2019). Similarly, amino modified aptamers hybridized with their fluorescein isothiocyanate (FTIC)-modified complementary DNA, were coupled to silica photonic crystal microspheres (SPCMs), with an inhibitory effect on the fluorescent signal caused by an increasing target concentration (Yue et al., 2014). In fact, good sensitivity can be achieved with SPCM suspensions, when bound to a hybridized duplex structure formed by a black

hole quencher (BHQ2)-labelled antiaptamer (quencher) and a NH_2(5')/Cy3(3') modified aptamer. An increasing FB1 concentration enlarged the separation between the dye and its corresponding quencher, promoting a higher fluorescent signal (Yang et al., 2017). Moreover, the hybridization between a NH_2/Cy3 modified aptamer and its BHQ2-antiaptamer was examined when immobilized to a TiO_2 modified silicon wafer, where the increment of fluorescence was triggered by the addition of FB1 (Liu et al., 2018).

Unlike other techniques, a less sensitive electrochemiluminescent (ECL) assay resulted from AuNP modified with a thiolated aptamer and an iridium complex, when fixed to an Au electrode by a partial complementary DNA. As the AuNP/Ir complex enhanced the electrode conductivity, the addition of FB1 decreased its ECL signal (Zhao et al., 2014). A very sensitive aptasensor for FB1 combined the interaction of a biotinylated aptamer and its biotinylated complementary DNA, conjugated to magnetic and NaYF4:Ce/Tb nanoparticles respectively. The addition of the target mycotoxin produced a decrease on the complex formation, therefore a signal decrease on the resulting fluorescence (Niazi et al., 2019).

2.4.1.2 Electrochemical detection with the 96 nt aptamer

As already stated, electrochemical methods have also been applicable to sensitive FB1 aptasensors, and their precise completion can be enhanced by the addition of materials such as AuNP and graphene-thionine (GS-TH) (Figure 2.8). Electrodes functionalized with AuNP are convenient for DNA attachment, and the complexity of its fabrication depends on the aptamer structure. For instance, the unmodified 96-mer molecule was docked to a AuNP modified glassy carbon electrode through a thiolated capture DNA. A higher sensitivity was promoted by the addition of GS-TH, due to its competition against FB1 for binding the aptamer, which also generated a decrease in the redox peak. Under this approach, GS-TH are integrated as a peak current enhancer for the Au-modified GCE, because of its ideal stability, surface area, biocompatibility and electrical conductivity reported through cyclic voltammetry (CV, -0.6 to 0.1 V), in which the presence of FB1 diminishes the signal (Shi et al., 2015). GCEs modified with GS-AuNPs-TH have also been used as signal amplifiers and anchor sites for the single quantification of FB1 with a thiolated aptamer, harnessing the π-π interactions among TH and GS, as well as the SH-Au bonds between aptamers and AuNPs. The cyclic voltammetry characterization denoted the redox reduction of TH, which is diminished after the immobilization of aptamers, with a higher decrease under the presence of FB1 due to electrode impedance (Zheng et al., 2021). Efforts for reducing the costs and increasing the capacity of aptasensors have focused

on a combination of powerful electrochemical techniques with portable devices. A screen-printed carbon electrode (auxiliary, reference and working electrodes included) modified with polydimethylsiloxane was selected for the electrodeposition of AuNP, and further attachment of a thiolated aptamer. The coil to G-quadruplex conformational transition, supported by the presence of FB1, was applied to strengthen the electron transfer resistance (ΔI), reflected as a reduction in the electrochemical impedance spectroscopy (EIS) response. The principle behind this approach was based on the inhibition of the electron transfer between the redox probe $[Fe(CN)_6]^{3-/4-}$ and the electrode surface, promoted by the electrostatic repulsion from the negative FB1-aptamer complex towards the negative redox probe (Ren et al., 2017). While the previous methods were able to quantify FB1 in a ng/L scale, upcoming electrochemical assays are reaching limits of detection in the pg/L range.

Gold electrodes worked as ideal supports for combined DNA structures, as verified for double-stranded DNA (aptamer-cDNA). The incubation with different concentrations of FB1 in this assay left some free and hybridized cDNA that had to be subsequently washed with exonuclease I. The remaining double-stranded DNA interacted with methylene blue whose electrochemical signal reached a LOD of 0.00015 µg/L. In this type of array, double-stranded DNA enriched with MB acted as a signal amplifier during the differential pulse voltammetry (DPV) and EIS measurements, where FB1 promoted the release of aptamers; thus, less double-stranded DNA was formed, and less MB could intercalate, which resulted in higher ΔI (Wei et al., 2019). A Y-shaped hybridized structure was also conjugated on a gold electrode. This approach included a DNA sequence complementary on different segments to two aptamers and the addition of gold nanorods for signal enlargement related to concentrations of FB1 as low as 0.00026 µg/L. It is worth mentioning that AuNRs denoted greater conductivity, biocompatibility, and surface area to that of AuNPs. Therefore, they were used for the thiolated immobilization of Fc-SH in order to increase the current, which was inhibited by the presence of FB1 as reported by EIS in a $Fe(CN)_6]^{3-/4-}$/KCl solution and DPV (-500 to 600 mV). Additionally, the Y-shaped DNA structure allowed the simultaneous analysis of OTA and FB1 (Wei et al., 2020). Another technique in the pg/L scale (0.0005 µg/L) was designed on a glassy carbon electrode modified with molybdenum disulfide (MoS_2) and gold nanoparticles for the attachment of aptamers and further immobilization with labelled cDNA, whose differential pulse voltammetry (DPV) decreased with the addition of FB1. In this case, the reduction of MoS_2 nanosheets improved the conductivity, electrochemical activity, and electron transfer of GCE as indicated through DPV (-0.6 to 0.6 V) and CV (-0.2 to 0.6 V) in $Fe(CN)_6]^{3-/4-}$ /KCl. Besides, this material worked as a support for AuNPs-aptamers, their hybridization

with cDNA-AuNPs, and their labelling with 6-(Ferrocenyl) hexanethiol and thionine probes for a dual well-resolved determination (Han et al., 2020).

Occasionally, electrochemical determinations are indirect measurements of labels and other compounds derived from the incubation with FB1. For instance, Fe_3O_4@Au magnetic beads were coupled with a thiolated complementary DNA, for the hybridization of amino-modified aptamers, conjugated with SiO_2@PbS hybrid spheres. An increasing concentration of FB1 produced a reduction on the number of hybridized labels, which after a magnetic separation were dissolved in acid for the square wave voltammetry of the remaining Pb^{2+} in a bismuth film modified GCE (Wang et al., 2017).. A colorimetric method coupled with an electrochemical mechanism, was designed through a GCE modified with silver enhanced AuNP-aptamer-cDNA-Fe_3O_4 nanocomposites and cDNA-Fe_3O_4 at different degrees due to aptamer-cDNA dehybridization by FB1. To achieve the closed bipolar electrode reaction (BPE), the modified GCE (cathode), a Pt wire (counter electrode) and a AgCl/Ag wire (reference electrode), were submerged in a H_2O_2/SDS solution. In turn, another Pt wire (anode), connected to the GCE, along with an ITO electrode, were placed in a different electrochemical cell filled with HCl, $K_3[Fe(CN)_6]$ and $FeCl_3$. In this design, varying target concentrations resulted in different GCE effective areas and current flow, reported as Prussian blue (PB) deposition on the ITO electrode. This indirect electrochemical procedure was translated into a colorimetric signal by means of the smartphone detection of deposited PB at the ITO electrode, submerged in the reporting solution along with the BPE anode (Zheng et al., 2020). Unlike other techniques, a less sensitive electrochemiluminescent (ECL) assay resulted from AuNPs modified with a thiolated aptamer and an iridium complex, when fixed to an Au electrode by a partial complementary DNA. As the AuNP/Ir complex enhanced the electrode conductivity, the addition of FB1 decreased its ECL signal (Zhao et al., 2014). Additionally, three aptasensors also explored the modification of electrodes with AuNP-thiolated aptamers (Chen et al., 2015b) and graphene-aptamers (Cheng and Bonanni, 2018; Tian et al., 2017), however they integrated the 80 nt aptamer (Chen et al., 2014) and its derived 40 nt sequence. These are discussed in Section 2.4.3.

2.4.1.3 Alternative and colorimetric detection with the 96 nt apatmer

As illustrated in Figure 2.9, alternative aptasensors comprised gold-modified microcantilevers, capable of containing thiolated aptamers, in which the differential deflection linearly increased with higher FB1 concentrations (Chen et al., 2015a). A different approached was proposed for aptamers functionalized with magnetic beads,

whose hybridization with cDNA-silver nanoparticles (AgNPs) was diminished by the presence of the target, with further inductively coupled plasma mass spectrometry of the Ag released as cDNA-AgNPs (Jiang et al., 2020).

In order to reduce the complexity of the assays, five colorimetric methods have been proposed for the unmodified version of this aptamer, which are converted into optical determinations of either the color intensity or the UV-Vis spectral properties of nanoparticles, labels and chromogenic substrates. On the first system, gold nanoparticles were functionalized with either a thiolated short-strand (DNA1) complementary to the unmodified aptamer or a thiolated short-strand complementary to DNA1 (DNA2). The association of the aptamer and DNA1 was interrupted by the addition of FB1, which also permitted the hybridization of AuNP-DNA1 and AuNP-DNA2, causing aggregation and color shift from red to blue, detected by the naked eyed and analyzed by UV-Vis absorption (Wang et al., 2013b). For the second approach, thymolphthalein was adsorbed on the surface of GO nanoparticles modified with a semi complementary DNA. The use of the unmodified 96-mer aptamer as a DNA linker, allowed the conjugation of the labelled GO with Fe_3O_4/GO, previously modified with a second semi complementary DNA. After target incubation, the Fe_3O_4/GO particles were magnetically removed, and a colorimetric detection was revealed by adjusting the pH of the remaining solution containing labelled GO (Hao et al., 2018a). Another colorimetric assay was proposed through the competition between a HRP-cDNA and FB1 for binding an aptamer immobilized on a streptavidin-coated microplate. Depending on the amount of FB1, a colorless TMB solution was catalyzed by the hybridized HRP-cDNA to obtain the blue oxTMB, whose yellow color was exposed by the stopping solution (sulfuric acid) and recorded as absorption at 450 nm (Tao et al., 2020). As denoted on the previous section, the FB1-regulated electrodeposition of Prussian blue on an ITO electrode was converted into smartphone-based colorimetric detection of the red, green and blue channels in Image J (Zheng et al., 2020). In contrast to previous reports, the sole application of the unmodified sequence (96 nt) was reported by our research group in an aptamer-FB1-AuNPs conjugate, stable to salt-induced aggregation at an increasing target concentration, under the presence of $MgCl_2$, which indicated stability to salt-induced aggregation at an increasing target concentration. A critical finding was the role of the detectors on the final sensitivity on a same biosensing system. In this regard, a high LOD was reported when the UV-Vis absorption peaks were analyzed (LOD: 0.003 µg/mL). Recent studies in our laboratory have shown a refined particle separation, innovatively carried out by Asymmetric Flow Field-Flow Fractionation (AF4), in which the analysis of UV-Vis (LOD: 0.000000056 µg/mL) and multiangle light scattering

(LOD: 0.00000016 μg/mL) fractograms were comparable to the most sensitive approaches (Mirón-Mérida et al., 2021).

2.4.2 Shorter sequences and minimers derived from the 96 nt aptamer

Five years after the dissemination of the first aptamer specific to FB1 (McKeague et al., 2010), the same research group explored the affinity of minimers (truncated aptamers) from the initial 96 nt aptamer. The different structures included the whole sequence, and its subsequent chains created by preserving the 3' stem loop motif, removing the 3', 5', or both primer binding regions (PBR).

Larger melting temperatures from minimers containing the 3' region, suggested their role on the stability and complete formation of hairpins (Frost et al., 2015). The same study compared the binding affinity through the calculation of the dissociation constant (Kd) by two assays: DNase I and magnetic beads. The DNase I assay indicated similar affinities between the minimer without the two PBR and the full-length oligonucleotide (Table 2.6); however, this method also carried considerable errors and denoted binding towards FB2. On the other hand, the magnetic beads confirmation assay proved the high affinity of minimers lacking the 3' and both PBR, as well as their overall upgraded binding, due to primary amine masking by the beads, suggesting a most favorable interaction with the tricarballylic acid regions (Frost et al., 2015). In silico and docking studies of the minimer without the 3' end, denoted poor and no binding when MST (Kd=3 nM) and magnetic beads (Kd=No binding) were utilized for the assessment of its affinity (Ciriaco et al., 2020). A reduction on the sequence length might lead to the development of simpler, yet more sensitive biosensors. The interaction within the shorter 60 nt strand without PBR and its complementary DNA was tested under the presence of different concentrations of FB1, in which the rate of double-stranded DNA formation was identified with the fluorescent dye PicoGreen (Gui et al., 2015). Regardless of the specificity issues presented by Frosts (Frost et al., 2015), the truncated sequence studied by Gui (Gui et al., 2015) was capable of discriminating ochratoxin A (OTA) aflatoxin B1 (AFB1), citrinin (CTN) and zearalenone (ZEN), while the specificity of the original long length aptamer was already confirmed for the null interaction with OTA, AFB1, AFB2, AFG1, AFG2, FB2, ZEN, L-cysteine, BSA, T-2 toxin and deoxynivalenol (DON)(Table 2.5). Still, even when this 60 nt aptamer-based method was correlated to a reduction on the assay and assay preparation times, its depicted LOD was higher than the values achieved with the full 96 nt sequence.

2.4.3 A novel oligonucleotide (80 nt) for the determination of FB1

Four years after the first reported sequence, a new aptamer selection was presented by using a library of single stranded DNA designed with 80 nt sequences, in which 40

random nucleotides (bold letters) were edged by 20 nt on each side. The SELEX process was executed with the aid of magnetic beads, and included negative (magnetic beads), positive (FB1 modified magnetic beads) and counter (free glycine, AFB1, AFB2, ZEN) selection rounds, which also served to confirm the aptamer selectivity. The selected aptamer: 5'-AGC AGC ACA GAG GTC AGA TG **C GAT CTG GAT ATT ATT TTT GAT ACC CCT TTG GGG AGA CAT** CCT ATG CGT GCT ACC GTG AA-3, showed a lower Kd (62 nM), hence a greater affinity to FB1 was expected for the development of more sensitive aptasensors than that with the 96 nt aptamers (Chen et al., 2014); however, this was not the case and the aptasensors so far reported using this aptamer have not shown the expected superior sensitivity, which was also confirmed by its fewer applications. In this regard, although this sequence indicated good binding affinity in MST assays (Kd=224 pM), no binding was detected through the assay with magnetic beads, which might suggest a variability of affinity in close relation to the target freedom or immobilization state (Ciriaco et al., 2020).

After its introduction, the full-length thiolated version was docked on glassy carbon electrodes in order to enhance its electron transfer resistance, whose decrement was caused by the addition of the target mycotoxin (Chen et al., 2015b). This electrochemical arrangement derived in a sensitive method, with a similar LOD (0.0014 µg/L) to previous electrochemical aptasensors for FB1 (0.0034 µg/L) (Chen et al., 2015b; Ren et al., 2017). Furthermore, a shorter version, consisting on its 40 random nucleotides, was casted on doped (B or N) and undoped graphene modified GCE, from which boron-doped graphene helped immobilize a higher amount of FB1, improving the impedimetric signal thus the sensitivity of the electrochemical sensor (Tian et al., 2017). This 40 nt aptamer was also immobilized on graphene oxide nanocolloids (GONCs), causing a reduction on the electroactivity from the oxygen containing groups. The addition of FB1 prompted the full detachment of the aptamer and the partial reestablishment of electroactivity, with potential for biosensing purposes and verified sensitivity under the presence of OTA and thrombin (Cheng and Bonanni, 2018). Although the latter corresponded to low assay and assay preparation times, both biosensors were not comparable to the applications with longer chains. Further research is needed to reveal the affinity mechanism for this aptamer to understand its sensitivity constrains and fully develop highly sensitive aptamer-based sensors.

2.4.4 Not specified sequences and alternative methods

Three studies published by the same research group did not specify the aptamers sequence for the detection of FB1. The first approach relied on the hybridization of Cy5.5-aptamer and its cDNA on gold nanorods, with a further measurement of their

SERS (LOD: 0.0003 μg/L) and fluorescent (LOD:0.0005 μg/L) signals under the presence of the target mycotoxin (He et al., 2020b). The second work, which so far is the most sensitive aptasensor for FB1, was reported with a LOD of 0.000003 μg/L. In this arrangement, the inner filter effect between UCNPs and gold nanorods, both linked by a hybridized aptamer, was reduced by disrupting the biocomplex through target incubation and stimulating fluorescence under excitation (980 nm) (He et al., 2020a). The third biosensor combined the modification of AuNPs with aptamers and 4-mercaptobenzoic acid as a Raman reporter, whose signal was reduced after target incubation through dehybridization from a cDNA-AuNP-(4-MBA) complex, with an LOD of 0.00002 μg/L (Wu et al., 2020). The effect of the electrochemical interaction between FB1 and fish sperm double-stranded DNA was examined on the impedimetric detection with a pencil graphite electrode, which provides a promising biosensing technique with other DNA structures apart from aptamers (Kesici et al., 2019). Nevertheless, the addition of five FB1 concentrations did not portray differentiated responses; therefore, more optimization would be ideal for the application of this type of non-specific sequences.

2.4.5 Multiplex detection

Aptasensors are not restricted to the sole determination of single mycotoxins, multiplex analysis can be accomplished with different arrays. Fluorescent (Wu et al., 2012) and magnetic (Jiang et al., 2020; Wang et al., 2017) nanoparticles, as well as their association (Niazi et al., 2019; Wang et al., 2019), were applied for the multiple detection of FB1 and OTA. Moreover, photonic crystal microspheres were able to support double (FB1, OTA) and triple (FB1, OTA, AFB1) mycotoxin quantifications (Yang et al., 2017; Yue et al., 2014). In a similar way to fluorescent particles, the application of fluorescent labels favored the establishment of optimum λ_{em} in combination with their specific reading methods (filters), for the detection of FB1 and OTA (Molinero-Fernández et al., 2017). The specific allocation of a cy3 aptamer and its BHQ antiaptamer on TiO_2 modified silicon wafers, was also suitable for the linear quantification of multiple mycotoxins (OTA, AFB1, FB1), where the fluorescence increment was spotted on a defined area of a wafer surface (Liu et al., 2018). The combination of two different fluorescent compounds with UCNPs induced two resolved responses under the presence of ZEN and FB1 (He et al., 2020a), while the functionalization of UCNPs and AuNPs with aptamers along with aptamer labelling were exploited in the multiplex SERS and fluorescence detection of ZEN, OTA and FB1, through a triple hybridization with a cDNA-AuNPs complex (Wu et al., 2020). Likewise, as previously mentioned, the combination of different allochroic dyes with magnetic and GO nanoparticles, was also convenient for the colorimetric detection of FB1, OTA, AFB1 and microcystin-LR (Hao et al., 2018a).

Recent improved electrochemical methods also allowed multiplex analysis, as in the case of glassy carbon electrodes modified with enhancers of electron mobility such as MoS_2 and AuNP. These were utilized for the simultaneous quantification of FB1 and ZEN produced by the different reduction peaks from FC6S and thionine, respectively, which functioned as labels for cDNA when simultaneously immobilized on colloidal gold (Han et al., 2020). Likewise, gold electrodes modified with a Y-shaped DNA conformation were efficient for detecting OTA and FB1 due to immobilization of thiolated thionine and ferrocene on gold nanorods, which in addition of enhanced electron transfer, exhibited distinctive peak currents (Wei et al., 2020).

2.4.6 Comparison between aptasensors for FB1: advantages, disadvantages and future pespectives

A principal component analysis (PCA) specific to all the aptamer-based biosensors for FB1 is indicated in Figure 2.10, by using LODmax, ATmax and APmax of 100 µg/L (Hao et al., 2018a), 720 minutes (Liu et al., 2018) and 12900 minutes (Wu et al., 2012), respectively. As already noted, assays with a hybridized 96 nt aptamer were mainly correlated to the lowest LOD's through fluorescent (Liu et al., 2018, Niazi et al., 2019; Wu et al., 2012; Wu et al., 2013; Yang et al., 2017), electrochemiluminescent (Zhao et al., 2014), optical (Hao et al., 2018a) and MS (Jiang et al., 2020) detections, along with fluorescent and SERS signals obtained from a non-specified hybridized aptamer (He et al., 2020a; Wu et al., 2020). On the other hand, the shortest assay times were correlated to applications with the 96 nt aptamer in its end-modified (Chen et al., 2015a; Molinero-Fernández et al., 2017; Molinero-Fernández et al., 2018; Ren et al., 2017) and hybridized forms (Han et al., 2020; Shi et al., 2015; Wei et al., 2020; 王红旗 et al., 2017), as well as electrochemical designs with some shorter sequences including a thiol modified 80 nt aptamer (Chen et al., 2015b) and an unmodified 40 nt (Tian et al., 2017) sequence. Likewise, the assay preparation time showed high correlation to 60 nt fluorescent (Gui et al., 2015), 40 nt electrochemical (Cheng and Bonanni, 2018), and 96 nt colorimetric (Mirón-Mérida et al., 2021) aptasensors. Nevertheless, as already stated, the high correlation of the 96 nt aptamer with a high sensitivity (low LODs) in combination with its convenient specificity, were relevant for the existence of more biosensors based on this long length sequence. The most sensitive aptasensors for FB1 have reported LODs equivalent to $1.9x10^{-5}$ µg/L for the utilization of fluorescent nanoparticles (Niazi et al., 2019), $3x10^{-6}$ µg/L from Au nanorods- fluorescent UCNPs (He et al., 2020), and $5.6x10^{-5}$ µg/L for an aptamer-FB1-AuNP complex analyzed by AF4-UV-Vis (Mirón-Mérida et al., 2021). UCNPs, fluorescent and ECL particles have suitable optical and chemical properties, precisely their lack of autofluorescence, background noise and absorption by biological

samples, along with their lower toxicity, greater stability, and higher photoresistance, when compared to organic fluorophores (Wu et al., 2012; Wu et al., 2013) and fluorescent dyes, indicating fluorescence bleaching and overlap (Yang et al., 2017). Even when sensitive, the assay times of many fluorescent aptasensors for FB1 exceeded 100 minutes (Liu et al., 2018; Wu et al., 2012; Wu et al., 2013; Wu et al., 2020), whose assay preparation time occasionally surpassed 24 h (Wu et al., 2012; Niazi et al., 2018; Wu et al., 2013; Yang et al., 2017; Yue et al., 2014; Zhao et al., 2014). Moreover, this type of methods requires fluorescence spectrophotometers, which might limit their on-site application.

Although, electrochemical aptasensors have indicated low costs, simple operation, good selectivity, affinity, miniaturization and stability, their polishing and other modification steps increase their assay preparation times (Han et al., 2020; Wei et al., 2019; Wei et al., 2020; Zhao et al., 2014), as already observed in some biosensing platforms (Shi et al., 2015; Wang et al., 2017; Zheng et al., 2020; Zheng et al., 2021). In this matter, SPCEs could function as a cheaper and time-effective alternative to methods with modified electrodes (Han et al., 2020). Furthermore, the use of different nanoparticles enhances the applicability of aptamers, however, their long synthesis and washing steps generate an increment on the assay preparation times (Hao et al., 2018a; Wang et al., 2013b). In addition, more robust techniques might be ideal for increasing the sensitivity of nanoparticle-based aptasensors. Precisely, as already discussed, the LODs of the signals from the unique complex produced by the incubation of the 96 nt aptamer, FB1 and AuNP in particular buffer conditions ($MgCl_2$ 1mM), was enhanced through the application of AF4 for resolving those complexes (Mirón-Mérida et al., 2021). Nevertheless, this analytical technique portrays long assay times and has the same constrains found in chromatographic methods. On the other hand, it is worth noting that no paper-based aptasensor has been developed for the quantification of FB1, whose application could reduce the cost and extend the applicability of such sensitive conformations.

Despite the similar scope of application between aptamers and antibodies, aptasensors are more versatile than immunosensors in terms of their lower sample volumes, simplicity, and absence of washing steps in the majority of the aptamer-based detections (Molinero-Fernández et al., 2017). As previously mentioned, contrary to aptasensors, immunochemical methods required high reagent volumes and normally result in the analysis of single mycotoxins where cross-reactivity is observed towards matrix compounds and structurally similar toxins (Yue et al., 2014). Besides, antibodies are expensive to produce, and their isoelectric point modulates their net charge polarity, ionic composition and pH, whereas some antibody immobilization methods affect their activity and might produce denaturation (Chen et

al., 2015a; Ren et al., 2017; Tang et al., 2014). On the contrary, aptamers portray advantages related to their less costly chemical synthesis, which yields high purity small size sequences with no batch variability, low immunogenicity, along with greater stability, reproducibility, shelf life, and reversible denaturation features. This in vitro procedure can also be exploited not only for the chemical modification and labelling of aptamers, but for the controlled selection of aptamers under any specific real testing conditions (Molinero-Fernández et al., 2017; Niazi et al., 2019; Ruscito et al., 2016; Shi et al., 2015; Yue et al., 2014). Nevertheless, the covalent immobilization of FB1 during SELEX might hinder the specificity of the selected aptamers, as binding could be oriented towards the modified version of the target rather than the free molecule (Ruscito et al., 2016). It has been observed that aptamer 3D folding depends on the buffer compounds and parameters (pH, ionic strength, temperature), which should be considered when creating a sensor in different environmental conditions (Evtugyn and Hianik, 2020). In this respect, the performance of two aptamers (96 and 40 nt) carried out by our research group through the development of a AuNP-based colorimetric assay unveiled the role of different binding buffers on the final assay specificity (Mirón-Mérida et al., 2021). For instance, unlike previous aptasensors (Cheng and Bonanni, 2018; Tian et al., 2017), assays with the 40 nt aptamer under the presence of Tris HCl denoted lack of specificity when OTA was included (Mirón-Mérida et al., 2021).

Multiplex aptasensors are strongly desired in food safety, where the simultaneous determination of mycotoxins is beneficial for the overall method cost and efficiency (Jiang et al., 2020; Wei et al., 2020). As previously discussed, multiplex aptasensing methods including FB1 analysis have been successfully developed mainly as fluorescent and electrochemical assays, with one bulk colorimetric design.

Furthermore, aptasensors are still debatable regarding their on-site application, especially when considering that many approaches still require expensive platforms and equipment, skilled users, refrigeration, and electrical installations (Ruscito et al., 2016). The commercialization of aptamer-based biosensor has been outshined by the development of chromatographic methods and ELISA-based kits, mainly because of the laborious SELEX process, which have resulted in the selection of a low number of new sequences specific to FB1. Yet, the application of bioinformatics for *in-silico* studies is a good alternative for coping with the disadvantages of SELEX (Yoo et al., 2020). Nevertheless, cost-effective, and simple biosensing techniques, with miniaturized and portable features are still required for in-field analysis, in which aptamers have shown an excellent potential as recognition elements (Ren et al., 2017). Inexpensive and sensitive in-field assays for FB1 could be accomplished with paper-based designs, in which the utilization of stable AuNPs is suitable due to their van der Waals interactions with aptamers, their surface area, biological compatibility,

and their simple and low-cost synthesis (Hou et al., 2020a; Jiang et al., 2020; Majdinasab et al., 2020). Apart from colorimetric sensors, fluorescent paper-based designs could integrate AuNP with FRET dyes (Zhang et al., 2020b) and fluorescent materials such as UCNPs, due to their wide absorption, photostability, high yield, easy modification, as well as their narrow yet symmetric emission spectra (Jiang et al., 2020; Wu et al., 2012). In summary, despite the excellent specificity and sensitivity indicated by aptamer-based biosensors for the quantification of FB1, there are many improvements to be applied. Computer-based simulations can be used for the investigation of new sequences specific to this mycotoxin, where more approachable and feasible methods are required for on-site analysis, especially in developing areas with limited infrastructure. As observed with other mycotoxins, more food matrices should be analyzed in new biosensing developments, as only cereals (rice, wheat, maize), beer and peanuts have been screened thus far.

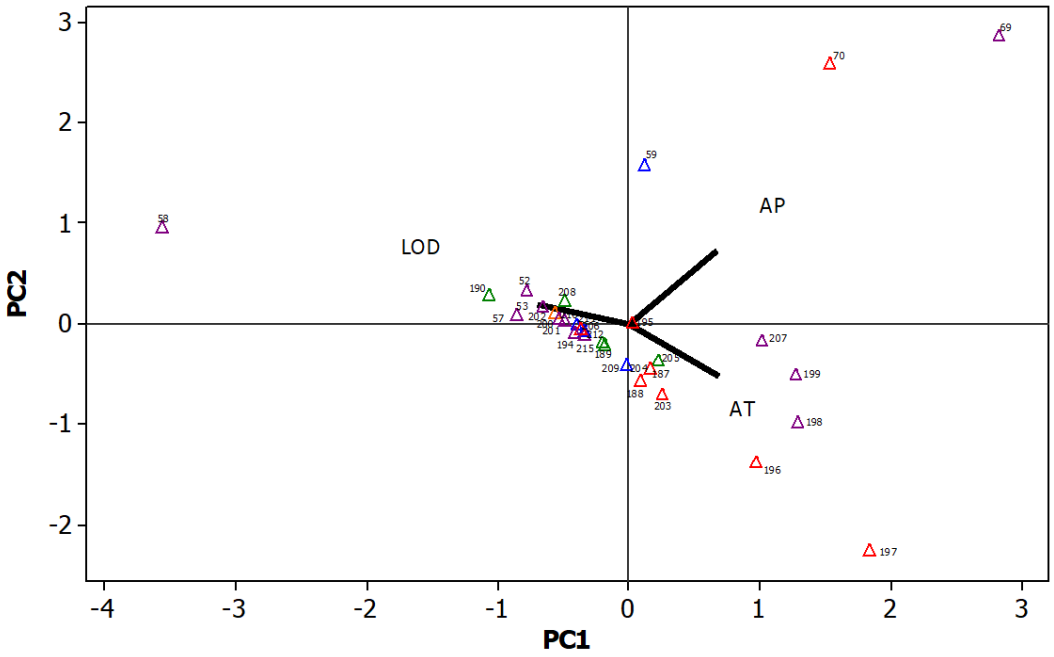

Figure 2.10 Principle component analysis for the correlation of all the reported aptasensors for optical (Δ), fluorescent (Δ), chemiluminescent (Δ), electrochemical (Δ), and other signals (Δ). The numbers correspond to the correlated references from Table A2

2.5 Conclusions

The use of aptamers for the quantification of fumonisin B1 is at the central focus in the field of biosensors with many areas of opportunity, on account of their relatively recent dissemination and the few strands already reported. Even when sensitive, aptasensors featured similar or lower detections limits than well-established immunosensing techniques, LC-MS assays and Raman-based methods, the recent application of MIPS has redirected the attention on the improvement of the LODs from aptamer-based biosensors. Additionally, despite the diversity of approaches performed with the two selected aptamers and their shortened forms, to date around 95% of all the aptasensors have been proposed as bulk experiments. Hence, there is considerable room of opportunity for the exploration of different supports, ideally paper matrices for the refinement of on-site testing. Additionally, reducing the extraction steps is a desirable quality for quick analysis of samples in remote areas.

Thus far, the specificity of the aptamers utilized for FB1 quantification has been confirmed against up to 19 different molecules, and in multiplex detections of up to 4 targets, while their limits of detection confirmed the feasibility of addressing contamination levels under the regulated limits. It is important to understand and uncover the role of the selected support, and binding conditions (binding buffer, temperature, time) on the selectivity and affinity of the resulting biosensor. Despite all the advances regarding aptamers, more efforts are necessary to obtain shorter strands with high affinity towards FB1 or novel targets, so the final sensing method can be simplified, yet be effective.

Chapter 3
Mathematical characterization of ink diffusion and imbibition processes in chromatography paper as a biosensing platform

Abstract

Materials used for biosensor development normally include silicon, glass and synthetic polymers, however, paper is a practical and cheap option for the reduction of manufacture costs with a wide range of applications. Paper-based biosensors have been widely produced, yet poorly characterized on the interaction of different type of molecules with its intricate microstructure. In this work, five ink solutions were prepared as model samples to examine their diffusion and imbibition behavior on grade 3MM chromatography paper. Different mathematical models, previously reported for porous matrices, were fitted and results revealed that upward wicking ($r^2 \geq 0.90$) equations described the experimental data during the initial stage (< 5 s) and yielded similar permeability values to those calculated from the matrix structural properties. The diffusion coefficient was determined up to attaining equilibrium using the diffusion equation in a cylinder element ($r^2 \geq 0.90$). This study enabled the characterization of the performance from 3MM chromatography paper, by using ink as a surrogate model of small molecules (e.g. mycotoxins) or small colloidal particles.

3.1 Introduction

Many concepts have been utilized for describing transport phenomena in porous media, which can be regarded as physical complex processes including convection, diffusion, imbibition and heat transfer, where the permeability of the porous medium has a strong influence on these phenomena and their time evolution (Cai et al., 2012a). Likewise, imbibition is a relevant concept to different fields ranging from petroleum and civil engineering, geophysics, everyday commodities (tissues, paper rolls), and of course, paper-based chromatography and biosensing techniques (Cai et al., 2012b; Suo et al., 2019). From the different material supports for sensing techniques, paper represents an attractive option, given its amenability for the development of fast, affordable and versatile assays, thus offering the possibility of identifying diverse targets. Paper-based biosensors are commonly designed as dipsticks, lateral flow

[2] Published as: Mirón-Mérida, V.A., Wu, M., Gong, Y.Y., Guo, Y., Holmes, M., Ettelaie, R. and Goycoolea, F.M., 2021. Mathematical characterization of ink diffusion and imbibition processes in chromatography paper as a biosensing platform. *Sensing and Bio-Sensing Research*. **32**, 100421.

tests, or paper-based analytical devices (μPADs) (Liu et al., 2019), in which nitrocellulose is the platform for the development of different signals. For instance, colorimetric determinations through the conjugation of gold nanoparticles (AuNPs) with antibodies, for the single (Lee et al., 2013; Moon et al., 2012) and multiplex quantification of compounds (Yu et al., 2018), the application of aptamer-funtionalized AuNPs (Dalirirad and Steckl, 2019), and the completion of chemical reactions (Cardoso et al., 2015; Pesenti et al., 2014) have been proposed as paper-based methods. The versatility and biocompatibility of paper have been exploited for the application of chemiluminescent compounds, substrates and quantum dots, resulting in the fabrication of single chemiluminescence (CL) (Liu et al., 2014), multiplex CL (Zhang et al., 2018) and luminescent (Duan et al., 2019) assays, respectively. Other innovative measurements include paper separation coupled with electrochemical analysis (Carvalhal et al., 2010), and the integration of surface-enhanced Raman scattering (SERS) on paper test lines (Wang et al., 2019). Therefore, understanding the diffusive and capillary effects controlling the mobility of samples is a relevant step during the design and construction of a paper-based biosensor.

Due to is fibrous nature, paper is a porous medium, where it has been predicted that water first moves into the pores by covering the fiber surface and moving into them, followed by the occupancy of the inter-fiber pores. This penetration process is faster when following the fiber direction along the plane to that in the perpendicular direction (Aslannejad et al., 2018). Studies focused on inkjet ink for coated paper have demonstrated that after the ink drop is applied on the paper surface, the initial movement is generated by inertia. Then, a quick competition takes place against spreading and the capillary forces integrating the ink into the porous structure. In a matter of milliseconds, ink separation is also observed, followed by adsorption within ~1 s. Although diffusion appears with the first manifestations of capillary imbibition, the diffusion effect is more notorious as the penetration of ink increases (~10 s). The last stages during inkjet printing are polymerization (~100 s) and drying (~1 h); however, these are usually not described during modelling. The given times are related to an onset point of such phenomena, as in reality, all of them coexist on the same porous matrix (Kettle et al., 2010). As observed in coated paper, small quantities of binder can affect the final rate of progress balance between the wetting force and the viscous drag, commonly denoted by the Young-Laplace equation (Lamminmäki et al., 2011).

At the initial stages of ink absorption in coated paper, imbibition is determined by the pore diameter, as capillary forces moved the liquid sample towards the coating area (Lamminmäki et al., 2012). This process is followed by diffusion due to wettability and swelling (Lamminmäki et al., 2012); nevertheless, this whole mechanism might differ in uncoated paper.

In general terms, the flow of liquid samples in a porous media such as paper, is driven by capillary forces occurring at the air-liquid interface, whose curvature and differences in surface tension produce the transport of samples, in a process commonly defined as passive pumping (Wang et al., 2013). Furthermore, the flow of samples within porous paper channels regarded as capillary tubes, has been described as a correlation of the penetration distance and the time, described by Washburn equation, also referred as Lucas-Washburn equation (Equation 3.1):

$$L(t) = \sqrt{\frac{rt\gamma cos\theta}{2\mu}} \tag{3.1}$$

Where L is the penetration distance, r is the average pore radius (capillary radius), γ is the surface tension, θ is the capillary wall-liquid contact angle, and μ the dynamic viscosity. For this estimation of the unidirectional penetration, the porous medium is addressed as an intricated array of tubes, where the channel width does not affect the travelled distance. Yet, as the wetting front is positively proportional to the square root of the pore radius, a faster imbibition profile would be expected for large capillaries (Borhan and Rungta, 1993; Liu et al., 2017; Mahmud et al., 2018; Shi et al., 2018; Shou et al., 2014). The latter has been contradicted by studying the impact of geometric sectioning on a porous medium for the asymmetric capillary flow of samples in a lateral flow arrangement, in which narrowed sections had a quicker movement (Shou et al., 2014). This entails that liquids tend to fill the finer pores within a paper layer, while inertia effects arise from large pores and a viscosity regulated absorption, commonly overlooked in Lucas-Washburn (Aslannejad et al., 2018; Liu et al., 2017). In this regard, the flow of samples can be manipulated, as proven by a cheap hybrid system combining digital microfluidics for the controlled incorporation and movement of samples with a 3MM Chr paper μPAD for a lateral flow detection system (Abadian et al., 2017). In some other studies, the radial penetration of different compounds was recorded on filter paper under fluorescent light, where two drop-phases were identified before and after total penetration in the porous substrate, through a microlenses equipped videocamera (Borhan et al., 1993). Filter paper was also used for the fabrication of pumps, where the passive pumping effect produced by capillary forces

denoted a linear correlation between a greater flow rate and an increasing sector angle (Wang et al., 2013).

Sample spreading in paper can be also accomplished by numerical simulations after obtaining a micro-tomography of the porous media with further validation of the droplet penetration by confocal microscopy (Aslannejad et al., 2018). Pore-scale two-phase simulations were also carried out by combining ion beam scanning electron microscopy with confocal laser microscopy validation (Aslannejad et al., 2021); however, both approaches analyzed such phenomena in a pL scale, with a highly controlled dosage of the selected model sample. Besides, many of these estimations require complicated computational and experimental settings (Qin and Brummelen, 2019), which only account for small sample volumes under different conditions misrepresenting the final biosensing approach and its wettability implications.

The Lucas-Washburn equation can be modified to fulfil the added effects of inertia, gravity, evaporation, and tortuosity (Suo et al., 2019). Similarly, although imbibition corresponds to the transport of fluids in the x, y and z directions, the Lucas-Washburn equation can be adjusted to the kinetics of radial penetration, in which the transport of fluids is mainly measured along the y-direction (Borhan and Rungta, 1993; Liu et al., 2017). The radial imbibition in a porous medium was analyzed in glass microspheres, in contact with a hole at the top of a container filled with wetting liquid. The analysis of the hemispherical front was explained with an expanded version of Darcy's law for radial flow, with an integration of Laplace pressure (Xiao et al., 2012) (Equation 3.2).

$$r_f = A^{1/3} t^{1/3} \tag{3.2}$$

Where, $A = [\frac{3kp_c r_s}{\mu}]^{1/3}$, $p_c = \frac{2\gamma cos\theta}{r_p}$ (Laplace capillary pressure), k, r_s, r_p, θ, γ and μ represent the permeability, initial front radius, pore radius, contact angle, surface tension and dynamic viscosity of the liquid, respectively, and t is time.

Likewise, wicking experiments performed on the upward propagation of hexadecane in cellulose webs confirmed the time-dependence of the liquid front point with a simplified version of Darcy's law with Lucas-Washburn equation (Callegari et al., 2011), given as (Equation 3.3)

$$L^2 - {l_0}^2 = \alpha^2 (t - t_0) \tag{3.3}$$

Where, $\alpha^2 = D$, $\alpha = \sqrt{\frac{2p_C\,k}{\mu\Phi}}$, $p_c = 2\gamma/r_p$, p_c=capillary pressure, Φ=porosity of material, t_o is initial time and *t* is time.

Additionally, capillary imbibition assays on filter paper revealed the influence of the matrix geometry on the mathematical models for describing fluid transport (Elizalde et al., 2015). A radial cylindrical flow through a trapezoidal strip was calculated with the following equation (Equation 3.4):

$$\frac{(1+al)^2}{2}\left[\ln(1+al)-\frac{1}{2}\right]+\frac{1}{4}=a^2Dt \tag{3.4}$$

where a=1/r_0, l=r-r_0, r_0=radius of the initial wetted area at t=0. While a radial spherical flow through a non-linear cross-sectional area was predicted by equation 3.5:

$$\frac{1}{6}\left[(1+al)^3-\frac{1}{2}\right]-\frac{1}{2}[(1+al)^2-1]=a^2Dt \tag{3.5}$$

In which, a =1/r_0, l=r-r_0, r_0=radius of the initial wetted area at t=0.

Both equations derived from a combination of mass conservation expressions of Darcy's law, and a subsequent simplification by integrating Lucas-Washburn equation under different geometrical cross-sectional areas (Xiao et al., 2012). In all the previously mentioned models, Darcy's law has been used for denoting the single-phase spontaneous imbibition within porous media, while neglecting the viscosity of air and the gravitational effects (Qin and van Brummelen, 2019).

Thus far, the assessment of the diffusion and capillary properties of paper-based systems have required especial cameras, lightning, reservoirs, chambers, or supports with multiple layers. Nevertheless, the application of real samples must be kept as simple as possible, and a better understanding of the diffusive and imbibition nature of paper under realistic circumstances must be gleaned. Furthermore, as most of the research has been focused on dipstick and lateral flow arrangements, μPADs are of particular interest especially given that the applications of higher volumes (40-70 μL) take place on the central zone of the μPADs (Cardoso et al., 2015; Gabriel et al., 2014; Mirón-Mérida et al., 2020). In this work, the diffusion of commercial blue ink (a mixture of pigments, glycerol and surfactants) used as a surrogate of small molecules (*e.g.*, mycotoxins), was studied on 3MM chromatography paper. To this purpose, different mathematical models were examined to describe the radial flow of ink in porous media at short times. Similarly, a diffusion equation for a cylinder was fitted to the whole process to calculate the corresponding apparent diffusion coefficients. The application of ink was selected to simplify the experimental set up by utilizing the easily observable ink front.

3.2 Materials and methods

3.2.1 Materials

Chromatography paper grade 3MM, filter paper grades 1 and 540 were acquired from Whatman™ (UK). Permanent marker (Medium Point 1.0mm Write-4-All Pen Permanent – Black) and stamp pad blue ink without oil were purchased from Stabilo (UK) and Pelikan® (Germany), respectively. All the solutions were prepared with MQ water.

3.2.2 Methods

3.2.2.1 Preparation of ink models

Five samples were prepared through aqueous dilutions of blue stamp pad ink from Pelikan at 10, 25, 50, 75 and 100% (w/w) –where 100% corresponds to the undiluted ink.

3.2.2.2 Rheological determinations

The rheological properties of the ink were determined using a Kinexus rotational rheometer (Malvern, UK), fitted with a stainless steel double gap measuring system (C25 cylinder) for measuring the dynamic viscosity (η) at different shear rates ($\dot{\gamma}$).

3.2.2.3 Density of the ink models

The density values (g/cm^3) of the five ink dilutions were measured in an Anton Paar Density Meter DMA 4500 M, based on the oscillating U-tube method, with a calibration density check for water.

3.2.2.4 Interfacial tension of ink models

Interfacial tension measurements were performed at 20 °C in a OCA 25 instrument, by analyzing a 10 µL drop shape according to the pendant drop method. In the aforementioned method, a spherical liquid drop will be formed on a dosing needle (ø=0.911 mm) due to the surface tension and gravity and can be analyzed with the Young-Laplace equation (Eq. 3.5) where ∆p is the pressure difference through the fluid interface, γ is the surface tension, R1 and R2 the radii of curvature (Fig B1a).

$$\Delta p = \gamma\left(\frac{1}{R1} + \frac{1}{R2}\right) \quad (3.6)$$

3.2.2.5 Contact angle of the ink models

The contact angle was measured at a contact line produced by an ink solution drop deposited on Whatman cellulose chromatography paper grade 3MM. According to the scalar Young equation:

$$\sigma_L \cos\theta_c = \sigma_S - \sigma_{SL} \quad (3.7)$$

where the contact angle (θ_c) is influenced by the vectorial equilibrium between the energies acting along the solid surface (σ_S), in opposite direction at the liquid-solid interface (σ_{SL}) and the liquid surface (σ_L) tension operating tangentially to the surface (Fig B1b).

3.2.2.6 Porosity of paper

Prior to the porosity experiments, the paper samples were left in a desiccator containing 500 g of fully dried silica gel (SiO_2) for 24 hours. The porosity measurement was obtained by the liquid displacement method (Guan et al., 2005), in which a 3MM chromatography paper square (V paper= 2 x 2 x 0.034 = 0.136 cm^3) was placed in a falcon tube containing 20 mL of absolute ethanol (ρ= 0.791g/mL) for 48 hours. Weights of the paper samples were recorded at different stages in order to obtain the volume (V) of impregnated ethanol after removal of the paper piece from the falcon tube. The porosity (ε) was calculated according to equation 3.8.

$$\varepsilon = \left(\frac{V\ impregnated\ ethanol}{V\ paper}\right) \quad (3.8)$$

3.2.2.7 Scanning electron microscopy and pore size determination in paper

The surfaces of dry 3MM chromatography paper were coated with a thin layer of iridium (4 nm) with a sputter coater Essington 208HR, and scanning electron microscopy images were obtained with a FEI Nova NanoSEM 450 operating at 3 kV. The average pore diameter of the observed fibers was calculated in image J, by calibrating the SEM images in µm/pixel.

3.2.2.8 Application of the ink models on paper

Prior to the mathematical fitting assays, 50 µL from each ink model were vertically applied on the center of chromatography paper grade 3MM squares (4.5 x 4.5 cm), fixed with masking tape to a horizontal metallic base. The ink front was recorded with

a mobile phone (IPhone 6s plus), and the circular area at different times was calculated with Image J, from which the front radius/distance was obtained.

3.2.2.8.1 Diffusion coefficient estimation in chromatography paper

The mathematical fitting for the diffusion in a cylinder was performed in Origin Pro 8.6 32 for all the experimental data until a constant area was reached, as stated in equation 3.9 (Crank, 1979) .

$$l_{rel} = \frac{l_t - l_0}{l_\infty} = \frac{4}{\pi^{\frac{1}{2}}}\left(\frac{Dt}{a^2}\right)^{1/2} - \frac{Dt}{a^2} - \frac{1}{3\pi^{1/2}}\left(\frac{Dt}{a^2}\right)^{3/2} \quad (3.9)$$

Where l_{rel} is the relative distance; $l_{t,}$ l_0 and l_∞ are the front ink distance at a time t, time 0, and at the diffusion equilibrium time, respectively. *D* represents the diffusion coefficient (m^2/s), t the diffusion time, and *a* is the radius achieved at the equilibrium stage.

3.2.2.8.2 Mathematical fitting of the radial flow in chromatography paper

Further mathematical model fittings of the recorded data were conducted in Origin Pro 8.6 32 Bit (2012) software, for equations 3.2, 3.3, 3.4, and 3.5 at short times (5 s), and their corresponding permeability values (experimental permeability) were calculated by integrating the measured parameters (contact angle, surface tension, viscosity, density) with the fitted values.

3.2.2.8.2.1 Permeability determinations for model selection

The experimental properties of 3MM chromatography paper (pore radius and porosity) were integrated to calculate the theoretical permeability (K), according to equation 3.10, also known as the Kozeny-Karman model (Xiao et al., 2012).

$$K = \frac{dm^2}{180}\frac{\varepsilon^3}{(1-\varepsilon)^2} \quad (3.10)$$

Where K= permeability, dm=diameter of pores, ε=porosity.

This equation derived from a more general approach for the calculation of the permeability in fibrous media described in equation 3.11 (Xu and Yu, 2008).

$$K = \frac{dm^2}{36k}\frac{\varepsilon^3}{(1-\varepsilon)^2} \quad (3.11)$$

Where k accounts for the Kozeny-Karman constant, previously calculated for monodispersed fibers in a random packing arrangement (Rahli et al., 1997). In the case of Equation 3.11, the k constant for beds packed with spherical particles was approximated to 5 (Xu and Yu, 2008), hence a value of 180 was indicated for this the expression.

Another expression for permeability (K) was reported by Callegary and collaborators for the analysis in ultra-fine cellulose webs (Callegari et al., 2011) as indicated in equation 3.12.

$$K = r^2 \frac{\varepsilon}{4k} \tag{3.12}$$

Where K= permeability, r=capillary radius, ε=porosity, and k=Kozeny-Karman factor measured as already indicated (Rahli et al., 1997).

The three expressions of the Kozeny-Carman model for the permeability of porous media, were selected as theoretical values, for the further comparison with the experimental permeability data and selection of the best descriptor of the ink movement in paper at short times (5 s).

3.2.2.8.3 Comparison of Lucas-Washburn equation with its modified expressions

An exploration of different versions of the Lucas-Washburn equation was completed by fitting equation 3.13 and equation 3.14 to the recorded front ink distance at a given time t (t≤5 s). The first model followed a nonlinear relation between l^2 and t, as denoted in equation 3.13 (Mahmud et al., 2018; Marmur, 2003).

$$l^2 = D * t \tag{3.13}$$

From which D could express the effect of either the pore radius as traditionally represented in Lucas-Washburn ($D=r\gamma\cos\theta/2\mu$) (Mahmud et al., 2018; Shou et al., 2014) or nongravitational effects by integrating Darcy's law in substitution of Hagen-Poiseuille equation ($D=2C\varepsilon\cos\theta/S(1-\varepsilon)\mu$) (Marmur, 2003). Furthermore, the exploration of inertia effects provided by the density of samples, was indicated as the linear relation between l and t in equation 3.14 from Schoelkopf (Kettle et al., 2010).

$$l = D * t \tag{3.14}$$

Where D= (2γcosθ/rρ)^0.5.

A validation step was carried out between the fitted D and the expected D values, where the latter were obtained through the integration of the average pore radius (r) of the paper matrix, in combination with the surface tension (γ), contact angle (θ), viscosity(μ) and density (ρ) of the ink models, as expressed in each case.

3.3 Results and discussion

3.3.1 Diffusion coefficient estimation in chromatography paper

A preliminary selection of the paper matrix was performed through the application of aliquots of diluted pure ink on Whatman filter paper grades 1, 540, and Whatman 3MM Chr paper. Despite the greatest area achieved with filter paper, the sample mobility on Whatman grade 1 and 540 was not adequate for homogenous spreading, as the pore size (11 μm particle retention) allowed penetration of the sample and some stained areas were found beyond the hydrophobic barriers (created according to Figure B2). Hence, the rest of the study was carried out with Whatman 3MM Chr paper. The diffusion through the porous layer of filter paper does not necessarily represent a negative attribute. In fact, this behavior has been exploited in the multiplex detection of DNA by paper-origami mechanisms (Yang et al., 2018).

The choice of colored blue ink was convenient for the simplification of the experimental settings and the ease to quantify its diffusion using image analysis techniques. To this end, a distinct circular front area was tracked using a mobile phone camera, without the aid of structural layers or external light sources. As displayed in Fig B3b, the area increment for the five ink models was plotted during 600 s, in which an increasing ink concentration led to a delay in reaching the steady stage, where a higher ink percentage was related to a greater front area. The physical properties of the five ink models are presented in Table 3.1. Note that an increasing ink percentage led to increasing viscosity and density values, and a decreasing interfacial surface tension (IST). On the other hand, although some reported wetting angle values for filter paper were equivalent to 89.84° (Wang et al., 2013), in this work, the measured contact angle was zero, as revealed by the absence of drop formation on the porous substrate produced by the immediate absorption of the ink drop (Fig B1d). This result was indeed expected, as a contact angle of zero is mainly produced by the hydrophilic nature of the fibers in contact with water, for that reason many printing papers and similar surfaces are treated and coated to increase the contact angle. In the case of untreated chromatography paper, a null contact angle implies greater spreading and penetration lengths (Aslannejad et al., 2018).

Table 3.1 Physicochemical characterization of the five ink models

Ink Concentration (%, v/v)	Density ρ (g/cm^3)	Dynamic viscosity μ (Pa s)	Contact angle Θ (°)	Interfacial surface tension γ (N/m)
10	1.0022	0.0012	0	0.0529
25	1.0148	0.0015	0	0.0475
50	1.0329	0.0021	0	0.0496
75	1.0527	0.0030	0	0.0493
100	1.0741	0.0047	0	0.0440

Ink diffusion on paper has been regarded as a Fickian process, in which migration takes place due to a concentration gradient triggered by Brownian motion (Kettle et al., 2010). Data fitting for Equation 3.9 was applied to all experimental points (Fig B4) until diffusion equilibrium (constant area) was reached. The equilibrium times varied depending on the ink model and were equivalent to ~10, ~20, ~150, ~300, and 300 s for the various ink samples at increasing concentrations (10 to 100%). As illustrated in Fig 3.1a, the selected mathematical expression was a good descriptor of the variability of the experimental data set, which was confirmed by the high determination coefficients ($0.93<r^2<0.96$) for the calculated D values (Figure 3.1a inset), and the linearity of the fitting curves between the mathematical and the experimental L_{rel}. In addition, as displayed in Fig 3.1b, the calculated D values diminished with a rising ink concentration, which suggested a positive effect from the water content on the rapid achievement of a constant phase.

Such impact on the coefficients (D), was expected after considering the effects on such parameters, mostly related to the composition of the stamp pad ink (21% glycerol, 16% sorbitan monooleate ethoxylated, 9% diethylene glycol, 6% pigment and 48% water). In this regard, an increasing viscosity combined with a decreasing surface tension have been previously related to a reduction in spreading and infiltration. Likewise, a higher density is expected to portray a slower imbibition performance (Schoonderwoerd, 2019), which is consistent with the results in this work. The mathematical expressions describing the relation between the numerical (L_m) and the experimental (Lrel) relative distance for each ink model, are indicated in Table 3.2. The satisfactory coefficients of determination (r^2=~0.96) demonstrated a good prediction of such linear relation, which can be also implied from the slope values in each equation (y=mx+b), where “m” was noticeably close to 1 for all the ink concentrations. A statistically significant correlation ($p<0.05$) was found among the experimental and numerical relative distances, as revealed by the correlation coefficients (R=~0.98) in Table 3.2.

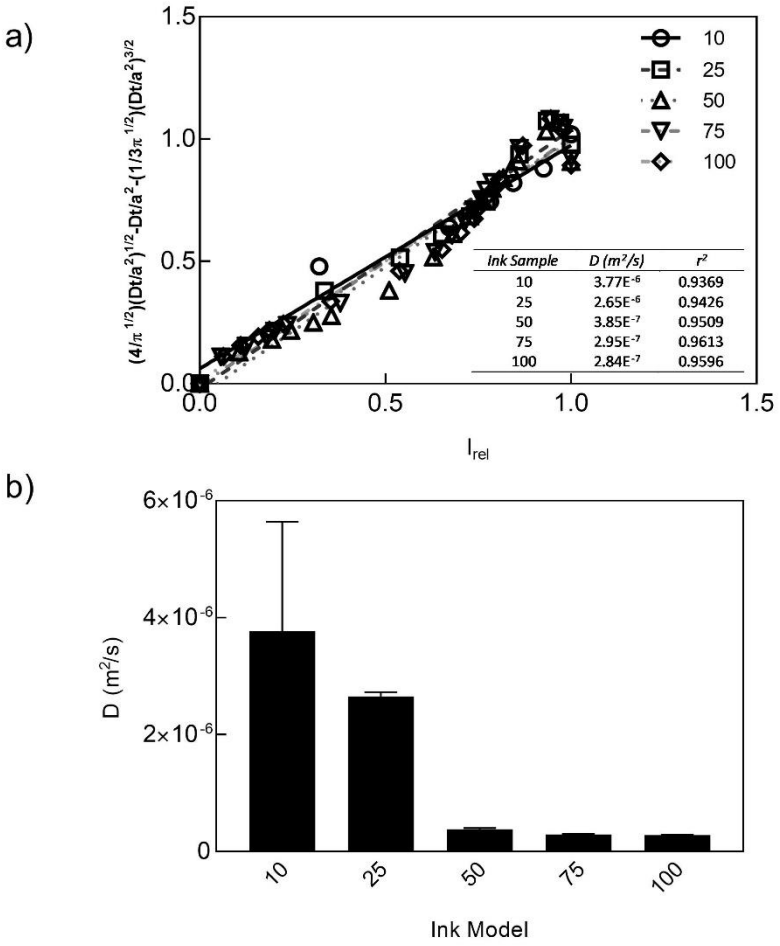

Figure 3.1 (**a**) Calculated relative distance (l_{rel}) from Equation 3.9 as a function of the experimental values and (**b**) its corresponding diffusion coefficients (D)

Table 3.2 Mathematical expressions and correlation between the calculated relative distance (Lm) and its corresponding experimental value (L_{rel})

Ink Concentration (%, v/v)	Equation	r^2	Correlation Coefficient R	*p*
10	Lm=0.9129 Lrel +0.0615	0.964	0.9819	8.43e-5
25	Lm=1.0612 Lrel -0.0224	0.9667	0.9832	3.4e-7
50	Lm=1.0536 Lrel-0.0496	0.9659	0.9828	3.61e-13
75	Lm= 1.011 Lrel -0.0068	0.9641	0.9818	1.01e-13
100	Lm=0.9788 Lrel+0.0127	0.9613	0.9804	1.94e-13

Apart from the effects of the physical parameters inherent to the applied sample, an important consideration for the mathematical modelling of ink diffusion on paper is the industrial nature of chromatography paper. The fluid's displacement velocity has been

proven to be also dependent on the cellulose microfibers microscopic arrangement. This feature is uncontrollably developed during paper production, where the fibers are oriented either in the production machine or the cross direction, thus limiting the speed of liquid penetration (Elizalde et al., 2016). A faster diffusion occurs in a parallel direction to the fibers, and when such diffusion is measured as parallel to the paper plane, the calculated coefficients are an average of all the fiber orientations. Moreover, this bulk behavior is observed in porous substrates at short times, whereas long-time approximations consider the connectivity of the porous network (Topgaard and Söderman, 2001).

3.3.2 Permeability comparison for equation fitting of radial penetration models

The SEM images for 3MM chromatography paper are shown in Figures 3.2a, in which a fibrous morphology was observed, similar to other porous uncoated cellulose-based materials where the fibers constitute their surface (Gabriel et al., 2016). Although channel discontinuity and variable channel widths are normal for this kind of matrix (Mahmud et al., 2018), a continuous profile of homogenous cylindric fibers is assumed for the mathematical fitting of radial penetration models as displayed in Figure 3.2b. Therefore, an average of 40 fiber width measurements from Figures 3.2a (200 µm scale) were recorded to estimate the pore diameter, whose value was equivalent to 13.86 ± 4.14 µm, equivalent to approximately the double of the already reported particle retention value (6 µm) for 3MM chromatography paper (Evans et al., 2014). In these regards, approximating the porous medium to a cylindrical capillary is a common strategy to simplify the penetration modelling, where the equivalent radius and equivalent contact angle are needed, yet the latter is commonly referenced as zero (Marmur, 2003). This value is also applied in the equation for capillary pressure (pc) for upward wicking (Equation 3), where $\cos\theta$ was not included (Callegari et al., 2011), and complies to the observed results in the physicochemical characterization (Table 3.1).

a)

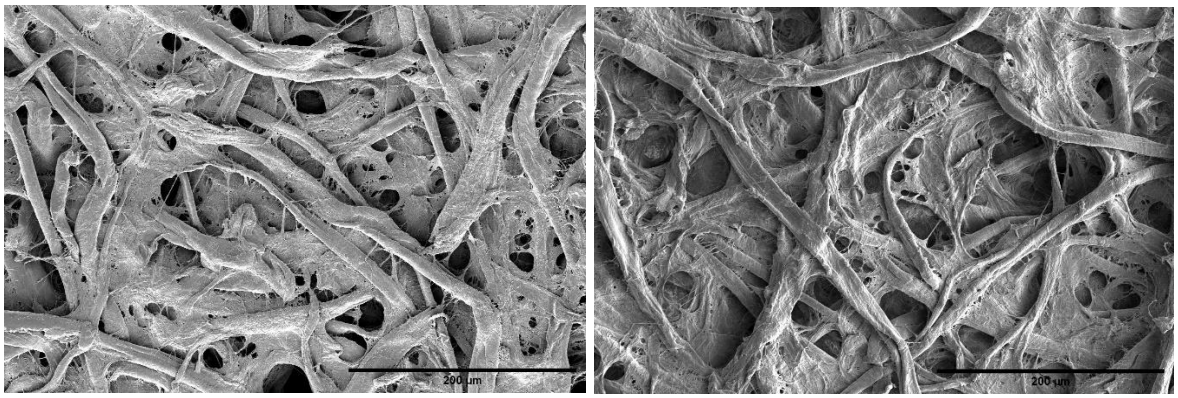

b)

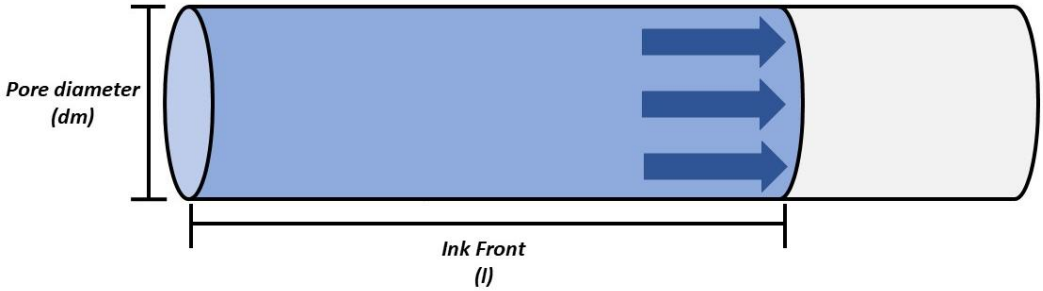

Figure 3.2 (**a**) SEM images of the morphology of untreated 3MM chromatography paper (200 µm scale) and (**b**) schematic representation of the paper fibers as capillary tubes.

Furthermore, the constants and r^2 values for equations 3.2, 3.3, 3.4 and 3.5 are indicated in Table 3.3, in which all the selected mathematical functions exhibited high determination coefficients (r^2) upon data fitting during the first 5 s (Figure 3.3). Some considerations for the application of such models are worth of note, namely the Stoke regime conditions such as stationary flow, absence of inertia, low Reynold numbers, and isothermal state (Elizalde et al., 2015). Other assumptions included a small liquid source, uniform radial velocity, a radial pressure gradient, and predominance of the capillary pressure over the hydrostatic pressure (Xiao et al., 2012).

The physical properties of the ink models (Table 3.1) and coefficients shown in Table 3.3 were integrated to estimate the permeability(k). This variable was used as a reference parameter for comparing different mathematical approaches, as calculating the permeability rendered a way to converge different experimental inputs in one specific estimation. A theoretical permeability was considered after replacing some terms in the Kozeny-Karman model (Xu and Yu, 2008) and its two variations (Callegari et al., 2011; Xiao et al., 2012), whose approach related the pore structure to the permeability when using the measured pore diameter (13.86 µm) and porosity (84.41

± 4 %) for 3MM chromatography paper. The estimated porosity value used in the Kozeny-Karman model for this work, closely matched the porosity of 83% reported for cellulose nanowebs (Callegari et al., 2011). Different studies described porosities ranging between 31-41% for foxing-free and foxed paper samples, a general 70% porosity for paper (Balakhnina et al., 2012), and 26.9, 68.2 and 63.7% for paper board, Whatman 1 filter paper and blotting paper, respectively (Songok and Toivakka, 2016).

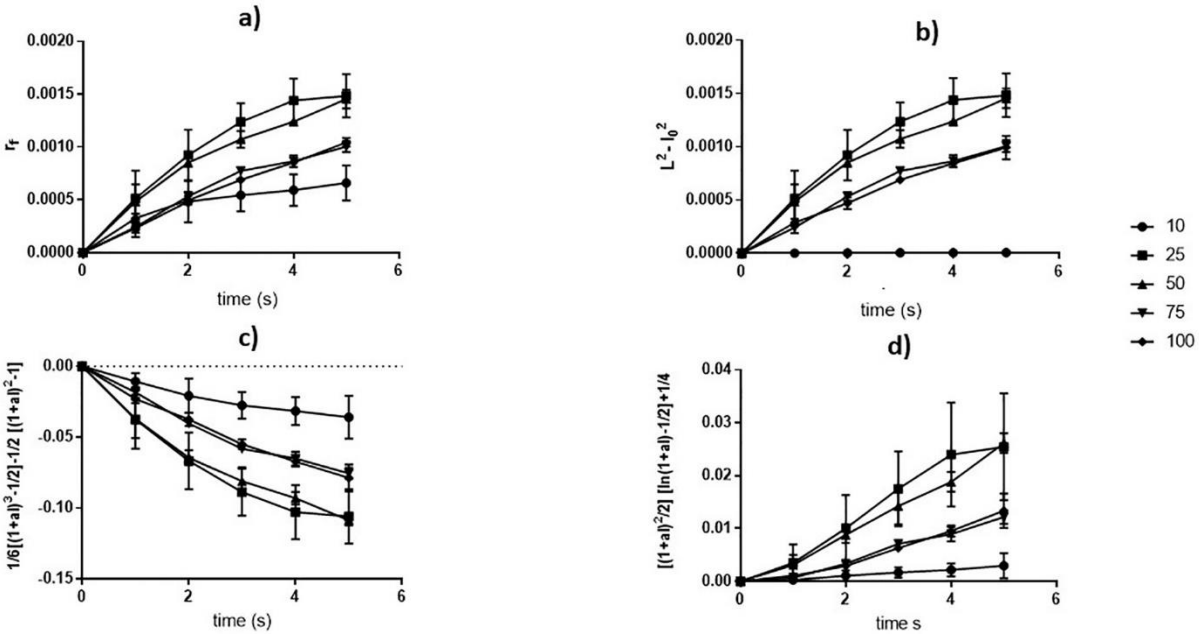

4

Figure 3.3 Variation with time of ink flow-related parameters used for the mathematical fitting of five ink models (% v/v as shown in labels) to: (**a**) hemispherical flow, (**b**) upward wicking, (**c**) cylindrical flow, and (**d**) spherical flow

Table 3.3 Theoretical permeability and mathematical fitting models for the radial penetration of the ink models in Whatman 3MM Chr paper

Ink Conc. (%, v/v)	Theoretical Permeability[I] Kozeny-Karman Model Variations			Radial immbibition[II] [Xiao et al., 2012]			Upward Wicking[III] [Callegari et al., 2011]			Cylindrical flow (Sector-shaped porous media)[IV] [Elizalde et al., 2015]			Spherical flow (Hemispherical porous media)[IV] [Elizalde et al., 2015]		
	$K = \mathrm{r}^2 \frac{\varepsilon}{4\mathrm{k}}$ [Callegari et al., 2011]	$K = \frac{dm^2}{36k} \frac{\varepsilon^3}{(1-\varepsilon)^2}$ [Xu and Yu, 2008]	$K = \frac{dm^2}{180} \frac{\varepsilon^3}{(1-\varepsilon)^2}$ [Xiao et al., 2012]	$r_f = A^{1/3} t^{1/3}$		$K = \frac{A^3 \mu}{3 p_c r_0}$	$L^2 - {l_0}^2 = \alpha^2 (t - t_0)$		$K = \frac{\alpha^2 \mu \varepsilon}{2 p_c}$	$\frac{(1+\mathrm{al})^2}{2}\left[\ln(1+\mathrm{al}) - \frac{1}{2}\right] + \frac{1}{4} = \mathrm{a}^2\mathrm{Dt}$		$K = \frac{h^2}{12}$	$\frac{1}{6}\left[(1+al)^3 - \frac{1}{2}\right] - \frac{1}{2}[(1+al)^2 - 1] = a^2 Dt$		$K = \frac{h^2}{12}$
	(m^2)	(m^2)	(m^2)	A ($m/s^{1/3}$)	r^2	*K* (m^2)	D (m^2/s)	r^2	*K* (m^2)	D (m^2/s)	r^2	*K* (m^2)	D (m^2/s)	r^2	*K* (m^2)
10	2.38×10^{-12}	3.10×10^{-11}	2.63×10^{-11}	3.66×10^{-4}	0.9110	2.17×10^{-16}	1.62×10^{-6}	0.9127	5.52×10^{-14}	2.74×10^{-8}	0.9167	1.22×10^{-18}	-3.94×10^{-7}	0.9072	2.52×10^{-16}
25	2.38×10^{-12}	3.10×10^{-11}	2.63×10^{-11}	5.79×10^{-4}	0.9525	9.99×10^{-16}	3.50×10^{-4}	0.8735	1.61×10^{-11}	2.55×10^{-7}	0.9593	1.92×10^{-16}	-1.19×10^{-6}	0.8875	4.19×10^{-15}
50	2.38×10^{-12}	3.10×10^{-11}	2.63×10^{-11}	7.48×10^{-4}	0.9117	3.07×10^{-15}	2.96×10^{-4}	0.9363	1.80×10^{-11}	2.19×10^{-7}	0.9715	2.51×10^{-16}	-1.08×10^{-6}	0.8835	6.12×10^{-15}
75	2.38×10^{-12}	3.10×10^{-11}	2.63×10^{-11}	5.07×10^{-4}	0.8531	1.40×10^{-15}	2.22×10^{-4}	0.9508	1.97×10^{-11}	9.98×10^{-8}	0.9456	1.20×10^{-16}	-7.25×10^{-7}	0.9494	5.91×10^{-15}
100	2.38×10^{-12}	3.10×10^{-11}	2.63×10^{-11}	5.03×10^{-4}	0.8715	2.49×10^{-15}	2.18×10^{-4}	0.9720	3.43×10^{-11}	9.33×10^{-8}	0.9331	3.02×10^{-16}	-6.60×10^{-7}	0.9706	1.51×10^{-14}

[I] *dm=diameter of pores (13.86±4.14 μm), ε=porosity (0.8441±0.04), k=4.246, r=$dm/2$;* [II] *$p_c = 2\gamma \cos\Theta / r$;* [III] *$p_c = 2\gamma / r$;* [IV] $h = (D^*6\mu)/(\Upsilon \cos\Theta)$

Based on the plotted results in Figures B5 and their mathematical expression for determining the k constant as a function of the porosity (Rahli et al., 1997), the Kozeny-Karman constant was calculated as 4.246, which was lower than the value of 5 utilized for spherical particles in Equation 3.10 with a corresponding permeability of $2.63x10^{-11}$ m^2 (Xiao et al., 2012). This constant (4.246) was substituted in Equations 3.11 and 3.12 (Callegari et al., 2011; Xu and Yu, 2008), which in combination with the pore radius/diameter and the porosity derived in permeabilities of $3.10x10^{-11}$ and $2.38x10^{-12}$ m^2, respectively. As demonstrated in Table 3.3 and Figure B6, the theoretical values from the Kozeny-Karman model in equations 3.10 and 3.11, yielded comparable magnitudes to the permeability expressed from the curve fitting of upward wicking (Equation 3.3) to experimental data. The Kozeny-Karman theoretical permeability showed an order of magnitude larger than previous values reported for cellulose acetate nanowebs ($k=1.1x10^{-13}$ m^2) (Callegari et al., 2011), yet closer to the reported $1.21x10^{-12}$ m^2 for a porous medium made of soda lime glass microspheres in a box (Xiao et al., 2012).

Despite the observed slight decrease on the diffusion coefficients, which, by formula, could be associated to viscosity increments and a decrease in the interfacial surface tension in a range from 25 to 100% (v/v) ink, the D value obtained from equation 3.3 could be considered as fairly constant parameter. Besides, the permeability results (K) results indicated a homogeneous permeability from 25 to 75% ink, with a good approximation to the theoretical calculation (Figure B6). It is worth mentioning that the diffusion coefficients shown in Figure 3.1a (inset) were similar in order of magnitude to some of the D values calculated from equation 3.4 (Table 3.3) for the cylindrical flow in porous media, which corresponds with the selected mathematical expression (Equation 3.9) also describing the diffusion process in a cylinder. Nevertheless, based on the permeability value approximation, as wicking was the most suitable model for explaining the radial movement of the ink models on 3MM chromatography paper, it can therefore be argued that within 5 seconds passive pumping occurred due to capillary forces leading the flow of the models into the porous system (Songok et al., 2016). In this regard, liquid spreading occurs as both a non-diffusive regime regulated by inertia, gravity and capillarity and a diffusive regime controlled by diffusion of the sample molecules (Kettle et al., 2010), hence both determinations of diffusion (section 3.1) and radial penetration are pertinent for the selected material.

3.3.3 Comparison of Lucas-Washburn equation with its modified expressions

Previous studies have utilized Lucas-Washburn equation for explaining the flow of liquids in porous supports such as paper, and it has been demonstrated that this equation alone was not suitable for describing the flow in porous media and membranes at microscale (Mahmud et al., 2018). By contrast with the Lucas-Washburn model, the modified equation has been suitable for describing the liquid flow in 3MM Chr paper strips, with a greater consistency after more wetting-drying cycles were repeated (Elizalde et al., 2016). However, as previously mentioned, Lucas-Washburn model establishes that large pores filled more rapidly than small pores, which has been contradicted as inertia and viscosity are suggested to play a main role during mathematical modelling (Aslannejad et al., 2018). As denoted in Section 3.3.2, the development of Lucas-Washburn equation into a model for upward wicking resulted in the high approximation of the permeability values to the theoretically determined ones by the Kozeny-Karman model. Data fitting ($t \leq 5s$) was carried out for Lucas-Washburn equations as a linear model (equations 3.13 and 3.14) to assess either their disadvantages or their adequate fitting to 3MM chromatography paper, as already discussed by some authors (Aslannejad et al., 2018; Elizalde et al., 2016). Equation fitting was performed as shown in the displayed curves in Figure 3.4a and 3.4b, from which the fitted D values were obtained and reported in Table 3.4. As shown in equation 3.13, when Poiseuille flow and the wetting force are considered, Lucas-Washburn equation denotes the imbibition length as a function of the square root of time in increments regulated by the surface tension, dynamic viscosity of the ink model, the contact angle between the ink and the paper matrix, along with the pore radius of the paper fibers expressed as capillary tubes (Liu et al., 2017). Despite the high determination coefficients (r^2), the fitted D values were not comparable with the expected calculations when integrating the physicochemical parameters of both the ink models and the paper matrix. On the other hand, spontaneous imbibition triggered by inertial effects can be described by modifying Lucas-Washburn model with Bosanquet model, in which the penetration length is directly proportional to the imbibition time (equation 3.14), mainly controlled by the density value (inertial regime) (Liu et al., 2017). Similar to the observed outcome in the first fitting, even when the fitted results resulted in high r^2 values, their magnitudes were not close enough to the expected numbers. Both results coincided with the reported behavior in wicking, where neither Lucas-Washburn nor Bosanquet adaptation were sufficient for its full characterization (Liu et al., 2017). In light of these pitfalls, another simplified model for explaining the kinetics of liquid capillary penetration

in porous media developed by Marmur (2003) was evaluated. In this case, a larger sample volume implied the integration of the gravitational effects on a transformed version of Lucas-Washburn by integrating Darcy's law rather than Poiseuille equation. Its nongravitational expression, similar to Equation 3.13 (l^2=D*t), was solved by applying the fitted D values and physicochemical parameters, to obtain C, S as well as the corresponding Kozeny-Karman permeability (Table 3.4), according to equations 3.15, 3.16 and 3.17.

$$D = \frac{2C\varepsilon\gamma cos\theta}{S(1-\varepsilon)\mu} \tag{3.15}$$

$$K = \frac{C}{S^2}\frac{\varepsilon^3}{(1-\varepsilon)^2} \tag{3.16}$$

$$S = \frac{2\varepsilon}{r(1-\varepsilon)} \tag{3.17}$$

Where ε is the porosity, θ=0, r is the pore radius, γ the interfacial surface tension, and μ is the dynamic viscosity. Regardless of the promising approach proposed by Marmur, as noted in Figure B7, the calculated permeability was not equivalent to any experimental or theoretical values previously determined in this work.

Therefore, apart from the diffusive behavior confirmed for a cylindric geometry, upward wicking can be considered for studying the radial imbibition in 3MM chromatography paper. In this regard, imbibition in cellulose fibers occurs by absorption in their internal cavities as well as the inter-fiber pores within the fibrous network (Chang et al., 2018). However, as previously studied (Elizalde et al., 2016), the application of Lucas-Washburn model is commonly accompanied by the assumption of pore saturation behind the ink front and pore uniformity (Chang et al., 2018), which in this work were accomplished by looking at the fibers as homogenous capillary tubes for a modified version of Lucas-Washburn for upward wicking, in which the large ink volume allowed the pore saturation behind the wetting front.

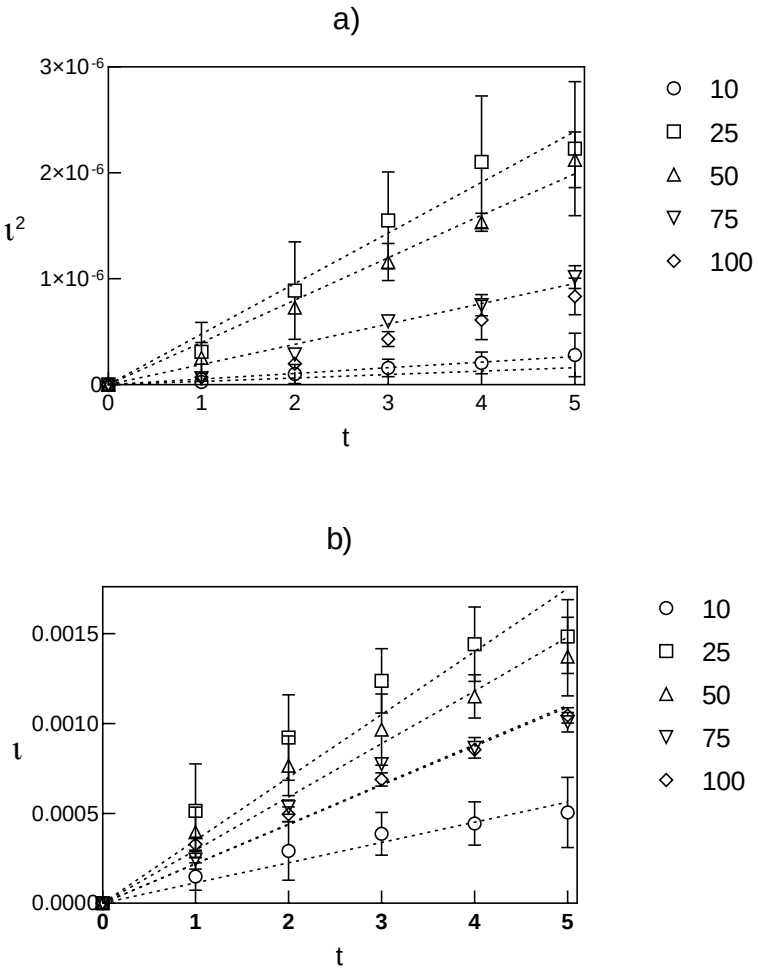

Figure 3.4 Theoretical (dashed lines) and experimental approximations (plotted points) of the imbibition length by Lucas-Washburn model after data fitting to (**a**) equation 3.13 and (**b**) equation 3.14. Each symbol corresponds to the indicated ink model.

Table 3.4 Comparison of the fitted and expected data for Lucas-Washburn equation as a linear expression

	$l^2 = D * t$				$l = D * t$		
Ink Concentration (%, v/v)	**D (m^2/s)**	**r^2**	**Expected[I]** $D = \frac{r\gamma\cos\theta}{2\mu}$	**Marmur Model[II]** $K = \frac{C}{S^2}\frac{\varepsilon^3}{(1-\varepsilon)^2}$	**D (m/s)**	**r^2**	**Expected[III]** $D = (\frac{2\gamma\cos\theta}{r\rho})^{0.5}$
10	$5.35x10^{-8}$	0.84	$1.48969x10^{-4}$	$1.82x10^{-15}$	$1.13x10^{-4}$	0.91	3.91
25	$4.78x10^{-7}$	0.96	$1.10211x10^{-4}$	$2.20x10^{-14}$	$3.50x10^{-4}$	0.87	3.68
50	$3.99x10^{-7}$	0.97	$8.31481x10^{-5}$	$2.43x10^{-14}$	$2.96x10^{-4}$	0.94	3.72
75	$1.91x10^{-7}$	0.95	$5.6538x10^{-5}$	$1.71x10^{-14}$	$2.21x10^{-4}$	0.95	3.68
100	$1.52x10^{-7}$	0.94	$3.22162x10^{-5}$	$2.39x10^{-14}$	$2.19x10^{-4}$	0.97	3.44

[I]γ*=interfacial surface tension, μ=dynamic viscosity,* θ=0; *[II] C=DS(1-ε)μ/2εγcosθ, S=2ε/r(1-ε), r=6.93 μm, ε= porosity (0.8441±0.04); [III] r=6.93 μm, ρ=density*

3.3 Conclusion

The equation for the diffusion in a cylinder, fitted in this work, allowed the description of all the data until a steady state was reached, with satisfactory correlation values. On the other hand, comparison of theoretically and experimentally based permeability values indicated that the model for upward wicking was the best descriptor for the capillary movement of a model substance in a porous, thin substrate. This study enabled the characterization of the performance of 3MM chromatography paper used as a biosensing support matrix (Mirón-Mérida et al., 2020), by using ink as a surrogate model of the flow of small molecules (e.g. mycotoxins) and colloidal particles. In keeping with previous studies at a small scale, the application of Lucas-Washburn equation for the description of the front distance at a microscale had null correlation to the experimental front radius, thus confirming the drawbacks from this general model. Nevertheless, our study enabled the characterization of both regimes, where a diffusive and non-diffusive spreading was simultaneously confirmed through the proximity of the experimental data with its theoretical determinations. We trust that a better understanding of the fundamental

phenomena governing the diffusion of small molecules in paper substrates will facilitate the development of biosensing applications.

Chapter 4
Genipin cross-linked chitosan for signal enhancement in the colorimetric detection of aflatoxin B1 on 3MM chromatography paper

Abstract

Detection of mycotoxins by conventional methods such as ELISA or LC-MS can be expensive and time-consuming. Therefore, paper-based biosensors can be effectively used for on-site analysis, due to their low cost and easy detection procedures. Nevertheless, even when the application of colorimetric methods on paper enhance the simplicity and affordability of multiple determinations, the signal intensity and final readout can be affected by a limited color uniformity. In this work, Ellman's method for the quantification of aflatoxin B1 was utilized as a model colorimetric assay on paper, in which the test zones were modified with chitosan-immobilized enzyme (AChE). A comparison of the crosslinking effect of genipin on two chitosans of varying molar mass and degree of acetylation, exhibited a greater signal enhancement from the sample with a higher degree of acetylation and molecular weight.

4.1 Introduction

From the different metabolites affecting crops and human health, mycotoxins represent a big concern when ingested through different food products. Among the diverse group of mycotoxins, aflatoxins have been widely studied and controlled as they represent a main issue in food safety and agricultural economy (Mangal et al., 2016). Aflatoxin B1, commonlly produced by *Aspergillus flavus* and *Aspergillus parasiticus,* has been widely explored because of its hight toxicity and carcinogenic effects (Nomura et al., 2018), caused by both long term and acute exposure (Roy et al., 2013). As an example of its impact, it has been estimated that aflatoxin contamination can cause a loss of 52.1 million to 1.68 billion dollars per year in the USA (Mitchell et al., 2016).

Conventional analysis methods for aflatoxin B1 include ELISA or LC-MS; however, despite their high sensitivity, they normally require long detection times and complicated procedures (Fu and Huang, 2008). One of the main advantages of paper-based biosensors is the flow of samples promoted by capillary forces, which can be

[3] Published as: Mirón-Mérida, V.A., Wu, M., Gong, Y.Y., Guo, Y., Holmes, M., Ettelaie, R. and Goycoolea, F.M. 2020. Genipin cross-linked chitosan for signal enhancement in the colorimetric detection of aflatoxin B1 on 3MM chromatography paper. *Sensing and Bio-Sensing Research*. **29**, p.100339.

translated to reductions on the analysis time and the application of specialized instruments (Yetisem and Akram, 2013). To control the diffusing behavior of varied solutions, a hydropobic detection area can be delimited on the paper-based biosensor through painted, stamped and printed wax (Cardoso et al., 2015; Lu et al., 2009; Yang et al., 2018) or laser cutting (Nie et al., 2013). Alternatively, permanent markers are a low cost and affordable option for designing hydrophobic barriers on paper (Gallibu et al., 2016).

Moreover, one of the main challenges to overcome in paper-based sensors is the enhancement of the final readout signal, which is commonly addressed by the use of nanomaterials, comprising metallic nanoparticles, fluorescent, electrochemical and colorimetric particles, along with the utilization of nucleic acids for signal amplification (Liu et al., 2014). Because of its simple operation, colorimetric assays are more feasible for remote applications and on-site determinations. However, color heterogeneity, mostly produced by a washing effect from the sample front, has been one of the main challenges in colorimetric techniques, which could be prevented with the impregnation of the detection zones with polymeric materials such as chitosan (Gabriel et al., 2016).

As a result of its biocompatibility, chitosan has been incorporated for antibody immobilization on paper-based electrodes and microfluidic paper-based analytical devices (μPADs) (Li et al., 2014; Wang et al., 2012), as well as enzyme immobilization on electrodes (Zhai et al., 2013). Nothwisthanding the successful application of polymeric compounds for signal improvement, its effectivenes might depend on the properties of the selected polymer, as well as the application method on the porous support. In this work, the application of two types of chitosan was evaluated on the colorimetric detection of aflatoxin B1 (AFB1) by Ellman's colorimetric method. The enzymatic immobilization with crosslinked chitosan demonstrated a better performance by the application of the sample with high molecular weight and a high degree of acetylation.

4.2 Materials and methods

4.2.1 Materials

Chromatography paper grade 3MM was acquired from Whatman™ (UK). Permanent marker (Medium Point 1.0mm Write-4-All Pen Permanent – Black) and stamp pad blue ink without oil were purchased from Stabilo (UK) and Pelikan® (Germany), respectively. Chitosan A (D.A. 17%, M.W. 28 000; HMC 70/5 batch number 212-170614-01) was purchased from Heppe Medical Chitosan GmbH (Hale, Germany), and Chitosan B (D.A.

28.8%, M.W. 1,460,000; batch number: SPchan-08127) was obtained in our laboratory from previously isolated squid pen β-chitin. Aflatoxin B1 from *Aspergillus flavus* (A6636), ochratoxin A (32937), fumonisin B1 (F1147), acetylcholinesterase from electrophorus electricus (electric eel) (AChE, C2888), and acetylthiocholine iodide (ATCh, A5751) were obtained from Sigma-Aldrich (St. Louis, MO, USA). Dithiobis (2-nitrobenzoic acid) (DTNB, 22582) was purchased from Thermo Fisher Scientific (USA). Tris HCl Buffer (UltraPure™ 1M pH 7.5, 15567027) was obtained from Invitrogen™(USA). Corn was brought from local Sainsbury's supermarket. Methanol (10675112) was obtained from Fisher Scientific (UK).

4.2.2 Methods

4.2.2.1 Construction of μPADs

Cellulose 3MM chromatography paper previously characterised in its imbibition and diffusion properties using ink models (Mirón-Mérida et al., 2021), was cut into squares (4.5 cm × 4.5 cm), and the hydrophobic boundaries were drawn with a permanent marker using either circular spots or a 'flower' shape arrangement with a 3-D printed template, as shown in Fig C1.

4.2.2.2 Preparation of solutions

Solutions containing 0.2% of either chitosan A or B powders were prepared by overnight stirring in 85 mM NaCl solution, stoichiometricaly acidified with acetic acid. Genipin was dissolved in 100% ethanol. AChE was dissolved in Tris HCl Buffer (pH 7.5 20 mM). DTNB and ATCh were dissolved in Tris HCl Buffer (pH 7.5 100 mM). Standards of aflatoxin B1 were dissolved in Tris HCl Buffer (pH 7.5 50 mM). Unless mentioned, other solutions were dissolved in Milli-Q water. Note: After preparation, DTNB solution should be immediately put on ice and store in the dark.

4.2.2.3 Performance of cross-linked chitosan on μPADs

A visual assessment on the effect of cross-linked chitosan was conducted under the presence of chitosan (0.2% w/w), blue ink, and genipin (59.25 μM), combined at percentage ratios (by vol.) of 92/2.3/5.7 for chitosan A, and 97.3/2.5/0.2 for chitosan B. To this purpose, different volumes (0-6 μL) of each mixture were applied on half of the detection areas (flower-shaped μPAD), while the other areas were added with a mixture of chitosan solution (0.2% w/w), ink, and water, at the same ratios. After the application step, the paper μPADs were incubated at either 25 or 37 °C for 1 h, followed by image scanning for subsequent visual comparison.

4.2.2.4 Color intensity of µPADs modified with cross-linked chitosan

Mixtures were prepared and applied as previously specified in section 4.2.2.3, followed by incubation at 25 °C for 1 h. The incubated µPADs were scanned and the color intensity was obtained in Image J for the 6 µL samples.

4.2.2.5 Detection zones preparation with cross-linked chitosan immobilized AChE

AChE (final concentration 50 U/mL) was mixed with 398 µL of a 0.2% chitosan solution (w/w) for 3 minutes (final volume 500 µL), followed by the addition of 16.2 µL and 13.8 µL genipin solution (59.25 mM) for Chitosan A and B respectively. After 3 minutes, the detection zones were modified with 1.6 µL of chitosan/genipin/AChE mixture or a 50 U/mL AChE solution. The treated papers were stored for 1.5 h at 25 °C, to allow the cross-linking reaction to proceed.

4.2.2.6 Colorimetric detection on µPADs (8 circular spots)

For the colorimetric assay, 3.2 µL of aflatoxin B1 solution at different concentrations (0 to 100 µM) and 1.6 µL of DTNB (final concentration: 500 µM) were subsequently added to each testing spot. After incubating for 3 min, 1.6 µL of ATCh solution (final concentration: 300 µM) was added and incubated for 5 min. All paper biosensors were scanned for further analysis in image J.

4.2.2.7 Colorimetric detection of standard solutions (‘flower’ shape µPAD)

For the ‘flower’ shaped assay, 2.5 µL of AChE or AChE/Genipin/Chitosan, were added to the edges of the µPAD, and the crosslinking reaction was carried at 25 °C for 2 h. Then 40 µL of aflatoxin B1 solution with different concentration (0 to 60 µM) were added at the center (loading zone), followed by 20 µL of DTNB solution. After 3-min incubation, 20 µL of ATCh solution was also applied at the center, and incubated for 5 min. All the paper biosensors were scanned for further analysis in image J.

4.2.2.8 Extraction and detection of aflatoxin B1 in corn samples

Corn (7 g) was spiked with 100 µL of aflatoxin B1 solution (161 µM), by mixing for 3 min in a centrifuge tube. The spiked sample extracted with 320 µL of 5% methanol (manual shaking). The extract achieved an expected concentration equivalent to 50 µM AFB1. The detection procedure was performed as stated in section 4.2.2.7, on a ‘flower’ shape µPAD.

4.2.2.9 Measurement of color intensity of paper biosensors in ImageJ

The color intensity of scanned detection zones was obtained in ImageJ software, where the image was inverted so the white color was transformed to black for the lowest color intensity (0). Correspondingly, the black color was inverted to white to observe the highest color intensity (256) (Hossain et al., 2009).

4.2.2.10 Degree of inhibition

The degree of inhibition from AFB1 was calculated with a modified version of a reported determination (Amine et al., 2016), in which the intensity of color was integrated to the calculation.

$$\%I = \frac{(IC0 - ICi)}{IC0} \; X \; 100 \qquad (4.1)$$

Where, *%I* is the degree of inhibition, *IC0* is the color intensity without aflatoxin B1, and *ICi* is the color intensity with aflatoxin B1.

4.3 Results and discussion

4.3.1 Performance of cross-linked chitosan on µPADs

Representative images of the scanned µPADs after incubation are displayed in Fig 4.1. As it can be noted, both chitosan A and B exhibited a homogenous surface when the sample was fixed through crosslinking with genipin, compared to the treated areas without cross-linker. Chitosan (polycationic) and cellulose (anionic) possess structural similarities, which allow binding between amino (chitosan) and aldehyde/carboxyl groups (paper), resulting in electrostatic adsorption (Da Róz et al., 2010; Vosmanská et al., 2015). Chitosan not only supports electrostatic interactions by protonation of its primary amine groups, but their acetyl functions also favor hydrophobic interactions while hydrogen bonds can also be formed via hydroxyl groups (Haugstad et al., 2015). Nonetheless, the sole application of ink by mixing with chitosan and water led to sample accumulation on specific areas of the test zone; thus suggesting that this coating method is not the most suitable for immobilization on 3MM chromatography paper, unlike its adequate deposition behavior seen on metallic electrodes (Zhai et al., 2013).

Based on Fig 4.1, it can be observed that, at both incubation temperatures, chitosan A had a more uniformly colored surface than does chitosan B. Such behavior could be

explained as a result of the higher degree of acetylation of chitosan B, which has been correlated with greater hydrophobicity, rigidity and steric effects (Bangyekan et al., 2006). The adsorption of chitosan on cellulose has been found to improve at pH values below its solubility limit (pH=6.0 ± 0.1 (Rinaudc et al., 1999), in which more electrostatic interactions will be promoted (Myllytie et al., 2009). In this case, the pH values for the solutions of chitosan A and B were 5.03 and 5.44 respectively, which also corresponds to a more consistent surface on the test zones treated with chitosan A. It is worth mentioning that, as incubation at 37^{o} C resulted in more heterogeneity, all the subsequent experiments were carried at 25 ^{o}C to avoid water evaporation promoting drier test zones.

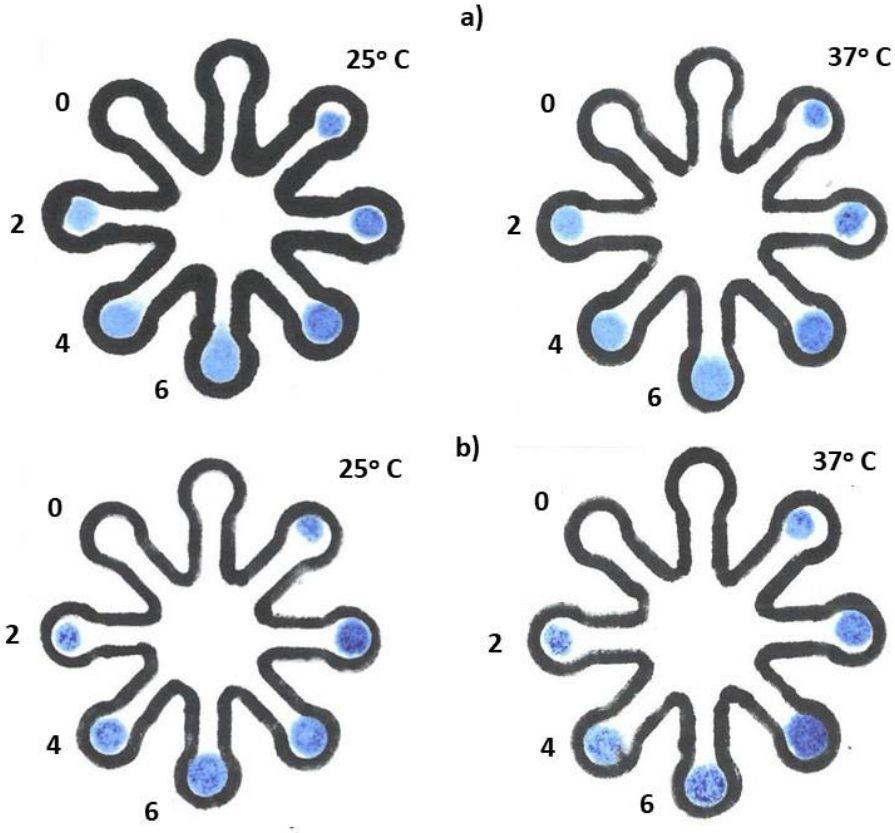

Figure 4.1 Symmetrical application of ink on the detection zones, with cross-linked (numbered areas) and mixed (no numbers) solutions of chitosan A (**a**) and chitosan B (**b**) at two incubation temperatures. Each number refers to the applied volume (µL) of sample

As previously mentioned, cross-linked chitosan conferred a better performance on the µPADs. Cross-linking of chitosan has been previously carried with glutaraldehyde, for the immobilization of capture antibodies on Whatman #1 paper (Wang et al., 2012), however,

genipin has been proposed as natural alternative for the formation of the chitosan network at room temperature, due to its lower cytotoxicity (Mi et al., 2000). Higher color intensities were achieved with cross-linked chitosan, as denoted in Fig 4.2. When genipin was not included, the differences between both types of chitosan was completely notorious, as chitosan B produced a greater intensity value. Such divergence relied on the image analysis method, in which an average of all the intensities was calculated for a region of interest, with greater measured intensities for a heterogeneous test zone. Yet the same color intensity was achieved when both chitosan were genipin cross-linked, which indicated a reduction on the heterogeneity of the testing areas (Fig 4.2).

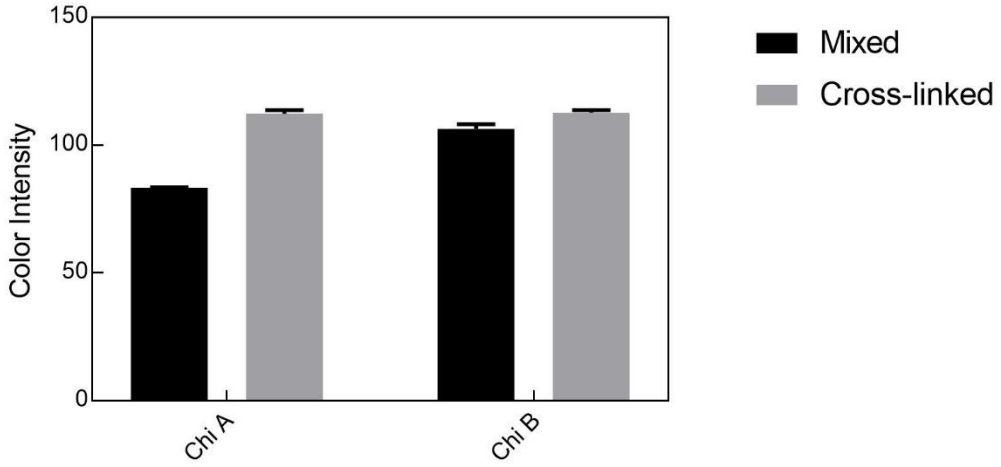

Figure 4.2 Color intensity of the applied ink in chitosan and water (mixed) and chitosan with genipin (cross-linked) after incubation (25°C, 1 h, 6µL, n=3)

The crosslinking mechanism of chitosan and genipin is known to occur in two stages. An initial fast reaction develops between the C3 carbon atom in genipin and a primary amine group from chitosan, resulting in a heterocyclic compound. A second, slower reaction, takes place by a nucleophilic replacement of the ester group in genipin and the formation of a secondary amide bond with chitosan (Butler et al., 2003). As the produced network presented a better performance on µPADs, the consecutive colorimetric assays were carried through enzyme immobilization with cross-linked chitosan at 25º C.

4.3.2 Performance of chitosan on the colorimetric detection of AFB1 on µPADs

The colorimetric determination of aflatoxin B1 was based on Elman's assay (Ellman et al., 1961), in which AFB1 acts as an inhibitor of AChE (see Supplementary Information).

This effect has been studied on gelatin-immobilized AChE, where neither the immobilization step nor the presence of up to 60% (v/v) methanol generated a negative effect on the enzymatic activity (Pohanka, 2013). Preliminary bulk assays confirmed no interference by both chitosan solutions with the final signal, at the concentration of AChE utilized in this work (Fig C3a); as well as a significant specificity ($p < 0.05$) of this colorimetric assay to AFB1, when compared with FB1 and ochratoxin A (Fig C3b). This result confirmed the feasibility of performing the assays in real food sampes (e.g. corn) without the interference of some other maize-related mycotoxins.

The percentages of inhibition displayed in Fig 4.3a, were calculated based on the color intensities achieved on each treated test zone at different concentrations of AFB1 (Fig C4). Unlike the invariable detection with free enzyme (no chitosan), the chitosan treated zones displayed an increasing inhibition rate when the concentration of AFB1 was raised. The greatest degrees of inhibition were determined as 31.27± 5.96% (chitosan A) and 41.13± 0.87% (chitosan B) upon addition of 60 and 100 µM AFB1, respectively. Thus, chitosan B had the most differentiated effect, as noted in Figure 4.3a by the highest gradient in percentage of inhibition. A more intense signal was also visually confirmed on AChE immobilized with cross-linked chitosan (Fig C5), which can be neglected as an inhibitory effect from chitosan due to its null intervention in the reaction mechanism (Fig C3a). Furthermore, the interaction of chitosan with cellulose promotes a convenient condition for electron transfer in the enzymatic reaction (Gabriel et al., 2016).

The SEM images (Fig 4.3b) confirmed a dry, heterogeneous profile in the absence of chitosan, while the addition of the cross-linked polymer resulted in a smooth, homogenous surface, where no particles were observed (Fig 4.3c and d). This film-like property of chitosan A (pH=5.03, $\boldsymbol{\gamma}$**=**0.07228 N/m, **µ** =0.0015 Pa·s) and chitosan B (pH=5.44, $\boldsymbol{\gamma}$**=**0.07306 N/m, **µ** =0.01Pa·s), could be related to its physical attributes, and possibly due to the crosslinking effect of genipin on preventing the re-crystallization of chitosan acetate.

Despite the reported slight inhibitory effect of genipin (18.18%) on the activity of AChE (Nam and Lee, 2013), a constant concentration of this cross-linking agent still revealed a distinctive color development at different AFB1 concentrations, as indicated in Fig C6. The equations describing the above-mentioned curves (Fig C6) are expressed in Table 4.1, as it can be recognized a linear function described the addition of AFB1 on the test zones with immobilized chitosan. In contrast with the assays with free enzyme, the addition of chitosan intensified the slope of the plotted curves, which was also supported by the high correlation coefficients (r^2), observed especially for chitosan B (0.9911).

Based on the assays with ink, the SEM images, the linearity of the resulting color intensities, and the well-defined effect of AFB1, it can be argued that cross-linked chitosan might result in an enhancement of the enzymatic reaction rate, thus resulting in greater color intensity and overall readout resolution of the assay. Similar to non-cross-linked chitosan, genipin cross-linked chitosan has been disclosed as a cytocompatible and biocompatible material, when compared with glutaraldehyde cross-linked chitosan (Lai et al., 2010).

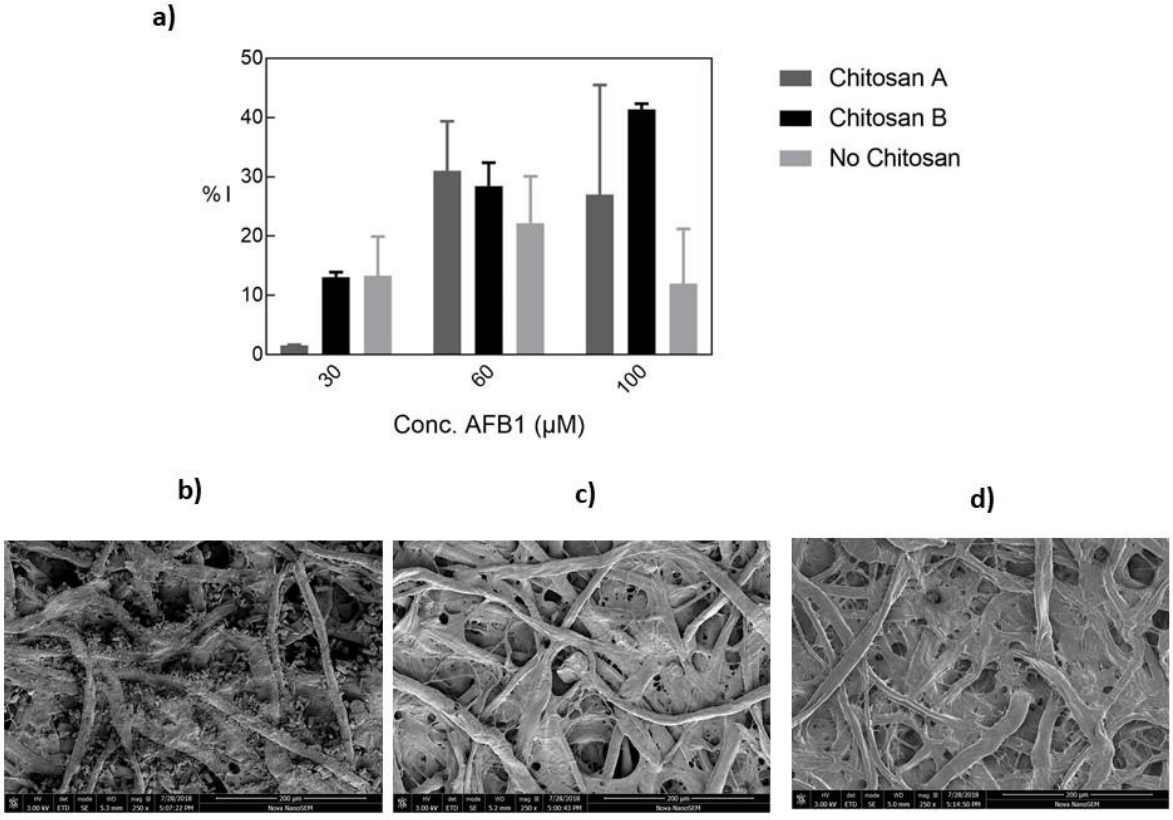

Figure 4.3 (**a**) Percentage of inhibition of AFB1 on the activity of free (no chitosan) and immobilized AChE (50 U/mL) with chitosan A and B. SEM images (200 µm) of the detection zones after the colorimetric determination with (**b**) free, (**c**) chitosan A and (**d**) chitosan B immobilized AChE (50 U/mL) at 25 ºC (reaction time: 8 min; n=3). The displayed “No chitosan” values are an average from the corresponding samples in Fig C4a and C4b

Table 4.1 Mathematical expression of the color intensity as a function of the concentration of AFB1

Sample	Equation*	r^2
No chitosan	CI= -0.0706 [AFB1] +55.493	0.4146
Chitosan A	CI= -0.1946 [AFB1] +58.617	0.7302
Chitosan B	CI= -0.3621 [AFB1] +85.624	0.9911

*CI=Color Intensity, [AFB1]=Concentration of AFB1 (µM). Data based on Fig C6.

In addition, genipin crosslinking is also expected to prevent the dissolution of chitosan acetate upon wetting of the test zone. When testing spiked corn samples, a yellow color was observed on the loading zone, which could be identified as zeaxanthin, the principal pigment of yellow corn (Sajilata et al., 2008). Yet, 3MM Chr paper allowed a separation between pigments and AFB1, as the latest metabolite moved along the channel as part of the sample run (Fig C7). As a consequence, the intensities reported in Fig 4.4 indicated the positive effect of the immobilization step on the accomplishment of similar values to their corresponding standard solutions.

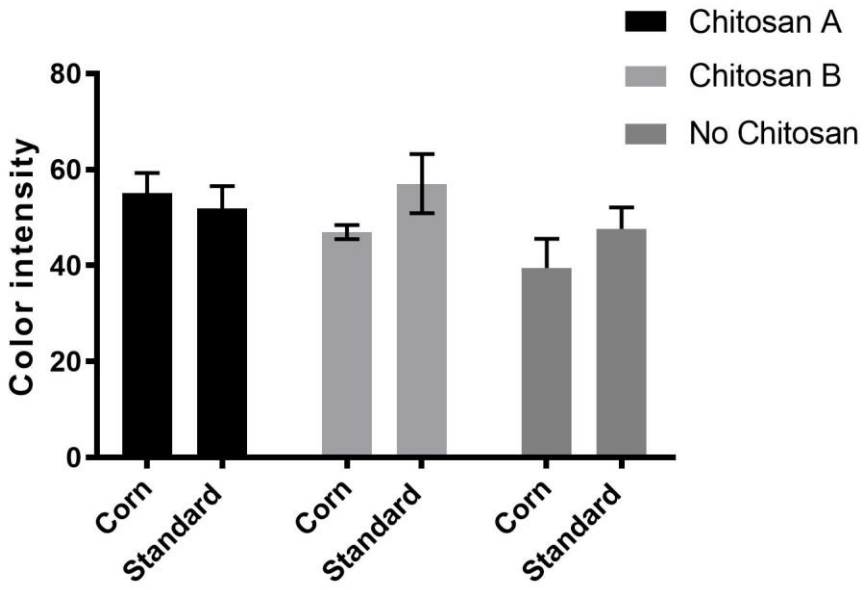

Figure 4.4 Comparison between the signals produced by corn samples and AFB1 standards (50 µM) inhibiting free and immobilized AChE with a) chitosan A and b) chitosan B (25 ºC, 8 min reaction time and 50 U/mL AChE, n=3)

4.4 Conclusion

A comparison between cross-linked and non-cross-linked chitosan was addressed on 3MM chromatography paper by ink immobilization. The color intensities and visual inspection depicted more homogeneity on the test zones with cross-linked chitosan.

Cross-linked chitosan also helped immobilize AChE, which simultaneously enhanced the color intensity of the test signal, as confirmed by the high resolution at different concentrations of AFB1 and the film formation on the detection zones. Chitosan with a high molecular weight and a higher degree of acetylation exhibited a better performance for the achievement of a homogeneous colorimetric reaction with a linear dependence to the concentration of AFB1. As the colorimetric method utilized in this work was merely a model technique for understanding the performance of chitosan on the immobilization of AChE for the quantification of AFB1, a validation step was omitted for this biosensing technique.

Chapter 5
Aptamer–target–gold nanoparticle conjugates for the quantification of fumonisin B1

Abstract

Fumonisin B1 (FB1), a mycotoxin classified as group 2B hazard, is of high importance due to its abundance and occurrence in varied crops. Conventional methods for detection are sensitive and selective; however, they also convey disadvantages such as long assay times, expensive equipment and instrumentation, complex procedures, sample pretreatment and unfeasibility for on-site analysis. Therefore, there is a need for quick, simple and affordable quantification methods. On that note, aptamers (ssDNA) are a good alternative for designing specific and sensitive biosensing techniques. In this work, the assessment of the performance of two aptamers (40 and 96 nt) on the colorimetric quantification of FB1 was determined by conducting an aptamer–target incubation step, followed by the addition of gold nanoparticles (AuNPs) and NaCl. Although $MgCl_2$ and Tris-HCl were, respectively, essential for aptamer 96 and 40 nt, the latter was not specific for FB1. Alternatively, the formation of Aptamer (96 nt)–FB1–AuNP conjugates in $MgCl_2$ exhibited stabilization to NaCl-induced aggregation at increasing FB1 concentrations. The application of asymmetric flow field-flow fractionation (AF4) allowed their size separation and characterization by a multidetection system (UV/Vis, MALS and DLS online), with a reduction in the limit of detection from 0.002 µg/mL to 56 fg/mL.

5.1 Introduction

Exposure to FB1 occurs not only in African (Wangia et al., 2019) and Latin-American (Wall-Martínez et al., 2019b) countries but also in several regions of Asia (Hu et al., 2019) and Europe (Martins et al., 2019). For that reason, monitoring and controlling contamination of food commodities with fumonisins becomes a highly pressing matter for protecting human health worldwide. Fumosinins are a group of toxins generated by diverse fungi including *Fusarium verticillioides* (Abbas et al., 1992), *Alternaria alternata* (Abbas et al., 1996), *Aspergillus niger* (Mansson et al., 2010), *Tolypocladium cylindrosporum*, *Tolypocladium geodes* and *Tolypocladium inflatum* (Mogensen et al., 2011). Their chemical structure commonly consists of alkylamines, whose substitution of up to seven side chains allows the formation of different analogs, group B being the most

[4] Published as : Mirón-Mérida, V.A., González-Espinosa, Y., Collado-González, M., Gong, Y.Y., Guo, Y. and Goycoolea, F.M. 2021. Aptamer–Target–Gold Nanoparticle Conjugates for the Quantification of Fumonisin B1. *Biosensors*. **11**(1), p.18.

common in nature (Rheeder et al., 2002). From the latter, Fumonisin B1($C_{34}H_{59}NO_{15}$) has been reported to be a latent risk in several food products, such as cereals and beverages.

Classified as group 2B hazard, FB1 (Figure D1) has a possible carcinogenic effect on human health (Ostry et al., 2017), as its toxicity has been related to the disruption of sphingolipid metabolism, oxidative stress and epigenetic changes (Liu et al., 2019), along with the interruption of barrier functions (Yuan et al., 2019). Nevertheless, current conventional methods for mycotoxin detection, including enzyme-linked immunosorbent assay (ELISA), high-performance liquid chromatography with fluorescence detection (HPLC-FLD) and liquid chromatography-mass spectrometry (LC-MS), are costly, time consuming, and difficult to be applied on site and require experienced users (Lee et al., 2013). Therefore, there is a need for developing sensitive, yet quick and affordable methods for quantifying mycotoxins.

Biosensors are a suitable alternative to conventional methods by means of their general mechanism, where any target detection is carried out by a biological receptor and transduced into a signal (optical, electrochemical, mechanical, etc.). From the different biorecognition receptors (enzymes, antibodies, nuclei acids, cells, etc.), the performance of aptamers has been exceptional (Ahmed et al., 2017). Aptamers are single-stranded DNA or RNA molecules with high molecular recognition toward different types of molecules, distinct binding affinities, target selectivity and high capability to discriminate slight chiral differences (McKeague et al., 2010). Their selection technique called Systematic Evolution of Ligands by Exponential enrichment (SELEX), involves incubating a DNA library with the specific target or other relevant molecules, followed by the amplification of potential binders after several selection and discrimination rounds (Chen et al., 2014). In addition to their good performance, compared to antibodies, aptamers are easy to modify, as well as reproducible by solid-phase chemical synthesis, which represents a reduction in cost and time. To date, two aptamers specific for FB1 composed of 96 and 80 nucleotides (nt) have been selected by SELEX and used in up to 31 different biosensing approaches (Chen et al., 2014; McKeague et al., 2010), through aptamer modifications, hybridization with complementary strands or reduction in the sequence length (Figure D2). Those applications have involved optical, chemiluminescence, electrochemical, surface-enhanced Raman spectroscopy (SERS), mass spectrometry (MS) and bending related signals, where the most sensitive methods were correlated with fluorescent and SERS read outs (Figure D2).

A decisive step during the design of aptamer-based biosensors is the selection of the target-aptamer incubation conditions (buffer, time and temperature). In such approaches,

Tris, Tris-HCl, phosphate buffer, NaCl, $CaCl_2$, KCl and $MgCl_2$ are normally added during the binding stage, which normally results in a 3D conformational change of aptamers upon binding (Chen et al., 2014). Apart from the sensitive response obtained through aptamer dehybridization from complementary sequences at specific binding sites, mycotoxin detection has been carried out by immobilization of aptamers onto the surface of different platforms such as graphene and gold nanoparticles. In this regard, gold nanoparticles (AuNPs) are suitable for developing colorimetric methods, which are still relevant due to its feasible application for on-site analysis and reduction in engineering costs. The thermodynamic instability of colloidal gold suspensions potentiates their flocculation. This aggregation, however, can be prevented when gold nanoparticles are coated with negatively charged citrate molecules, or at low ionic strength and pH above the isoelectric point of citrate. Particle aggregation in this case occurs when an aqueous dispersant medium containing the nanoparticles has a high enough ionic strength to screen their electrostatic repulsion charges caused by their citrate stabilization (e.g., salt-induced aggregation) (Pamies et al., 2014). AuNPs are commonly analyzed in terms of their absorbance by using surface plasmon resonance related to their color modification (red to blue) by aggregation with cationic compounds, changes in the suspension pH and ionic strength (Li et al., 2016; Pandey et al., 2016). The SPR spectra of AuNPs are closely related to their particle size, which plays an important role in their absorption, scattering and excitation behavior (Amendola et al., 2017). Adsorption on AuNPs can be promoted through aptamer (ssDNA) uncoiling, whose bases are exposed to the negative surface of AuNPs, thus enabling their interaction by van der Waals forces (Yue et al., 2014).

In addition to the spectrophotometric analysis of AuNPs, particle size characterization can be achieved by more robust methods capable of probing the interaction between aptamers and AuNPs in the presence of a target molecule. For instance, asymmetric flow field-flow fractionation (AF4) is a technique that allows the separation of particles and aggregates in a size range from 1 nm to 1 µm, based on their diffusion coefficient in aqueous media. This analytical method offers several advantages, such as minimal sample alteration and efficient quantitative analysis of the physico-chemical parameters of the study materials such as their concentration and particle size by multidetection (UV/Vis, fluorescence, multiangle light scattering (MALS) and differential refractive index (dRI)) (Hagendorfer et al., 2011). The general AF4 operation principle is based on the generation of a parabolic laminar flow profile within the separation channel transporting the particles. The action of a perpendicular flow, known as cross flow (CF) across the semipermeable membrane, drives separation according to the diffusion coefficient of

particles. Some AF4 methods have been developed for studying the properties of AuNPs as either standard samples (Hagendorfer et al., 2011) or additives (Mudalige et al., 2018), as well as to study the target-binding relation between aptamers and their specific targeted proteins (Schachermeyer et al., 2013).

In this paper, we developed a bulk colorimetric method to examine the efficiency of two aptamers, namely, the first 96 nt sequence and a shortened version (40 nt) from the 80 nt aptamer, to quantify FB1 in different binding buffers and assessed its potential as a robust biosensing method. The general procedure involved incubating FB1 with aptamers, followed by another incubation stage with AuNPs, addition of NaCl and subsequent analysis by UV/Vis spectroscopy (λ = 400–800 nm). In addition, the characterization of the formation of Aptamer (96 nt)–FB1–AuNP conjugates was carried out by multidetection AF4, thus uncovering a promising application on the sensitive detection of this mycotoxin.

5.2 Materials and methods

5.2.1 Materials

Fumonisin B1 (FB1, CAT FB1147), aflatoxin B1(AFB1, CAT A6636) from *Aspergillus flavus*, ochratoxin A (OTA, CAT 32937) and sodium azide (CAT 71290) were obtained from Sigma-Aldrich (St. Louis, MO, USA). Tris-HCl Buffer (UltraPure™ 1M pH 7.5, CAT 15567027) was acquired from Invitrogen™(USA). Sodium chloride (CAT BP358-1), methanol (CAT A454-1) and phosphate buffered saline (PBS, pH 7.4, CAT BP2944-100) tablets were purchased from Fisher Scientific (Loughborough, UK). Magnesium chloride (CAT J364) and potassium chloride (CAT 1.04936) were both bought from VWR (Lutterworth, UK) and BioChemica (Barcelona, Spain), respectively. Novachem surfactant 100 (C-SUR-100, lot 162167) was purchased from Postnova Analytics (Landsberg am Lech, Germany). All experiments were conducted using Mili-Q water (MQ water). Synthesized, dried and HPLC-purified aptamers specific for FB1 (Aptamer 40 nt: 5′-C GAT CTG GAT ATT ATT TTT GAT ACC CCT TTG GGG AGA CAT- 3′ and Aptamer 96 nt: 5′-ATA CCA GCT TAT TCA ATT AAT CGC ATT ACC TTA TAC CAG CTT ATT CAA TTA CGT CTG CAC ATA CCA GCT TAT TCA ATT AGA TAG TAA GTG CAA TCT-3′) were purchased from Biomers.net (Germany) and diluted in sterile Milli-Q water.

5.2.2 Synthesis and characterization of gold nanoparticles (AuNP)

Two stock solutions (stock 1 and 2) of gold nanoparticles (AuNP) were synthesized by citrated reduction (Derbyshire et al., 2012). The concentration of AuNP was determined according to the Lambert–Beer equation, Equation (5.1), based on a wavelength scan (400–800 nm) performed using a Specord 210 Plus Analytic Jena spectrophotometer (Jena, Germany).

$$A = C * \varepsilon * L \quad (5.1)$$

where A is the absorbance, C the molar concentration, ε is the molar extinction coefficient (3.67×10^8 $M^{-1}cm^{-1}$-specific for AuNP with a surface plasmon resonance (SPR) peak wavelength of 520 nm) and L the path length (1 cm).

Particle size distribution (nm) of AuNPs was determined in triplicate by dynamic light scattering with non-invasive back scattering (DLS-NIBS) at a measurement angle of 173° at 25 °C, in a Malvern Zetasizer NanoZS (Malvern Instruments, UK) fitted with a red laser (λ = 632.8 nm), and software in automatic mode.

5.2.3 Adsorption of aptamers on gold nanoparticles (AuNP)

To perform the adsorption of aptamers on AuNPs, first, AuNPs (30 µL) were separately mixed with different concentrations of NaCl (1:1 *v*/*v*) to find their SPR peak shifting point (aggregation point). Then, different aptamer:AuNP mol ratios were mixed and incubated for 90 min at room temperature (RT~ 22 °C), from which 30 µL was mixed in a 96-well microplate with the selected NaCl molar concentration (1:1 *v*/*v*). Measurements to find the point of aptamer adsorption (until non-aggregation was observed) were conducted through a 400–800 nm scan using a Tecan Spark 10 M plate reader (Tecan, Reading, UK).

5.2.4 Assays with aptamer 40 nt

5.2.4.1 Effect of Tris-HCl, PBS, and its combination on the binding effect of aptamer 40 nt

Three concentrations of FB1 (0, 10 and 100 µg/mL), including two high values to secure and observable effect, were dissolved in either Tris-HCl buffer 31.1 mM, PBS 12.79 mM (NaCl equivalents) or a combination of both, and were then incubated with aptamer 40 nt in a vial (calculated to a final volume of 5 µL per microplate-well), for 60 min at 37 °C. After this step, a volume of AuNPs (stock 1) necessary to reach the selected aptamer:AuNP molar ratio (117:1) was added and incubated at 37 °C for 2 h. From this solution, 30 µL were placed on a microplate well and combined with NaCl 0.4 M (1:1 v:v)

and subsequently subjected to a wavelength scan (λ = 400–800 nm) on a Tecan microplate reader. Based on the wavelength scan characterization, the absorbance ratio at 650 and 520 nm ($A_{650/520}$) was then calculated. Although some approaches utilized the absorbance value at 450 nm for the calculation of a similar ratio, the obtained SPR peak complied with the expected values between 520 and 580 nm (Haiss et al., 2007), hence the selected ratio ($A_{650/520}$) was specific for the AuNPs utilized in this work. The general procedure applied as a biosensing technique in this work is outlined in Figure 5.1a.

5.2.4.2 Effect of different buffers on the performance of aptamer 40 nt

An increasing concentration of FB1 dissolved in different binding buffers was combined with aptamer 40 nt (final volume: 5 µL per well), for 60 min at 37 °C. The addition of AuNPs (stock 1) to achieve a molar ratio of 117:1 was conducted according to Table 5.1. The $A_{650/520}$ ratio values after the addition of NaCl 0.4 M (1:1 v:v) were used to calculate the limit of detection (LOD) for each assay, according to Equation (5.2) (Quesada-González et a., 2019).

$$LOD = Blank + 3\sigma_{blank} \quad (5.1)$$

where the Blank accounts for the signal exhibited by the blank (sample with no FB1), and $3\sigma_{blank}$ is three times the standard deviation of the blank. The proposed mechanism for aptamer 40 nt is displayed in Figure 5.1b.

5.2.4.3 Reduction in the aptamer: AuNP molar ratio

A folding step was integrated by placing a vial containing Aptamer 40 nt (dissolved in the binding buffer for this section), in a water bath at 94 °C for 5 min, followed by 15 min on ice. FB1 was also dissolved in binding buffer (Tris-HCl buffer 15 mM, NaCl 85 mM, $CaCl_2$ 1mM, KCl 5mM and $MgCl_2$ 2mM), and then incorporated (final volume: 5 µL per well) and incubated for 60 min at RT. Stock 1 of AuNPs was added to achieve the required aptamer:AuNPs molar ratio (47:1 to 117:1) and left in a shaking incubator (Titramax 1000, Heidolph, UK) at 300 RPM for another 60 min at RT, followed by the addition of NaCl 0.4 M (1:1 ratio v:v) and calculation of its $A_{650/520}$ ratio and LODs.

5.2.4.4 Specificity of aptamer 40 nt

The specificity of aptamer 40 nt was tested on the addition of FB1, OTA or AFB1 (13.8 µM), with an aptamer:AuNPs molar ratio of 117:1 in Tris-HCl 14.06 mM with 1 h binding at 37 °C and 105 min of AuNP adsorption at RT. In addition, an aptamer:AuNPs ratio of 47:1 in buffer from Section 5.2.4.3 (folding included) was used for testing the specificity against OTA after 1 h binding (RT) and 1 h adsorption (RT).

5.2.5 Assays with aptamer 96 nt

5.2.5.1 Adsorption of aptamer 96 nt on AuNPs

Aptamer 96 nt was dissolved in $MgCl_2$ 1 mM and folded through a 5 min incubation in a water bath (94 °C), followed by 15 min immersion on ice. Then, different concentrations of FB1 (0.01–10 µg/mL) in $MgCl_2$ 1 mM were added and incubated at 37 °C for 30 min, followed by the addition of stock 2 AuNPs (30:1 molar ratio) for 1h at RT. A wavelength scan (λ = 200–800 nm) was performed on 30 µL of the mixture combined in a 96-well microplate with NaCl 0.2 M (1:1 v:v) for calculating the $A_{650/520}$ ratio. Additionally, the difference in absolute area was calculated in Origin Pro v. 8.6 software, between the curves of each sample and the respective blank (without FB1). The proposed mechanism for aptamer 96 nt is displayed in Figure 5.1c.

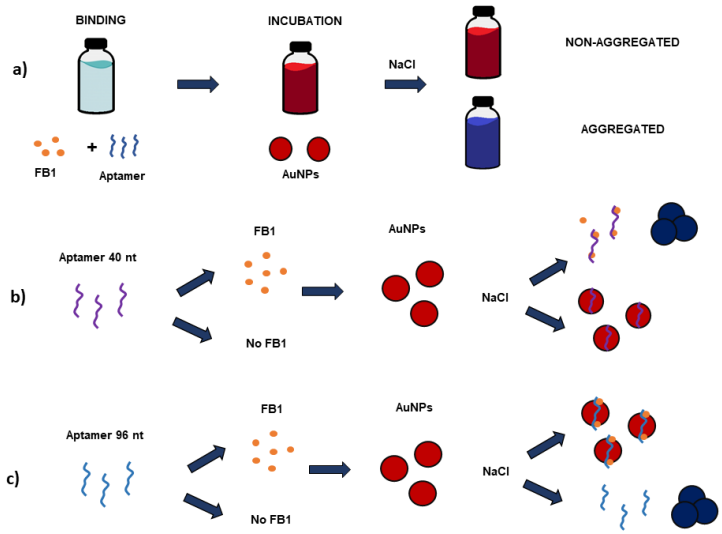

Figure 5.1 (**a**) Bulk aptasensor for the colorimetric determination of FB1with both aptamers through the binding mechanism proposed for the quantification of FB1 with (**b**) aptamer 40 nt and (**c**) aptamer 96 nt

5.2.5.2 Specificity of aptamer 96 nt

The specificity of aptamer 96 nt was also tested on the addition of FB1, OTA or AFB1 (1.38 µM), by following the incubation conditions in Section 5.2.5.1. Such mycotoxins were selected due to their relevance and simultaneous occurrence in some food products (also related to some synergistic effects).

5.2.5.3 Asymmetric Flow Field-Flow Fractionation (AF4)

After the adsorption of aptamer 96 nt on AuNPs at different FB1 concentrations (0.001–10 µg/mL), as indicated in Section 5.2.5.1, NaCl 0.2 M was added. The suspensions were subjected to AF4 conducted in an AF2000 Multiflow system from Postnova Analytics UK Ltd. (Malvern, UK). The method for the size separation of AuNPs stabilized with the aptamer–FB1 complex occurred within the channel (Postnova Z-AF4-CHA-611) having a 350 µM spacer and was performed in a 10 kDa cut-off regenerated cellulose membrane (Z-AF4-MEM-612-10KD). The temperature of the channel was controlled by a thermostat (PN4020) and set at 30 °C for all experiments. A solution of 0.05% Novachem® with sodium azide (3 mM) to avoid bacterial growth in the channel was used as the carrier liquid and prepared in Milli-Q water filtered through a 0.1 µm membrane filter (VCWP Millipore). The autosampler was equipped with a 500 µL loop allowing the injection of a 100 µL sample. All the samples were measured using the following optimized AF4 method that first consisted in an injection step at a flow of 0.2 mL/min; the sample was then focused for 6 min at a rate of 1.30 mL/min with a cross-flow (CF) set at 1 mL/min. After the focusing step and a transition period of 0.2 min, the CF was decreased with an exponent decay as follows: CF was kept first constant at 1 mL/min for 0.2 min, then decreased with an exponent decay of 0.2 to 0.1 mL/min over a 40 min period and finally kept constant at 0.1 mL/min for a further 20 min. The detector flow was kept along the process constant at 0.5 mL/min to ensure detectors baseline stability. Eluted samples were finally passed and analyzed through a series of online multiple detectors: first through a dual UV/Vis detector (PN3211) set at λ = 520 and 600 nm, a refractive index detector, RI (PN3150), a 21 angle multiangle light scattering detector, MALS (PN3621) and finally through an online dynamic light scattering detector (Zetasizer Nano ZS). All recorded signals were analyzed at increasing concentrations of FB1. Specifically, the areas under UV and MALS signals were determined in Origin Pro v. 8.6 software, with normalization of the base line from each fractogram.

5.2.5.4 Prediction of the aptamer folded structure

The folded structure of nucleic acids was predicted using MFold Web Server, according to the folding conditions for aptamer 40 nt and aptamer 96 nt.

5.2.5.5 Circular dichroism spectroscopy

Far-UV circular dichroism (CD) spectroscopy was conducted in a Jasco J715 spectropolarimeter with a 6-cell changer and Peltier temperature control, from λ = 200 to

340 nm. The incubation was performed as described in Section 5.2.5.1, at a concentration of 10 µg/L for FB1.

5.3 Results and discussion

5.3.1 Effect of buffer incubation on the quantification of FB1 with aptamer 40 nt

The UV/Vis absorption spectra obtained for the citrate-stabilize gold nanoparticles (AuNPs) in stock 1 (6.93 nM) had a maximum peak at a wavelength of 520 nm. The aggregation of colloidal gold nanoparticles, due to charge screening, is produced by salts and cationic compounds, and can be visually observed by a change in the dispersion color from red to blue, and spectrophotometrically confirmed by a peak shift from the absorbance from λ = 520 to ~650 nm. As denoted in Figure D3a, the properties for stock 1 (Average Size = 18.49 ± 0.4 nm, PdI = 0.199 ± 0.017) indicated an aggregation point after the addition of NaCl 0.4 M in a 1:1 v:v ratio (Figure D3b). Hence, this point served as the main reference for the adsorption of aptamer 40 nt on AuNPs.

Before any incubation with aptamers, the effect of different buffers was tested on both AuNP stock solutions. A key finding was uncovering the effect that Tris-HCl buffer 50 mM (pH 7.5) exerted on the resulting aggregation of both AuNP stocks (1 and 2). Therefore, we conducted a more detailed study to assess the effect of Tris-HCl and PBS ionic strength. This study revealed that 33 mM was the maximum buffer concentration capable of inducing particle aggregation. On the other hand, the concentration of NaCl in PBS to reach the aggregation point was established at 0.4 M (data not shown). In addition, the possible aggregation effects from such buffers were diminished by an initial aptamer–target incubation, and the later addition of AuNPs. Unlike the approach using AuNPs reported here, binding buffer formulations including concentrations as high as 20 mM $CaCl_2$, 20 mM $MgCl_2$ and 120 Mm NaCl have been documented with silica spheres (Yang et al., 2017; Yue et al., 2014) and fluorescence detection methods (Tian et al., 2017).

The study of the effect of different buffers was driven by the variety of buffers applied for aptamer-based detection of FB1 (Mirón-Mérida et al., 2020). Therefore, all the tested buffer conditions in this work, were selected based on their previously reported inclusion during the binding step of several aptasensors for FB1. As shown in Figure 5.2a, the effect of incubation in Tris-HCl buffer (pH 7.5, 31.1 mM), PBS (pH 7.4, 12.79 mM) and its combination on the binding effect of aptamer 40 nt toward FB1 was assessed. It was observed that under the same binding conditions, Tris-HCl buffer and a Tris-HCl/PBS mixture provided optimal performance at an increasing concentration of FB1 (0–100 µM).

The trend of such increments was similar between the incubation with Tris-HCl and that in the mixed buffer. In contrast, PBS resulted in an opposite effect on the $A_{650/520}$ value. A non-significant difference was found between Tris-HCl and mixed buffer (p = 0.33) at the highest toxin concentration (10 µM), which denoted their similar effect on FB1 binding. Yet, as a more linear trend can be observed when employing the mixture of both buffers (Figure 5.2a), this was selected for exploring a wider range of mycotoxin concentrations (0.0086–8.6 µg/mL). As suggested by the linear curves shown in Figure 5.2b, the incubation of aptamer 40 nt with increasing FB1 concentrations, in the presence of Tris-HCl and its combination with PBS, decreased the number of available aptamer strands due to aptamer binding, so that less aptamer was adsorbed on AuNPs and thus they were not protected from NaCl-induced aggregation corresponding to the visible appearance of a blue color (Figure 5.1b) (Figure D4a), and an increment on the $A_{650/520}$ value.

The result of incubating aptamer 40 nt and FB1 in the presence of four different buffers is displayed in Figure 5.2b. As noted, the incubation with $MgCl_2$ (Assay 1) and its combination with NaCl (Assay 2) were unfavorable for the quantification of FB1, which was confirmed by the determination coefficients (r^2) and the high LODs in Table 5.1. In accordance with Figure 5.2a, Tris-HCl and its mixture with PBS (Assays 3 and 4) afforded greater r^2 and lower LODs, from which the sole application of Tris-HCl resulted in an enhancement effect on the method sensitivity, which resulted in an overall greater performance by means of the NH_3^+ group in Tris-HCl, compared to the ions (Cl^-, Na^+, K^+) from PBS. Despite such confirmed effect, incubation under the presence of Tris-HCl buffer with further AuNP adsorption (Assay 4) was not specific for FB1, as corroborated in Figure 5.2c, where the addition of the same concentration of FB1, OTA and AFB1 did not show significant differences between the signals for OTA and FB1 (p = 0.065). In both cases, the aptamer–mycotoxin incubation step resulted in less unbound aptamer strands at increasing target concentrations, which diminished the amount of aptamer adsorb on AuNPs, hence more particle aggregation was observed. Aptamer 40 nt is a shortened version of an 80 nt sequence (Kd = 62 nM), selected in 100 mM NaCl, 20 mM Tris-HCl, 2 mm $MgCl_2$, 5 mM KCl, 1mM $CaCl_2$ and 0.02% Tween 20 (Chen et al., 2014). The application of shorter sequences corresponds to an attempt to reduce synthesis costs, while increasing its affinity by selecting specific binding regions (Chen et al., 2014; Frost et al., 2015).

To apply the favorable effects of Tris-HCl buffer and reduce its lack of specificity, more cationic compounds, such as NaCl, $CaCl_2$, KCl and $MgCl_2$, were included, along with a reduction in the aptamer:AuNP ratio (117:1 to 47:1), and examined the improvement of

the LODs as indicated in Table 5.2. The inclusion of counterions such as Na^+ is intended in this case to reduce the repulsion between negative charges from the DNA backbone; calcium promotes the formation of coordination complexes with carboxyl groups present in FB1, whereas the use of monovalent ions (K^+) is commonly applied to steady guanine tetrads (McKeague et al., 2010). Even when this strategy enhanced the sensitivity in terms of the increment of $A_{650/520}$, from 0.54 to 0.0007 µg/mL, while simultaneously increasing the r^2 values of the curves from Figure 5.2d, the incubation with OTA at a molar ratio of 47:1 (aptamer:AuNP) was highly correlated (R = 0.998, p = 0.002) to the values obtained through the determination of FB1 at a 58:1 molar ratio, as observed in the overlapping curves (F58:1 and O47:1) from Figure 5.2d.

Table 5.1 Different binding conditions for aptamer-based quantification of FB1 (aptamer 40 nt) [1]

Assay	Binding Buffer	Incubation with AuNP Time/Temperature (min/°C)	Equation A_{650}/A_{520} =	r^2	Range of Tested Concentrations (µg/mL)
1	$MgCl_2$ 0.19 mM	120/37	−0.008 ln [X] + 0.2977	0.6542	0.008–8.0
2	NaCl 0.06M + $MgCl_2$ 0.1mM	120/37	0.0164 ln [X] + 0.3025	0.6795	0.0074–7.4
3	PBS (eq. 12 mM NaCl) + Tris-HCl buffer 17 mM	120/37	0.0442 ln [X] + 0.6709	0.737	0.0086–8.6
4	Tris HCl buffer 14.06 mM	105/20	0.0419 ln [X] + 0.9072	0.8311	0.0096–9.66

[1] X = FB1concentration in µg/mL. Assay conditions: Aptamer:AuNP (mol:mol):117:1; FB1–aptamer incubation: 60 min (37 °C). The limits of detection (LOD) in µg/mL were 4.16 (assay 1), 0.35 (assay 2), 0.11 (assay 3) and 0.03 (assay 4), however none of values were significant (r^2≤0.9).

Table 5.2 Equations and LODs for the aptamer-based quantification of FB1 with aptamer 40 nt at different molar ratios

Assay [1]	Equation 2 $A_{650/520}$ =	r^2	Range of Tested Concentrations (µg/mL)
$F_{117:1}$	0.0248 ln[X] + 0.4434	0.695	0.0096–9.66
$F_{58:1}$	0.0276 ln [X] + 0.8332	0.833	0.00096–9.66
$F_{47:1}$	0.0192 ln [X] + 0.9169	0.84	0.000096–9.66
$O_{47:1}$	0.0624 ln [X] + 0.8937	0.76	0.0096–9.66

[1] F: Assays with FB1; O: Assays with Ochratoxin A; Numbers as subscript indicate the aptamer: AuNP molar ratio; [2] X = FB1concentration in µg/mL. Note: Buffer: Tris-HCl buffer 15 mM + NaCl 85 mM + $CaCl_2$ 1 mM + 5 mM KCl + $MgCl_2$ 2 mM; FB1 aptamer incubation: 60 min (RT); incubation with AuNP: 60 min RT. The limits of detection (LOD) in µg/mL were 0.54 ($F_{117:1}$), 0.001 ($F_{58:1}$), 0.0007 ($F_{47:1}$) and 0.06 ($O_{47:1}$), however none of values were significant (r^2≤0.9).

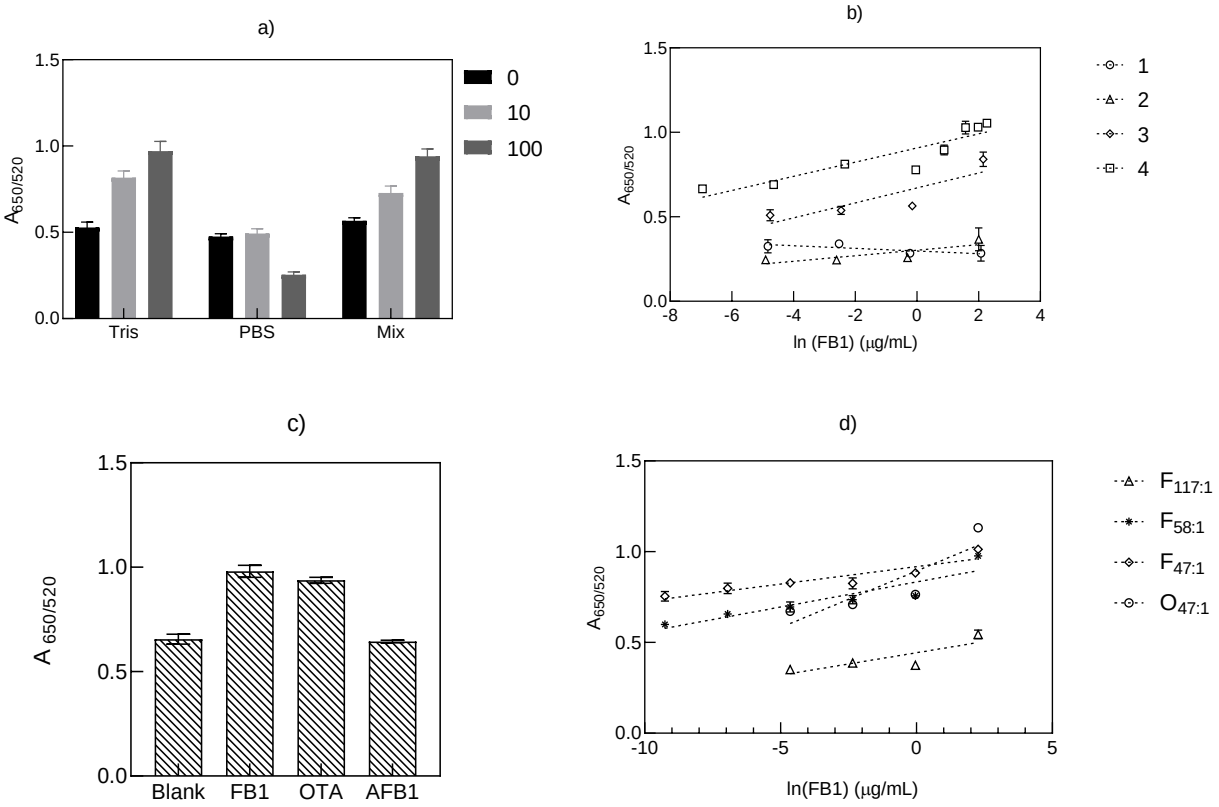

Figure 5.2 Effect of the incubation of aptamer 40 nt with FB1 on the $A_{650/520}$ ratio in (**a**) Tris-HCl buffer 31.1 mM, PBS 12.79 mM (NaCl equivalence) and a combination of both (Mix) to a final concentration of 31.1 (Tris-HCl) and 12.79 mM (PBS in NaCl equivalence), under the same binding conditions (*n* = 6), and (**b**) different buffers at the conditions outlined in Table 1 (the numbers correspond to each assay, *n* = 3). (**c**) Specificity of assay 4 incubated with other mycotoxins (13.8 µM, *n* = 4) and (**d**) the effect of the reduction in the aptamer: AuNP molar ratio (as shown in the legend subscripts) in the incubation with FB1 (F) and OTA (O)(*n* = 4)

Likewise, the equation parameters and LOD reported for OTA (0.06 µg/mL) revealed the absence of specificity from aptamer 40 nt to FB1, under the selected conditions and the biosensing technique presented in this section. The latter was opposite to the specificity reported for aptamer 40 nt through an electrochemical approach in the presence of OTA and thrombin incubated in PBS and Tris buffers (Cheng and Bonanni, 2018). Although Tris-HCl was confirmed as an ideal buffer for aptamer 40 nt, the lack of specificity could explain the existence of only two aptamer 40 nt-based methods since their disclosure in 2017 (Tian et al., 2017), and the role of the incubation conditions and sensing platform on the variable specificity of a certain sequence. In keeping with this argument, a recent

study based on in silico docking assays evaluated the affinity of the 80 nt aptamer, from which aptamer 40 nt was obtained. Unlike the high affinity to free FB1, no binding was observed when FB1 was immobilized in magnetic beads (Ciriaco et al., 2020).

Such unspecific binding can also be addressed in terms of buffer pH (7.4–7.5) in which FB1 appears as zwitterion due to the pKa values of its trycarballylic acid (3.49, 4.56, 5.83) and the amine group (pKa >9) resulting in non-specific electrostatic interactions with aptamer 40 nt, similar to the adsorption on several materials (Baglieri et al., 2013), which was also observed through the role of the ionic forms of OTA from its carboxyl (pKa = 4.3–4.4) and phenolic hydroxyl groups (pKa = 7–7.3) (Zhao et al., 2015). Based on these results, we confirmed that the specificity and good performance of aptamers depends on the binding buffer and binding conditions, along with the selected sensing mechanism. Although Tris-HCl combined with PBS buffer indicated a good sensing capability from aptamer 40 nt, its lack of specificity was revealed under the presence of OTA.

5.3.2 Quantification of FB1 with aptamer 96 nt

Stock 2 of AuNPs also had a maximum peak at a λ = 520 nm; nevertheless, the aggregation profile induced by NaCl was described by a slight reduction in the absorbance at λ = 520 nm and a pronounced peak increment from λ = 550 to 650 nm (Figure D5b). As previously mentioned, the characteristics of AuNPs are relevant to describe and understand their resulting signals. Hence, the properties of stock 2 (Average size = 21.65 ± 0.22 nm, PdI = 0.087 ± 0.016) are displayed in Figure D5a and b, where NaCl 0.2 M 1:1 ratio (v:v) indicated the main constrain for the adsorption of aptamer 96 nt at an aptamer:AuNP molar ratio of 30:1 (Figure D5c). In this regard, when compared to stock 1, the application of a lower concentration of NaCl on AuNPs with adsorbed aptamer 96 nt corresponds to the lower concentration of stock 2 (2.21 nM) when compared to stock 1 (6.93 nM).

From all the buffers previously tested for aptamer 40 nt, only $MgCl_2$ exhibited a positive performance for the proposed bulk technique with aptamer 96 nt; therefore, it was selected for detecting FB1. The addition of 5 mM $MgCl_2$ showed aggregation of stock 2 AuNPs by a colorimetric shift from red (stable AuNPs) to purple (i.e., an indicative of a certain degree of aggregation). A reduced concentration of $MgCl_2$ (1 mM) was, therefore, used to diminish those negative effects. Adding Mg^{2+} ions in binding buffers contributes to their blocking effect toward the repulsion of the negative charges from the DNA backbone, which allows a more compact folding (McKeague et al., 2010). Unlike other aptasensors, it seemed that the incubation of aptamer 96 nt with FB1 in $MgCl_2$ did not

lead to a conformational change in its structure, thus resulting in the formation of an aptamer–FB1–AuNP complex (Figure 5.1c), stable against NaCl-induced aggregation at increasing concentrations of FB1 (Figures D5d and D6d). The formation of an aptamer–target–AuNP conjugate was also observed for the determination of serotonin with AuNPs and aptamers dissolved in 2 mM $MgCl_2$ (pH 7.4), where a serotonin–aptamer complex was capable of protecting AuNPs from salt-induced aggregation, especially at high serotonin concentrations (Chávez et al., 2017).

As shown in Table 5.3, a reduction in the LOD value was achieved with aptamer 96 nt, where the value for the $A_{650/520}$ ratio (0.003 µg/mL), calculated from the curve in Figure 5.3a, was lowered when the absolute area was analyzed instead (0.002 µg/mL). To increase the sensitivity of the analysis as well as minimize reproducibility issues, calculation of the absolute area was conducted. The estimation of the differential area under the curve between the blank and its corresponding standard curve points improved the linearity and slope. This mathematical comparison, where each experiment had a reference point (blank), could reduce the variability of the results when changing the stock solutions, using AuNPs with varying shapes and particle sizes, or when observing stock aggregation upon storage. Therefore, before its subtraction, the spectrum of the corresponding blank must be acquired during each batch run. Contrary to the issues observed for aptamer 40 nt, the proposed method evinced high specificity from aptamer 96 nt toward FB1 as displayed in Figure 5.3b,c for the $A_{650/520}$ ratio and absolute area, respectively. In both cases, AFB1 and OTA had similar signals to the blank values, where FB1 displayed a distinct result. In different biosensing approaches, aptamer 96 nt has been confirmed as specific to FB1 in the presence of almost 19 compounds, which justifies its use in 24 biosensors (Mirón-Mérida et al., 2020). From these results, we observed the positive effect of $MgCl_2$ for the biorecognition of aptamer 96 nt to FB1, through the formation of an aptamer 96 nt–FB1–AuNPs conjugate. Such mechanism was specific to FB1, with a protective effect to salt-induced aggregation at increasing target concentrations.

Table 5.3 Equations and LOD for aptamer-based quantification of FB1 with aptamer 96 nt through different signals [1]

Signal		Equation	r^2	Range of Tested Concentrations (µg/mL)	LOD (µg/mL)
$A_{650/520}$		$A_{650/520}$ = −0.074 ln [X] + 0.5153	0.9179	0.01–10	0.003
Absolute Area		AA = 1.34 ln [X] + 8.298	0.9243	0.01–10	0.002
Peak Area 520 nm	Peak 1	Area = 0.0002 ln [X] + 0.0036	0.9763	0.001–10	1.68
	Peak 2	Area = − 0.0005 ln [X] + 0.0065	0.8735	0.001–10	0.0001
Peak Area 600 nm	Peak 1	Area = 0.0017 ln [X] + 0.0334	0.872	0.001–10	7.83
	Peak 2	Area= − 0.006 ln [X] + 0.0946	0.858	0.001–10	0.000000056
Peak 2 Area /Peak 1 Area	520 nm	P1/P2 = − 0.268 ln [X] + 1.8427	0.7639	0.001–10	0.007
	600 nm	P1/P2 = − 0.364 ln [X] + 2.9186	0.9637	0.001–10	0.0006
Peak 2 Area– Peak 1 Area	600 nm	P–P2 = − 0.008 ln [X] + 0.059	0.9525	0.001–10	0.0000016
28º		Area = − 0.07 ln [X] + 0.4632	0.9128	0.001–10	0.00000016
Diameter		D = − 9.498 ln [X] + 124.61	0.9514	0.001–10	0.000959

[1] X = FB1concentration in µg/mL. Buffer: $MgCl_2$ 1mM; FB1 aptamer 96 nt incubation: 30 min (37 °C); incubation with AuNP: 60 min (RT); AuNP:Aptamer molar ratio 30:1. LODs were selected as significant when $r^2 \leq 0.9$. A comparison of significant values with current sensitive methods is presented in Figure 7.2.

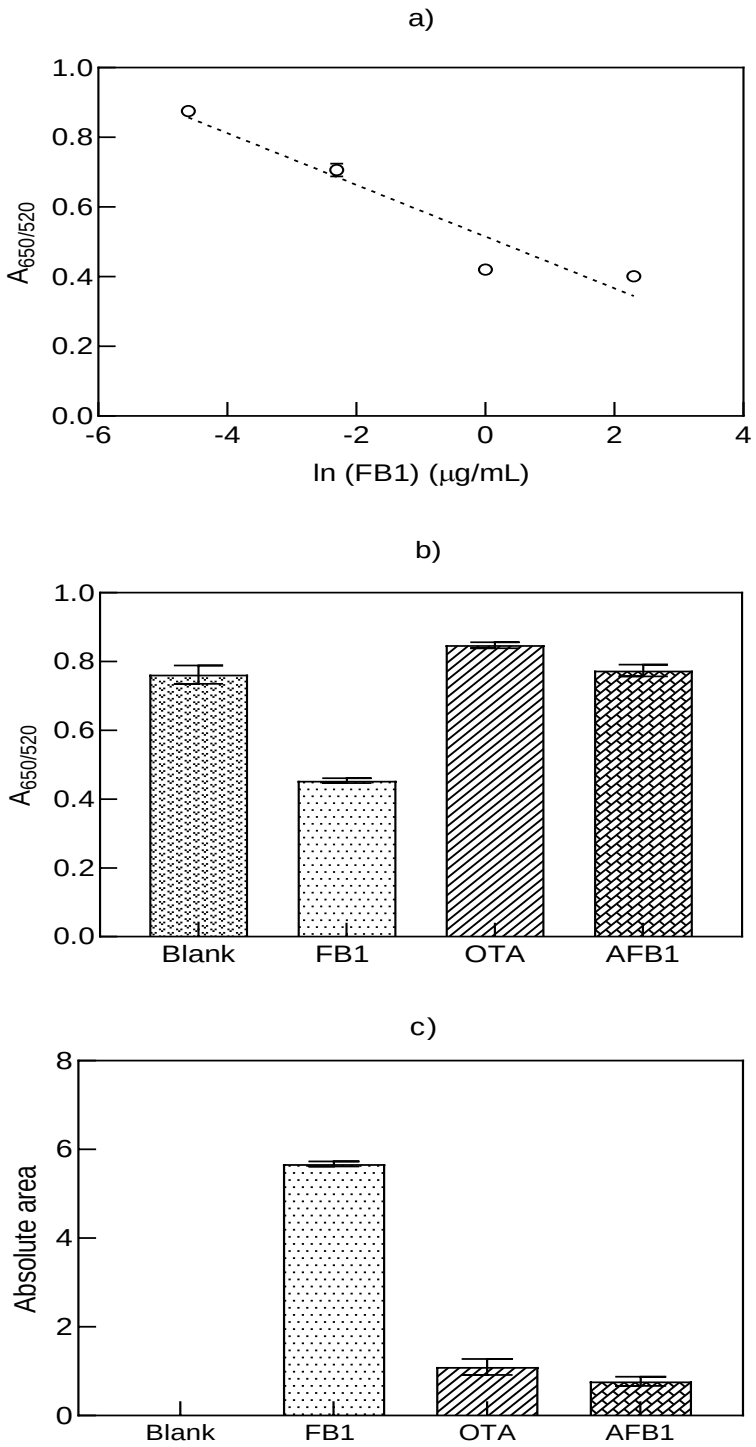

Figure 5.3 (**a**) Standard curve for the quantification of FB1 with aptamer 96 nt in $MgCl_2$ through the analysis of the $A_{650/520}$ ratio. Specificity test under the presence of FB1, AFB1 and OTA at a concentration of 1.38 µM for the (**b**) $A_{650/520}$ ratio and the (**c**) absolute area values (*n* = 3)

5.3.3 Asymmetric Flow Field-Flow Fractionation (AF4) of the aptamer 96 nt–FB1–AuNP conjugates

The characterization of different aptamer 96 nt–FB1–AuNP conjugates after the addition of NaCl 0.2 M was further examined by multidetection AF4, to confirm the combined role of the aptamer 96 nt–FB1 complex in the adsorption and protection of AuNPs against NaCl-driven aggregation at different target concentration. As a first step, it was determined both visually and spectrophotometrically that the UV/Vis signal at λ = 520 and 600 nm after AF4 separation showed higher peaks at lower FB1 contents (results not shown). AF4 relies on the separation of particles of varying size depending on their hydrodynamic and diffusion properties, where the initial elution corresponded to small stabilized particles (Peak 1), whereas larger particles (Peak 2) eluted after, before passing through the detectors as shown in representative fractograms (Figures D6a and D6b). According to the AF4 principle, longer elution times correspond to particles of larger sizes, which in many cases could also be diagnostic of aggregation. Compared to the spectrophotometric analysis, AF4 contributed to the refinement of the detected signals, with a much greater resolution at lower target concentrations. Even when two peaks were detected at λ = 520 and 600 nm, the peak corresponding to the highest particle sizes (Peak 2) had a more favored trend for its potential application in biosensing techniques, as displayed in Figure 5.4a,b. The selection of this peak was consistent with the lower LODs achieved when analyzing the values of Peak 2 at both wavelengths (Table 5.3). The UV/Vis signal at λ = 600 nm was mainly ascribed to the aggregation profile of AuNPs; for that reason, the peaks between 40 and 60 min were larger and more noticeable among different concentrations of FB1 (Figure D6b).

The reported analytical method demonstrated the presence of stabilized and aggregated particles in the same suspension, rather than their complete aggregation or stabilization through the adsorption/desorption of aptamer FB1. Such profile was regulated by the concentration of FB1 where fewer aggregated particles were detected at higher target concentrations (Figure D6b). The presence of different particle sizes could also be attributed to the native heterogeneity of the selected stock, which is a common issue in AuNPs, derived during their manufacturing/synthesis process, and previously confirmed by AF4 as an arrangement of particles with different size, shape and zeta potential (Riley et al., 2019).

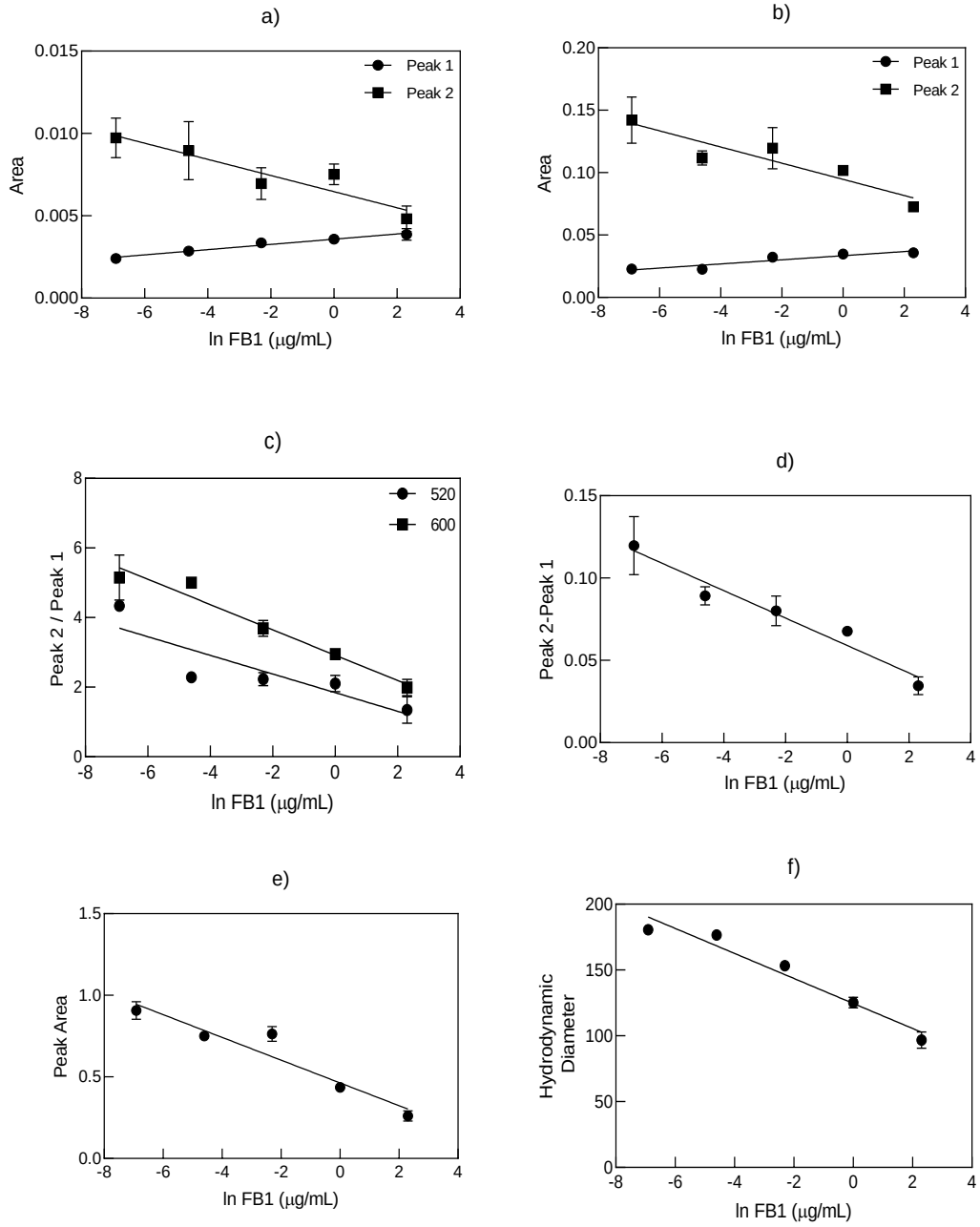

Figure 5.4 Standard curves for the quantification of FB1 with aptamer 96 nt through the analysis of the AF4 fractograms from the UV/Vis peak areas at (**a**) 520 nm, (**b**) 600 nm, (**c**) peak ratio between Peak 2 (larger particles) and Peak 1 (smaller particles), (**d**) peak area differences at 600 nm, (**e**) MALS peak area at 28° and (**f**) hydrodynamic diameter determined by DLS for the Aptamer (96 nt)–FB1–AuNPs conjugates in NaCl 0.2M.(*n* = 3)

To achieve a better separation resolution of different particle populations, a regenerated cellulose membrane was reported due to its high recovery of AuNPs (Hagendorfer et al., 2011), associated with its charge, which depends on the pH value of the carrier solvent.

Here, as the carrier solvent has a pH = 9.5, the regenerated cellulose membrane bears a net negative charge (zeta potential < ~ −20 mV) (González-Espinosa et al., 2019), which decreases the interaction between the membrane and AuNPs, thus favoring their elution. In addition, the application of a combination of ionic and non-ionic surfactants, such as Novachem® 0.05%, in the carrier solvent was considered for preventing particle aggregation and accumulation on the cellulose membrane, as reported for other surfactants, which also improved the retention profiles (Cho and Hackley., 2010). Similarly, surfactants also decrease particle loss, null peaks, particle separation and recovery loss (Hagendorfer et al., 2011).

Even though the retention time during AF4 fractionation can be correlated with particle size, and the MALS signal detection can be used for the determination of the radius of gyration (Cho and Hackley., 2010; Schmidt et al., 2011), in our study, we focused on the analysis of the peak areas of the different signals. Therefore, the effect of FB1 on the adsorption of aptamers on AuNPs was studied as a whole system, regardless of the differences in the absolute particle size. Despite the initial characterization purpose for the application of AF4 on the conjugates at varying FB1 concentrations, the low LODs achieved, especially after analyzing the peak areas at 600 nm (56 fg/mL), unveiled its promising usage as a biosensing technique.

As highlighted in the equations and LODs (Table 5.3) from Figure 5.4c,d, neither the Peak 2/Peak 1 ratio for both wavelengths (7 and 0.6 ng/mL, respectively), nor the subtraction of Peak 1 from Peak 2 at 600 nm (1.6 pg/mL), were as sensitive as the sole analysis of Peak 2 at 600 nm. Similarly, the parameters quantified from the MALS signal at 28° (LOD = 0.16 pg/mL) and the hydrodynamic diameter obtained by DLS (LOD = 0.96 ng/mL), plotted in Figure 5.4e,f, respectively, resulted in lower sensitivity compared to the values determined from UV signals at 600 nm (Table 5.3). Although the MALS signal at 90° has been analyzed for AuNPs (Cho and Hackley., 2010; Schmidt et al., 2011), in this work, more distinctive peaks between samples were found at 28°, which allowed the examination of various degrees of aggregation with a better signal-to-noise ratio. Such MALS signal (28°) was adequate for representing the effects of an increasing concentration of FB1 on the same system by analysis of its peak area, which also demonstrated that smaller angles from MALS are more sensitive to larger particles. Interestingly, the hydrodynamic diameter complied with the UV/Vis fractograms and spectrophotometric analysis, where greater hydrodynamic diameters corresponded to the presence of aggregated particles at lower FB1 contents. To the best of our knowledge, AF4 has not been yet used for the quantification of mycotoxins. One study applied this

technique for quantifying the molecular weight of an aptamer–streptavidin–immunoglobulin G (IgG) complex in a biosensing technique for OTA (Samokhvalov et al., 2017). In summary, the analysis of the aptamer 96 nt–FB1–AuNPs conjugates by AF4 revealed the presence of varied degrees of aggregated and non-aggregated particles at different target concentrations. From all the detected signals, the analysis of the UV/Vis peak area at 600 nm was the most suitable for portraying such variability, with a promising scope for the application of AF4 as a new biosensing technique in the fg/mL range.

5.3.4 Interaction of the conjugate elements (Aptamer 96 nt–FB1–AuNPs)

The biosensing approach in this work did not require any complementary strand or aptamer modification (label), especially when considering that the latter might decrease its binding affinity. Here, the selection of the incubation buffer is also a relevant step for the success of the aptamer-target binding stage (Wu et al., 2013). As shown in Figure 5.5a, when compared to aptamer 40 nt (dG = −8.07), the structure of aptamer 96 nt (dG = −12.46) has elongated hairpins and loops, due to its longer sequence.

A study on the binding affinity of minimers from aptamer 96 nt (Kd= 100 nM) reported that the 30 nt sequence next to the 3′ primer binding region (AGATAGTAAGTGCAATCT-3′) is related to target binding (Figure 5.5a). However, the regions following the 5′ end (5′-ATACCAGCTTATTCAATT) are also necessary for the overall binding efficiencies, which correspond to the favorable dissociation constant of the sequence without both primer binding regions (60 nt, Kd = 195 nM) (Frost et al., 2015). Nevertheless, binding assays for this minimer denoted low or null binding towards FB1 (Ciriaco et al., 2020), which explains the majority of applications with the complete 96 nt sequence. In addition, the amine group in FB1 has been used in immobilization approaches during SELEX, motivated by the immunodominant epitope region in FB1 (close to the concurrence of tricarballylic acid to C-11 and C-20), which is distant from such functional group (Chen et al., 2014). Even when the presence of multiple free dihedrals within the structure of FB1 requires more configurational space during binding, high binding propensity has been reported between FB1 and the backbone of different FB1 aptamers, including aptamer 96 nt (Ciriaco et al., 2020)

Based on this, the formation of aptamer 96 nt–FB1–AuNPs conjugates first occurred by incubation of the binding region and backbone in aptamer 96 nt with its epitope zone in FB1, where a conformational change was unlikely to have occurred due to the length of the aptamer and the role of the negative backbone charges from both primer binding regions, which could have generated steric hindrance and simultaneous binding in some

regions. Therefore, the conjugation was followed by immobilization of the aptamer 96 nt–FB1 complex on AuNPs by means of the NH_2 group in FB1, which was previously evaluated on the prevented aggregation from binding buffers through the sole incubation with the target molecule, but was weak against salt-induced aggregation (Figure D4b). We thus suggest that the mechanism was completed by the formation of an aptamer 96 nt–FB1 layer by non-covalent attachment of the primer regions to the surface of AuNPs. This proposal is consistent with the increased density of aptamer 96 nt–FB1 complexes on AuNPs, and the prevented aggregation upon the addition of salt.

Circular dichroism (CD) spectra of $MgCl_2$ and FB1 were very close to the solvent baseline (Figure 5.5c). In turn, the CD spectra for the aptamer 96 nt showed two trough bands at λ = 205 and 250 nm and a positive peak band at 280 nm region before and after binding with FB1. The CD spectrum was close to previous analysis on this sequence, which denoted helicity of its parallel arrangement (Baaske et al., 2010). The same negative (250 nm) and positive (280 nm) bands were previously described as an indicator of an A-form hairpin duplex structure, where the flat zone from 265 to 285 nm was attributed to base pair formation between A-T and G-C (Chen et al., 2014; Lin et al., 2011). However, the 3-D representation of the most stable docked pose in aptamer 96 nt was indicated as a B-form duplex structure, as A-forms are mostly favored in RNA (Ciriaco et al., 2020). The peak similarity from both spectra also confirmed the absence of a conformational change upon binding.

Depending on the selected immobilization and biosensing method, when a long-length aptamer is used, the FB1-modulated conformational change might not be observed, as only some regions of the aptamer display affinity. Such absence of conformational change was also confirmed by gel electrophoresis, as indicated in Figure D7, where a slight increase of 2.5% was calculated for the band intensities of aptamer 96 nt incubated with the maximum FB1 concentration (10.02 µg/mL) compared to the bands for aptamer 96 nt in $MgCl_2$ 1mM. The aforementioned was opposite to the trend observed in other reports, when an increasing target concentration enhanced the band intensities from the aptamer–target complex due to conformational change (Jing et al., 2011). To conclude, based on the CD and gel electrophoresis results, it was understood that no conformational change was found upon target binding, which also corresponded to the long structure of aptamer 96 nt, predicted in Mfold.

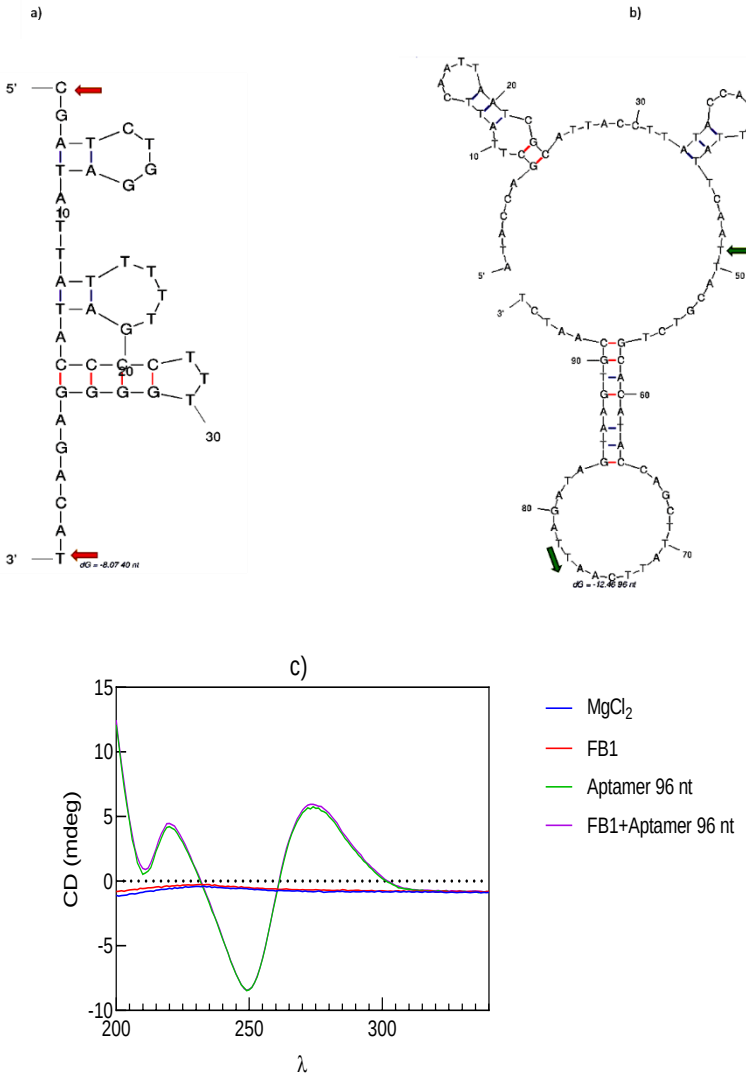

Figure 5.5 Predicted folded structures of (**a**) aptamer 40 nt (dG = −8.07, folding conditions: 0°C, [Na^{+}]=85 mM [Mg^{++}]=2 mM) (**b**) aptamer 96 nt (dG = −12.46, folding conditions: 0°C, [Mg^{++}]=1 mM)). Target binding regions are indicated in red arrows (aptamer 40 nt) based on the 40 randomize sequences studied by Chen and collaborators (2014) and green arrows (aptamer 96 nt) based on the minimers studied by Frost and collaborators (2015). (**c**) Circular dichroism spectrum of aptamer 96 nt in the absence and presence of FB1 (10 µg/L) incubated in $MgCl_2$

As a first attempt toward the subsequent full validation of the developed method, we evaluated the matrix-matched quantification of FB1 in various liquid and solid food samples. For instance, the incubation of aptamers with its target in either buffer or a corn extract showed color differences among both samples, after the addition of AuNPs

(Figure D8a). Likewise, the analysis in spiked vodka displayed different aggregation spectra to those from FB1 in binding buffer ($MgCl_2$ 1mM), as shown in Figure D8b,c. While spirits can be directly measured and injected into the AF4 system, a pretreatment step is required for the analysis of more complex samples such as corn extracts. As plotted in Figure D2, the LOD, for the specific quantification of FB1 by the reported aptamer–target–AuNP complex ($A_{650/520}$ absolute area), is comparable to that for some fluorescent and electrochemical aptasensors specific for this mycotoxin. Yet, the application of AF4 is a promising technique for the analysis of FB1, which regardless of the increased assay time resulted in a low LOD value comparable with the most sensitive aptamer-based sensors reported for this purpose. The novelty of this approach lies in the integration of a label free single probe assay with the 96 nt ssDNA sequence, without the inclusion of other complementary strands, supports or DNA modification (SH, NH_2, biotin, FAM, Cy5.5). Additionally, to the best of our knowledge, this is the first report on the use of AF4 for evaluating the performance of an aptamer on the formation of a conjugate enhanced by the presence of its target molecule, thus revealing to be a highly sensitive and specific method.

5.4 Conclusions

This work presents a comparison on the performances of two aptamers for the colorimetric quantification of FB1. The results indicated that, along with the aptamer sequence, the selected buffer and incubation conditions play an important role in the final sensitivity and specificity of each assay. In this regard, incubation with Tris-HCl and $MgCl_2$ was suitable for the 40 and 96-mer aptamers, respectively. Contrary to previous reports (Cheng and Bonanni, 2018), the assay with a short length aptamer (40 nt) was not specific for FB1, as similar results were observed through the incubation with OTA. A different mechanism has been proposed for the long aptamer (96 nt), previously reported for several aptamer-based approaches. In this case, an aptamer–FB1–AuNP conjugate was formulated in the presence of $MgCl_2$ 1 mM, showing stability to salt-aggregation at an increasing concentration of FB1(0.001–10 µg/mL). Unlike other aptasensors, the 96 nt aptamer offered a simplified approach as a label-free ssDNA sequence was applied without the need of end modifications or complementary strands. Analysis of the spectrophotometric signals resulted in LODs similar to other sensitive techniques; however, the exploration of the aggregation profile by AF4 with multidetection (UV/Vis, MALS, DLS) derived in a promising sensing technique with sensitivity in the fg/mL level, which is an advantageous result when compared with ongoing biosensing methods for

the detection of FB1, as displayed in Figure 7.2. The characterization of the complex formation revealed the absence of DNA conformational change upon binding, yet this new mechanism might be suitable for the direct analysis of different food matrices, where there is scope for exploring other targets, such as emerging mycotoxins. To our knowledge, this is the first aptasensing technique for FB1 applying the 96 nt aptamer sequence without any end modification, label or complementary strand. Likewise, there is no evidence for the use of AF4 in the exploration of aptamer–target–AuNPs interactions.

Further validation and standardization steps are still required for the commercial application and possible scaling to paper-based techniques, which might enhance the opportunities for on-site quantifications, while decreasing the total manufacturing cost. Nevertheless, this work established a new mechanism for detecting FB1 with a 96 nt aptamer in bulk, while at the same time presents for the first time the use of a more robust method, as it is AF4, resulting in LODs with strong advantages over more complex designs.

Chapter 6
Application of β-chitin scaffolds and N-isobutyryl chitosan hydrogels as potential decontaminants in food

Abstract

Food contamination is a serious global problem that affects a variety of crops and food products. Common examples of this are the contamination with pesticides and mycotoxins, which can occur at different production stages, therefore novel non-destructive approaches for removing several contaminants in food are needed. The use of polymers such as a chitin powder and cross-linked chitosan has been reported as effective for the adsorption of mycotoxins in liquid samples, as well as buffers and simulated gastric conditions. In this work, the swelling properties of a scaffold produced from processed chitin fibres, were compared with the same attributes from a pre-swollen N-isobutyryl chitosan (NIBC) derivative hydrogel. The swelling equilibrium in PBS buffer was achieved in less than 10 min, and some performance and physical differences were related to the type of polymer and the processing steps (e.g., freezing method). Diffusion coefficients were obtained after fitting the data form "t_0" to "$t_{equilibrium}$" using a slab Fickian diffusion model and helped characterise such porous matrices with a promising application in food detoxification.

6.1 Introduction

Around 25% of the harvested agricultural goods are contaminated with mycotoxins. This represents a challenge as these metabolites are stable to hight temperatures (100-200 °C) and therefore cannot be eliminated during some processing (pasteurization) and cooking methods (baking, roasting, frying, extrusion). Fungal growth, resulting in mycotoxin contamination, commonly occurs during postharvest drying, handling, packaging, storage and transportation (Kamle et al., 2019). The occurrence of fumonisin B1 (FB1), the most abundant analogue in nature from group B, is mostly prevalent in *Fusarium* species and has been widely described in corn and corn-based products. In addition to this agricultural good, FB1 has been reported in other food commodities such as rice, beans, sorghum, cowpea, soybeans, triticale, asparagus, wheat and wheat-based products, cassava, garlic, onion, tea, figs, peanuts, black radish, medicinal plants, dietary plants; as well as in liquid products including beer and milk (Kamle et al., 2019; Scott, 2012; Shepard et al., 2007). Fumonisin ear rot is favoured by drought, insect damage, other fungal infections, and plant breeding (Miller, 2010). This mycotoxin is neurotoxic,

genotoxic and cause liver, kidney and pulmonary damage in some animal species and might be related to growth impairment in children (Agriopoulou et al., Chen et al., 2018; Scott, 2012). Consequently, the maximum tolerable daily intake (PMTDI) has been reduced from 2 to 1 μg/kg, and several methods for contamination reduction have been explored in pre- and postharvest stages (Chen et al., 2018). Preharvest strategies for reducing fungal growth include good agricultural practices (crop rotation, weed elimination, fertilizers, regulated fungicides, insecticides, and herbicides), good manufacturing practices, suitable storage and environmental factors (temperature, humidity, moisture value), and genetic modification of crops. Nevertheless, they tend to be costly, have poor efficacy, and low yields. Alternative procedures are focused on preventing fungal growth and its related activities through the application of antagonistic microorganisms and antioxidants (e.g., phenolic compounds, essential oils), whose effect has been successfully confirmed in vitro (Agriopoulou et al., 2020; Chen et al., 2018). Fungal growth reduction and prevention is affected either by physical (temperature, humidity, modified atmospheres, irradiation, bases, chitosan, ozone,), chemical (antifungals, photodynamics, electrolyzed oxidizing water (EOW), cold plasma,) and biological approaches (microorganisms, plant extracts) (Agriopoulou et al., 2020; Liu et al., 2020). On the other hand, general postharvest treatments for mycotoxin reduction involve physical (sorting, dehulling, milling, storage, heat, irradiation), chemical (adsorbents, alkalis, acids, EOW, plasma), biological (degradation by enzymes, fermentation, yiest, fungi, bacteria) and novel applications (nanoparticles, plant extracts, biological polymers) (Agriopoulou et al., 2020; Chen et al., 2018; Liu et al., 2020). Fumonisin decontamination has been attempted through the application of adsorbent materials, microbial biodegradation and enzymatic detoxification (Chen et al., 2018). The reduction of FB1 during cooking might correspond to its interaction with some food components into conjugates, or its chemical modification, as in the case of nixtamalization, an alkaline method for corn in which trycarballylic acid separates from FB1 to form less toxic hydrolysed fumonisins. However, the variable distribution of FB1 within the structure of cereals, make them difficult to eliminate (Chen et al., 2018; Kamle et al., 2019). An environmentally friendly alternative is the application of adsorbent materials based on natural polymers. Many effects from polymers were discovered through the degradation effects of some microorganisms, where physical adsorption took place by cell wall compounds such as peptidoglycans in bacteria; β-1,3-glucan, chitin, β-1,6-glucan and glycosylated mannoproteins in yeast (Liu et al., 2020).

Chitin is the structural polymer in some invertebrates (crustaceans, insects), where they form the shell as fibres (20-30%) crosslinked with proteins (30-40%) and reinforced by salts (30-50% calcium carbonate), pigments (astaxanthin, astathin, canthaxanthin, lutein, β-carotene) and lipids (0-14 %); and it also constitutes the cell wall material in fungi and algae (Aranaz et al., 2009; Díaz-Rojas et al., 2006; Peniche et al., 2008). Chemically, chitin is a linear aminopolysaccharide comprised by N-acetylglucosamine (A residues) linked (β (1→4)) residues (Figure 6.1a and b). Chitosan, chitin's main derivative, is comprised by glucosamine (D residues) and remaining A residues (Figure 6.1a and b).

The crystalline structure of chitin can be classified as either α- (the most common in crustaceans), β- (produced by squid pen with higher protein and less carbonate content), or γ- (altered version from α- or β- found in mushrooms), where chitin is arranged in sheets/stacks, which can follow an antiparallel (α), parallel (β) or alternating (γ) structure (Figure 6.1c, d and e) (Aranaz et al., 2009; Elieh-Ali-Komi and Hamblin, 2016; Tamura et al., 2011). Because of its parallel arrangement, β -chitin exhibits greater solubility, swelling, and reactivity, compared to α-chitin (Kurita et al., 1994). Due to this crystalline structure, chitin is intractable and insoluble in aqueous and organic solvents (Tamura et al., 2011), yet it can be isolated from raw materials (crab, shrimp shells, squid pen) through grinding, followed by acidic demineralization, alkaline or enzymatic deproteinization, and sometimes decolorization (shrimp shell astaxantine) (Aranaz et al., 2009). Chitin is mostly obtained for the production of chitosan, and glucosamine (15 000 ton per year) (Díaz-Rojas et al., 2006).

Chitosan naturally occurs in certain fungal species and is mainly obtained from the deacetylation of chitin in strong alkaline conditions (40-50 % NaOH/KOH) and high temperature, however as this process occurs in varied degrees, chitosan in fact comprises a family of chitins with varied degrees of acetylation (DA%), given by the molar percentage of A residues. Currently, the industrial production of chitosan worldwide requires large amounts of water, energy, and results in the generation of corrosive wastewater (Aranaz et al., 2009; Peniche et al., 2008). Many applications from both, chitin and chitosan, are related to their nontoxic, biodegradable, biocompatible and antimicrobial nature (Jayakumar et al., 2011). Chitosan has been used for controlling the growth of *Fusarium* species and reducing the production of fumonisin. Furthermore, essential oils can be added into chitosan for the reduction of DON in grains (Agriopoulou et al., 2020). Shrimp isolated chitin and shrimp shell have evinced up to 54% and 94% binding to AFM1 in liquid phase, respectively (Assaf et al., 2018).

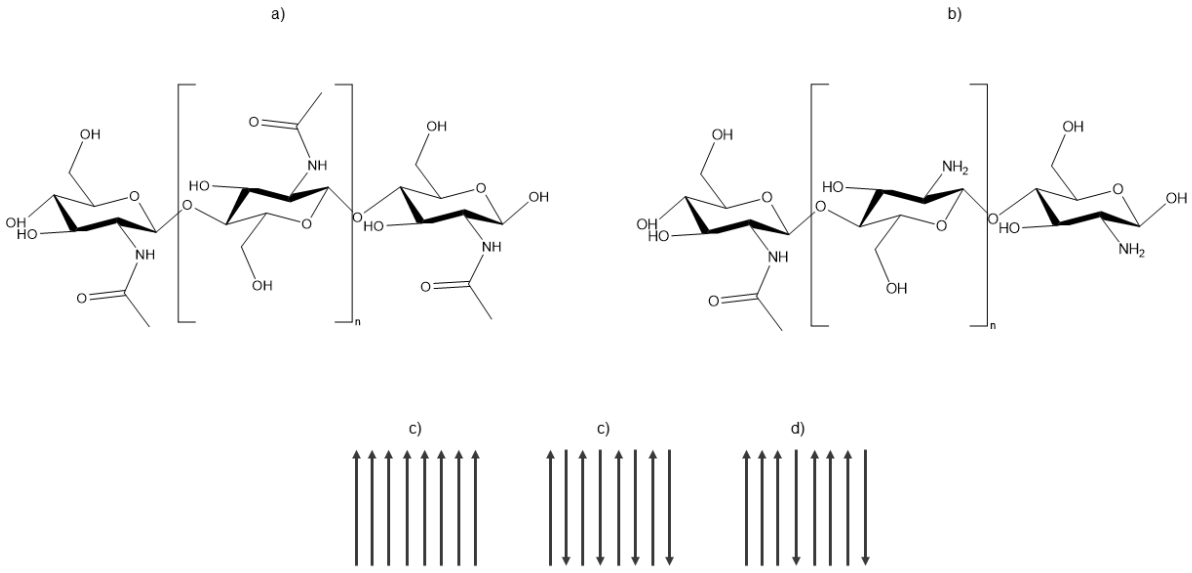

Figure 6.1 Chemical structure of (**a**) chitin (DA 100%) and (**b**) chitosan. Polymorphic configuration of (**c**) α-chitin, (**d**) β-chitin and (**e**) γ-chitin

However, certain drawbacks are the high polysaccharide concentration required for long incubation times, the binding instability performed by such materials, and the need of dissolving chitosan in acidic conditions, which is unsuitable for some application in food (Liu et al., 2020; Sun et al., 2020). Some strategies for solving those issues are the application of solid chitosan and chitin in liquid samples (wine) (Quintela et al., 2020), the use of powdered chitosan for the reduction of the content of FB1 and other 7 mycotoxins in solid matrices (palm kernel cake) (Abbasi Pirouz et al., 2020), the transformation of chitosan into particles (Mine Kurtbay et al., 2008; Solís-Cruz et al., 2017) or layers and its combination with adsorbent materials such as rectorite (Sun et al., 2020), montmorillonite (Wang et al., 2020), graphene oxide (Abbasi Pirouz et al., 2018), and Fe_3O_4 (Luo et al., 2017).

Another strategy to enhance the binding properties of chitin- and chitosan- based adsorbent materials is their transformation into structures with greater surface area. Because of its fibrous nature, chitin can be a reinforcing agent in scaffolds (Li and Feng, 2005), whose structure should portray high porosity, integrity, biodegradability (Elieh-Ali-Komi and Hamblin, 2016). On the other hand, unlike cross-linked chitosan, from the multiple structured materials formed with chitosan, N-isobutyryl chitosan (NIBC) gels, formed through the acylation of chitosan with isobutyric anhydride, have been poorly explored as mycotoxin binders (Félix et al., 2005; Zhao et al., 2015). Besides, yet another alternative strategy to enhance the binding of mycotoxins could be the use of molecularly

imprinted polymers (MIPs). Conventional MIPs are synthesised by polymerizing a given polymeric material in the presence of a target template molecule, which after its removal, leaves a functional group-shaped imprint, in which the specific molecule or its analogues can rebind (Wulff et al., 1997). Biopolymer- based MIPs are obtained by crosslinking of a given polymer in the presence of the template.

MIPs coupled to several materials have been successfully reported as one of the most sensitive platforms for the detection of FB1 (Mirón-Mérida et al., 2021). Chitosan-based MIPs have been produced by covalent crosslinking with either genipin (Espinosa-García et al., 2007) or glutaraldehyde (Aburto and Le Borgne, 2004) for the selective readsorption of *o*-xylene and dibenzothiophene sulfone, respectively. To the best of our knowledge, MIPs based on physically formed chitosan hydrogels and scaffolds have not been reported.

In this work, two polysaccharide-based materials, namely chitin scaffolds and NIBC gels, were produced and incubated with FB1 contaminated milk and beer, where the differences in temperature and pH might affect the final binding performance. In addition, the structural and swelling properties of both materials were assessed to understand their potential as mycotoxin binders. On the other hand, molecularly imprinted NIBC hydrogels were formulated with two chitosan samples for the selective adsorption of L-phenylalanine as a template molecule and surrogate of OTA.

6.2 Materials and methods

6.2.1 Materials

Squid (*Illex argentinus*) gladius (squid pen) was supplied in frozen state by the company TIGMAK Natural Polymers (London). Chitosan I (code HMC 90/1000, batch number 212-150915-01, DA=14%, Mw=228,000 g/mol) and Chitosan II (code HMC 80/1000, batch number 212-020413-02, DA=23%, Mw=308,900 g/mol) were provided by HMC+ (Heppe Medical Chitosan, Halle, Germany). Phosphate buffered saline (PBS, pH 7.4, Cat. BP2944-100), and methanol (HPLC grade, code 4013101) were purchased from Fisher Scientific (Loughborough, UK). Fumonisin B1 (FB1, Cat. FB1147) was acquired from Sigma-Aldrich (Dorset, UK). Formic acid and 25% ammonium hydroxide were obtained from Honeywell (Bucharest, Romania). HPLC grade acetic acid (code 5438080100) and L-α-phenylalanine (Cat. A1344.0100) were acquired from VWR international (Lutterworth, UK). Isobutyric anhydride (code 8005040100) was bought from Merck KGaA (Darmstadt, Germany), while IPA beer (Founders Brewing Companu, Grand Rapids, US) and British

whole milk were purchased from Sainsbury's (London, UK). Unless otherwise stated, MilliQ water was used throughout.

6.2.2 Methods

6.2.2.1 Isolation of β-chitin from squid pen

β-chitin was isolated from squid pen under a novel process developed in our laboratory as indicated in Figure 6.2. Briefly, squid pens were dried on an Excalibur dehydrator Paralexx TM (40 °C, 13h), and ground in hammer mill (size ≤ 45μm). The ground pen was mixed in 2 M NaOH at 65 °C, stirred under high shear with a 16" Heavy-Duty Big Stik® immersion blender for one hour, washed to neutrality with tap and distilled water. A gel paste was obtained and dried at 40 °C (fan-forced air dryer) and grinded in a hammer mill.

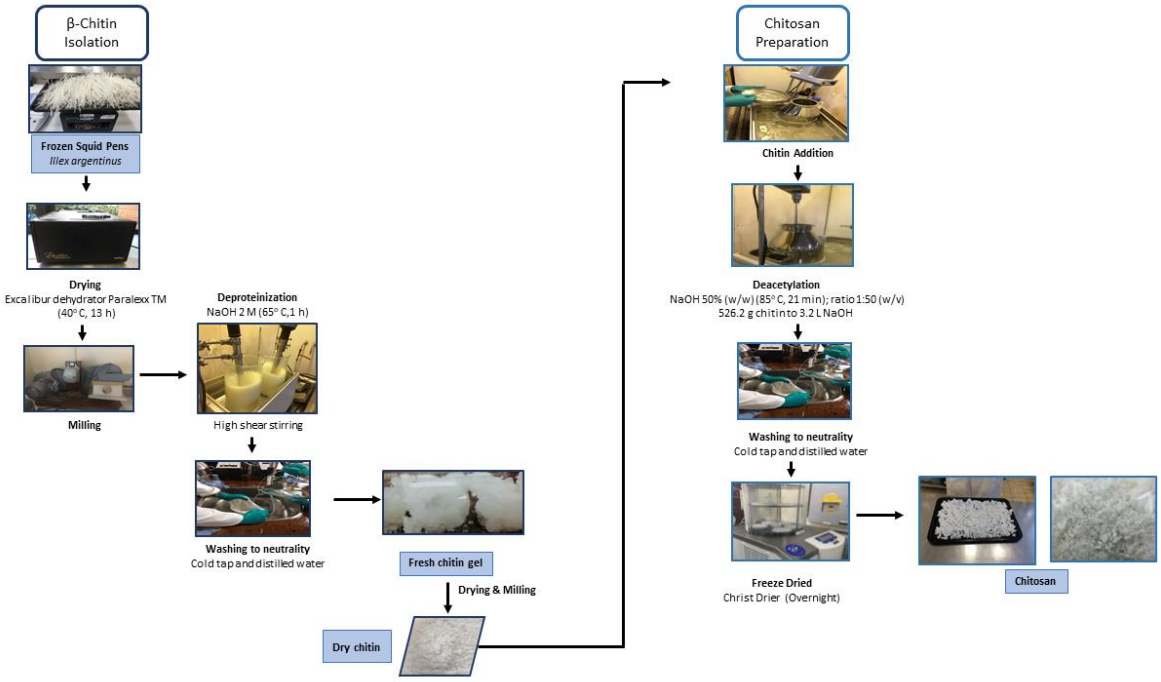

Figure 6.2 β-chitin isolation process and its deacetylation into chitosan

6.2.2.2 Deacetylation of β-chitin to chitosan

As indicated in Figure 6.2, dry ground chitin was deacetylated in alkaline conditions (NaOH 50% w/w) at 85 °C (water bath) for 21 minutes in a 5 L 316L stainless steel churn coupled with an overhead stirrer at 750 rpm (VOS 14, VWR). The hydrolysed product was

filter through a mesh (muslin cloth) and wash until neutrality with cold tap water and distilled water. The final material (chitosan III) was freeze-dried for 12 hours in an Alpha 1-4 LD Plus freeze-dryer (Christ Martin, Germany) and ground in a hammer mill.

6.2.2.3 Preparation of β-chitin scaffolds for mycotoxin binding

A 5% (w/w) chitin dispersion was prepared in water and homogenized in ultrasound by a sonicator probe (Sonics Vibra-Cell VC130 at 100 amplitude) for 6 min. In order to obtain two sizes, four and seven grams of this solution were poured into plastic cylindrical containers. Half of the samples were frozen in liquid nitrogen (-196 °C), while the other half was treated by conventional freezing (-8 °C). All samples were then freeze dried for 72 h in an Alpha 1-4 LD Plus Freeze-dryer (Christ Martin, Germay). The water activity (a_w) of the materials was determined in a Rotonics HygroLabC1 HC2 water activity meter.

6.2.2.4 Synthesis of N-isobutyryl chitosan gels (NIBC) for mycotoxin binding

Chitosan I (6 g/L) was dissolved by stirring chitosan overnight in acetic acid (0.1 M). Gels were produced in a petri dish by dissolving isobutyric anhydride (0.093 mL) in methanol (4.452 mL) with a subsequent addition of the chitosan solution (4.55 mL) and methanol (4.452 mL). The stoichiometric ratio of isobutyric anhydride to glucosamine was 4.0. The mixture was left quiescent for 5 h until gel formation was reached; the alcogels were gently removed from the petri dish, washed with water at 60 °C until neutral pH, conventionally frozen (-8 °C) and freeze dried until further use. The a_w was measured as stated in the previous section.

6.2.2.5 Scanning electron microscopy (SEM) imaging

The scaffold materials were coated with a 4 nm layer of iridium (Sputter coater Cressington 208HR) and imaged in a FEI Nova NanoSEM 450 at 3 kV. The pore size was calculated in ImageJ from the images at a 200 µm scale.

6.2.2.6 FTIR

FTIR analysis was performed in a Agilent 4500 portable spectrometer (A2 Technologies, Danbury, USA) in absorbance mode (Clean scans: 4; Threshold: 0.002), through a spectral range of 4000 to 650 cm^{-1} (1024 sample and background scans, 4 cm^{-1} resolution), and using polystyrene as control sample.

6.2.2.7 Swelling kinetics analysis

Chitin and NIBC scaffolds were divided into sections with approximately similar mass and shape. Each piece was put in a 20 mL vial containing PBS (pH= 7.4) and incubated at

different temperature (4 °C, room temperature or 37 °C). Prior to each measurement the samples were placed on Whatman cellulose No.1 filter paper for eliminating any liquid excess, followed by weight measurement, which was recorded at varying time intervals.

6.2.2.7.1 Calculation of the swelling ratio

The swelling ratio (S) was calculated by including the mass of the hydrated sample (W_h) and the mass of the dry sample (W_s) before swelling, according to the following equation (Goycoolea et al., 2011):

$$S = \frac{W_h - W_s}{W_s} \tag{6.1}$$

6.2.2.7.2 Apparent diffusion coefficient for β-chitin scaffolds

The apparent diffusion coefficient (D) of chitin scaffolds was calculated in Origin 2019b software through a Lavenberg Marquardt iteration algorithm applied to equation of diffusion in a cylinder for small times (Crank et al., 1979):

$$\frac{M_t}{M_\infty} = \frac{4}{\pi^{1/2}}\left(\frac{Dt}{a^2}\right)^{1/2} - \frac{Dt}{a^2} - \frac{1}{3\pi^{1/2}}\left(\frac{Dt}{a^2}\right)^{3/2} \tag{6.2}$$

Where M_t is the amount of diffusing substance entering the scaffold at time t, M_∞ is the amount at equilibrium (t=3 min), a is the radius of the cylindrical scaffold.

6.2.2.7.3 Apparent diffusion coefficient for NIBC

For the apparent diffusion coefficient (D), NIBC were taken as plane sheets for the mathematical fitting in Origin 2019b software through a Lavenberg Marquardt iteration algorithm of the following equation (Crank et al., 1979):

$$\frac{M_t}{M_\infty} = 1 - \sum_{n=0}^{\infty} \frac{8}{(2n+1)^2\pi^2} exp\{-D(2n+1)^2\pi^2 t/4l^2\} \tag{6.3}$$

Where M_t is the amount of diffusing substance entering the sheet at time t, M_∞ is the amount at equilibrium (t=3 min), l is the thickness of the plane sheet and n=16.

6.2.2.8 Adsorption of FB1 in beer and milk

6.2.2.8.1 FB1 adsorption in beer and milk

Both beer (CO_2-free) and milk were spiked with FB1 to a final concentration of 1µg/mL. Then dry chitin scaffolds (20 and 50 mg), and PBS swelled chitosan hydrogels (6 and 10 mg dry mass) were incubated with 10 mL of the spiked samples at 37 °C for 90 min in a shaking incubator at 200 rpm (Titramax 1000, Heidolph, UK).

6.2.2.8.2 Sample preconditioning

Once the adsorbents were removed, 100 µL of the remaining sample were diluted to 10 mL with PBS (pH= 7.4), and were loaded onto a 3CC Oasis MAX cartridge, preconditioned with 2 mL methanol/water (1:1, v/v). Two washing steps were carried out by subsequently passing 2 mL of 5% ammonium hydroxide and 2 mL methanol. FB1 was then eluted with 4 mL of 2% formic acid in methanol, and this eluted part was evaporated and reconstituted in 1 mL of 10% (v/v) acetonitrile. Then, 50 µL from the latter were diluted with 20% (v/v) acetonitrile to a final volume of 1 mL.

6.2.2.8.3 LC-MS analysis

The analysis of FB1 was performed in an ultra-high-performance liquid chromatography (Thermo Vanquish) coupled with a triple quadrupole MS system (Thermo Quantitativa) with electrospray ionization (capillary voltage: -3.3 kV, source temperature: 335 °C). The separation of 10 µL sample took place in a Water BEH C18 column (50 x 2.1 mm, I.D. 1.7 µm) by a gradient consisting of a initial 90% mobile phase A (0.1% formic acid in water) and 10% mobile phase B (methanol), to 100% mobile phase B over 15 min, at a flow rate of 0.35 mL/min. Mass spectrometry was performed in multiple reaction monitoring mode with product ion scan at m/z 721.4 (M-H-for FB1), 157 (quantification ion) and 563 (qualification ion). The quantification of FB1 was carried out in Quan Browser software, based on a standard curve (5 pg/mL to 10 ng/mL) with detection limit of 2 pg/mL.

6.2.2.8.4 Adsorption efficiency in milk and beer

The FB1 adsorption efficiency (%) was calculated according to the following equation:

$$\% = \frac{C_i - C_S}{C_i} x100 \qquad (6.4)$$

Where C_s is the residual concentration of FB1after adsorption and C_i is the concentration of the blank sample.

6.2.2.8.5 Amount of bound FB1

The mass of FB1 adsorbed per gram of adsorbent (Q_{eq}, mg/g) was calculated according to the following equation:

$$Q_{eq} = \frac{[(C_i - C_S)xV]}{M} \quad (6.5)$$

Where C_s is the residual concentration of FB1 after adsorption (µg/mL), C_i is the concentration of the blank sample (µg/mL), V is the solution volume (mL), and M is the amount of adsorbent (mg).

6.2.2.9 Molecularly imprinted NIBC hydrogels

6.2.2.9.1 Gel imprinting

Control NIBC gels (non-imprinted) were prepared with both chitosan samples (Chitosan I and Chitosan II) according with the protocol described in section 6.2.2.4, considering an isobutyric anhydride to glucosamine stoichiometric ratio of 4. Similarly, for the imprinting experiments, chitosan solutions (I or II) were prepared by dissolving chitosan in 0.1 M acetic acid (6 g/L) for 16-18 h, followed by the addition of 5.925 mL of methanol, and 4.55 mL of isobutyric anhydride in methanol added with 50 µg of L-phenylalanine (L-phe).The mixture was left in a petri dish at RT for 6 h, to allow gel formation. Once the gels were fully set, three washings were carried out with 100 mL of washing solvent (water/methanol/trifluoroacetic acid 60/39.9/0.1% v/v), followed by two washings with water at 60 °C. Aliquots from the five washings were collected and analysed by HPLC, while the washed gels were frozen at -20 °C, freeze dried for 72 h and stored in a desiccator until further use.

6.2.2.9.2 HPLC analysis

The concentration of L-phe in the washings was quantified by HPLC according to several methods (Allen et al., 1999; Agrafiotou et al., 2009; Haghighi et al., 2015). Briefly, the analysis was carried in a Shimadzu Prominence equipment with UV/Vis detector. The separation of 10 µL injection took place in a 5 µm Phenomenex Kinetex column (4.6x 150 mm), with 60 % vol, Milli-Q water-39.9 % vol. methanol-0.1% vol. trifluoroacetic acid as the mobile phase (flow rate 1 mL/min) for the isocratic elution of L-phe in 12 min run time. A standard curve was run (10-100 µg/mL) from which the L-phe concentration was

calculated by the linear regression of the area under the curve as a function of the concentration. Peak analysis was carried out in SciDaVis software.

6.3 Results and discussion

6.3.1 Characterization of polymeric materials

It is worth mentioning that a comparison between two NIBC hydrogels was attempted. However, a high molecular weight-high degree of acetylation chitosan sample (Chitosan III), obtained from the deacetylation of β-chitin (used in the scaffolds) through the process in Figure 6.2, was not successful for the formation of NIBC hydrogels as shown in Figure E1. Therefore, all the NIBC experiments were carried out with a lower molecular weight-lower degree of acetylation commercial chitosan.

6.3.1.1 Scanning Electron Microscopy

The appearance of the obtained materials, along with the imaging of the morphology of the microstructure of cross-section by SEM are shown in Figure 6.3. Both β-chitin scaffolds (N_2 and conventionally frozen, water content: 94.83%, a_w=0.042) and the NIBC gels (a_w=0.457) displayed a porous structure, however the latter revealed fewer pores with a more compact and smooth structure, yet large diameter (26.64±5.1 μm). In this regard, as shown in the greater magnification images, β-chitin scaffolds produced after N_2 freezing had smaller interconnected pores (10.57±1.9 μm) compared to those from conventional freezing (25.74±10.5 μM), whose surface and pore morphology were similar to previous studies (Maeda et al., 2008). The results are consistent with studies in chitosan hydrogel biomaterials where the internal microstructure depends on the cross-linking and gel formation method (Hong et al., 2007).

The differences between the microstructural features of both β-chitin scaffolds stems on the freezing method utilized before freeze drying. While conventional freezing (-8°C) is considered a slow method, the temperature of liquid nitrogen (-196 °C) is low enough for being regarded as a fast freezing method due to its higher heat transfer coefficient. The formation of large ice crystals generates a greater pore size and, in some cases structure alteration due to the the cooling rate (Sanz et al., 1999). In the case of β-chitin scaffolds, the higher freezing rate in liquid N_2 explains the formation of smaller pores, probably because of the instant appearance of small ice crystal on the surface (Otero et al., 2000).

6.3.1.2 FTIR studies

The FTIR spectra of the β-chitin scaffolds in Figure 6.4a, in all the cases for the dry sample, the scaffold incubated in PBS and FB1 in PBS (1 μg/mL), the characteristic bands

for the amide I (1660 cm^{-1}), amide II (1550 cm^{-1}) and amide III (973 cm^{-1}) were around the expected values (1631,1551 cm^{-1}), except for amide III in which the representative peak was found at around 1025-1026 cm^{-1}. The amide I band (1631 cm^{-1}) appeared as one peak, which differentiates β-chitin from α-chitin (two peaks). The region near 3500 cm^{-1} is given by the -OH groups, which was also observed in all the spectra. The crystalline structure of β-chitin contains intrasheet hydrogen bonds between amide I (-C=O) and amide II (-NH-), denoted by the small peak at 1650 cm^{-1} (Jang et al., 2004). Intersheet H- bonds between amide and oxygen from the carbonyl groups in adjacent chains, produce a parallel arrangement of poly-N-acetylglucosamine chains with no intersheet hydrogen bonds, resulting in a more flexible type of chitin (Elieh-Ali-Komi and Hamblin, 2016).

On the other hand, the FTIR spectra for the NIBC gels also displayed the bands specific for amides (HNC=O) I (1629 cm^{-1}) and II (1540 cm^{-1}). In addition, the presence of O-acyl ester groups, denoted by the band absence at 1750 cm^{-1}, along with the presence of methyl groups, indicated by the three bands between 2840 and 3000 cm^{-1}(v -C-H), and bands at ~1374 (δ_S-$CH(CH_3)_2$), ~1023 (γ -CH_3). As it can be noted in Figures 6.4a and b, similar wavenumber and absorbance intensity values were found between the dry and PBS incubated samples, with a somewhat lower absorbance intensity for the materials incubated with FB1. However, the differences may lie within experimental error of the FTIR determinations using a portable FTIR device. Further clarification in this regard can be obtained in future transmission FTIR studies in KBr tablets, in which the amount of sample can be controlled and associated to peak shifts upon binding (Peng et al., 2016).

6.3.2 Swelling and diffusion properties for β-chitin scaffolds and NIBC gels

The swelling ratio of β-chitin scaffolds at room temperature is shown in Figure 6.5a, where it can be noted that for both freezing methods the swelling equilibrium was achieved in less than 10 minutes. Of note, a greater swelling ratio was achieved when more amount of scaffold was incubated in PBS. Although the liquid N_2 frozen scaffolds showed greater swelling than the conventionally frozen systems (12.28±0.77 for 4 g, 14.22±2.11 for 7 g), the resulting material fell apart from 40 min onwards (Figure E2). This is attributable to the quick freezing method that led to a mechanically weaker structured. Perhaps, the larger pore size observed by SEM in conventionally frozen scaffolds allowed good swelling ratios (7.73±0.69 for 4 g, 12.25±0.69 for 7 g) within its strengthened structure achieved through slow freezing. A greatest degree of swelling can be observed when the pore structure is more open, yet interconnected (Goycoolea et al., 2011), as observed in conventionally frozen samples.

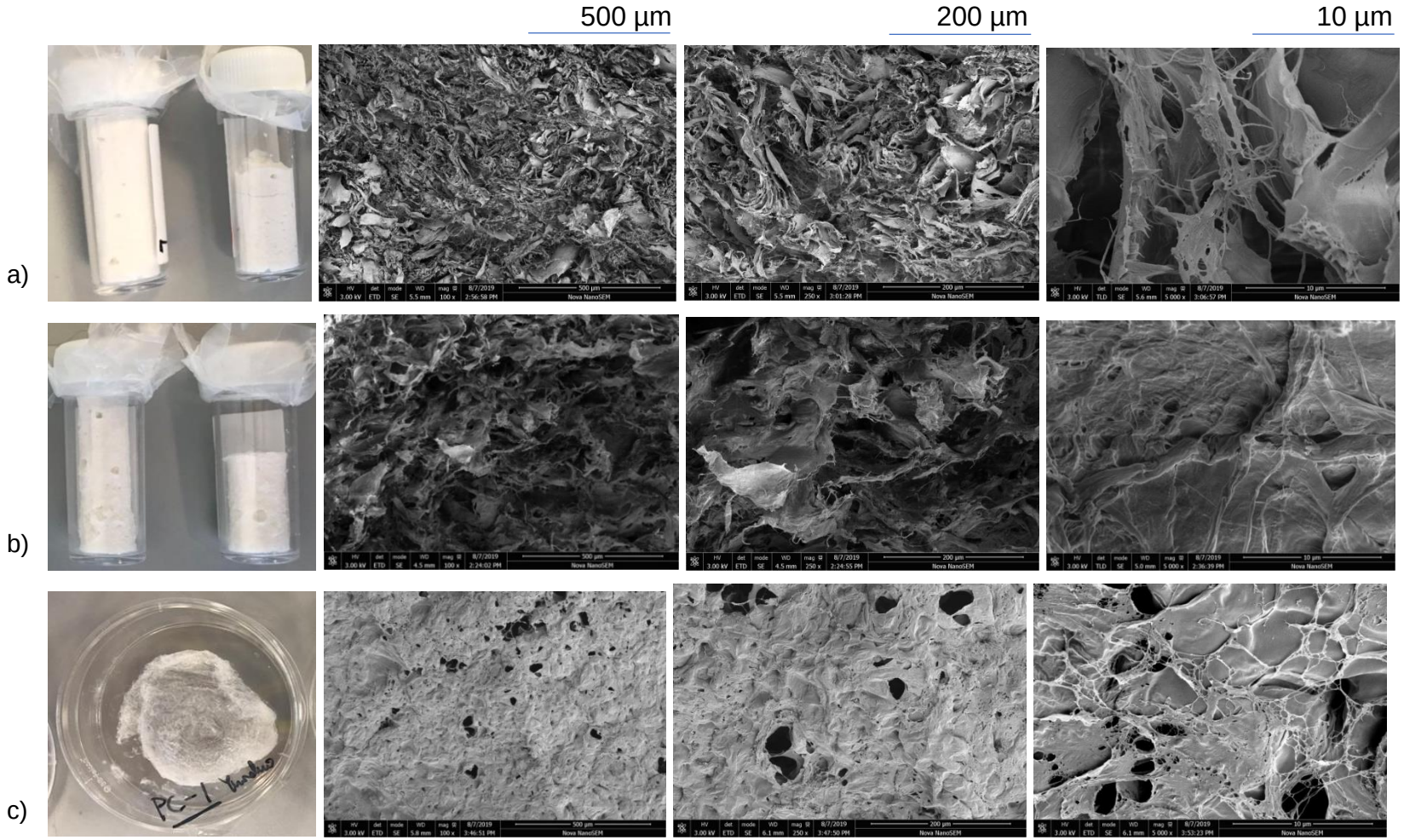

Figure 6.3 Photographs and SEM images for (**a**) N_2 and (**b**) conventionally frozen chitin scaffolds and (**c**) NIBC hydrogels (chitosan I)

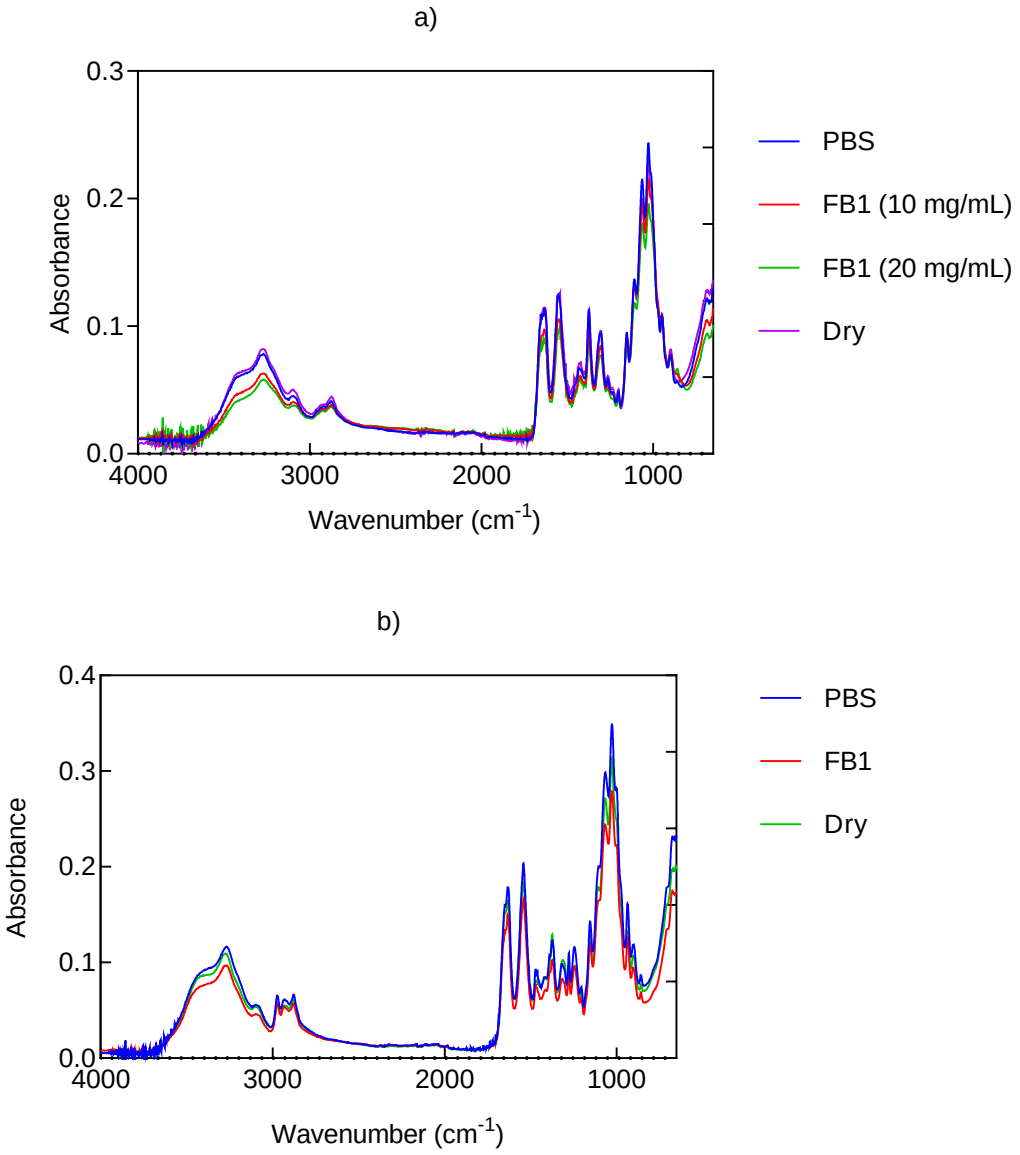

Figure 6.4 FTIR spectra of (**a)** β-chitin scaffolds as dry, incubated with PBS (10 mg/mL) and FB1 (1 µg/mL) in PBS (10 and 20 mg/mL) samples; and (**b**) NIBC hydrogels (chitosan I) as dry, incubated with PBS (0.68 mg/mL) and FB1 (1 µg/mL) in PBS (1 mg/mL) samples (n=3)

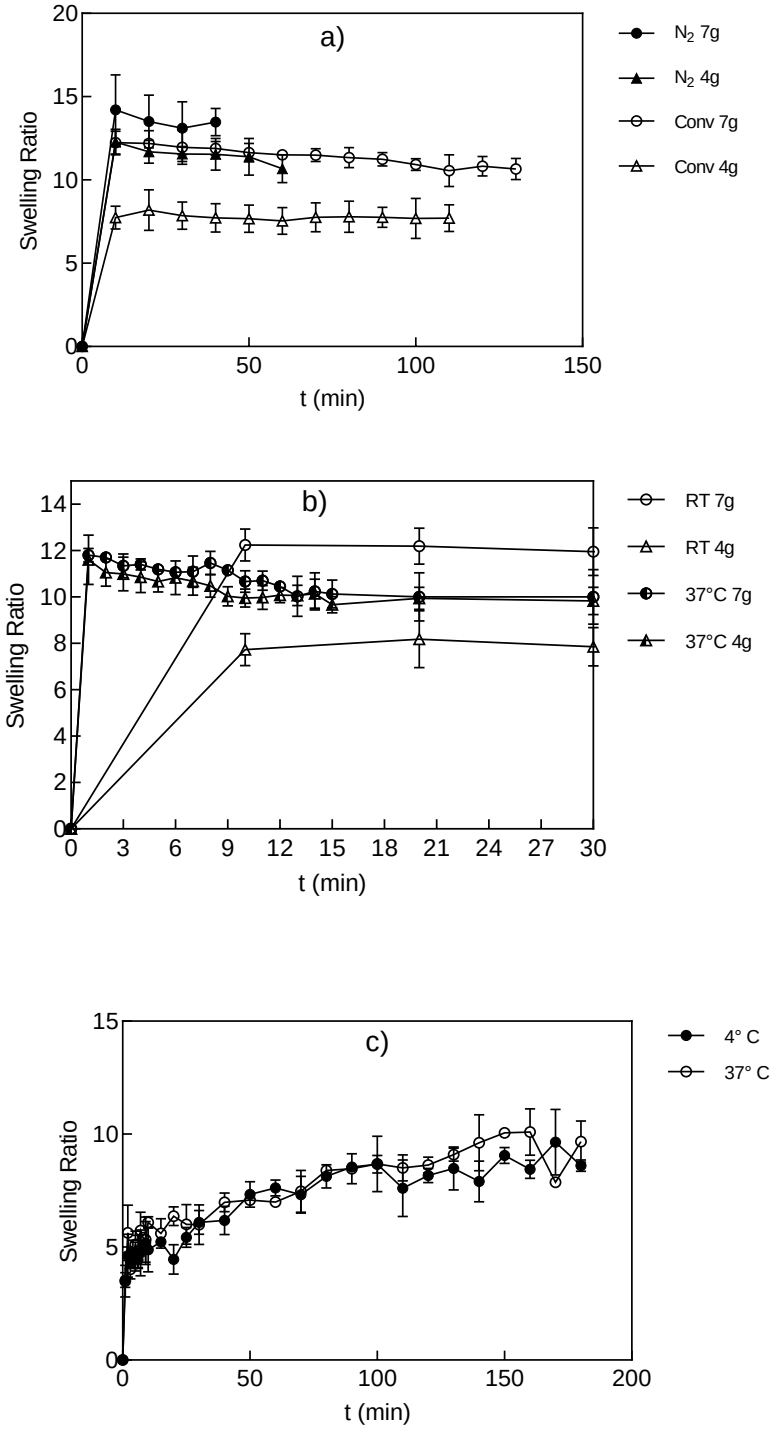

Figure 6.5 Swelling isotherms in PBS (pH 7.4) of (**a**) β-chitin scaffolds (6 mg/mL) at two preparation weights (4 and 7g) frozen by conventional (Conv) and liquid nitrogen (N_2) methods (RT), (**b**) conventionally frozen β-chitin scaffolds (6 mg/mL) at two incubation temperatures (RT and 4 °C) for two preparation weights (4 and 7g), (**c**) and NIBC gels (0.5 mg/mL) at two incubation temperatures (RT and 4 °C) (n=3)

Based on the observed performance, an exploration on the incubation temperature was carried out in conventionally frozen β-chitin scaffolds (Figure 6.5b), where similar swelling equilibrium (t=1 min) values were observed at 37 °C, regardless of the mass density of scaffold material (11.60±1.07 for 4 g, 11.81±0.29 for 7 g). Unlike the observed in chitin scaffolds, there was no effect from the incubation temperatures in NIBC gels (Figures 6.5c), as indicated by the similar attained swelling equilibrium values (t= 3 min) of 4.62±0.29 (4 °C) and 5.63±1.22 (37 °C). In general, the swelling ratios obtained with the materials in this work were higher than the reported values for a copolymer-based hydrogel (Akala et al., 1998) and crosslinked chitosan gels (Hong et al., 2007). Nevertheless, the values for the β-chitin scaffolds were comparable to the swelling degree (14) reported for the same material (Maeda et al., 2008); while the equilibrium swelling ratios from NIBC hydrogels were lower to those (10.33± 1.15) reported for chitosan gels produced from alkali chitin. The swelling properties are influenced by the pH value, where more swelling is favoured at a pH below 7.6, in which the solvent uptake is promoted by the number of protonated $-NH_3^+$ groups (Goycoolea et al., 2011). Although swelling takes place through the convective flow of solvent through the pores, followed by its diffusion throughout the polymer network (Goycoolea et al., 2011), which might imply a more favoured performance in large pore materials (conventionally frozen scaffolds, NIBC hydrogels); the swelling ratios of chitosan hydrogels can be reduced by increasing the degree of crosslinking (Rohindra et al., 2004), which might explain the lower swelling ratios from NIBC-hydrogels to those in β-chitin scaffolds.

6.3.2.1 Apparent diffusion coefficients (D) of chitin scaffolds and NIBC hydrogels.

The apparent diffusion coefficients of β-chitin scaffolds incubated at 37 °C had a greater magnitude for the scaffold produced with less amount of chitin dispersion, as presented in Table 6.1. The high correlation coefficients (r^2) demonstrated an appropriate fitting to such mathematical expression, which was derived from a model resolved to a cylindrical shape from Fick's diffusion equation (Goycoolea et al., 2011).

Lower values were found for NIBC gels as indicated in Table 6.2, where the apparent diffusion coefficients calculated from the data until equilibrium (3 min) at 4°C and RT, were fitted through 17 iterations (n=16) to the equation 6.3 for the diffusion on a plane sheet (Crank et al., 1979). As noted, the selected mathematical model was a good descriptor of the data variability given by the good correlation coefficients (r^2). In such equation, swelling occurs in a thin hydrogel layer, as the in-plane range is bigger compared to the thickness dimension, therefore the adsorption is mainly carried at the

top surface, with imperceptible contribution from the edges. Because of that assumption, the flux takes place in the thickness direction, as a function of time and position (Yoon et al., 2010). Based on the average diffusion coefficients achieved at both temperatures, the incubation at 37 °C was selected for mycotoxin binding experiments due to its higher value. In addition, it has been reported that higher temperatures could enhance the swelling properties, due to dissociation of the hydrogen bonds in the amino groups, leading to the presence of more free water within the gel network (Rohindra et al., 2004).

Table 6.1 Apparent diffusion coefficients for chitin scaffolds incubated at 37 °C in PBS (pH 7.4)

Sample	Length (cm)	Radius (cm)	D ($x10^{-5}$ m^2 s^{-1})	r^2
4 g	2.2	0.65	$1.93±4.51e^{-7}$	0.99±0.003
7 g	4	0.6	$1.62±2.64e^{-7}$	0.99±0.005

Table 6.2 Apparent diffusion coefficients for NIBC hydrogels incubated in PBS (pH 7.4) at varying temperatures

Temperature	Thickness (mm)	Area (mm^2)	D ($x10^{-7}$ m^2 s^{-1})	r^2
4 °C	3.44±0.21	941.84±36.62	$1.29±4.09e^{-8}$	0.97±0.03
37 °C			$1.77±4.04e^{-8}$	0.88±0.09

6.3.3 Adsorption of FB1 from PBS, beer and milk by chitin and NIBC scaffolds

The results for the adsorption efficiency and bound FB1 in beer and milk are shown in Figure 6.6. Higher adsorption efficiency values were found when the materials were incubated in beer, as denoted in all the materials. In addition, even when in the case of beer the incubation with a higher density (mass) chitin scaffold portrayed a greater adsorption percentage (Figure 6.6a), the incubation with NIBC hydrogels revealed more FB1 bound per gram of polymeric material for both food samples (Figure 6.6b). Studies on the adsorption of OTA also reported a better performance from chitosan compared to that from chitin (Quintela et al., 2012). The marked difference between both materials can be explained in terms of the N-acylation process of NIBC hydrogels, which could enhance the adsorption. This is in concert with previous reports on cross-

linked chitosan, where the role of -OH, and -NH_2 groups in binding patulin was underscored (Peng et al., 2016).

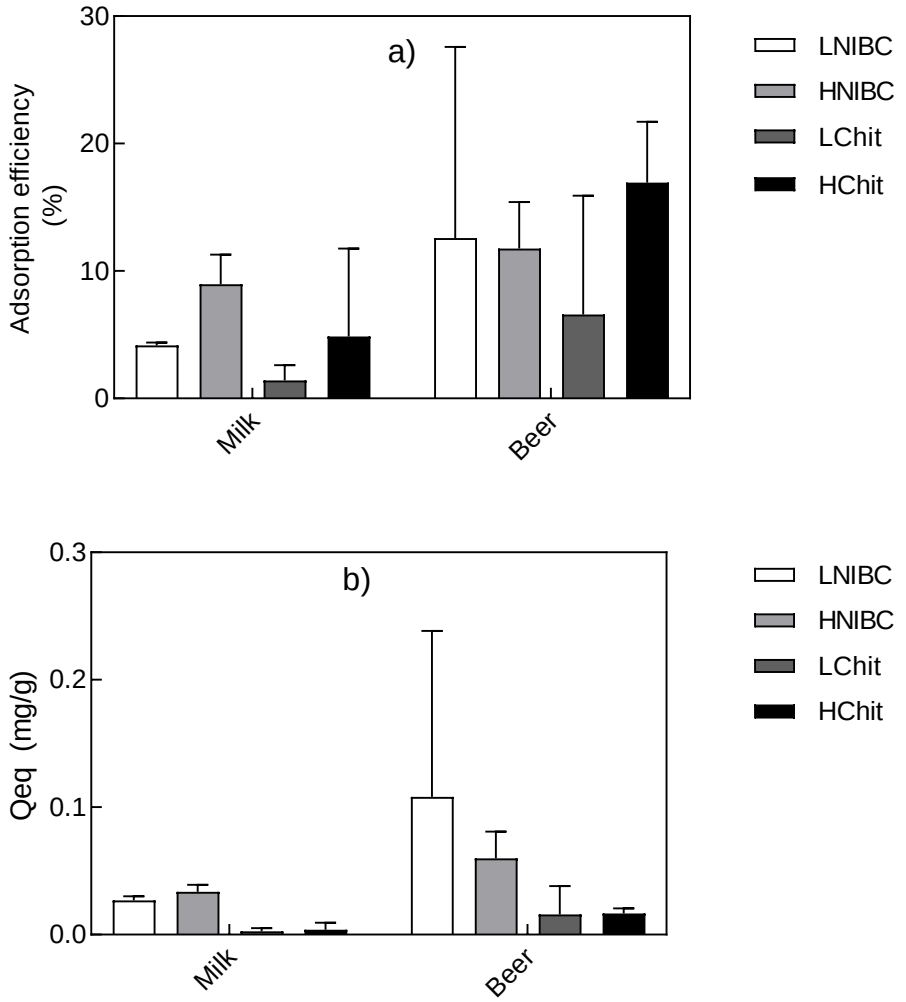

Figure 6.6 (**a**) Adsorption efficiency(%) and (**b**) bound FB1 (mg/g) for NIBC hydrogels at 0.6 (LNIBC) and 1 mg/mL (HNIBC), and chitin scaffolds at 2.2 (LChit) and 5 (HChit) mg/mL in milk (pH 6.56) and beer (pH 4.54).(n=2 as two consecutive days)

The low adsorption efficiencies found in milk upon incubation with low (1.41%) and high (4.87%) β-chitin and low (4.17%) and high (8.97%) NIBC hydrogels, might suggest the interaction of this materials with some milk components such as proteins. This is consistent with the notion that, prior to its isolation, chitin naturally occurs in association with proteins and carbohydrates (Elieh-Ali-Komi and Hamblin, 2016). In addition, at a higher incubation temperature, as in the case of 37 °C, some proteins might exhibit a certain unfolding degree, which enhances the probability for their

fixation to the adsorption materials (Assaf et al., 2018). Another reason of the higher adsorption and bound FB1 displayed by NIBC hydrogels in beer might be related to lower pH of beer (pH 4.54) compared to that of milk (pH 6.56). As chitosan contains -OH and -NH_2 groups, which lead to the formation of hydrogen bonds, low pH values result in protonated amino groups (intrinsic pKo ~ 6.0 ± 0.1,) (Rinaudo et al., 1999). Furthermore, the structure of FB1 has aliphatic amino groups (pKa>9), tricarballylic acid (3.49<pKa<5.83) which suggest that the molecule is present as zwitterion in milk, thus promoting electrostatic interactions (Baglieri et al., 2013). Nevertheless, the lower pH of beer in which the amino groups of chitosan appear protonated with the presence of positive charges, while negative charges are provided by the tricarballylic acid in FB1, seems consistent with the proposal that binding of FB1 by NIBC hydrogel matrices is most likely to promoted by the concomitant contribution of electrostatic and hydrophobic interactions. It is worth mentioning that milk was selected for this set of experiments because of its composition, where the mixture of water, fats, minerals, proteins, sugars, and vitamins, is regarded as a complex/challenging matrix, commonly utilized for assessing the effectivity of novel biosensors due to the presence of interfering components (Ahmed et al., 2017).

6.3.4 Molecularly imprinted NIBC hydrogels (MINIBC)

In an attempt to fabricate a chitosan–based scaffold material with high FB1 adsorption capacity, a molecularly imprinting protocol of NIBC (MINIBC) hydrogels was evauated using the aminoacid L-phe as an structural analog of ochratoxin A (Espinosa-García et al., 2007). To this end, as a first step, the N-acylation reaction and gelation of NIBC was carried out in the presence of a stoichiometric excess of L-phe and assessed qualitatively whether this interfered with the gel formation process. As shown in Figure E3, the NIBC hydrogels prepared in the presence of L-phe did not differ in appearance from control NIBC hydrogels regardless of the chitosan sample utilized in their synthesis. In both cases, the N-acylation of chitosan was completed with further achievement of a transparent water insoluble hydrogel similar to previously reported NIBC chitosan gels (Félix et al., 2005). It was interesting to confirm this, notwithstanding that the acylation of aminocarboxylic acids is promoted by carboxylic acids, anhydrides or halides, which leads to the possible interference of amino groups in L-phe through its acylation with N-isobutyric anhydride. The particular acylation of phenylalanine with anhydrides results in low yields of an impure product (Franzmann, 1983). To the best of our knowledge, the presence of L-phe during molecular imprinting did not affect the formation of NIBC hydrogels, which portrayed similar properties to those found in control hydrogels (Figure E4).

As a second step in the synthesis of MINIBC hydrogels, the removal of L-phe by consecutive washings was assessed. HPLC UV/Vis chromatograms of the five washings collected from molecularly imprinted NIBC hydrogels (chitosan I) is shown in Figure 6.7, in which L-phe was eluted at a retention time (Rt) of 2.6-3 min, and its peak area was analysed for quantifying µg/mL in all the washings.

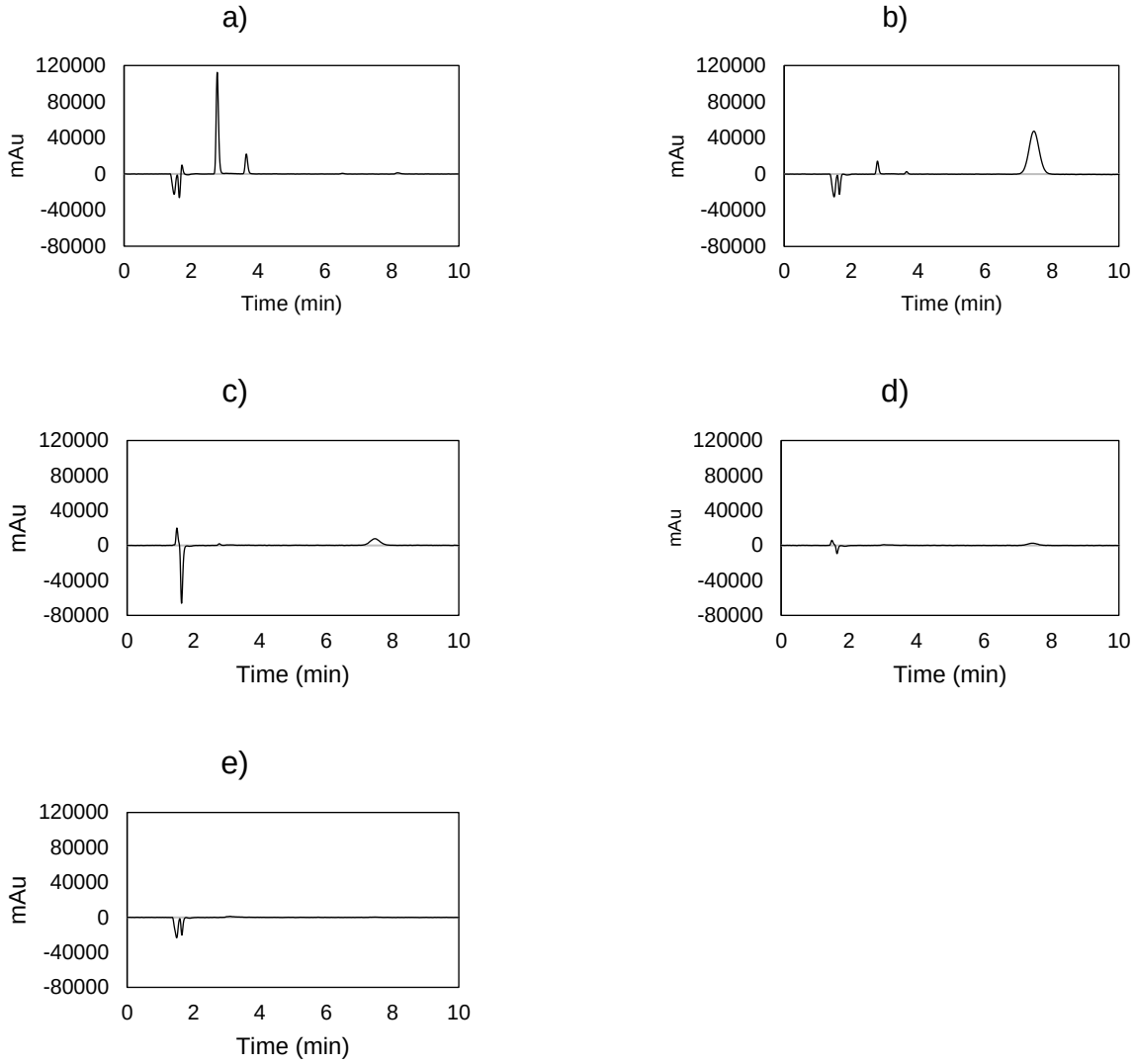

Figure 6.7 (**a**) Reversed-phase HPLC-UV/Vis chromatograms for the (**a**) first, (**b**) second and (**c**) third washing with 60 vol.-% Milli-Q water:39.9 vol.-% methanol:0.1 vol.-% trifluoroacetic acid, and washings number (**d**) four and (**e**) five with Milli-Q water at 60 °C for NIBC hydrogels imprinted with L-phenylalanine (Chitosan 1)

As noted, the height of this peak diminished after the third washing, where the L-phe peak was not visible. Small peaks (200-500 mAu) with Rt of 1.5-1.9 and 3-3.5 min were found before and after the L-phe peak, respectively. Additionally, a high intensity peak (>40000 mAu) was observed around 7-8 min, especially in washing 2. Those additional peaks might be other chemical compounds generated during gel formation as reported in a L-phe molecularly imprinted crosslinked chitosan membrane (Figure E5), where more inorganic compounds are produced to enhance the density of the hybrid network (Jiang et al., 2006).

The amount of L-phe quantified in each washing is depicted in Figure 6.8 for both NIBC hydrogels, where the amount of template decreased throughout each washing. Compared to the concentration calculated from the first washing (31.07 µg/mL), MINIBC hydrogels from chitosan I showed a reduction of L-phe of 85% after the second washing (4.53 µg/mL), with minimal amounts after washings 3 (0.71 µg/mL) ,4 (0.14 µg/mL) and 5 (0.051 µg/mL). On the other hand, MINIBC produced from chitosan II also had a downward trend, where more L-phe was quantified after the first (21.48 µg/mL) and second washings (13.65 µg/mL) with a 63.54% reduction, and subsequently washed off after the third washing (2.33 µg/mL).

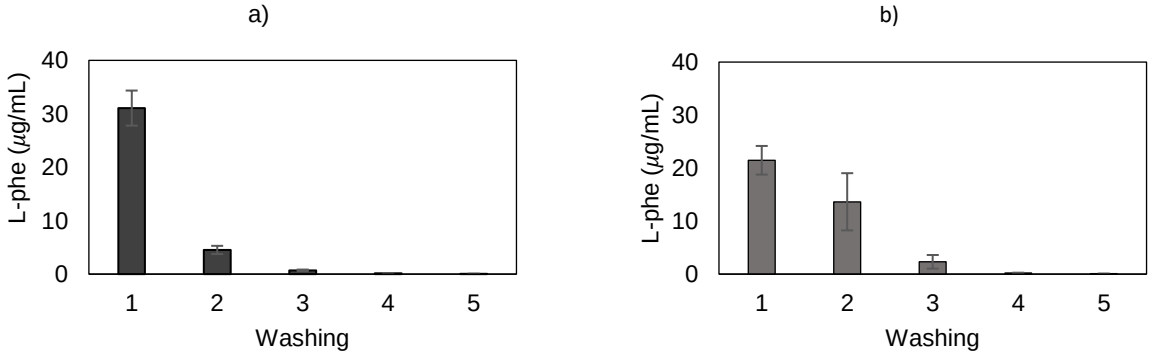

Figure 6.8 Mean concentration of L-phe in each washing of molecularly imprinted hydrogels produced with (**a**) chitosan I and (**b**) chitosan II (n=3)

Significant differences were found for the results of the first washing between both MINIBC samples ($p<0.0174$), which also indicated the effect of a greater DA and MW in chitosan II for a higher L-phe retention. The interaction of chitosan with L-phe depends on the structure of both the polymeric polysaccharide (Figure 6.1) and the amino acid (Figure E6). Because of its amino and hydroxyl groups, chitosan has the potential of forming hydrogen bonds with amino acids (Jiang et al., 2006). Likewise, L-phe contains a benzene ring and hydrocarbon units (amino groups and carboxylic acid), for cation and hydrophobic interactions, respectively (Dougherty, 1996). From

the noncovalent interactions, the aromatic side chain in phenylalanine could interact with chitosan through cation-π interactions, as the benzene ring exhibit a non-spherical charge distribution (quadrupole moment) with potential binding especially in gas phase (Dougherty, 1996). However, due to N-acylation reaction NIBC are bound to be devoid of free amino groups (Félix et al., 2005). Hence, it is suggested that hydrophobic interaction occurred between chitosan and L-phe, where a greater binding was found in MINIBC hydrogels from chitosan II, whose higher DA value (23%) is expected to exhibit more hydrophobic interactions, also favoured by the hydrophobicity from the aromatic group in L-phe (Luan et al., 1992; Sorlier et al., 2001).

The observable gradual reduction in the amount of washed L-phe, especially in chitosan II, suggested that the aminoacid used as template was retained during gel formation and subsequently washed (template removal).

6.4 Conclusions

This study was aimed to analyse the structural differences of two polymeric materials, namely β-chitin scaffolds and NIBC hydrogels along with their performance as potential adsorbents for FB1. Results indicated improved swelling from conventionally frozen materials (prior to freeze drying) with greater swelling and mycotoxin adsorption properties from NIBC hydrogels. The pH regulated adsorption mechanism suggested that β-chitin scaffolds bound FB1 through electrostatic interactions, while NIBC hydrogels bound this mycotoxin through hydrophobic interactions. This is a preliminary exploration as more optimization efforts should be carried out in terms of the incubation conditions and experimental setting. The finalized application is expected to be implemented as either cartridges/columns for sample pre-treatment or as a supply change step for the decontamination of samples from diverse fields (clinic and food analysis, feed decontamination, etc.)

Due to the advantageous properties of NIBC hydrogels, an exploration of their potential as MIP material was explored using L-phenylalanine as a surrogate model of ochratoxin A. The results revealed the potential imprinting L-phe within the NIBC matrix, with an apparent more notorious effect from chitosan of higher degree of acetylation. The presence of this amino acid did not interfere with both gelation and imprinting, and its removal was achieved with ease. This study enabled to confirm that the two general steps entailed in the synthesis of a molecularly imprinted NIBC hydrogel material were successfully achieved using L-phe as an analog template during the N-acylation of chitosan using isobutyric anhydrdide. It remains to be confirmed in future studies whether the imprinting effect against the template analyte was achieved, as originally hypothesised. Such studies must evaluate the rebinding

of L-phe in comparison with non-imprinted control NIBC hydrogels, and whether greater affinity and selectivity can be achieved against ochratoxin A and other compounds of relevance that share structural features with L-phe. This approach may also prove relevant for the synthesis of other molecularly imprinted materials such as electrospun nanofibers and nanoparticles. It is expected that the developed approach derives in high affinity materials with chiral recognition as disclosed for some chitosan-based materials (Jiang et al., 2006).

Chapter 7
General discussion

7.1 Introduction

Mycotoxins remain as relevant secondary metabolites due to their hazardous effects towards humans and their worldwide occurrence in several food products. Contamination with such toxic compounds takes place during pre- and post-harvest stages, with high risk of consumption if they remain undetected or no detoxification strategies are applied. Although mycotoxins are commonly quantified by widely explored instrumental methods such as liquid chromatography and enzyme-linked immunosorbent assay, the development of biosensing techniques with multiple biorecognition elements has led to advancements in the limit of detection, quantification time and sample preparation for these novel approaches. The early estimated mycotoxin contamination rate of 25 % has been updated to almost 80% of the agricultural goods produced worldwide. This corresponds to recent improvements in new analytical methods, where excellent sensitivities have been achieved (Liu et al., 2020). Therefore, in order to control, monitor, and prevent mycotoxin outbreaks the aid of biosensing techniques is more than adequate especially considering that conventional methods require long times, expensive instruments, and specialized users, which in some cases render them unsuitable for on-site analysis (Lee et al., 2013). During the length of this PhD project, the core of the investigation efforts was mainly focused on understanding, improving, and developing biosensing methods for the quantification of mycotoxins, including AFB1 and FB1.

On the other hand, even when chemical adsorbents (clays, activated charcoal, modified polymers) have been extensively used for mycotoxin detoxification, their utilization in food products might be restricted or banned because of their secondary effects (Liu et al., 2020). Hence, the development of approaches based on polymeric structures from natural sources, represents an environmentally friendly alternative for mycotoxin decontamination, where in the case of waste-based materials, can be included in a circular economy model. For those reasons, the last part of this work consisted in a preliminary exploration of the performance of waste-based polymeric materials, namely β-chitin scaffolds and NIBC hydrogels, as either potential mycotoxin decontaminants or promising supports in molecular imprinting.

These new developments are a solution, especially in low- and middle-income countries where mycotoxins are related to high mortality and morbidity rates, and their screening at field/farming levels through low cost, user-friendly systems is a necessity (Wild et al., 2015). Likewise, the application of waste-based materials from the food

industry in biosensing and decontamination, for instance chitin and chitosan from the crustacean industry, increases the profit of their manufacturing process, while reducing its environmental impact which might be related to less mycotoxin incidences (Assaf et al., 2018; Liu et al., 2020).

As addressed in the literature review in **Chapter 2**, the development of new biosensing techniques is appropriate for the accomplishment of sensitive methods. In the case of the detection and quantification of fumonisin B1 (FB1), even when antibodies were applied as biorecognition elements, their versatile utilization in combination with nanomaterials such as quantum dots and carbon nanotubes derived in limit of detections as sensitive as 0.00000046 µg/L (Masikini et al., 2015) and 0.0000038 µg/L (Masikini et al., 2016), mainly mediated by electrochemical responses. The advantages of electrochemical detections were also explored for the application of molecularly imprinted polymer nanoparticles (MIPs), with the lowest limit of detection (LODs) of 0.000000002 µg/L for FB1, promoted by the interaction between FB1 and the recognition site (cavity) (Munawar et al., 2020). The optimal performance from MIPs motivated the exploration of molecular imprinting in natural polymers such as chitosan derivatives, discussed in **Chapter 6**, where N-isobutyryl chitosan (NIBC) hydrogels are conceived as a promising matrix for the detection and adsorption of different targets. Furthermore, the use of aptamers (ssDNA) for the detection of FB1 has resulted in competitive LODs, equivalent to 0.000003 µg/L (He et al., 2020) and 0.0000019 µg/mL (Niazi et al., 2019), when fluorescent nanoparticles and dyes were employed. From this review, a gap was identified as the majority of aptasensors utilized modified DNA sequences, or complex designs with complementary strands, which limits their application as an affordable and point-of-care method. Yet, when optimized, simple aptasensing techniques, including the widely reported colorimetric detection of mycotoxins with gold nanoparticles (AuNPs), could reach sensitive levels as demonstrated in **Chapter 5**, where the appropriate signal was translated to a LOD of 0.000000056 µg/L (Mirón-Mérida et al., 2021). Another finding from the review in **Chapter 2**, was the absence of paper-based aptasensors for the detection of FB1. In view of this, the exploration of the diffusive properties of paper matrices and the improvement of a paper-based enzymatic detection of aflatoxin B1 (AFB1), were respectively explored in **Chapter 3** and **Chapter 4**.

As outlined in Figure 7.1, the first investigation stream was focused on the study of paper as a biosensing platform. In order to assess diffusion and imbibition phenomena in a paper matrix, in **Chapter 3**, aqueous ink solutions were prepared as model samples, whose application and flow was recorded in 3MM chromatography paper. The study was divided in two parts, the first experimental setting aimed to apply the

model samples to obtain their flow data overtime, from which different mathematical models were fitted for calculating the diffusion coefficients. Such mathematical expressions included models for explaining the radial flow (Xiao et al., 2012), wicking (Callegari et al., 2011), cylindrical and spherical imbibition (Elizalde et al., 2015). The second experimental part was carried out on the characterization of the ink models, from which a greater ink concentration exhibited higher densities, dynamic viscosity values, and a decreasing interfacial surface tension. The measurement of the contact angle was not achieved as the porosity of the paper matrix did not allow the required drop formation. The association of these experimental data, the fitted diffusion coefficients, and the measured porosity of paper (ethanol displacement) was included in the selected equations, for the calculation of their corresponding permeability. The comparison of the latter (experimental permeability) with a theoretical permeability, given by Kozeny-Karman model (Xiao et al.,2012), functioned as validation step for the mathematical fitting.

Another exploration of paper as a biosensing platform was performed in **Chapter 4**, where Elman's colorimetric method was selected as a model mechanism for the quantification of AFB1, based on its inhibitory effect towards acetylcholinesterase (AChE) (Ellman et al., 1961). The aim of this chapter was to evaluate the effect of chitosan on the enhancement of the colour intensity, through the application of Ellman's reaction on a microfluidic-paper-based analytical device (μPADs). This approach rather than establishing a new biosensing method for detecting AFB1, worked as a suitable platform for unveiling the differences in colour, when AChE was immobilized in genipin cross-linked and free chitosan, with varying degrees of acetylation (DA) and molecular weight (MW). A better performance for the target-regulated colorimetric signal was acquired with the homogenous effect of a high DA and high MW chitosan sample crosslinked onto the test zones of the μPADs (Figure 7.1).

The second research stream was oriented towards the aptamer-based detection of mycotoxins, precisely FB1. Another finding from the review of **Chapter 2** was the reported existence of two FB1 specific aptamers selected by systematic evolution of ligands by exponential enrichment (SELEX), the main method in which a DNA pool is incubated in different selection rounds with the target molecule, followed by the partition of aptamer-target complexes and the amplification of the high affinity sequences (Gopinath, 2007). These aptamers were composed by 80 and 96 nucleotides (nt), from which the longest sequence has been used in more biosensors compared to other aptamers for FB1 (**Chapter 2**). Therefore, **Chapter 5** was focused on the comparison of the 96 nt aptamer with a 40 nt ssDNA, derived from the main 80 nt sequence. An exploration of the binding conditions (buffer, temperature, time) was

carried out for a colorimetric method designed through the adsorption of aptamers on the surface of AuNPs, and its FB1-governed aggregation induced by NaCl. Unlike the short sequence, the 96 nt aptamer was the most sensitive and portrayed specificity to FB1. This was harnessed in the development of a bulk biosensing analytical method, by coupling in it with robust methods such as asymmetric flow field-flow fractionation (AF4) with multi-angle laser light scattering (MALS) and UV/Vis detection (Figure 7.1).

The last experimental stream explored the potential application of natural polymers, namely chitin and chitosan, for the decontamination of mycotoxins. To this end, **Chapter 6** included the preparation of polymeric materials such as β-chitin scaffolds and NIBC hydrogels for the investigation of their structural and swelling properties and their performance as adsorbents of FB1 in milk and beer. Even though β-chitin exceled in their swelling ratios, NIBC hydrogels were more efficient in terms of the amount of FB1 adsorbed to the polymeric material (Figure 7.1). Finally, derived from the efficiency of NIBC structures, its utilization as a potential molecularly imprinted polymer was also assessed. A surrogate molecule (L-phenylalanine) was used as a template, with no observable interference on the hydrogel formation during the N-acylation reaction. L-Phe was successfully removed from the putative molecularly imprinted NIBC hydrogels after subsequent washing steps (Figure 7.1). Nevertheless, both results require further optimization and exploration, hence they should be regarded as preliminary estimations of the potential of these polymeric materials.

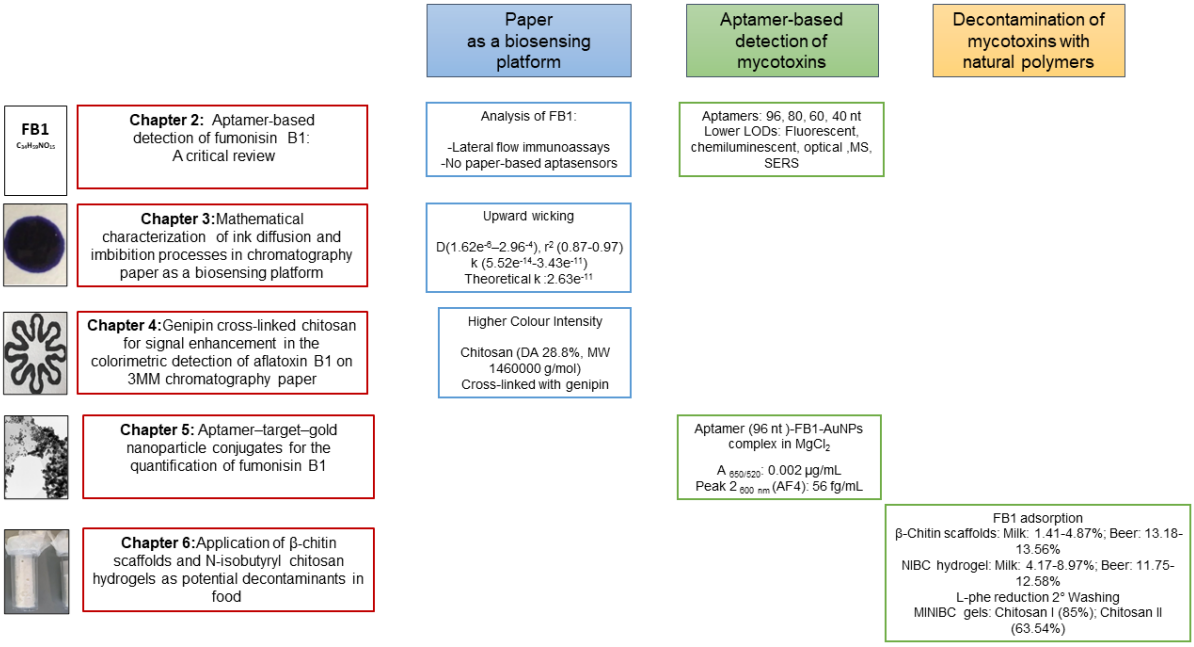

Figure 7.1 Schematic representation of the thesis with relevant results

7.2 Summary of the main experimental results

7.2.1 Aptamer-based detection of FB1

As already mentioned in **Chapter 2**, apart from the excellent performance of some immunosensors and MIPs, aptamers are a satisfactory alternative with ideal limits of detection and assay times. Occasionally, aptamers are considered as artificial antibodies, with the advantages from their cost-effective preparation, fast synthesis, small size, and wide versatility (Gopinath, 2007). As noted in Figure 7.2, from the total 32 reviewed aptasensors documented from 2012, 28.13% have been reported from 2012 to 2016, while a greater number of developments (71.88%) has broadened from 2017 to date. Nevertheless, in order to be competitive to other sensitive techniques, the first goal in biosensing is the achievement of good detection limits. In this regard, only 11 aptasensors (34.37%) reported LODs below 1 ng/L (0.001 µg/L). In agreement with a majority of designs with the 96 nt aptamer (n=24,75%), from the 11 most sensitive aptamer-based biosensors, 63.63% were designed with this long-length sequence, while 36.36% were reported without specifying the length and sequence of the utilized aptamer. As denoted in Figure 7.2, an evident benefit from electrochemical, Raman and fluorescent analysis was observed. Unspecified sequences achieved high sensitivities when coupled with surface-enhanced Raman scattering, previously described as a powerful and reliable method (He et al., 2020b; Wu et al., 2020b), along with fluorescent mechanisms (He et al., 2020a; He et al., 2020b), which in both cases were enhanced by the hybridization of aptamers with complementary strands. On the other hand, principles using the 96 nt were also favoured by their translation into fluorescent and electrochemical signals. In the case of fluorescent analysis, dyed complementary DNA (Yue et al., 2014), fluorescent labelled combined with quencher labelled sequences (Liu et al., 2018), and fluorescent-magnetic nanoparticles (Niazi et al., 2019) were ideal for a robust performance, through aptamer hybridization. Moreover, electrochemical analysis is an affordable, reusable, simple, and occasionally miniaturized alternative for a selective mycotoxin detection, whose signal can be enhanced via aptamer hybridization (Han et al., 2020; Wei et al., 2019; Wei et al., 2020). As discussed in **Chapter 5**, when the binding conditions and selected signals are optimized, simple techniques could be directed into powerful biosensing methods. This was denoted in the formation of an aptamer-target-AuNPs conjugate, where the specific performance of aptamer 96 nt in $MgCl_2$, resulted in an aptasensor comparable to those previously discussed. As indicated in Figure 7.2. (red x symbol), the aptamer-based optical assay in this work was enhanced by the analysis of samples by AF4, which refined the LOD to a value at the same level of electrochemical-, fluorescent- and Raman-based methods, with the advantage of the absence of complementary strands or labelling agents (Mirón- Mérida et al., 2021). This

successful application was mainly boosted by the combination of robust analytical methods and the inclusion of the specific ions, capable to reduce nonspecific binding and promote the formation of aptamer-target complexes (Gopinath, 2007).

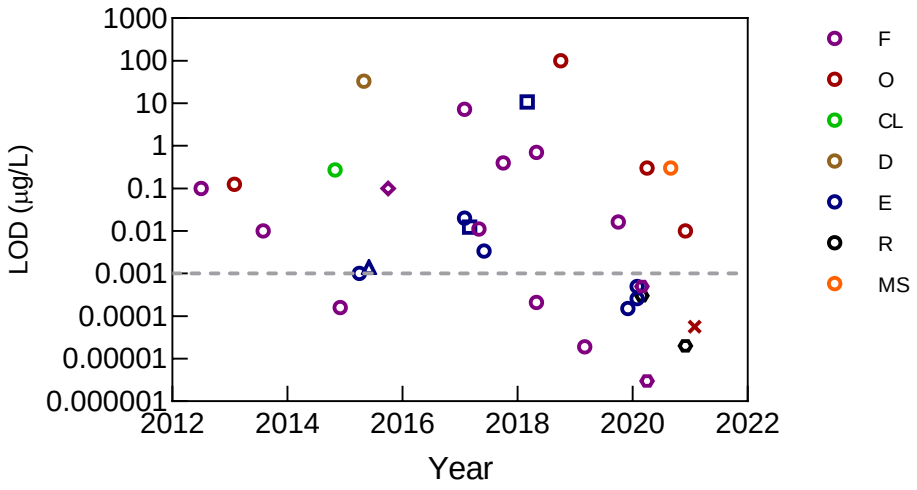

Figure 7.2 Aptamer-based biosensors reported since 2012 for the detection of FB1 through fluorescent (F), optical (O), chemiluminescent (CL), deflection (D), electrochemical (E), Raman (R), and mass spectrometry (MS) with a 96 nt (circle), 80 nt (triangle), 60 nt (rhombus), 40 nt (square) and not specified (hexagon) sequence. The LOD from the biosensing approach of this thesis through the inclusion of AF4-MALS (peak area 600 nm) is presented as a red x symbol.

7.2.2 Diffusion of samples in paper matrices

As addressed in **Chapter 3**, five ink diffusion models were well fitted to selected models of radial flow (Xiao et al., 2012), upward wicking (Callegari et al., 2011), cylindrical and spherical imbibition (Elizalde et al., 2015) of samples in porous media. Nevertheless, the calculation of the experimental permeability, by including the measured values with the fitted diffusion coefficients, was compared to the theoretical permeability, estimated with Kozeny-Karman model (Xiao et al.,2012), for the confirmation of the most suitable expression for describing the flow of the selected model sample within the structure of 3MM chromatography paper. Aside from the numerical confirmation, a graphical comparison of all the values at different ink concentrations is displayed in Figure 7.3, where a close similarity between the theoretical values and the experimental determination from upward wicking, validated the adequate expression of data variability by this mathematical model.

This validation was considered conclusive, especially as the Kozeny-Karman model only relates structural parameters from the porous matrix, namely the diameter of the

porous media and its overall porosity, to calculate the permeability (Callegari et al., 2011; Xia et al., 2012), while the model for describing upward wicking combines Lucas-Washburn equation and Darcy's law for the estimation of the wetting front by the influence of both the media and the sample parameters (Callegari et al., 2011). This validation method has been previously reported in a semi-infinite porous material, where the experimental ($1.12x10^{-12}$ m^2) and numerical/theoretical ($9.5x10^{-13}$ m^2) permeabilities had values in close proximity to those calculated from the validation for upward wicking with the theoretical permeability in **Chapter 3** and Figure 7.3 (Xiao et al., 2012). Considering that upward wicking governs the flow of samples in 3MM chromatography paper, implies that the matrix is regarded as an array of capillaries, where the porosity and the pressure of the wetting front (capillary pressure) are essential. However, as the length scale of the structure of paper fibres is in the nanoscale, the capillary pressure does not depend on Jurin height (no gravitational effect) and is therefore linked to the viscous resistance and the pore size (Callegari et al., 2011).

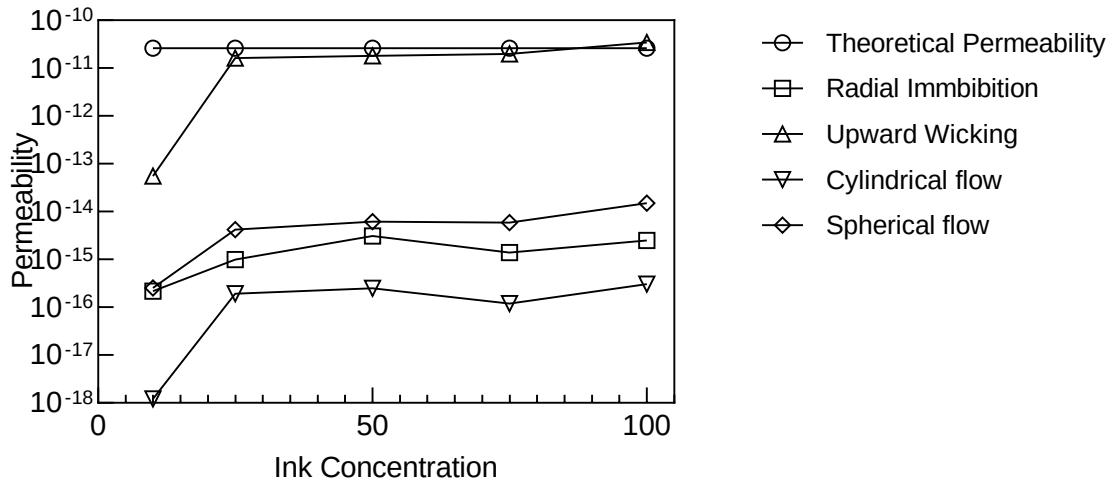

Figure 7.3 Experimental and theoretical permeabilities estimated for the flow of ink models in 3MM chromatography paper

Furthermore, according to the model for upward wicking the capillary pressure is equivalent to the wetting front pressure, and drives the motion process, which is mainly affected by the viscous resistance from the sample. This suction pressure promotes the flow through the system of capillaries within the inner structure of paper, where the nanofiber crossings do not contribute to the overall movement as compared to the permeability value (Callegari et al., 2011).

7.2.3 The effect of chitosan on microfluidic-paper-based analytical devices (μPADs)

The logic behind the application of chitosan on paper, relies on its biodegradability and excellent mechanical and barrier properties, which have been exploited in cellulose fibre coating, where the molecular weight determines the homogeneity and continuity of the formed layer (Despond et al., 2004). Likewise, the good compatibility, thermal stability, and low water absorption, between chitosan and cellulose, in which the crystallinity, lamination, and handling remains unaffected (Maciel et al., 2010; Fernandez et al., 2010), were significant for its exploration as enhancement agent in μPADs.

As reported in **Chapter 4**, the addition of chitosan without any cross-linking mechanism resulted in heterogeneity at the test zone, which was visually observable in ink model samples. Although chitosan has been impregnated on μPADs in account of the electrostatic and non-electrostatic (structural backbone resemblance) interactions between chitosan and cellulose. As hydrogen bonds occur between protonated chitosan and paper motifs (carbohydrate polymers), simple modification with chitosan might result in higher hydrophobicity related to its acetyl groups and resulting colour heterogeneity (Gabriel et al., 2015). The aforementioned was observed in Chitosan B (DA: 28.8%), whose higher acetylation indicated more colour heterogeneity and no significant differences were found between its simple impregnation and covalent crosslinking on paper ($p=0.054$) using genipin, in comparison to Chitosan A (DA 17%), where a significantly higher ($p=0.001$) colour intensity was achieved by genipin cross-linking (**Chapter 4**). A chitosan treatment without cross-linking could be useful in terms of its film forming capacity and more reactive area in enzymatic reactions (Gabriel et al., 2016). However, compatibility by means of the cationic nature of chitosan and the anionic role of cellulose, is not enough for the achievement of a good biosensing performance. For that reason, cross-linking agents need to be applied to covalently link chitosan to the paper matrix, as already reported in antibodies immobilized with glutaraldehyde cross-linked chitosan (Wang et al., 2012). In **Chapter 4**, genipin, an aglycone derived from the iridoid glycoside called geniposide, was used instead of the far more toxic and studied crosslinker glutaraldehyde, where despite the results in ink models, the immobilization of AChE in crosslinked chitosan showed a better linearity from Chitosan B ($r^2=0.9911$) at an increasing AFB1 concentration (**Chapter 4**). In agreement with the obtained results, both Chitosan A ($p=0.35$) and Chitosan B ($p=0.05$) did not show significant differences among the analysis of AFB1 in corn samples and a similar concentration in buffer. The superior enhancement from Chitosan B could correspond to its greater acetylation degree which generates and increase in the hydrophobicity (Sorlier et al., 2001).

Cross-linking of chitosan with genipin, has been reported as the resulting product of two reaction mechanisms. One is a fast nucleophilic attack between the primary amine (chitosan) on the C3 carbon in genipin. This is followed by an opening of the dihydropyran ring in genipin to form a heterocyclic compound (genipin) with the glucosamine residue in chitosan. The other is a slower nucleophilic substitution of the ester group of genipin (C11) to form a secondary amide linkage with chitosan. Further crosslinking occurs via the formation of dimer, trimer, and tetramer bridges (Mi et al., 2000) (Figure 7.4).

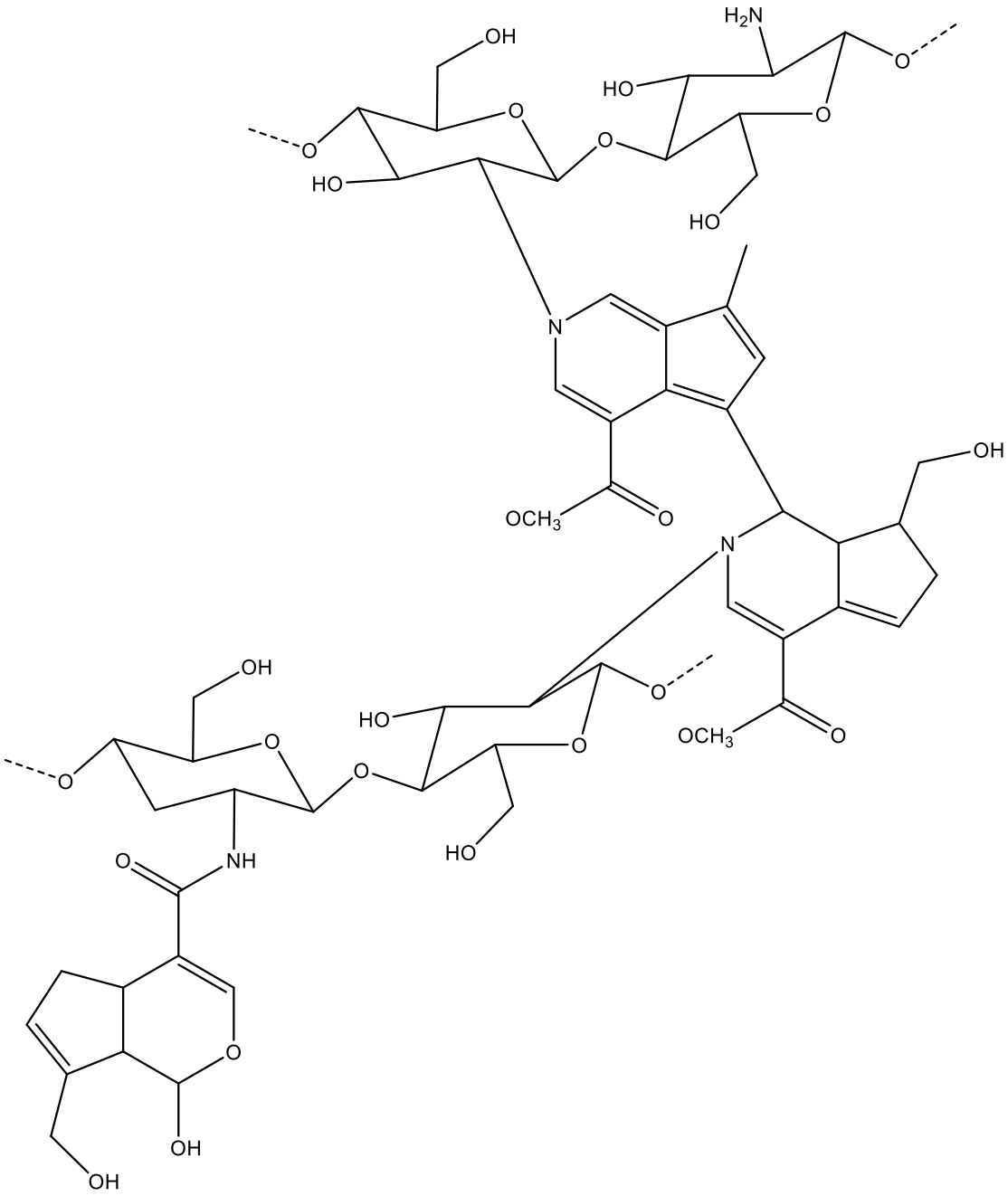

Figure 7.4 Representation of two chitosan chains cross-linked with one mol of genipin

7.2.4 An aptamer-target-AuNP conjugate for the quantification of FB1

In **Chapter 5**, the role of different buffers during aptamer-target binding was explored for two aptamers specific for FB1. A short length aptamer (40 nt) was selected due to the novelty of its utilization, and previous reported utilization for the selective detection of FB1 in an electrochemical graphene oxide platform, whose specificity was confirmed under the presence of ochratoxin A (OTA) and thrombin (Cheng and Bonnanni, 2018). This sequence was derived from an 80 nt aptamer, where the primer binding sites were removed and only the randomized sequence was kept for biosensing (Chen et al., 2014). Ideally, a reduction in the aptamer length has been found with potential biosensing affinity enhancement (Frost et al., 2015), by means of its greater mobility and the sole inclusion of the target-specific sequence, from which primer binding sites are eliminated to avoid non-specific interactions. Unfortunately, the utilized biosensing procedure, comprising aptamer-target binding followed by incubation with AuNPs and salt-induced aggregation, was not suitable for the specific interaction of aptamer 40 nt with FB1.

Nevertheless, aptamer 96 nt, the so far most utilized sequence in aptamer-based detection of FB1 (**Chapter 2**), exhibited high affinity to FB1 when $MgCl_2$ 1 mM was utilized as binding buffer. The novelty of this method, besides the utilization of a label-free single probe method for aptamer 96 nt with a simple set of incubations, was the formation of an aptamer-target-AuNPs complex, similar to the mechanism reported for a serotonin aptamer in $MgCl_2$ (Chávez et al., 2017). Unlike other aptamer-based methods with AuNPs, the presence of FB1 enhanced the formation of such sensitive complex, rather than promoting aptamer desorption from the surface of AuNPs. As this interaction has not been widely explored and explained, the results from circular dichroism and AF4, contributed to glean a better understanding of its nature, where a conformational change was not observed upon target binding (**Chapter 5**).

Another important finding was the realisation of the relevance of the selected signals for the acquisition of greater sensitivities. As shown in Figure 7.5, the use of a plate reader resulted in high LODs, which exceeded the expected values from powerful biosensing methods. On the contrary, the analysis of the same aptamer-FB1-AuNPs conjugates using AF4 fractionation allowed the separation of the different size-based populations of particles, within the same bulk sample. This efficient fractionation in combination with the appropriate detectors, contributed to achieving outstanding LODs, particularly for multi-angle laser light scattering (MALS) and UV/Vis (peak area at 600 nm), which were below 1 ng/L (Figure 7.5). When comparing the most sensitive signals from both instruments, the utilization of AF4 generates a > 4 orders of magnitude (35714-fold) reduction compared to the lowest LOD from a wavelength

scan, in a TECAN plate reader. As previously discussed throughout **Chapter 5**, in AF4 the separation takes place in a flat channel where a perpendicular cross flow initially moves small particles along a semi-permeable membrane, followed by the elution of larger particles at longer retention times (Bocca et al., 2020). This method is useful, considering that monodispersed particles could face aggregation and partial dissociation, which complicates their characterization by other bulk techniques such as DLS or UV/Vis spectroscopy wavelength scans. In fact, UV signals yield limited analysis for the detection of interfering background elements (Gray et al., 2012). Therefore, once the particles have reached the different detectors, MALS appears as a sensitive technique for detecting the presence of varied sizes, while UV detection is suitable for their quantification. On that note, UV detection has been indicated as more sensitive to smaller molecules; while MALS detection has been more notorious in bigger particles, in which the intensity of the scattered light is convenient for detecting angular dependency (Bocca et al., 2020), hence carrying out both detections was necessary for a full characterization of the effect exerted by FB1 during the formation of different conjugates.

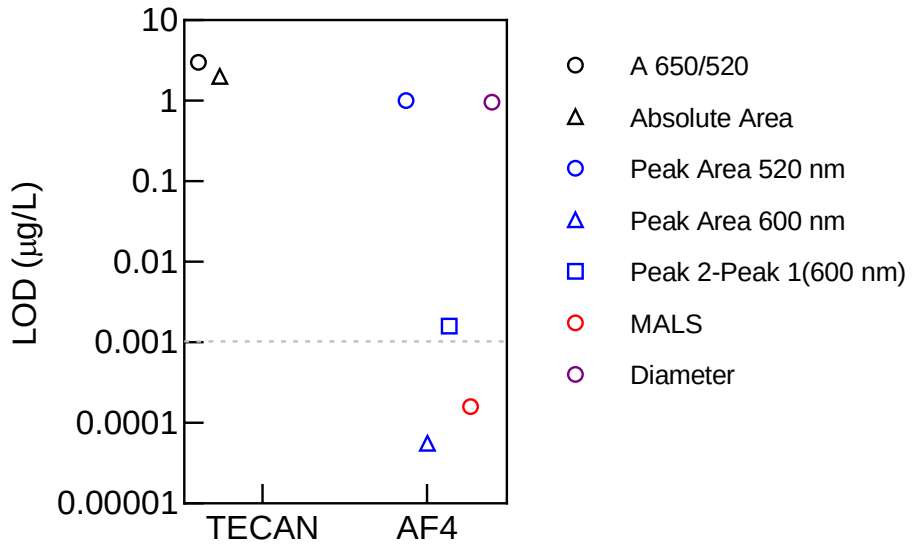

Figure 7.5 Limit od detection (LOD) obtained with the signals from the analysis in TECAN plate reader and AF4

7.2.5 Preliminary mycotoxin decontamination by β-chitin- and chitosan-based materials

The preparation of β-chitin scaffolds and NIBC hydrogels was presented in **Chapter 6**, in which structural differences were highlighted in terms of their pore diameter and abundance within the polymeric matrix. The presence of larger pores in conventionally frozen scaffolds, produced a more stable structure during swelling experiments, while N_2 frozen β-chitin scaffolds came apart after 40 min of swelling incubation. Such behaviour was key to work with conventionally frozen materials, from which β-chitin scaffolds achieved greater swelling ratios (11.60-11.81%) than those from NIBC chitosan (4.62-5.63 %), with a similar trend on the calculated apparent diffusion coefficients. β-chitin scaffolds have been produced with the aid of compounds such as apatite, calcium carbonate, calcium phosphate, silica and $CaCl_2$/ethanol (Maeda et al., 2008), however, the method reported in **Chapter 6** was triggered by the effect of ultrasound in the increased number of chitin fibres.

After the incubation of both materials with FB1 spiked milk and beer, no significant differences were found among the adsorption efficiency values for all the treatments in milk ($p=0.357$) and beer (0.753). However, a significantly higher amount of bound FB1 ($p=0.005$) was observed from both NIBC hydrogel treatments in milk (pH 6.56). Although, no significant differences were observed between the treatments in beer ($p=0.531$), in general more bound FB1 was achieved after incubating in this food product (pH 4.54), where the pH might play a decisive role in the overall performance of both polymeric structures. Yet, more experiments are needed to determine the optimum incubation and binding conditions, as well as the effect of the pH from the selected sample.

A compilation of the results and incubation conditions of different chitin and chitosan-based adsorption methods is presented in Table 7.1. As demonstrated, the attempt in **Chapter 6** for adsorbing FB1 had lower impact in comparison to other tested materials, despite the adequate swelling properties displayed by β-chitin and NIBC hydrogels and the long incubation times shown in Table 7.1. This underscores the demand for an optimization of the incubation conditions. A null effect from the molecular weight of chitosan was observed on the absorption capacity of cross-linked chitosan (Zhao et al., 2015).

The more promising performance from NIBC hydrogels led to its exploration as potential molecularly imprinted material. A hydrogel can be defined as a 3D network of polymer chains, composed by two or more elements, in which the macromolecule-related spaces are filled with water. In terms of their cross-linking preparation, hydrogels are divided in either chemical (permanent concatenations) or physical

(entanglements or physical interactions comprising hydrogen bonds, ionic or hydrophobic interactions) (Ahmed, 2015). The gel formation by N-acylation of chitosan with isobutyric anhydride, has been disclosed as a physical method, based on the hydrophobic interactions between water and isobutyryl substituents, where the self-association of hydrophobic isobutyryl groups results in a “cage-like” structure (Felix et al., 2005). The use of L-phenylalanine was proposed as an analogue of OTA, in terms of their benzene ring as indicated In Figure 7.6.

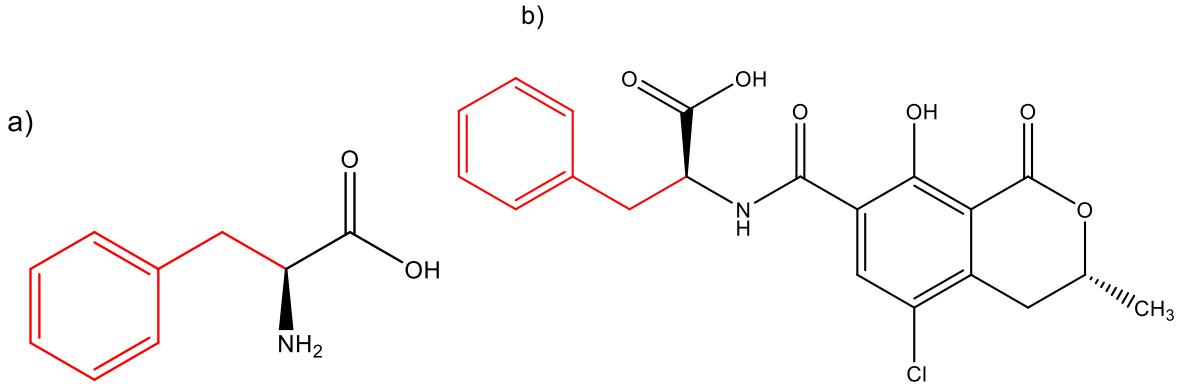

Figure 7.6 Structural representation of (**a**) L-phenylalanine and (**b**) ochratoxin A with their highlighted structural similarities (red)

Chitosan can interact with some mycotoxins through hydrogen bonds, as it contains -OH and -NH_2 groups, providing a positive charge in acidic conditions. On the other hand, OTA appears as a negative compound due to its carboxyl group from the phenylalanine moiety (Mine Kurtbay et al., 2008). OTA removal with chitin and chitosan has been disclosed as a dosage dependent technique (Quintela et al., 2012), which should be considered in future experiments.

Table 7.1 Chitin and chitosan-based methods for mycotoxin adsorption

Material	Mycotoxin	Sample	Incubation	Bound mycotoxin (mg/g)	Adsorption Efficiency (%)	Reference
Chitosan beads (low viscose)	OTA	Red Wine	RT, 90 min	0.225	~100	Mine Kurtbay et al., 2008
Chitin, chitosan	OTA	Red Wine	RT, 2 h	NA	29% (Chitin) 67% (Chitosan)	Quintela et al., 2012
Glutaraldehyde cross-linked chitosan, chitosan-sodium tripolyphosphate, chitosan beads (Low: <2X10^5, medium: 2-2.5x10^5, high:>5x10^5 MW)	AFB1, OTA ZEN, FB1 DON, T-2 toxin	Citrate buffer (pH 3.1, 1 mM) Phosphate buffer (pH 8.3, 1 mM	37 °C, 90 min, 200 rpm	5.67(AFB1), 15.7(FB1)	73 (AFB1), 97 (OTA), 94 (ZEN), 99 (FB1), <30 (DON, T-2 Toxin)	Zhao et al., 2015
Glutaraldehyde cross-linked xanthated chitosan resin	Patulin	Apple juice	30 °C, 18 h, pH 4	20-130	NA	Peng et al., 2016
Chitosan coated Fe_3O_4 particles	Patulin	Juice-pH simulation aqueous	30 °C, 5 h, pH 4, 120 rpm	6.67	NA	Luo et al., 2017
Heat-treated shrimp shells Chitin	AFM1	Milk	37 °C, 30 min-24 h	NA	14.29-94.74	Assaf et al., 2018
Chitosan carbon particles (Cts) & Chitosan carbon particles and rectorite biocomposite (Cts@Rec) (High viscosity ≥99 wt%, MW: 200 000)	ZEN	Gastric conditions (pH 3.5)	37 °C, 240 min	14.56 (Cts) 13.90 (Cts@Rec)	NA	Sun et al., 2020
Chitosan (DA 15%)	AFB1, AFB2, AFG1, AFG2, OTA, ZEN, FB1, FB2, trichothecenes, DON, HT-2, T-2 toxin	Palm kernel cake	35 °C, 8 h, pH 4	NA	94.35 (AFB1), 45.90 (AFB2), 82.11 (AFG1), 84.29 (AFG2), 90.03 (OTA), 51.30 (ZEN), 90.53 (FB1), 90.18 (FB2),	Abbasi Pirouz et al., 2020
Chitosan (low viscosity <200 mPa s, DA 20%) functionalized montmorillonite	AFB1, ZEN	Simulated gastric fluid (pH 3.5) Simulated intestinal fluid (pH 6.5)	37 °C, 120 min	10 (ZEN)	75-100(ZEN) 60-95 (AFB1)	Wang et al., 2020
β-chitin scaffold NIBC hydrogels	AFB1	Milk (pH 6.56) Beer (pH 4.54)	37 °C, 90 min	0.02-0.1 (NIBC) 0.002-0.026 (Chitin)	4.16-12.58 (NIBC) 1.41-16.94 (Chitin)	Chapter 6

AF: Aflatoxin, DON: Deoxynivalenol, NA: Not applicable, OTA: Ochratoxin A, RT: Room temperature, ZEN: zearalenone

7.3 Conclusions and future perspectives

The present thesis has demonstrated the presence of wicking forces in the diffusion of samples withing chromatography paper, which has significance in its performance as a µPAD platform where signal enhancement was achieved by the application of cross-linked chitosan on the colorimetric detection of mycotoxins. The importance of an affordable, simple, yet sensitive and effective biosensing technique for mycotoxin quantification was outlined through the utilization of aptamers (ssDNA), where exceptional detection values were accomplished when novel analytical methods were included. Finally, an exploratory finding from this thesis was the potential utilization of waste-based polymers as structural materials for mycotoxin adsorption from which mechanisms such as N-acylation and molecular imprinting, represent an opportunity for integrating new materials with beneficial implications to the environment. Derived from these results the main suggestions for future research that could be explored in subsequent projects are indicated as follows:

Literature review additional findings

- As molecularly imprinted polymers have achieved the most sensitive designs for the analysis of FB1 (Munawar et al., 2020), molecular imprinting of new materials, especially chitin and chitosan based structures, could be explored in combination with FB1 and other relevant and emerging mycotoxins (OTA, AFB1, ZEN, DON).
- No paper-based biosensor has been reported for FB1 (Mirón-Mérida et al., 2020), therefore, there is a broad scope for study in here, where lateral-flow assays, µPADs or hybrids of electrochemical chips and paper platform detection are suitable options for the scaling of some reported techniques to a paper matrix.
- As mimimers derived from the 96 nt were reported with low affinities (Ciriaco et al., 2020), new short sequences should be developed, especially as the majority of biosensing approaches utilized aptamer 96 nt, which could limit the its applicability and potential powerful detection due to its long length, where unspecific interactions might occur.

Paper as a biosensing platform

- As already confirmed by the high r^2 values from the mathematical fitting indicated a good expression of data variability at short times (e.g., wicking models), which in that case might suggest the presence of not only one diffusion mechanism for the whole data set. Hence, the interconnection of different

physical phenomena (diffusion, wicking, and chromatography) could be assessed at longer times.

- The application of assays for the calculation of flow velocity (equation 7.1), are recommended for a better understanding of the diffusive behaviour of the ink models.

$$v = \frac{dL}{\mathrm{dt}} \tag{7.1}$$

Where flow velocity is a simple measure of the distance achieved by a fluid (dL) in a porous media as a function of time (dt) (Xiao et al., 2013).

- The creation of hydrophobic boundaries with methods such as solid ink printing, also known as wax printing, could be explore for a more controlled sample flow, with the advantages of no further processing (contrary to photolithography) (Dungchai et al., 2011). Quick and low-cost assays can be achieved by using wax patterned paper, because of the malleability, hydrophobicity, and low viscosity of melted wax (Lu et al., 2009).
- The application of chitosan for immobilization of enzymes on test zones can be subject to a study of tthe effects from a wider variety of chitosan samples. Chitosans of different DA and MW values could be addressed, especially after identifying that many references ignore the relevance of both properties on a differentiated biosensing performance.

Aptamer-based detection of mycotoxins

- Data obtained from the spectral analysis in a TECAN plate reader could be treated to enhance its limit of detection. A suggested approach consists on the extrapolation of a base line from all the curves (wavelength scans) as a cubic polynomial function. A subtraction of such base line from the experimental data could generate a new set of curves, from which the values of A_{650}, A_{520}, $A_{650/520}$ and $(A_{650}+1)/(A_{520}+1)$ ideally might portray lower LODs.
- The paper-based detection of FB1 by the aptamer (96 nt)-FB1-AuNPs conjugates could be designed by immobilizing cysteamine on an intermediate test zone, where free AuNPs (no aptamer adsorbed) will be captured by the thiol group in cysteamine, generating a red dot/line (Daliririrad and Steckl, 2019).
- The analysis by multidetection AF4 should be furthered and validated in different food samples, from which a matrix matched calibration is suggested, due to the spectral variety displayed during preliminary assays.

Decontamination of mycotoxins with natural polymers

- An optimization of the incubation conditions (pH, time and temperature) is necessary to improve the adsorption efficiency and the amount of bound mycotoxin, especially after observing that the time to swelling equilibrium was not sufficient for a good binding. An experimental design should be ideal for this step, in which the indicated parameters could be varied within a selected range (Abbasi Pirouz et al., 2020).
- Perhaps, the inclusion of other mycotoxins such as AFB1 and OTA, either individually or in co-occurrence, could provide better results. In any case, adsorption isotherms should be performed to analyse the kinetics of adsorption by different models (Peng et al., 2016; Zhao et al., 2015).
- Prior to any analysis with NIBC hydrogels, template re-binding studies have to be carried to verify a successful molecular imprinting process, partially confirmed by the washing results (Espinosa-García et al., 2007). The gelation process (rheometer) and structural properties (SEM, FTIR) under the presence of the template molecule MINIBC, should be determined to complete the characterization step (Espinosa- Garcia et al., 2007). In addition, an identification of the reaction products, observed by HPLC and the study of the selectivity of NIBC materials (e.g. enantioselectivity) are recommended (Espinosa-García et al., 2007; Jiang et al., 2006).

7.4 Final Discussion

In general, this thesis resulted in the acquisition of relevant knowledge, applicable to different fields. First, a literature review on the aptamer-based detection of FB1 was more than necessary, especially due to the fact that just 11 years ago, the first aptamer specific to this mycotoxin was disclosed to the world. This definitely establishes a space for the selection of more sensitive sequences, the reduction of the length from existing aptamers without compromising their excellent binding affinities, as well as the generation of more sensitive, yet simple, aptasensing designs, ideally paper-based biosensors for FB1 that neither have been reported, nor commercialized at a large scale.

In this regard, understanding the physical processes involved in the movement of samples withing the paper matrix was an important point from this thesis. In fact, from the estimations and mathematical fitting in 3MM chromatography paper, it was clear that the movement of samples should be regarded as a combined set of phenomena, where diffusion and imbibition simultaneously occur in combination with other physical processes. This must be considered during the design stage of paper-based

biosensors, where understanding the evolution of the sample front across time is necessary for the preparation of sample conjugation, control, and test zones. Besides, the simplicity of this study was sufficient for describing the flow of the model samples, from which less complicated settings might be necessary for describing the transport phenomena in this type of porous media, with more proximity to real experimental conditions, contrary to the current approaches.

Another important outcome, with applicability on future designs is the dependence of the physicochemical properties of chitosan to the final biosensing performance. Whether its application is for colorimetric, paper-based, or electrochemical biosensors, this thesis outlined the importance of knowing and controlling parameters such as the degree of acetylation and the molecular weight of chitosan, due to their impact on the obtained biosensing signal. In addition, this is a very fundamental design step that is commonly overlooked on many articles reporting the application of chitosan for immobilization and signal enhancement.

Although a sensitive limit of detection was achieved with the integration of the Aptamer-AuNP-FB1 complex with AF4-MALS, this is still an analytical method carrying the disadvantages of this type of techniques, namely the utilization of large amounts of solvent, long assay times, sample pre-treatment, trained operators, and the proper infrastructure for the optimal maintenance of this equipment. Therefore, the application of this bulk assay on a paper-based design is desirable and should be the next step towards the commercialization of this development, especially when considering that, opposite to existing ELISA kits, lateral flow tests and microfluidics, no aptamer-based biosensor in paper exists in the market.

Finally, the recent development of β-chitin scaffolds by our research group as well as the lack of applications for the NIBC hydrogels, set an opportunity area for the exploration of multiple developments, not only for mycotoxin decontamination, but tissue engineering, cell growth, meat analogues, drug delivery, biosensing among others. Although, some inconclusive results were observed in milk and beer, more explorations could be carried out in other samples rather than food products, in which the possibility of contamination with the waste-based material can be disregarded through analysis where the sample is not reintroduced into any process (e.g., clinical samples). The successful utilization of these materials as decontaminants and supports for molecular imprinting will result in a state-of-the-art development, hence the continuation of this preliminary results as a university or industrial projects is recommended, if not fundamental due to the amount knowledge already gathered through this thesis.

Chapter 8
References

Abadian, A., Manesh, S.S. and Ashtiani, S.J. 2017. Hybrid paper-based microfluidics: combination of paper-based analytical device (µPAD) and digital microfluidics (DMF) on a single substrate. *Microfluidics and Nanofluidics*. **21**(4), p.65.

Abbas, H.K. and Riley, R.T. 1996. The presence and phytotoxicity of fumonisins and AAL-toxin in Alternaria alternata. *Toxicon.* **34**(1), pp.133-136.

Abbas, H., Vesonder, R.F., Boyette, C.D., Hoagland, R.E. and Krick, T. 1992. Production of fumonisins by Fusarium moniliforme cultures isolated from jimsonweed in Mississippi. *Journal of Phytopathology*. **136**(3), pp.199-203.

Abbasi Pirouz, A., Abedi Karjiban, R., Abu Bakar, F. and Selamat, J. 2018. A novel adsorbent magnetic graphene oxide modified with chitosan for the simultaneous reduction of mycotoxins. *Toxins*. **10**(9), p.361.

Abbasi Pirouz, A., Selamat, J., Zafar Iqbal, S. and Iskandar Putra Samsudin, N. 2020. Efficient and Simultaneous Chitosan-Mediated Removal of 11 Mycotoxins from Palm Kernel Cake. *Toxins*. **12**(2), p.115.

Abdallah, M.F., Audenaert, K., Lust, L., Landschoot, S., Bekaert, B., Haesaert, G., De Boevre, M. and De Saeger, S. 2020. Risk characterization and quantification of mycotoxins and their producing fungi in sugarcane juice: A neglected problem in a widely-consumed traditional beverage. *Food Control*. **108**, p.106811.

Abdallah, M.F., Krska, R. and Sulyok, M. 2018. Occurrence of ochratoxins, fumonisin B2, aflatoxins (B1 and B2), and other secondary fungal metabolites in dried date palm fruits from Egypt: a mini-survey. *Journal of food science*. *83*(2), pp.559-564.

Abia, W.A., Warth, B., Ezekiel, C.N., Sarkanj, B., Turner, P.C., Marko, D., Krska, R. and Sulyok, M. 2017. Uncommon toxic microbial metabolite patterns in traditionally home-processed maize dish (fufu) consumed in rural Cameroon. *Food and Chemical Toxicology*. **107**, pp.10-19.

Aburto, J. and Le Borgne, S. 2004. Selective adsorption of dibenzothiophene sulfone by an imprinted and stimuli-responsive chitosan hydrogel. *Macromolecules*. **37**(8), pp.2938-2943.

Agriopoulou, S., Stamatelopoulou, E. and Varzakas, T. 2020. Advances in occurrence, importance, and mycotoxin control strategies: prevention and detoxification in foods. *Foods*. **9**(2), p.137.

Ahmed, E.M. 2015. Hydrogel: Preparation, characterization, and applications: A review. *Journal of advanced research*. **6**(2), pp.105-121.

Ahmed, M.U., Zourob, M., Tamiya, E. 2017. *Food Biosensors*. UK: Royal Society of Chemistry.

Akala, E. O., Kopečková, P. and Kopeček, J. 1998. Novel pH-sensitive hydrogels with adjustable swelling kinetics. *Biomaterials*. **19**(11-12), pp.1037-1047.

Amendola, V., Pilot, R., Frasconi, M., Maragò, O.M. and Iatì, M.A. 2017. Surface plasmon resonance in gold nanoparticles: a review. *Journal of Physics: Condensed Matter*. **29**(20), p.203002.

Amine, A., Arduini, F., Moscone, D. and Palleschi, G. 2016. Recent advances in biosensors based on enzyme inhibition. *Biosensors and Bioelectronics*. **76**, pp.180-194.

Anderson, G.P., Kowtha, V.A. and Taitt, C.R. 2010. Detection of fumonisin B1 and ochratoxin A in grain products using microsphere-based fluid array immunoassays. *Toxins*. **2**(2), pp.297-309.

Anfossi, L., Calderara, M., Baggiani, C., Giovannoli, C., Arletti, E. and Giraudi, G. 2010. Development and application of a quantitative lateral flow immunoassay for fumonisins in maize. *Analytica chimica acta*. **682**(1-2), pp.104-109.

Anfossi, L., d'Arco, G., Calderara, M., Baggiani, C., Giovannoli, C. and Giraudi, G. 2011. Development of a quantitative lateral flow immunoassay for the detection of aflatoxins in maize. *Food Additives and Contaminants*. **28**(2), pp.226-234.

Anfossi, L., Di Nardo, F., Cavalera, S., Giovannoli, C., Spano, G., Speranskaya, E.S., Goryacheva, I.Y. and Baggiani, C. 2018. A lateral flow immunoassay for straightforward determination of fumonisin mycotoxins based on the quenching of the fluorescence of CdSe/ZnS quantum dots by gold and silver nanoparticles. *Microchimica Acta*. **185**(2), pp.1-10.

Annunziata, L., Stramenga, A., Visciano, P., Schirone, M., De Colli, L., Colagrande, M.N., Campana, G. and Scortichini, G. 2017. Simultaneous determination of aflatoxins, T-2 and HT-2 toxins, and fumonisins in cereal-derived products by

QuEChERS extraction coupled with LC-MS/MS. *Analytical and bioanalytical chemistry*. **409**(21), pp.5143-5155.

ApSimon, J. W. 2001. Structure, synthesis, and biosynthesis of fumonisin B1 and related compounds. *Environmental Health Perspectives*. **109**(suppl 2), pp. 245-249.

Aranaz, I., Mengíbar, M., Harris, R., Paños, I., Miralles, B., Acosta, N., Galed, G. and Heras, Á. 2009. Functional characterization of chitin and chitosan. *Current chemical biology*. **3**(2), pp.203-230.

Arduini, F., Amine, A., Moscone, D. and Palleschi, G., 2010. Biosensors based on cholinesterase inhibition for insecticides, nerve agents and aflatoxin B 1 detection. *Microchimica Acta*. **170**(3-4), pp.193-214.

Arduini, F., Errico, I., Amine, A., Micheli, L., Palleschi, G. and Moscone, D. 2007. Enzymatic spectrophotometric method for aflatoxin B detection based on acetylcholinesterase inhibition. *Analytical Chemistry*. **79**(9), pp.3409-3415.

Aslannejad, H., Fathi, H., Hassanizadeh, S. M., Raoof, A. and Tomozeiu, N. 2018. Movement of a liquid droplet within a fibrous layer: direct pore-scale modeling and experimental observations. *Chemical Engineering Science*. **191**, pp.78-86.

Aslannejad, H., Loginov, S. V., van der Hoek, B., Schoonderwoerd, E. M., Gerritsen, H. C. and Hassanizadeh, S. M. 2021. Liquid droplet imbibition into a thin coating layer: direct pore-scale modeling and experimental observations. *Progress in Organic Coatings*. **151**, p.106054.

Assaf, J.C., El Khoury, A., Atoui, A., Louka, N. and Chokr, A. 2018. A novel technique for aflatoxin M1 detoxification using chitin or treated shrimp shells: in vitro effect of physical and kinetic parameters on the binding stability. *Applied microbiology and biotechnology*.**102**(15), pp.6687-6697.

Baaske, P., Wienken, C.J., Reineck, P., Duhr, S. and Braun, D. 2010. Optical thermophoresis for quantifying the buffer dependence of aptamer binding. *Angewandte Chemie International Edition*. **49**(12), pp.2238-2241.

Baglieri, A., Reyneri, A., Gennari, M. and Nègre, M. 2013. Organically modified clays as binders of fumonisins in feedstocks. *Journal of Environmental Science and Health, Part B*. **48**(9), pp.776-783.

Balakhnina, I.A., Brandt, N.N., Chikishev, A.Y., Pelivanov, I.M. and Rebrikova, N.L. 2012. Optoacoustic measurements of the porosity of paper samples with foxings. *Applied Physics Letters*. **101**(17), p.174101.

Bánáti, H., Darvas, B., Fehér-Tóth, S., Czéh, Á. and Székács, A. 2017. Determination of mycotoxin production of Fusarium species in genetically modified maize varieties by quantitative flow immunocytometry. *Toxins*. **9**(2), p.70.

Bangyekan, C., Aht-Ong, D. and Srikulkit, K. 2006. Preparation and properties evaluation of chitosan-coated cassava starch films. *Carbohydrate polymers*. **63**(1), pp.61-71.

Bartók, T., Szécsi, Á., Szekeres, A., Mesterházy, Á. and Bartók, M. 2006. Detection of new fumonisin mycotoxins and fumonisin-like compounds by reversed-phase high-performance liquid chromatography/electrospray ionization ion trap mass spectrometry. *Rapid Communications in Mass Spectrometry: An International Journal Devoted to the Rapid Dissemination of Up-to-the-Minute Research in Mass Spectrometry*. **20**(16), pp.2447-2462.

Bennett, J.W. and Klich, M.A. eds. 1992. *Aspergillus: biology and industrial applications* (pp. 134-7). Boston: Butterworth-Heinemann.

Bennett, J.W. and Klich, M. 2003. Mycotoxins. *Clinical Microbiology Reviews*. **16**(3), pp.497-516.

Berne, B.J. and Pecora, R. 2000. *Dynamic light scattering: with applications to chemistry, biology, and physics*. Courier Corporation.

Berthiller, F., Cramer, B., Iha, M.H., Krska, R., Lattanzio, V.M.T., MacDonald, S., Malone, R.J., Maragos, C., Solfrizzo, M., Stranska-Zachariasova, M. and Stroka, J. 2018. Developments in mycotoxin analysis: an update for 2016-2017. *World Mycotoxin Journal*. **11**(1), pp.5-32.

Bessaire, T., Perrin, I., Tarres, A., Bebius, A., Reding, F. and Theurillat, V. 2019. Mycotoxins in green coffee: Occurrence and risk assessment. *Food control*. **96**, pp.59-67.

Bezuidenhout, S.C., Gelderblom, W.C., Gorst-Allman, C.P., Horak, R.M., Marasas, W.F., Spiteller, G. and Vleggaar, R. 1988. Structure elucidation of the fumonisins, mycotoxins from Fusarium moniliforme. *Journal of the Chemical Society, Chemical Communications*. **11**, pp.743-745.

BIOMIN. 2015. 2014 BIOMIN mycotoxin survey results: Why advanced multiple mycotoxin detection matters. [Online]. BIOMIN. [Accessed on 2 February 2021]. Available from: https://issuu.com/biomin/docs/mag_scisol_special_02_mtx_en_0515

Bocca, B., Battistini, B. and Petrucci, F. 2020. Silver and gold nanoparticles characterization by SP-ICP-MS and AF4-FFF-MALS-UV-ICP-MS in human samples used for biomonitoring. *Talanta*. **220**, p.121404.

Bordin, K., Rosim, R.E., Neeff, D.V., Rottinghaus, G.E. and Oliveira, C.A.F. 2014. Assessment of dietary intake of fumonisin B1 in São Paulo, Brazil. *Food chemistry*.**155**, pp.174-178.

Bordin, K., Rottinghaus, G.E., Landers, B.R., Ledoux, D.R., Kobashigawa, E., Corassin, C.H. and Oliveira, C.A. 2015. Evaluation of fumonisin exposure by determination of fumonisin B1 in human hair and in Brazilian corn products. *Food control*. **53**, pp.67-71.

Borhan, A. and Rungta, K.K. 1993. An experimental study of the radial penetration of liquids in thin porous substrates. *Journal of colloid and interface science*. **158**(2), pp.403-411.

Branham, B.E. and Plattner, R.D. 1993. Isolation and characterization of a new fumonisin from liquid cultures of Fusarium moniliforme. *Journal of natural products*. **56**(9), pp.1630-1633.

Bouhet, S., Le Dorze, E., Peres, S., Fairbrother, J.M., and Oswald, I.P. 2006. Mycotoxin fumonisin B_1 selectively down-regulates the basal IL-8 expression in pig intestine: *in vivo* and *in vitro* studies. *Food and Chemical Toxicology*. **44**, 1768-1773.

Butler, M.F., Ng, Y.F. and Pudney, P.D. 2003. Mechanism and kinetics of the crosslinking reaction between biopolymers containing primary amine groups and genipin. *Journal of Polymer Science Part A: Polymer Chemistry*. **41**(24), pp.3941-3953.

Cai, J., You, L., Hu, X., Wang, J. and Peng, R. 2012a. Prediction of effective permeability in porous media based on spontaneous imbibition effect. *International Journal of Modern Physics C*. **23**(7), pp.1250054.

Cai, J., Hu, X., Standnes, D. C. and You, L. 2012b. An analytical model for spontaneous imbibition in fractal porous media including gravity. Colloids and Surfaces A: Physicochemical and Engineering Aspects. **414**, pp.228-233.

Callegari, G., Tyomkin, I., Kornev, K.G., Neimark, A.V. and Hsieh, Y.L. 2011. Absorption and transport properties of ultra-fine cellulose webs. *Journal of colloid and interface science*. **353**(1), pp.290-293.

Campa, R., Miller, J.D. and Hendricks, K. 2004. Fumonisin in tortillas produced in small-scale facilities and effect of traditional masa production methods on this mycotoxin. *Journal of agricultural and food chemistry*. **52**(14), pp.4432-4437.

Carballo, D., Font, G., Ferrer, E. and Berrada, H. 2018. Evaluation of mycotoxin residues on ready-to-eat food by chromatographic methods coupled to mass spectrometry in tandem. *Toxins*. **10**(6), p.243.

Cardoso, T.M., Garcia, P.T. and Coltro, W.K.2 015. Colorimetric determination of nitrite in clinical, food and environmental samples using microfluidic devices stamped in paper platforms. *Analytical Methods*. **7**(17), pp.7311-7317.

Carvalhal, R.F., Simão Kfouri, M., de Oliveira Piazetta, M.H., Gobbi, A.L. and Kubota, L.T. 2010. Electrochemical detection in a paper-based separation device. *Analytical chemistry*. **82**(3), pp.1162-1165.

Castillo, G., Spinella, K., Poturnayová, A., Šnejdárková, M., Mosiello, L. and Hianik, T. 2015. Detection of aflatoxin B1 by aptamer-based biosensor using PAMAM dendrimers as immobilization platform. *Food Control*. **52**, pp.9-18.

Cerón-Bustamante, M., Ward, T. J., Kelly, A., Vaughan, M. M., McCormick, S. P., Cowger, C., Leyva-Mir, S.G., Villaseñor-Mir, H., Ayala-Escobar, V. and Nava-Díaz, C. 2018. Regional differences in the composition of Fusarium head blight pathogens and mycotoxins associated with wheat in Mexico. *International journal of food microbiology*. **273**, pp. 11-19.

Chang, S., Seo, J., Hong, S., Lee, D. G. and Kim, W. 2018. Dynamics of liquid imbibition through paper with intra-fibre pores. *Journal of Fluid Mechanics*. **845**, pp.36-50.

Chávez, J.L., Hagen, J.A. and Kelley-Loughnane, N. 2017. Fast and selective plasmonic serotonin detection with aptamer-gold nanoparticle conjugates. *Sensors*. **17**(4), p.681.

Chen, C., Riley, R.T. and Wu, F. 2018. Dietary fumonisin and growth impairment in children and animals: A review. *Comprehensive Reviews in Food Science and Food Safety*. **17**(6), pp.1448-1464.

Chen, X., Bai, X., Li, H. and Zhang, B. 2015a. Aptamer-based microcantilever array biosensor for detection of fumonisin B-1. *RSC Advances*, *5*(45), pp.35448-35452.

Chen, X., Huang, Y., Duan, N., Wu, S., Xia, Y., Ma, X., Zhu, C., Jiang, Y., Ding, Z. and Wang, Z. 2014. Selection and characterization of single stranded DNA aptamers recognizing fumonisin B1. *Microchimica Acta*. **181**(11-12), pp.1317-1324.

Chen, X., Huang, Y., Ma, X., Jia, F., Guo, X. and Wang, Z. 2015b. Impedimetric aptamer-based determination of the mold toxin fumonisin B1. *Microchimica Acta*. **182**(9), pp.1709-1714.

Chen, X., Liang, Y., Zhang, W., Leng, Y. and Xiong, Y. 2018a. A colorimetric immunoassay based on glucose oxidase-induced AuNP aggregation for the detection of fumonisin B1. *Talanta*. **186**, pp.29-35.

Chen, C., Mitchell, N.J., Gratz, J., Houpt, E.R., Gong, Y., Egner, P.A., Groopman, J.D., Riley, R.T., Showker, J.L., Svensen, E. and Mduma, E.R. 2018b. Exposure to aflatoxin and fumonisin in children at risk for growth impairment in rural Tanzania. *Environment international*. **115**, pp.29-37.

Cheng, Z.X. and Bonanni, A. 2018. All-in-One: Electroactive Nanocarbon as Simultaneous Platform and Label for Single-Step Biosensing. *Chemistry–A European Journal*. ***24***(24), pp.6380-6385.

Cheng, Z.X., Ang, W.L. and Bonanni, A. 2019. Electroactive Nanocarbon Can Simultaneously Work as Platform and Signal Generator for Label-Free Immunosensing. *ChemElectroChem*. **6**(14), pp.3615-3620.

Cho, T.J. and Hackley, V.A. 2010. Fractionation and characterization of gold nanoparticles in aqueous solution: asymmetric-flow field flow fractionation with MALS, DLS, and UV–Vis detection. *Analytical and bioanalytical chemistry*. **398**(5), pp.2003-2018.

Choi, G. and Choi, S. 2016. Cellular flow in paper-based microfluidics. *Sensors and Actuators B: Chemical*. **237**, pp.1021-1026.

Chotchuang, T., Cheewasedtham, W., Jayeoye, T.J. and Rujiralai, T. 2019. Colorimetric determination of fumonisin B1 based on the aggregation of cysteamine-functionalized gold nanoparticles induced by a product of its hydrolysis. *Microchimica Acta*. **186**(9), pp.1-10.

Ciegler, A. 1972. Bioproduction of ochratoxin A and penicillic acid by members of the Aspergillus ochraceus group. *Canadian Journal of Microbiology*. **18**(5), pp. 631-636.

Cinar, A. and Onbaşı, E. 2019. Mycotoxins: The hidden danger in foods. In *Mycotoxins and food safety*. IntechOpen.

Ciriaco, F., De Leo, V., Catucci, L., Pascale, M., Logrieco, A.F., DeRosa, M.C. and De Girolamo, A. 2020. An in-silico pipeline for rapid screening of DNA aptamers against mycotoxins: The case-study of Fumonisin B1, Aflatoxin B1 and Ochratoxin A. *Polymers*. **12**(12), p.2983.

Cladière, M., Delaporte, G., Le Roux, E. and Camel, V.,2018. Multi-class analysis for simultaneous determination of pesticides, mycotoxins, process-induced toxicants and packaging contaminants in tea. *Food chemistry*. **242**, pp.113-121.

Clogston, J.D. and Patri, A.K. 2011. Zeta potential measurement. In *Characterization of nanoparticles intended for drug delivery* (pp. 63-70). Humana Press.

Colvin, B.M. and Harrison, L.R. 1992. Fumonisin-induced pulmonary edema and hydrothorax in swine. *Mycopathologia*. **117**(1-2), pp.79-82.

Cometa, M. F., Lorenzini, P., Fortuna, S., Volpe, M. T., Meneguz, A. and Palmery, M. 2005. In vitro inhibitory effect of aflatoxin B1 on acetylcholinesterase activity in mouse brain. *Toxicology*. **206**(1), pp. 125-135.

Crank, J., 1979. *The mathematics of diffusion*. Oxford university press.

Cytodiagnostics. *Gold Nanoparticle Properties*. [Online]. [Accesed 07 January 2021]. Available from: https://www.cytodiagnostics.com/pages/gold-nanoparticle-properties

Da Silva, L.P., Madureira, F., de Azevedo Vargas, E., Faria, A.F. and Augusti, R. 2019. Development and validation of a multianalyte method for quantification of mycotoxins and pesticides in rice using a simple dilute and shoot procedure and UHPLC-MS/MS. *Food chemistry*. **270**, pp.420-427.

Dagnac, T., Latorre, A., Fernández Lorenzo, B. and Llompart, M. 2016. Validation and application of a liquid chromatography-tandem mass spectrometry based method for the assessment of the co-occurrence of mycotoxins in maize silages from dairy farms in NW Spain. *Food Additives & Contaminants: Part A*. **33**(12), pp.1850-1863.

Dalirirad, S. and Steckl, A.J. 2019. Aptamer-based lateral flow assay for point of care cortisol detection in sweat. *Sensors and Actuators B: Chemical*. **283**, pp.79-86.

Dall'Asta, C., Mangia, M., Berthiller, F., Molinelli, A., Sulyok, M., Schuhmacher, R., Krska, R., Galaverna, G., Dossena, A. and Marchelli, R. 2009. Difficulties in

fumonisin determination: the issue of hidden fumonisins. *Analytical and Bioanalytical Chemistry*. **395**(5), pp.1335-1345.

Danezis, G.P., Anagnostopoulos, C.J., Liapis, K. and Koupparis, M.A. 2016. Multi-residue analysis of pesticides, plant hormones, veterinary drugs and mycotoxins using HILIC chromatography–MS/MS in various food matrices. *Analytica chimica acta*. **942**, pp.121-138.

Da Róz, A.L., Leite, F.L., Pereiro, L.V., Nascente, P.A.P., Zucolotto, V., Oliveira Jr, O.N. and Carvalho, A.J.F. 2010. Adsorption of chitosan on spin-coated cellulose films. *Carbohydrate polymers*. **80**(1), pp.65-70.

Darwish, W. S., Ikenaka, Y., Nakayama, S. M. and Ishizuka, M. 2014. An overview on mycotoxin contamination of foods in Africa. *Journal of Veterinary Medical Science*. **76**(6), pp. 789-797.

De Baere, S., Croubels, S., Novak, B., Bichl, G. and Antonissen, G. 2018. Development and validation of a UPLC-MS/MS and UPLC-HR-MS method for the determination of fumonisin B1 and its hydrolysed metabolites and fumonisin b2 in broiler chicken plasma. *Toxins*. **10**(2), p.62.

De Hoffmann, Edmond. "Mass spectrometry." *Kirk-Othmer Encyclopedia of Chemical Technology* (2000).

Derbyshire, N., White, S.J., Bunka, D.H., Song, L., Stead, S., Tarbin, J., Sharman, M., Zhou, D. and Stockley, P.G. 2012. Toggled RNA aptamers against aminoglycosides allowing facile detection of antibiotics using gold nanoparticle assays. *Analytical chemistry*. **84**(15), pp.6595-6602.

Despond, S., Espuche, E., Cartier, N. and Domard, A. 2005. Barrier properties of paper–chitosan and paper–chitosan–carnauba wax films. *Journal of applied polymer science*. **98**(2), pp.704-710.

Dhakal, R., Windham, G.L., Williams, W.P. and Subudhi, P.K. 2016. Quantitative trait loci (QTL) for reducing aflatoxin accumulation in corn. *Molecular breeding*. **36**(12), p.164.

Díaz-Rojas, E.I., Argüelles-Monal, W.M., Higuera-Ciapara, I., Hernández, J., Lizardi-Mendoza, J. and Goycoolea, F.M. 2006. Determination of chitin and protein contents during the isolation of chitin from shrimp waste. *Macromolecular bioscience*. **6**(5), pp.340-347.

Di Nardo, F., Baggiani, C., Giovannoli, C., Spano, G. and Anfossi, L. 2017. Multicolor immunochromatographic strip test based on gold nanoparticles for the determination of aflatoxin B1 and fumonisins. *Microchimica Acta*. **184**(5), pp.1295-1304.

Dougherty, D.A. 1996. Cation-π interactions in chemistry and biology: a new view of benzene, Phe, Tyr, and Trp. *Science*. **271**(5246), pp.163-168.

Du, L.J., Chu, C., Warner, E., Wang, Q.Y., Hu, Y.H., Chai, K.J., Cao, J., Peng, L.Q., Chen, Y.B., Yang, J. and Zhang, Q.D. 2018. Rapid microwave-assisted dispersive micro-solid phase extraction of mycotoxins in food using zirconia nanoparticles. *Journal of Chromatography A*. **1561**, pp.1-12.

Duan, H., Li, Y., Shao, Y., Huang, X. and Xiong, Y. 2019. Multicolor quantum dot nanobeads for simultaneous multiplex immunochromatographic detection of mycotoxins in maize. *Sensors and Actuators B: Chemical*. **291**, pp.411-417.

Dungchai, W., Chailapakul, O. and Henry, C.S. 2011. A low-cost, simple, and rapid fabrication method for paper-based microfluidics using wax screen-printing. *Analyst*. **136**(1), pp.77-82.

Elieh-Ali-Komi, D. and Hamblin, M.R. 2016. Chitin and chitosan: production and application of versatile biomedical nanomaterials. *International journal of advanced research*. **4**(3), p.411.

Elizalde, E., Urteaga, R. and Berli, C.L. 2016. Precise capillary flow for paper-based viscometry. *Microfluidics and Nanofluidics*. **20**(10), pp.1-8.

Elizalde, E., Urteaga, R. and Berli, C.L. 2015. Rational design of capillary-driven flows for paper-based microfluidics. *Lab on a Chip*. **15**(10), pp.2173-2180.

Ellman, G.L., Courtney, K.D., Andres Jr, V. and Featherstone, R.M. 1961. A new and rapid colorimetric determination of acetylcholinesterase activity. *Biochemical Pharmacology*. **7**(2), pp.88-95.

Engel, A., Plöger, M., Mulac, D. and Langer, K. 2014. Asymmetric flow field-flow fractionation (AF4) for the quantification of nanoparticle release from tablets during dissolution testing. *International Journal of Pharmaceutics*. **461**(1-2), pp. 137-144.

Eskola, M., Kos, G., Elliott, C.T., Hajšlová, J., Mayar, S. and Krska, R. 2020. Worldwide contamination of food-crops with mycotoxins: Validity of the widely cited 'FAO estimate'of 25%. *Critical reviews in food science and nutrition*. **60**(16), pp.2773-2789.

Espinosa-García, B.M., Argüelles-Monal, W.M., Hernández, J., Félix-Valenzuela, L., Acosta, N. and Goycoolea, F.M. 2007. Molecularly Imprinted Chitosan− Genipin Hydrogels with Recognition Capacity toward o-Xylene. *Biomacromolecules*. **8**(11), pp.3355-3364.

European Commission. 2018. RASFF portal. [Online]. European Union. [Accessed on 07 April 2020]. Available from: https://ec.europa.eu/food/safety/rasff_en

Evans, E., Gabriel, E.F.M., Coltro, W.K.T. and Garcia, C.D. 2014. Rational selection of substrates to improve color intensity and uniformity on microfluidic paper-based analytical devices. *Analyst*. **139**(9), pp.2127-2132.

Evtugyn, G. and Hianik, T. 2020. Aptamer-based biosensors for mycotoxin detection. In *Nanomycotoxicology* (pp. 35-70). Academic Press.

Ezquerra, A., Vidal, J.C., Bonel, L. and Castillo, J.R. 2015. A validated multi-channel electrochemical immunoassay for rapid fumonisin B1 determination in cereal samples. *Analytical Methods.* **7**(9), pp.3742-3749.

Félix, L., Hernández, J., Argüelles-Monal, W.M. and Goycoolea, F.M. 2005. Kinetics of gelation and thermal sensitivity of N-isobutyryl chitosan hydrogels. *Biomacromolecules*. **6**(5), pp.2408-2415.

Fernandes, S.C., Freire, C.S., Silvestre, A.J., Neto, C.P., Gandini, A., Berglund, L.A. and Salmén, L. 2010. Transparent chitosan films reinforced with a high content of nanofibrillated cellulose. *Carbohydrate Polymers*. **81**(2), pp.394-401.

Flores-Flores, M.E. and González-Peñas, E. 2017. An LC–MS/MS method for multi-mycotoxin quantification in cow milk. *Food chemistry*. **218**, pp.378-385.

Food and Agriculture Organization of the United Nations. 2004. Worldwide regulations for mycotoxins in food and feed in 2003. [Online]. FAO. [Accessed on 31 October 2017]. Available from: http://www.fao.org/docrep/007/y5499e/y5499e00.htm

Food Standards Agency. 2019. Consolidated annual report and accounts 2018/2019. [Online]. United Kingdom: APS Group [Accessed on 20 December 2020]. Available from: https://www.food.gov.uk/sites/default/files/media/document/fsa-annual-report-accounts-2018-19-consolidated.pdf

Food Standards Agency. 2019. Incidents annual reports 2006-2017. [Online]. United Kingdom [Accesed on 10 April 2020]. Available from: https://www.food.gov.uk/about-us/reports-and-accounts

Franzmann, G., Dynamit Nobel A.G. 1983. *METHOD for the N-acylation of aminocarboxylic acids*. U.S. Patent 4,380,646.

Frisvad, J.C., Smedsgaard, J., Samson, R.A., Larsen, T.O. and Thrane, U. 2007. Fumonisin B2 production by Aspergillus niger. *Journal of Agricultural and Food Chemistry*. **55**(23), pp.9727-9732.

Frost, N.R., McKeague, M., Falcioni, D. and DeRosa, M.C. 2015. An in solution assay for interrogation of affinity and rational minimer design for small molecule-binding aptamers. *Analyst*. **140**(19), pp.6643-6651.

Fultz, B. and Howe, J.M. 2012. *Transmission electron microscopy and diffractometry of materials*. Springer Science & Business Media.

Fu, Z., Huang, X. and Min, S. 2008. Rapid determination of aflatoxins in corn and peanuts. *Journal of Chromatography A*. **1209**(1-2), pp.271-274.

Gabriel, E.F., Garcia, P.T., Cardoso, T.M., Lopes, F.M., Martins, F.T. and Coltro, W.K. 2016. Highly sensitive colorimetric detection of glucose and uric acid in biological fluids using chitosan-modified paper microfluidic devices. *Analyst*. **141**(15), pp.4749-4756.

Gallibu, C., Gallibu, C., Avoundjian, A. and Gomez, F.A. 2016. Easily fabricated microfluidic devices using permanent marker inks for enzyme assays. *Micromachines*. **7**(1), p.6.

García, S. and Heredia, N. 2006. Mycotoxins in Mexico: Epidemiology, management, and control strategies. *Mycopathologia*. **162**(3), pp. 255-264.

Gazzotti, T., Lugoboni, B., Zironi, E., Barbarossa, A., Serraino, A. and Pagliuca, G. 2009. Determination of fumonisin B1 in bovine milk by LC–MS/MS. *Food Control*. **20**(12), pp.1171-1174.

Gbashi, S., Madala, N. E., De Saeger, S., De Boevre, M., Adekoya, I., Adebo, O. A. And Njobeh, P. B. 2018. The socio-economic impact of mycotoxin contamination in Africa. Fungi and mycotoxins-their occurrence, impact on health and the economy as well as pre-and postharvest management strategies (ed. Njobeh, PB). pp.1-20.

Gbore, F.A. 2010. Brain and hypophyseal acetylcholinesterase activity of pubertal boars fed dietary fumonisin B1. *Journal of animal physiology and animal nutrition*. **94**(5), pp.e123-e129.

Gelderblom, W.C.A., Jaskiewicz, K., Marasas, W.F.O., Thiel, P.G., Horak, R.M., Vleggar, R. and Kriek, N.P.J. 1988. Fumonisins- Novel mycotoxins with cancer-

promoting activity produced by *Fusarium moniliforme*. *Applied and environmental microbiology*. **54**(7), pp. 1806-1811.

Gelderblom, W.C., Kriek, N.P.J., Marasas, W.F.O. and Thiel, P.G. 1991. Toxicity and carcinogenicity of the Fusanum monilzforine metabolite, fumonisin B1, in rats. *Carcinogenesis*. **12**(7), pp.1247-1251.

Ghaderinezhad, F., Amin, R., Temirel, M., Yenilmez, B., Wentworth, A. and Tasoglu, S. 2017. High-throughput rapid-prototyping of low-cost paper-based microfluidics. *Scientific reports*. **7**(1), pp.1-9.

Ghali, R., Ghorbel, H. and Hedilli, A. 2009. Fumonisin determination in Tunisian foods and feeds. ELISA and HPLC methods comparison. *Journal of agricultural and food chemistry*. **57**(9), pp.3955-3960.

Gilbert-Sandoval, I., Wesseling, S. and Rietjens, I.M. 2020. Occurrence and probabilistic risk assessment of fumonisin B1, fumonisin B2 and deoxynivalenol in nixtamalized maize in Mexico City. *Toxins.* **12**(10), p.644.

Gong, Y.Y., Torres-Sanchez, L., Lopez-Carrillo, L., Peng, J.H., Sutcliffe, A.E., White, K.L., Humpf, H.U., Turner, P.C. and Wild, C.P. 2008. Association between tortilla consumption and human urinary fumonisin B1 levels in a Mexican population. *Cancer Epidemiology and Prevention Biomarkers*. **17**(3), pp.688-694.

González-Espinosa, Y., Sabagh, B., Moldenhauer, E., Clarke, P. and Goycoolea, F.M. 2019. Characterisation of chitosan molecular weight distribution by multi-detection asymmetric flow-field flow fractionation (AF4) and SEC. *International journal of biological macromolecules*. **136**, pp.911-919.

González-Jartín, J.M., Alfonso, A., Rodríguez, I., Sainz, M.J., Vieytes, M.R. and Botana, L.M. 2019. A QuEChERS based extraction procedure coupled to UPLC-MS/MS detection for mycotoxins analysis in beer. *Food chemistry*. **275**, pp.703-710.

Gopinath, S.C.B. 2007. Methods developed for SELEX. *Analytical and bioanalytical chemistry*. **387**(1), pp.171-182.

Goud, K.Y., Reddy, K.K., Satyanarayana, M., Kummari, S. and Gobi, K.V. 2020. A review on recent developments in optical and electrochemical aptamer-based assays for mycotoxins using advanced nanomaterials. *Microchimica Acta*. **187**(1), pp.1-32.

Goycoolea, F.M., Fernández-Valle, M.E., Aranaz, I. and Heras, A. 2011. pH-and Temperature-Sensitive Chitosan Hydrogels: Swelling and MRI Studies. *Macromolecular Chemistry and Physics*. **212**(9), pp.887-895.

Gray, E.P., Bruton, T.A., Higgins, C.P., Halden, R.U., Westerhoff, P. and Ranville, J.F. 2012. Analysis of gold nanoparticle mixtures: a comparison of hydrodynamic chromatography (HDC) and asymmetrical flow field-flow fractionation (AF4) coupled to ICP-MS. *Journal of Analytical Atomic Spectrometry*. **27**(9), pp.1532-1539.

Guan, J., Fujimoto, K.L., Sacks, M.S. and Wagner, W.R. 2005. Preparation and characterization of highly porous, biodegradable polyurethane scaffolds for soft tissue applications. *Biomaterials*. **26**(18), pp.3961-3971.

Gui, H., Jin, Q., Zhang, Y., Wang, X., Yang, Y., Shao, C., Cheng, C., Wei, F., Yang, M. and Song, H. 2015. Development of an aptamer/fluorescence dye PicoGreen-based method for detection of fumonisin B1. *Sheng wu gong cheng xue bao= Chinese journal of biotechnology*. **31**(9), pp.1393-1400.

Guo, L., Wang, Z., Xu, X., Xu, L., Kuang, H., Xiao, J. and Xu, C. 2020. Europium nanosphere-based fluorescence strip sensor for ultrasensitive and quantitative determination of fumonisin B 1. *Analytical Methods*. **12**(43), pp.5229-5235.

Gutleb, A.C., Morrison, E. and Murk, A.J. 2002. Cytotoxicity assays for mycotoxins produced by Fusarium strains: a review. *Environmental Toxicology and Pharmacology*. **11**(3-4), pp.309-320.

Hagendorfer, H., Kaegi, R., Traber, J., Mertens, S.F., Scherrers, R., Ludwig, C. and Ulrich, A. 2011. Application of an asymmetric flow field flow fractionation multi-detector approach for metallic engineered nanoparticle characterization–prospects and limitations demonstrated on Au nanoparticles. *Analytica Chimica Acta*. **706**(2), pp.367-378.

Haiss, W., Thanh, N. T., Aveyard, J. and Fernig, D. G. 2007. Determination of size and concentration of gold nanoparticles from UV− Vis spectra. *Analytical Chemistry*. **79**(11), pp. 4215-4221.

Hamed, A.M., Arroyo-Manzanares, N., García-Campaña, A.M. and Gámiz-Gracia, L. 2017. Determination of Fusarium toxins in functional vegetable milks applying salting-out-assisted liquid–liquid extraction combined with ultra-high-performance liquid chromatography tandem mass spectrometry. *Food Additives & Contaminants: Part A*. **34**(11), pp.2033-2041.

Han, Z., Tang, Z., Jiang, K., Huang, Q., Meng, J., Nie, D. and Zhao, Z. 2020. Dual-target electrochemical aptasensor based on co-reduced molybdenum disulfide and Au NPs (rMoS2-Au) for multiplex detection of mycotoxins. *Biosensors and Bioelectronics*.**150**, p.111894.

Hao, N., Lu, J., Zhou, Z., Hua, R. and Wang, K. 2018a. A pH-resolved colorimetric biosensor for simultaneous multiple target detection. *ACS sensors*. **3**(10), pp.2159-2165.

Hao, K., Suryoprabowo, S., Hong, T., Song, S., Liu, L., Zheng, Q. and Kuang, H. 2018b. Immunochromatographic strip for ultrasensitive detection of fumonisin B1. *Food and Agricultural Immunology*. **29**(1), pp.699-710.

Harrison, G. and Barlow, A.J. 1981. 3. Dynamic viscosity measurement. In *Methods in experimental physics* (Vol. **19**, pp. 137-178). Academic Press.

Harsányi, G. 1995. *Polymer films in sensor applications*. USA: Technomic Publishing Company, Inc.

Haugstad, K.E., Håti, A.G., Nordgård, C.T., Adl, P.S., Maurstad, G., Sletmoen, M., Draget, K.I., Dias, R.S. and Stokke, B.T. 2015. Direct determination of chitosan–mucin interactions using a single-molecule strategy: Comparison to alginate–mucin interactions. *Polymers*. **7**(2), pp.161-185.

He, D., Wu, Z., Cui, B., Jin, Z. and Xu, E. 2020a. A fluorometric method for aptamer-based simultaneous determination of two kinds of the fusarium mycotoxins zearalenone and fumonisin B 1 making use of gold nanorods and upconversion nanoparticles. *Microchimica Acta*.**187**(4), pp.1-8.

He, D., Wu, Z., Cui, B. and Xu, E., 2020b. Aptamer and gold nanorod–based fumonisin B1 assay using both fluorometry and SERS. *Microchimica Acta*, *187*(4), pp.1-8.

Hines, H.B., Brueggemann, E.E., Holcomb, M. and Holder, C.L. 1995. Fumonisin B1 analysis with capillary electrophoresis–electrospray ionization mass spectrometry. *Rapid communications in mass spectrometry*. **9**(6), pp.519-524.

Ho., J.A. and Durst, R.A. 2000. Development of a flow-injection liposome immunoanalysis system for fumonisin B1. *Analytica Chimica Acta*. **414**(1-2), pp.61-69.

Holcomb, M. and Thompson Jr, H.C. 1995. Analysis of fumonisin B1 in corn by capillary electrophoresis with fluorescence detection of the FMOC derivative. *Journal of Microcolumn Separations*. **7**(5), pp.451-454.

Holcomb, M., Thompson, H.C. and Hankins, L.J. 1993. Analysis of fumonisin B1 in rodent feed by gradient elution HPLC using precolumn derivatization with FMOC and fluorescence detection. *Journal of agricultural and food chemistry*. **41**(5), pp.764-767.

Hong, S. and Kim, W. 2015. Dynamics of water imbibition through paper channels with wax boundaries. *Microfluidics and Nanofluidics*. **19**(4), pp.845-853.

Hong, Y., Song, H., Gong, Y., Mao, Z., Gao, C. and Shen, J. 2007. Covalently crosslinked chitosan hydrogel: properties of in vitro degradation and chondrocyte encapsulation. *Acta biomaterialia*. **3**(1), pp.23-31.

Hort, V., Nicolas, M., Travel, A., Jondreville, C., Maleix, C., Baéza, E., Engel, E. and Guérin, T. 2020. Carry-over assessment of fumonisins and zearalenone to poultry tissues after exposure of chickens to a contaminated diet–A study implementing stable-isotope dilution assay and UHPLC-MS/MS. *Food Control*. **107**, p.106789.

Hossain, S.Z., Luckham, R.E., Smith, A.M., Lebert, J.M., Davies, L.M., Pelton, R.H., Filipe, C.D. and Brennan, J.D. 2009. Development of a bioactive paper sensor for detection of neurotoxins using piezoelectric inkjet printing of sol− gel-derived bioinks. *Analytical chemistry*. **81**(13), pp.5474-5483.

Hou, S., Ma, J., Cheng, Y., Wang, H., Sun, J. and Yan, Y. 2020a. One-step rapid detection of fumonisin B1, dexyonivalenol and zearalenone in grains. *Food Control.* **117**, p.107107.

Hou, S., Ma, J., Cheng, Y., Wang, H., Sun, J. and Yan, Y., 2020b. Quantum dot nanobead-based fluorescent immunochromatographic assay for simultaneous quantitative detection of fumonisin B1, dexyonivalenol, and zearalenone in grains. *Food Control*, *117*, p.107331.

Hu, J., Wang, S., Wang, L., Li, F., Pingguan-Murphy, B., Lu, T.J. and Xu, F. 2014. Advances in paper-based point-of-care diagnostics. *Biosensors and Bioelectronics*. **54**, pp.585-597.

Hu, L., Liu, H., Yang, J., Wang, C., Wang, Y., Yang, Y. and Chen, X. 2019. Free and hidden fumonisins in raw maize and maize-based products from China. *Food Additives & Contaminants: Part B*. **12**(2), pp.90-96.

Huang, X., Huang, T., Li, X. and Huang, Z. 2020. Flower-like gold nanoparticles-based immunochromatographic test strip for rapid simultaneous detection of fumonisin B1 and deoxynivalenol in Chinese traditional medicine. *Journal of pharmaceutical and biomedical analysis*. **177**, p.112895.

Huang, P., Kong, W., Wang, S., Wang, R., Lu, J. and Yang, M. 2018. Multiclass mycotoxins in lotus seeds analysed by an isotope-labelled internal standard-based UPLC-MS/MS. *Journal of Pharmacy and Pharmacology*. **70**(10), pp.1378-1388.

Jang, M.K., Kong, B.G., Jeong, Y.I., Lee, C.H. and Nah, J.W. 2004. Physicochemical characterization of α-chitin, β-chitin, and γ-chitin separated from natural resources. *Journal of Polymer Science Part A: Polymer Chemistry*. **42**(14), pp.3423-3432.

Jayakumar, R., Prabaharan, M., Kumar, P.S., Nair, S.V. and Tamura, H. 2011. Biomaterials based on chitin and chitosan in wound dressing applications. *Biotechnology advances*. **29**(3), pp.322-337.

Jedziniak, P., Panasiuk, Ł., Pietruszka, K. and Posyniak, A. 2019. Multiple mycotoxins analysis in animal feed with LC-MS/MS: Comparison of extract dilution and immunoaffinity clean-up. Journal of separation science. 42(6), pp.1240-1247.

Jeng, C. C., Chong, P. J., Chiu, C. C., Jiang, G. J., Lin, H. J., Wu, R. J. and Wu, C. H. 2014. A dynamic equilibrium method for the SnO2-based ozone sensors using UV-LED continuous irradiation. *Sensors and Actuators B: Chemical*. **195**, pp. 702-706.

Jiang, D., Huang, C., Shao, L., Wang, X., Jiao, Y., Li, W., Chen, J. and Xu, X. 2020. Magneto-controlled aptasensor for simultaneous detection of ochratoxin A and fumonisin B1 using inductively coupled plasma mass spectrometry with multiple metal nanoparticles as element labels. *Analytica Chimica Acta*. **1127**, pp.182-189.

Jiang, Z., Yu, Y. and Wu, H. 2006. Preparation of CS/GPTMS hybrid molecularly imprinted membrane for efficient chiral resolution of phenylalanine isomers. *Journal of membrane science*. **280**(1-2), pp.876-882.

Jie, M., Yu, S., Yu, F., Liu, L., He, L., Li, Y., Zhang, H., Qu, L., Harrington, P.D.B. and Wu, Y. 2018. An ultrasensitive chemiluminescence immunoassay for fumonisin B1 detection in cereals based on gold-coated magnetic nanoparticles. *Journal of the Science of Food and Agriculture*. **98**(9), pp.3384-3390.

Jing, M. and Bowser, M.T. 2011. Methods for measuring aptamer-protein equilibria: a review. *Analytica chimica acta*. **686**(1-2), pp.9-18.

Jodra, A., López, M.Á. and Escarpa, A. 2015. Disposable and reliable electrochemical magnetoimmunosensor for Fumonisins simplified determination in maize-based foodstuffs. *Biosensors and Bioelectronics*. **64**, pp.633-638.

Kadir, M.K. and Tothill, I.E. 2010. Development of an electrochemical immunosensor for fumonisins detection in foods. *Toxins*. **2**(4), pp.382-398.

Kamle, M., Mahato, D.K., Devi, S., Lee, K.E., Kang, S.G. and Kumar, P. 2019. Fumonisins: Impact on agriculture, food, and human health and their management strategies. *Toxins*. **11**(6), p.328.

Karlovsky, P., Suman, M., Berthiller, F., De Meester, J., Eisenbrand, G., Perrin, I., Oswald, I.P., Speijers, G., Chiodini, A., Recker, T. and Dussort, P. 2016. Impact of food processing and detoxification treatments on mycotoxin contamination. *Mycotoxin research*. **32**(4), pp.179-205.

Kebede, H., Liu, X., Jin, J., and Xing, F. 2020. Current status of major mycotoxins contamination in food and feed in Africa. *Food Control*. **110**, p.106975.

Kecskeméti, Á., Nagy, C., Biró, P., Szabó, Z., Pócsi, I., Bartók, T. and Gáspár, A. 2020. Analysis of fumonisin mycotoxins with capillary electrophoresis–mass spectrometry. *Food Additives & Contaminants: Part A*. **37**(9), pp.1553-1563.

Kellerman, T.S., Marasas, W.F.O., Thiel, P.G., Gelderblom, W.C.A., Cawood, M. and Coetzer, J.A.W. 1990. Leukoencephalomalacia in two horses induced by oral dosing of fumonisin B_1. *Onderstepoort Journal of Veterinary Research*. **57**,269-275.

Kesici, E. and Erdem, A. 2019. Impedimetric detection of Fumonisin B1 and its biointeraction with fsDNA. *International journal of biological macromolecules*. **139**, pp.1117-1122.

Kettle, J., Lamminmäki, T. and Gane, P. 2010. A review of modified surfaces for high speed inkjet coating. *Surface and coatings Technology*. **204**(12-13), pp.2103-2109.

Khaneghah, A.M., Fakhri, Y., Gahruie, H.H., Niakousari, M. and Sant'Ana, A.S. 2019. Mycotoxins in cereal-based products during 24 years (1983–2017): A global systematic review. *Trends in Food Science & Technology*. **91**, pp.95-105.

Knutsen, H.-K., Alexander, J., Barregård, L., Bignami, M., Brüschweiler, B., Ceccatelli, S., Cottrill, B., Dinovi, M., Edler, L., Grasl-Kraupp, B., Hogstrand, C., Hoogenboom, L., Nebbia, C.S., Petersen, A., Rose, M., Roudot, A.-C., Schwerdtle, T., Vleminckx, C., Vollmer, G., Wallace, H., Dall'Asta, C., Eriksen, G.-S., Taranu, I., Altieri, A., Roldán-Torres, R. and Oswald, I.P. 2018. Risks for animal health related to the presence of fumonisins, their modified forms and hidden forms in feed. *EFSA Journal*. **16**(5), p.e05242.

Kurita, K., Ishii, S., Tomita, K., Nishimura, S.I. and Shimoda, K. 1994. Reactivity characteristics of squid β-chitin as compared with those of shrimp chitin: High potentials of squid chitin as a starting material for facile chemical modifications. *Journal of Polymer Science Part A: Polymer Chemistry*. **32**(6), pp.1027-1032.

Lai, J.Y., Li, Y.T. and Wang, T.P. 2010. In vitro response of retinal pigment epithelial cells exposed to chitosan materials prepared with different cross-linkers. *International journal of molecular sciences*. **11**(12), pp.5256-5272.

Lakowicz, J. R. 1999. *Introduction to fluorescence*. In Principles of fluorescence spectroscopy. USA: Springer.

Lamberti, I., Tanzarella, C., Solinas, I., Padula, C. and Mosiello, L. 2009. An antibody-based microarray assay for the simultaneous detection of aflatoxin B 1 and fumonisin B 1. *Mycotoxin research.* **25**(4), pp.193-200.

Lamminmäki, T. T., Kettle, J. P., Puukko, P. J. T. and Gane, P. A. C. 2011. The chromatographic separation of anionic dye in inkjet coating structures. *Colloids and Surfaces A: Physicochemical and Engineering Aspects*. **377**(1-3), pp.304-311.

Lamminmäki, T. T., Kettle, J. P., Puukko, P. J. T., Ridgway, C. J. and Gane, P. A. C. 2012. Short timescale inkjet ink component diffusion: An active part of the absorption mechanism into inkjet coatings. *Journal of colloid and interface science*. **365** (1), pp.222-235.

Lamprecht, S.C., Marasas, W.F.O., Alberts, J.F., Cawood, M.E., Gelderblom, W.C.A., Shephard, G.S., Thiel, P.G. and Calitz, F.J. 1994. Phytotoxicity of fumonisins and TA-toxin to corn and tomato. *Phytopathology*. **84**(4), pp.383-391.

Latham, M. P., Zimmermann, G. R. and Pardi, A. 2009. NMR chemical exchange as a probe for ligand-binding kinetics in a theophylline-binding RNA aptamer. *Journal of the American Chemical Society*. **131**(14), pp. 5052-5053.

Lattanzio, V.M., Nivarlet, N., Lippolis, V., Della Gatta, S., Huet, A.C., Delahaut, P., Granier, B. and Visconti, A. 2012. Multiplex dipstick immunoassay for semi-quantitative determination of Fusarium mycotoxins in cereals. *Analytica chimica acta*. **718**, pp.99-108.

Lautert, C., Ferreiro, L., Wolkmer, P., Paim, F. C., Da Silva, C. B., Jaques, J. A., Lopes, S.T.A. and Santurio, J. M. 2014. Individual in vitro effects of ochratoxin A, deoxynivalenol and zearalenone on oxidative stress and acetylcholinesterase in lymphocytes of broiler chickens. *Springerplus*. **3**(1), pp. 1-7.

Lee, K.M. and Herrman, T.J. 2016. Determination and prediction of fumonisin contamination in maize by surface–enhanced Raman spectroscopy (SERS). *Food and bioprocess technology*. **9**(4), pp.588-603.

Lee, S., Kim, G. and Moon, J. 2013. Performance improvement of the one-dot lateral flow immunoassay for aflatoxin B1 by using a smartphone-based reading system. *Sensors*. **13**(4), pp.5109-5116.

Li, C., Mi, T., Oliveri Conti, G., Yu, Q., Wen, K., Shen, J., Ferrante, M. and Wang, Z. 2015. Development of a screening fluorescence polarization immunoassay for the simultaneous detection of fumonisins B1 and B2 in maize. *Journal of agricultural and food chemistry*. **63**(20), pp.4940-4946.

Li, H. and Rothberg, L. 2004(a). Colorimetric detection of DNA sequences based on electrostatic interactions with unmodified gold nanoparticles. *Proceedings of the National Academy of Sciences*. **101**(39), pp.14036-14039.

Li, H. and Rothberg, L.J. 2004(b). Label-free colorimetric detection of specific sequences in genomic DNA amplified by the polymerase chain reaction. *Journal of the American Chemical Society*. **126**(35), pp.10958-10961.

Li, L., Chen, W., Li, H., Iqbal, J., Zhu, Y., Wu, T. and Du, Y. 2020. Rapid determination of fumonisin (FB1) by syringe SPE coupled with solid-phase fluorescence spectrometry. *Spectrochimica Acta Part A: Molecular and Biomolecular Spectroscopy*. **226**, p.117549.

Li, L., Li, W., Ma, C., Yang, H., Ge, S. and Yu, J. 2014. Paper-based electrochemiluminescence immunodevice for carcinoembryonic antigen using nanoporous gold-chitosan hybrids and graphene quantum dots functionalized Au@ Pt. *Sensors and Actuators B: Chemical*. **202**, pp.314-322.

Li, M., Kong, W., Li, Y., Liu, H., Liu, Q., Dou, X., Ou-Yang, Z. and Yang, M. 2016. High-throughput determination of multi-mycotoxins in Chinese yam and related products by ultra fast liquid chromatography coupled with tandem mass spectrometry after one-step extraction. *Journal of Chromatography B*. **1022**, pp.118-125.

Li, T.Q., Henriksson, U., Klason, T. and Ödberg, L. 1992. Water diffusion in wood pulp cellulose fibers studied by means of the pulsed gradient spin-echo method. *Journal of colloid and interface science*. **154**(2), pp.305-315.

Li, X.M. and Feng, Q.L. 2005. Dynamic rheological behaviors of the bone scaffold reinforced by chitin fibres. In *Materials Science Forum* (Vol. 475, pp. 2387-2390). Trans Tech Publications Ltd.

Li, Z., Sheng, W., Liu, Q., Li, S., Shi, Y., Zhang, Y. and Wang, S. 2018. Development of a gold nanoparticle enhanced enzyme linked immunosorbent assay based on monoclonal antibodies for the detection of fumonisin B 1, B 2, and B 3 in maize. *Analytical Methods*. **10**(28), pp.3506-3513.

Li, Y.S., Zhou, Y., Lu, S.Y., Guo, D.J., Ren, H.L., Meng, X.M., Zhi, B.H., Lin, C., Wang, Z., Li, X.B. and Liu, Z.S. 2012. Development of a one-step test strip for rapid screening of fumonisins B1, B2 and B3 in maize. *Food Control*. **24**(1-2), pp.72-77.

Ligler, F.S., Taitt, C.R., Shriver-Lake, L.C., Sapsford, K.E., Shubin, Y. and Golden, J.P. 2003. Array biosensor for detection of toxins. *Analytical and bioanalytical chemistry*. **377**(3), pp.469-477.

Lin, P.H., Chen, R.H., Lee, C.H., Chang, Y., Chen, C.S. and Chen, W.Y. 2011. Studies of the binding mechanism between aptamers and thrombin by circular dichroism, surface plasmon resonance and isothermal titration calorimetry. *Colloids and Surfaces B: Biointerfaces*. **88**(2), pp.552-558.

Lin, Y., Zhou, Q., Lin, Y., Tang, D., Niessner, R. and Knopp, D. 2015. Enzymatic hydrolysate-induced displacement reaction with multifunctional silica beads doped with horseradish peroxidase–thionine conjugate for ultrasensitive electrochemical immunoassay. *Analytical chemistry*. **87**(16), pp. 8531-8540.

Lin, X. and Guo, X. 2016. Advances in biosensors, chemosensors and assays for the determination of fusarium mycotoxins. *Toxins*. **8**(6), p.161.

Lin, Y., Zhou, Q., Tang, D., Niessner, R., Yang, H. and Knopp, D. 2016. Silver nanolabels-assisted ion-exchange reaction with CdTe quantum dots mediated

exciton trapping for signal-on photoelectrochemical immunoassay of mycotoxins. *Analytical Chemistry*. **88**(15), pp.7858-7866.

Lin, Y., Zhou, Q., Tang, D. 2017a. Dopamine-loaded liposomes for in-situ amplified photoelectrochemical immunoassay of AFB1 to enhance photocurrent of Mn^{2+}-doped $Zn_3(OH)_2V_2O_7$ nanobelts. *Analytical Chemistry*. **89**(21), pp.11803-11810.

Lin, Y., Zhou, Q., Tang, D., Niessner, R. and Knopp, D. 2017b. Signal-on photoelectrochemical immunoassay for aflatoxin B1 based on enzymatic product-etching MnO_2 nanosheets for dissociation of carbon dots. *Analytical Chemistry*. **89**(10), pp.5637-5645.

Lin, Y., Zhou, Q., Zeng, Y. and Tang, D. 2018. Liposome-coated mesoporous silica nanoparticles loaded with L-cysteine for photoelectrochemical immunoassay of aflatoxin B 1. *Microchimica Acta*. **185**(6), pp.1-9.

Liu, D., Huang, Y., Wang, S., Liu, K., Chen, M., Xiong, Y., Yang, W. and Lai, W. 2015. A modified lateral flow immunoassay for the detection of trace aflatoxin M1 based on immunomagnetic nanobeads with different antibody concentrations. *Food Control*. **51**, pp.218-224.

Liu, G., Fu, S., Lu, Z., Zhang, M., Ridgway, C. and Gane, P. 2017. Contrasting liquid imbibition into uncoated versus pigment coated paper enables a description of imbibition into new-generation surface-filled paper. *The European Physical Journal E*. **40**(111), pp.1-11.

Liu, H., Luo, J., Kong, W., Liu, Q., Hu, Y. and Yang, M. 2016. UFLC-ESI-MS/MS analysis of multiple mycotoxins in medicinal and edible Areca catechu. *Chemosphere*. **150**, pp.176-183.

Liu, L., Yang, D. and Liu, G. 2019. Signal amplification strategies for paper-based analytical devices. *Biosensors and Bioelectronics*.**136**, pp.60-75.

Liu, R., Li, W., Cai, T., Deng, Y., Ding, Z., Liu, Y., Zhu, X., Wang, X., Liu, J., Liang, B. and Zheng, T. 2018. TiO_2 nanolayer-enhanced fluorescence for simultaneous multiplex mycotoxin detection by aptamer microarrays on a porous silicon surface. *ACS applied materials & interfaces*. **10**(17), pp.14447-14453.

Liu, W., Kou, J., Xing, H. and Li, B. 2014. Paer-based chromatographic chemiluminescence chip for the detection of dichlorvos in vegetables. *Biosensors and Bioelectronics*. **52**, pp.76-81.

Liu, X., Fan, L., Yin, S., Chen, H. and Hu, H. 2019. Molecular mechanisms of fumonisin B1-induced toxicities and its applications in the mechanism-based interventions. Toxicon.**167**, pp.1-5.

Liu, Y., Galani-Yamdeu, J.H., Gong, Y.Y. and Orfila, C. 2020a. A review of postharvest approaches to reduce fungal and mycotoxin contamination of foods. *Comprehensive Reviews in Food Science and Food Safety*. **19**(4), pp.1521-1560.

Liu, Z., Hua, Q., Wang, J., Liang, Z., Li, J., Wu, J., Shen, X., Lei, H. and Li, X. 2020b. A smartphone-based dual detection mode device integrated with two lateral flow immunoassays for multiplex mycotoxins in cereals. *Biosensors and Bioelectronics*. **158**, p.112178.

Lu, L. and Gunasekaran, S. 2019. Dual-channel ITO-microfluidic electrochemical immunosensor for simultaneous detection of two mycotoxins. *Talanta*. **194**, pp.709-716.

Lu, L., Seenivasan, R., Wang, Y.C., Yu, J.H. and Gunasekaran, S. 2016. An electrochemical immunosensor for rapid and sensitive detection of mycotoxins fumonisin B1 and deoxynivalenol. *Electrochimica Acta*. **213**, pp.89-97.

Lu, T., Zhan, S., Zhou, Y., Chen, X., Huang, X., Leng, Y., Xiong, Y. and Xu, Y. 2018. Fluorescence ELISA based on CAT-regulated fluorescence quenching of CdTe QDs for sensitive detection of FB 1. *Analytical Methods*. **10**(48), pp.5797-5802.

Lu, Y., Shi, W., Jiang, L., Qin, J. and Lin, B. 2009. Rapid prototyping of paper-based microfluidics with wax for low-cost, portable bioassay. *Electrophoresis*. **30**(9), pp.1497-1500.

Luan, C.H., Parker, T.M., Gowda, D.C. and Urry, D.W. 1992. Hydrophobicity of amino acid residues: differential scanning calorimetry and synthesis of the aromatic analogues of the polypentapeptide of elastin. *Biopolymers: Original Research on Biomolecules*. **32**(9), pp.1251-1261.

Luan, Y., Chen, J., Li, C., Xie, G., Fu, H., Ma, Z. and Lu, A. 2015. Highly sensitive colorimetric detection of ochratoxin A by a label-free aptamer and gold nanoparticles. *Toxins*. **7**(12), pp.5377-5385.

Luo, Y., Zhou, Z. and Yue, T. 2017. Synthesis and characterization of nontoxic chitosan-coated Fe3O4 particles for patulin adsorption in a juice-pH simulation aqueous. *Food chemistry*. **221**, pp.317-323.

Ma, H., Sun, J., Zhang, Y., Bian, C., Xia, S. and Zhen, T. 2016. Label-free immunosensor based on one-step electrodeposition of chitosan-gold nanoparticles biocompatible film on Au microelectrode for determination of aflatoxin B1 in maize. *Biosensors and Bioelectronics*. **80**, pp.222-229.

Maeda, Y., Jayakumar, R., Nagahama, H., Furuike, T. and Tamura, H. 2008. Synthesis, characterization and bioactivity studies of novel β-chitin scaffolds for tissue-engineering applications. *International journal of biological macromolecules*. **42**(5), pp.463-467.

Maciel, V.B., Yoshida, C.M. and Franco, T.T. 2012. Development of a prototype of a colourimetric temperature indicator for monitoring food quality. *Journal of food engineering*. **111**(1), pp.21-27.

Magnoli, A.P., Poloni, V.L. and Cavaglieri, L. 2019. Impact of mycotoxin contamination in the animal feed industry. *Current Opinion in Food Science.* **29**, pp.99-108.

Magoha, H., De Meulenaer, B., Kimanya, M., Hipolite, D., Lachat, C. and Kolsteren, P. 2014. Fumonisin B1 contamination in breast milk and its exposure in infants under 6 months of age in Rombo, Northern Tanzania. *Food and chemical toxicology*. **74**, pp.112-116.

Mahmud, M., Blondeel, E.J., Kaddoura, M. and MacDonald, B.D. 2018. Features in microfluidic paper-based devices made by laser cutting: How small can they be?. *Micromachines*. **9**(5), p.220.

Majdinasab, M., Ben Aissa, S. and Marty, J.L. 2021. Advances in Colorimetric Strategies for Mycotoxins Detection: Toward Rapid Industrial Monitoring. *Toxins*. **13**(1), p.13.

Malvern Panalytical. *Viscosity*. [Online]. [Accesed 07 January 2021]. Available from: https://www.malvernpanalytical.com/en/products/measurement-type/viscosity

Mangal, M., Khan, F., Bansal, S. and Oberoi, H.S. 2016. Validation of PCR based detection system for aflatoxin producing molds. *Indian Journal of Experimental Biology*. **54**(7), pp.472-476.

Mansson, M., Klejnstrup, M.L., Phipps, R.K., Nielsen, K.F., Frisvad, J.C., Gotfredsen, C.H. and Larsen, T.O. 2010. Isolation and NMR characterization of fumonisin B2 and

a new fumonisin B6 from Aspergillus niger. *Journal of agricultural and food chemistry*. **58**(2), pp.949-953.

Mao, L., Ji, K., Yao, L., Xue, X., Wen, W., Zhang, X. and Wang, S. 2019. Molecularly imprinted photoelectrochemical sensor for fumonisin B1 based on GO-CdS heterojunction. *Biosensors and Bioelectronics*. **127**, pp.57-63.

Maragos, C.M. 1995. Capillary zone electrophoresis and HPLC for the analysis of fluorescein isothiocyanate-labeled fumonisin B1. *Journal of Agricultural and Food Chemistry*. **43**(2), pp.390-394.

Maragos, C.M. 1997. Detection of the mycotoxin fumonisin B1 by a combination of immunofluorescence and capillary electrophoresis. *Food and Agricultural Immunology*. **9**(3), pp.147-157.

Maragos, C.M., Jolley, M.E., Plattner, R.D. and Nasir, M.S. 2001. Fluorescence polarization as a means for determination of fumonisins in maize. *Journal of agricultural and food chemistry*. **49**(2), pp.596-602.

Marasas, D.J. and WFO, J. 1988. Fusarium moniliforme contamination of maize in oesophageal cancer areas in Transkei. *South African Medical Journal*. **74**(3), pp.110-114.

Marin, S.. and Ramos, A. J. 200). Natural contamination with mycotoxins in forage maize and green coffee in Nayarit State (Mexico). *Revista Iberoamericana de Micologia*, **18**(3), pp.141-144.

Marin, S., Ramos, A.J., Cano-Sancho, G. and Sanchis, V. 2013. Mycotoxins: Occurrence, toxicology, and exposure assessment. *Food and chemical toxicology*. **60**, pp.218-237.

Marmur, A. Kinetics of penetration into uniform porous media: testing the equivalent-capillary concept. *Langmuir*. **19**(14), pp.5956-5959.

Martins, C., Vidal, A., De Boevre, M., De Saeger, S., Nunes, C., Torres, D., Goios, A., Lopes, C., Assunção, R. and Alvito, P. 2019. Exposure assessment of Portuguese population to multiple mycotoxins: The human biomonitoring approach. *International journal of hygiene and environmental health*. **222**(6), pp.913-925.

Masikini, M., Mailu, S.N., Tsegaye, A., Njomo, N., Molapo, K.M., Ikpo, C.O., Sunday, C.E., Rassie, C., Wilson, L., Baker, P.G. and Iwuoha, E.I. 2015. A fumonisins

immunosensor based on polyanilino-carbon nanotubes doped with palladium telluride quantum dots. *Sensors*. **15**(1), pp.529-546.

Masikini, M., Williams, A.R., Sunday, C.E., Waryo, T.T., Nxusani, E., Wilson, L., Qakala, S., Bilibana, M., Douman, S., Jonnas, A. and Baker, P.G. 2016. Label free poly (2, 5-dimethoxyaniline)–multi-walled carbon nanotubes impedimetric immunosensor for fumonisin B1 detection. *Materials*. ***9***(4), p.273.

McKeague, M., Bradley, C.R., Girolamo, A.D., Visconti, A., Miller, J.D. and DeRosa, M.C. 2010. Screening and initial binding assessment of fumonisin B1 aptamers. *International Journal of Molecular Sciences*. **11**(12), pp.4864-4881.

Meakin, P. 1983. Formation of fractal clusters and networks by irreversible diffusion-limited aggregation. *Physical Review Letters*. **51**(13), p.1119.

Mi, F.L., Sung, H.W. and Shyu, S.S. 2000. Synthesis and characterization of a novel chitosan-based network prepared using naturally occurring crosslinker. *Journal of Polymer Science Part A: Polymer Chemistry*. **38**(15), pp.2804-2814.

Miller, J.D. 2001. Factors that affect the occurrence of fumonisin. *Environmental health perspectives*.**109**(suppl 2), pp.321-324.

Mine Kurtbay, H., Bekçi, Z., Merdivan, M. and Yurdakoç, K. 2008. Reduction of ochratoxin A levels in red wine by bentonite, modified bentonites, and chitosan. *Journal of agricultural and food chemistry*. **56**(7), pp.2541-2545.

Mirasoli, M., Buragina, A., Dolci, L.S., Simoni, P., Anfossi, L., Giraudi, G. and Roda, A. 2012. Chemiluminescence-based biosensor for fumonisins quantitative detection in maize samples. *Biosensors and Bioelectronics*. **32**(1), pp.283-287.

Miró-Abella, E., Herrero, P., Canela, N., Arola, L., Borrull, F., Ras, R. and Fontanals, N. 2017. Determination of mycotoxins in plant-based beverages using QuEChERS and liquid chromatography–tandem mass spectrometry. *Food Chemistry*. **229**, pp.366-372.

Mirón Mérida, V.A., Gong, Y.Y. and Goycoolea, F. 2021. Aptamer-based detection of fumonisin B1: A critical review. *Analytica Chimica Acta*. 338395.

Mirón-Mérida, V.A., González-Espinosa, Y., Collado-González, M., Gong, Y.Y., Guo, Y. and Goycoolea, F.M. 2021. Aptamer–Target–Gold Nanoparticle Conjugates for the Quantification of Fumonisin B1. *Biosensors*. **11**(1), p.18.

Mirón-Mérida, V.A., Wu, M., Gong, Y.Y., Guo, Y., Holmes, M., Ettelaie, R. and Goycoolea, F.M. 2020. Genipin cross-linked chitosan for signal enhancement in the colorimetric detection of aflatoxin B1 on 3MM chromatography paper. *Sensing and Bio-Sensing Research*. **29**, p.100339.

Mirón-Mérida, V.A., Wu, M., Gong, Y.Y., Guo, Y., Holmes, M., Ettelaie, R., Goycoolea, F.M. 2021. Mathematical characterization of ink diffusion and imbibition processes in chromatography paper as a biosensing platform. *Sensing and Biosensing Research*. **32**, p.100421.

Misihairabgwi, J. M., Ezekiel, C. N., Sulyok, M., Shephard, G. S. and Krska, R. 2019. Mycotoxin contamination of foods in Southern Africa: A 10-year review (2007–2016). *Critical Reviews in Food Science and Nutrition*. **59**(1), pp. 43-58.

Missmer, S.A., Suarez, L., Felkner, M., Wang, E., Merrill Jr, A.H., Rothman, K.J. and Hendricks, K.A. 2006. Exposure to fumonisins and the occurrence of neural tube defects along the Texas–Mexico border. *Environmental health perspectives*. **114**(2), pp.237-241.

Mitchell, N.J., Bowers, E., Hurburgh, C. and Wu, F. 2016. Potential economic losses to the US corn industry from aflatoxin contamination. *Food Additives & Contaminants: Part A*. **33**(3), pp.540-550.

Mogensen, J.M., Møller, K.A., Von Freiesleben, P., Labuda, R., Varga, E., Sulyok, M., Kubátová, A., Thrane, U., Andersen, B. and Nielsen, K.F. 2011. Production of fumonisins B2 and B4 in Tolypocladium species. *Journal of Industrial Microbiology and Biotechnology*. **38**(9), pp.1329-1335.

Molina-Pintor, I. B., Ruíz-Arias, M. A., Guerrero-Flores, M. C., Rojas-García, A. E., Barrón-Vivanco, B. S., Medina-Díaz, I. M., Bernal-Hernández, Y.Y., Ortega-Cervantes, L., Rodriguez-Cervantes, C.H., Ramos, A.J., Sanchis, V., Marin, S. and González-Arias, C. A. 2021. Preliminary survey of the occurrence of mycotoxins in cereals and estimated exposure in a northwestern region of Mexico. International *Journal of Environmental Health Researc*h. pp. 1-15.

Molinelli, A., Grossalber, K. and Krska, R. 2009. A rapid lateral flow test for the determination of total type B fumonisins in maize. *Analytical and bioanalytical chemistry*. **395**(5), pp.1309-1316.

Molinero-Fernández, Á., Jodra, A., Moreno-Guzmán, M., López, M.Á. and Escarpa, A. 2018. Magnetic reduced graphene oxide/nickel/platinum nanoparticles

micromotors for mycotoxin analysis. *Chemistry–A European Journal*. **24**(28), pp.7172-7176.

Molinero-Fernández, A., Moreno-Guzmán, M., López, M.A. and Escarpa, A. 2017. Biosensing strategy for simultaneous and accurate quantitative analysis of mycotoxins in food samples using unmodified graphene micromotors. *Analytical chemistry*. **89**(20), pp.10850-10857.

Moon, J., Kim, G. and Lee, S. 2012. A gold nanoparticle and aflatoxin B1-BSA conjugates based lateral flow assay method for the analysis of aflatoxin B1. *Materials*. **5**(4), pp.634-643.

Movasaghi, Z., Rehman, S. and ur Rehman, D.I. 2008. Fourier transform infrared (FTIR) spectroscopy of biological tissues. *Applied Spectroscopy Reviews*. **43**(2), pp.134-179.

Mudalige, T.K., Qu, H. and Linder, S.W. 2015. An improved methodology of asymmetric flow field flow fractionation hyphenated with inductively coupled mass spectrometry for the determination of size distribution of gold nanoparticles in dietary supplements. *Journal of Chromatography A*. **1420**, pp.92-97.

Mudalige, T.K., Qu, H., Van Haute, D., Ansar, S.M. and Linder, S.W. 2018. Capillary electrophoresis and asymmetric flow field-flow fractionation for size-based separation of engineered metallic nanoparticles: A critical comparative review. *TrAC Trends in Analytical Chemistry*. **106**, pp.202-212.

Mullett, W., Lai, E.P. and Yeung, J.M. 1998. Immunoassay of fumonisins by a surface plasmon resonance biosensor. *Analytical Biochemistry*. **258**(2), pp.161-167.

Munawar, H., Garcia-Cruz, A., Majewska, M., Karim, K., Kutner, W. and Piletsky, S.A. 2020. Electrochemical determination of fumonisin B1 using a chemosensor with a recognition unit comprising molecularly imprinted polymer nanoparticles. *Sensors and Actuators B: Chemical*. **321**, p.128552.

Munawar, H., Safaryan, A.H., De Girolamo, A., Garcia-Cruz, A., Marote, P., Karim, K., Lippolis, V., Pascale, M. and Piletsky, S.A. 2019. Determination of Fumonisin B1 in maize using molecularly imprinted polymer nanoparticles-based assay. *Food chemistry*. **298**, p.125044.

Munawar, H., Smolinska-Kempisty, K., Cruz, A.G., Canfarotta, F., Piletska, E., Karim, K. and Piletsky, S.A. 2018. Molecularly imprinted polymer nanoparticle-based

assay (MINA): application for fumonisin B1 determination. *Analyst.* **143**(14), pp.3481-3488.

Myllytie, P., Salmi, J. and Laine, J. 2009. The influence of pH on the adsorption and interaction of chitosan with cellulose. *BioResources*. **4**(4), pp.1647-1662.

Napolitano, A., Fogliano, V., Tafuri, A. and Ritieni, A. 2007. Natural occurrence of ochratoxin A and antioxidant activities of green and roasted coffees and corresponding byproducts. *Journal of Agricultural and Food Chemistry*. **55**(25), pp.10499-10504.

Nafuka, S.N., Misihairabgwi, J.M., Bock, R., Ishola, A., Sulyok, M. and Krska, R. 2019. Variation of fungal metabolites in sorghum malts used to prepare Namibian traditional fermented beverages Omalodu and Otombo. *Toxins*. **11**(3), p.165.

Nam, Y. and Lee, D. 2013. Ameliorating effect of zhizi (Fructus gardeniae) extract and its glycosides on scopolamine-induced memory impairment. *Journal of Traditional Chinese Medicine*. **33**(2), pp.223-227.

Nguyen, V.T., Kwon, Y.S. and Gu, M.B. 2017. Aptamer-based environmental biosensors for small molecule contaminants. *Current opinion in biotechnology*. **45**, pp.15-23.

Niazi, S., Khan, I.M., Yan, L., Khan, M.I., Mohsin, A., Duan, N., Wu, S. and Wang, Z. 2019. Simultaneous detection of fumonisin B 1 and ochratoxin A using dual-color, time-resolved luminescent nanoparticles (NaYF 4: Ce, Tb and NH 2-Eu/DPA@ SiO 2) as labels. *Analytical and bioanalytical chemistry*. **411**(7), pp.1453-1465.

Nie, J., Zhang, Y., Lin, L., Zhou, C., Li, S., Zhang, L. and Li, J. 2012. Low-cost fabrication of paper-based microfluidic devices by one-step plotting. *Analytical chemistry*. **84**(15), pp.6331-6335.

Nie, J., Liang, Y., Zhang, Y., Le, S., Li, D. and Zhang, S. 2013. One-step patterning of hollow microstructures in paper by laser cutting to create microfluidic analytical devices. *Analyst*. **138**(2), pp.671-676.

Nomura, M., Aoyama, K. and Ishibashi, T. 2018. Sterigmatocystin and aflatoxin B 1 contamination of corn, soybean meal, and formula feed in Japan. *Mycotoxin research*. **34**(1), pp.21-27.

Noonim, P., Mahakarnchanakul, W., Nielsen, K.F., Frisvad, J.C. and Samson, R.A. 2009. Fumonisin B2 production by Aspergillus niger in Thai coffee beans. *Food Additives and Contaminants*. **26**(1), pp.94-100.

Osteresch, B., Viegas, S., Cramer, B. and Humpf, H.U. 2017. Multi-mycotoxin analysis using dried blood spots and dried serum spots. *Analytical and bioanalytical chemistry*. **409**(13), pp.3369-3382.

Ostry, V., Malir, F., Toman, J. and Grosse, Y. 2017. Mycotoxins as human carcinogens—the IARC Monographs classification. *Mycotoxin research*. **33**(1), pp.65-73.

Otero, L., Martino, M., Zaritzky, N., Solas, M. and Sanz, P. D. 2000. Preservation of microstructure in peach and mango during high-pressure-shift freezing. *Journal of Food Science*. **65**(3), pp. 466-470.

Pagkali, V., Petrou, P.S., Makarona, E., Peters, J., Haasnoot, W., Jobst, G., Moser, I., Gajos, K., Budkowski, A., Economou, A. and Misiakos, K. 2018. Simultaneous determination of aflatoxin B1, fumonisin B1 and deoxynivalenol in beer samples with a label-free monolithically integrated optoelectronic biosensor. *Journal of hazardous materials*. **359**, pp.445-453.

Pamies, R., Cifre, J.G.H., Espín, V.F., Collado-González, M., Baños, F.G.D. and de la Torre, J.G. 2014. Aggregation behaviour of gold nanoparticles in saline aqueous media. *Journal of nanoparticle research*. **16**(4), p.2376.

Pandey, P.C. and Pandey, G. 2016. Synthesis of gold nanoparticles resistant to pH and salt for biomedical applications; functional activity of organic amine. *Journal of Materials Research*. **31**(21), p.3313.

Park, J., Kim, D.H., Moon, J.Y., An, J.A., Kim, Y.W., Chung, S.H. and Lee, C. 2018. Distribution analysis of twelve mycotoxins in corn and corn-derived products by LC-MS/MS to evaluate the carry-over ratio during wet-milling. *Toxins*. **10**(8), p.319.

Paterson, R. R. M. and Lima, N. 2011. Further mycotoxin effects from climate change. *Food Research International*. **44**(9), pp. 2555-2566.

Pawlak, A. and Mucha, M. 2003. Thermogravimetric and FTIR studies of chitosan blends. *Thermochimica acta*. **396**(1-2), pp.153-166.

Peltomaa, R., Amaro-Torres, F., Carrasco, S., Orellana, G., Benito-Peña, E. and Moreno-Bondi, M.C. 2018. Homogeneous quenching immunoassay for fumonisin B1 based on gold nanoparticles and an epitope-mimicking yellow fluorescent protein. *ACS nano*. **12**(11), pp.11333-11342.

Peltomaa, R., Benito-Peña, E., Barderas, R., Sauer, U., Gonzalez Andrade, M. and Moreno-Bondi, M.C. 2017. Microarray-based immunoassay with synthetic mimotopes for the detection of fumonisin B1. *Analytical chemistry*. **89**(11), pp.6216-6223.

Peng, X., Liu, B., Chen, W., Li, X., Wang, Q., Meng, X. and Wang, D. 2016. Effective biosorption of patulin from apple juice by cross-linked xanthated chitosan resin. *Food Control*. **63**, pp.140-146.

Peniche, C., Argüelles-Monal, W. and Goycoolea, F.M. 2008. Chitin and chitosan: major sources, properties and applications. In *Monomers, polymers and composites from renewable resources* (pp. 517-542). Elsevier.

Pesenti, A., Taudte, R.V., McCord, B., Doble, P., Roux, C. and Blanes, L. 2014. Coupling paper-based microfluidics and lab on a chip technologies for confirmatory analysis of trinitro aromatic explosives. *Analytical chemistry*. **86**(10), pp.4707-4714.

Peters, J., Thomas, D., Boers, E., de Rijk, T., Berthiller, F., Haasnoot, W. and Nielen, M.W. 2013. Colour-encoded paramagnetic microbead-based direct inhibition triplex flow cytometric immunoassay for ochratoxin A, fumonisins and zearalenone in cereals and cereal-based feed. *Analytical and bioanalytical chemistry*. **405**(24), pp.7783-7794.

Petrarca, M.H., Rodrigues, M.I., Rossi, E.A. and de Sylos, C.M. 2014. Optimisation of a sample preparation method for the determination of fumonisin B1 in rice. *Food chemistry*. **158**, pp.270-277.

Pfeiffer, F. and Mayer, G. 2016. Selection and biosensor application of aptamers for small molecules. *Frontiers in chemistry*. **4**, p.25.

Pitt, J. I., Taniwaki, M. H. and Cole, M. B. 2013. Mycotoxin production in major crops as influenced by growing, harvesting, storage and processing, with emphasis on the achievement of Food Safety Objectives. *Food Control*, **32**(1), pp. 205-215.

Pitt, J.I., Wild, C.P., Baan, R.A., Gelderblom, W.C., Miller, J.D., Riley, R.T. and Wu, F. 2012. *Improving public health through mycotoxin control. (Ed.)*. Lyon, France: International Agency for Research on Cancer.

Pohanka, M. 2013. Spectrophotomeric assay of aflatoxin B1 using acetylcholinesterase immobilized on standard microplates. *Analytical Letters*. **46**(8), pp.1306-1315.

Postnova. *Field-Flow Fractionation*. [Online]. [Accesed 09 January 2021]. Available from: https://www.postnova.com/field-flow-fractionation.html

Puiu, M., Istrate, O., Rotariu, L. and Bala, C. 2012. Kinetic approach of aflatoxin B1–acetylcholinesterase interaction: A tool for developing surface plasmon resonance biosensors. *Analytical biochemistry*. **421**(2), pp.587-594.

Qin, C. Z. and van Brummelen, H. 2019. A dynamic pore-network model for spontaneous imbibition in porous media. *Advances in Water Resources*. **133**, p.103420.

Qu, J., Xie, H., Zhang, S., Luo, P., Guo, P., Chen, X., Ke, Y., Zhuang, J., Zhou, F. and Jiang, W. 2019. Multiplex flow cytometric immunoassays for high-throughput screening of multiple mycotoxin residues in milk. *Food Analytical Methods*.**12**(4), pp.877-886.

Quan, Y., Zhang, Y., Wang, S., Lee, N. and Kennedy, I.R. 2006. A rapid and sensitive chemiluminescence enzyme-linked immunosorbent assay for the determination of fumonisin B1 in food samples. *Analytica Chimica Acta*. **580**(1), pp.1-8.

Quesada-González, D., Stefani, C., González, I., de la Escosura-Muniz, A., Domingo, N., Mutjé, P. and Merkoçi, A. 2019. Signal enhancement on gold nanoparticle-based lateral flow tests using cellulose nanofibers. *Biosensors and Bioelectronics*. **141**, p.111407.

Quintela, S. 2020. Mycotoxins in Beverages: Occurrence, Regulation, Economic Impact and Cost-Effectiveness of Preventive and Removal Methods. In: *Safety Issues in Beverage Production:* Academic Press, pp. 147-186.

Quintela, S., Villarán, M.C., De Armentia, I.L. and Elejalde, E. 2012. Ochratoxin A removal from red wine by several oenological fining agents: bentonite, egg albumin, allergen-free adsorbents, chitin and chitosan. *Food Additives & Contaminants: Part A*. **29**(7), pp.1168-1174.

Rahli, O., Tadrist, L., Miscevic, M. and Santini, R. Fluid flow through randomly packed monodisperse fibers: The Kozeny-Carman parameter analysis. *J. Fluids Eng.* **119**(1), pp.188-192.

Régnier, M., Polizzi, A., Lukowicz, C., Smati, S., Lasserre, F., Lippi, Y., Naylies, C., Laffitte, J., Bétoulières, C., Montagner, A. and Ducheix, S. 2019. The protective role of liver X receptor (LXR) during fumonisin B1-induced hepatotoxicity. *Archives of toxicology*. **93**(2), pp.505-517.

Ren, W., Huang, Z., Xu, Y., Li, Y., Ji, Y. and Su, B. 2015. Urchin-like gold nanoparticle-based immunochromatographic strip test for rapid detection of fumonisin B 1 in grains. *Analytical and bioanalytical chemistry*. **407**(24), pp.7341-7348.

Ren, C., Li, H., Lu, X., Qian, J., Zhu, M., Chen, W., Liu, Q., Hao, N., Li, H. and Wang, K. 2017. A disposable aptasensing device for label-free detection of fumonisin B1 by integrating PDMS film-based micro-cell and screen-printed carbon electrode. *Sensors and Actuators B: Chemical*. **251**, pp.192-199.

Ren, W., Xu, Y., Huang, Z., Li, Y., Tu, Z., Zou, L., He, Q., Fu, J., Liu, S. and Hammock, B.D. 2020. Single-chain variable fragment antibody-based immunochromatographic strip for rapid detection of fumonisin B1 in maize samples. *Food chemistry*. **319**, p.126546.

Rheeder, J.P., Marasas, W.F. and Vismer, H.F. 2002. Production of fumonisin analogs by Fusarium species. *Applied and environmental microbiology*. **68**(5), pp.2101-2105.

Riley, K.R., El Hadri, H., Tan, J., Hackley, V.A. and MacCrehan, W.A. 2019. High separation efficiency of gold nanomaterials of different aspect ratio and size using capillary transient isotachophoresis. *Journal of Chromatography A*. **1598**, pp.216-222.

Riley, R.T. and Merrill Jr, A.H. 2019. Ceramide synthase inhibition by fumonisins: a perfect storm of perturbed sphingolipid metabolism, signaling, and disease. *Journal of lipid research*. **60**(7), pp.1183-1189.

Riley, R.T., Torres, O., Matute, J., Gregory, S.G., Ashley-Koch, A.E., Showker, J.L., Mitchell, T., Voss, K.A., Maddox, J.R. and Gelineau-van Waes, J.B. 2015. Evidence for fumonisin inhibition of ceramide synthase in humans consuming maize-based foods and living in high exposure communities in Guatemala. *Molecular nutrition & food research*. **59**(11), pp.2209-2224.

Rinaudc, M., Pavlov, G. and Desbrieres, J. 1999. Solubilization of chitosan in strong acid medium. *International Journal of Polymer Analysis and Characterization*. **5**(3), pp.267-276.

Rinaudo, M., Pavlov, G. and Desbrieres, J. 1999. Influence of acetic acid concentration on the solubilization of chitosan. *Polymer*. **40**(25), pp.7029-7032.

Rohindra, D.R., Nand, A.V. and Khurma, J.R. 2004. Swelling properties of chitosan hydrogels. *The South Pacific Journal of Natural and Applied Sciences*. **22**(1), pp.32-35.

Rosi, N.L. and Mirkin, C.A. 2005. Nanostructures in biodiagnostics. *Chemical reviews*. **105**(4), pp.1547-1562.

Roze, L. V., Beaudry, R. M., Keller, N. P. and Linz, J. E. 2004. Regulation of aflatoxin synthesis by FadA/cAMP/protein kinase A signaling in Aspergillus parasiticus. *Mycopathologia*. **158**(2), pp. 219-232.

Roy, M., Harris, J., Afreen, S., Deak, E., Gade, L., Balajee, S.A., Park, B., Chiller, T. and Luby, S. 2013. Aflatoxin contamination in food commodities in Bangladesh. *Food Additives and Contaminants: Part B*. **6**(1), pp.17-23.

Ruscito, A., Smith, M., Goudreau, D.N. and DeRosa, M.C. 2016. Current status and future prospects for aptamer-based mycotoxin detection. *Journal of AOAC International*. **99**(4), pp.865-877.

Sabet, F. S., Hosseini, M., Khabbaz, H., Dadmehr, M. and Ganjali, M. R. 2017. FRET-based aptamer biosensor for selective and sensitive detection of aflatoxin B1 in peanut and rice. *Food Chemistry*. **220**, pp.527-532.

Sajilata, M.G., Singhal, R.S. and Kamat, M.Y. 2008. The carotenoid pigment zeaxanthin—a review. *Comprehensive reviews in food science and food safety*. **7**(1), pp.29-49.

Salopek, B., Krasic, D. and Filipovic, S. 1992. Measurement and application of zeta-potential. *Rudarsko-geolosko-naftni zbornik*. **4**(1), p.147.

Samokhvalov, A.V., Safenkova, I.V., Eremin, S.A., Zherdev, A.V. and Dzantiev, B.B. 2017. Use of anchor protein modules in fluorescence polarisation aptamer assay for ochratoxin A determination. *Analytica chimica acta*. **962**, pp.80-87.

Sanz, P.D., De Elvira, C., Martino, M., Zaritzky, N., Otero, L. and Carrasco, J.A. 1999. Freezing rate simulation as an aid to reducing crystallization damage in foods. *Meat Science*. **52**(3), pp.275-278.

Šarkanj, B., Ezekiel, C.N., Turner, P.C., Abia, W.A., Rychlik, M., Krska, R., Sulyok, M. and Warth, B. 2018. Ultra-sensitive, stable isotope assisted quantification of multiple urinary mycotoxin exposure biomarkers. *Analytica chimica acta*. **1019**, pp.84-92.

Savi, G.D., Piacentini, K.C., Marchi, D. and Scussel, V.M. 2016. Fumonisins B1 and B2 in the corn-milling process and corn-based products, and evaluation of estimated daily intake. *Food Additives & Contaminants: Part A*. **33**(2), pp.339-345.

Schachermeyer, S., Ashby, J. and Zhong, W. 2013. Aptamer–protein binding detected by asymmetric flow field flow fractionation. *Journal of Chromatography A*. **1295**, pp.107-113.

Schmidt, B., Loeschner, K., Hadrup, N., Mortensen, A., Sloth, J.J., Bender Koch, C. and Larsen, E.H. 2011. Quantitative characterization of gold nanoparticles by field-flow fractionation coupled online with light scattering detection and inductively coupled plasma mass spectrometry. *Analytical chemistry*. **83**(7), pp.2461-2468.

Schmitz, F.R.W., Valério, A., de Oliveira, D. and Hotza, D. 2020. An overview and future prospects on aptamers for food safety. *Applied Microbiology and Biotechnology*. pp.1-11.

Schoonderwoerd, E. M. 2019. *Modelling the imbibition of an ink-like fluid into the thin coating layer of paper*. Master's thesis, Utrecht University.

Scott, P.M. 2012. Recent research on fumonisins: a review. *Food additives & contaminants: part A*. **29**(2), pp.242-248.

Shao, Y., Duan, H., Zhou, S., Ma, T., Guo, L., Huang, X. and Xiong, Y. 2019. Biotin–streptavidin system-mediated ratiometric multiplex immunochromatographic assay for simultaneous and accurate quantification of three mycotoxins. *Journal of agricultural and food chemistry*. **67**(32), pp.9022-9031.

Sharma, A., Khan, R., Catanante, G., Sherazi, T. A., Bhand, S., Hayat, A. and Marty, J. L. 2018. Designed strategies for fluorescence-based biosensors for the detection of mycotoxins. *Toxins*. **10**(5), p. 197.

Sharma, S.K., Poudel Sharma, S., Miller, D., Parel, J.M.A. and Leblanc, R.M. 2019. Interfacial behavior of fumonisin B1 toxin and its degradation on the membrane. *Langmuir*. **35**(7), pp.2814-2820.

Sheng, W., Wu, H., Ji, W., Li, Z., Chu, F. and Wang, S. 2018. Visual Non-Instrumental On-Site Detection of Fumonisin B1, B2, and B3 in Cereal Samples Using a Clean-Up Combined with Gel-Based Immunoaffinity Test Column Assay. *Toxins*. **10**(4), p.165.

Shephard, G.S., Sydenham, E.W., Thiel, P.G. and Gelderblom, W.C.A. 1990. Quantitative determination of fumonisins B1 and B2 by high-performance liquid

chromatography with fluorescence detection. *Journal of Liquid Chromatography*. **13**(10), pp.2077-2087.

Shephard, G.S., Van Der Westhuizen, L. and Sewram, V. 2007. Biomarkers of exposure to fumonisin mycotoxins: a review. *Food additives and contaminants*. **24**(10), pp.1196-1201.

Shi, Y., Yassin, M. R. and Dehghanpour, H. 2018. A modified model for spontaneous imbibition of wetting phase into fractal porous media. *Colloids and Surfaces A: Physicochemical and Engineering Aspects*. **543** (2018), pp.64-75.

Shi, Z.Y., Zheng, Y.T., Zhang, H.B., He, C.H., Wu, W.D. and Zhang, H.B. 2015. DNA electrochemical aptasensor for detecting fumonisins B1 based on graphene and thionine nanocomposite. *Electroanalysis*. **27**(5), pp.1097-1103.

Shim, W. B., Kim, M. J., Mun, H. and Kim, M. G. 2014. An aptamer-based dipstick assay for the rapid and simple detection of aflatoxin B1. *Biosensors and Bioelectronics*. **62**, pp.288-294.

Shim, W.B., Yang, Z.Y., Kim, J.S., Kim, J.Y., Kang, S.J., Woo, G.J., Chung, Y.C., Eremin, S.A. and Chung, D.H. 2007. Development of immunochromatography strip-test using nanocolloidal gold-antibody probe for the rapid detection of aflatoxin B1 in grain and feed samples. *Journal of microbiology and biotechnology*. **17**(10), pp.1629-1637.

Shou, D., Ye, L., Fan, J., Fu, K., Mei, M., Wang, H. and Chen, Q. 2014. Geometry-induced asymmetric capillary flow. *Langmuir*. **30**(19), pp.5448-5454.

Shu, M., Xu, Y., Dong, J.X., Zhong, C., Hammock, B.D., Wang, W.J. and Wu, G.P. 2019. Development of a noncompetitive idiometric nanobodies phage immumoassay for the determination of fumonisin B1. *Food and Agricultural Immunology*. **30**(1), pp.510-521.

Shu, M., Xu, Y., Wang, D., Liu, X., Li, Y., He, Q., Tu, Z., Qiu, Y., Ji, Y. and Wang, X. 2015. Anti-idiotypic nanobody: A strategy for development of sensitive and green immunoassay for Fumonisin B1. *Talanta*. **143**, pp.388-393

Siler, D.J. and Gilchrist, D.G. 1982. Determination of host-selective phytotoxins from Alternaria alternata f. sp. lycopersici as their maleyl derivatives by high-performance liquid chromatography. *Journal of Chromatography A*. **238**(1), pp.167-173.

Silva, L.J., Pena, A., Lino, C.M., Fernández, M.F. and Mañes, J. 2010. Fumonisins determination in urine by LC-MS-MS. *Analytical and bioanalytical chemistry.* **396**(2), pp.809-816.

Smith, L.L., Francis, K.A., Johnson, J.T. and Gaskill, C.L. 2017. Quantitation of fumonisin B1 and B2 in feed using FMOC pre-column derivatization with HPLC and fluorescence detection. *Food chemistry*. **234**, pp.174-179.

Smolinska-Kempisty, K., Guerreiro, A., Canfarotta, F., Cáceres, C., Whitcombe, M.J. and Piletsky, S. 2016. A comparison of the performance of molecularly imprinted polymer nanoparticles for small molecule targets and antibodies in the ELISA format. *Scientific reports*. **6**(1), pp.1-7.

Snyder, L.R., Kirkland, J.J. and Dolan, J.W. 2011. *Introduction to modern liquid chromatography*. John Wiley & Sons.

Solís-Cruz, B., Hernández-Patlán, D., Beyssac, E., Latorre, J.D., Hernandez-Velasco, X., Merino-Guzman, R., Tellez, G. and López-Arellano, R. 2017. Evaluation of chitosan and cellulosic polymers as binding adsorbent materials to prevent aflatoxin B1, fumonisin B1, ochratoxin, trichothecene, deoxynivalenol, and zearalenone mycotoxicoses through an in vitro gastrointestinal model for poultry. *Polymers*. **9**(10), p.529.

Sonavane, G., Tomoda, K. and Makino, K. 2008. Biodistribution of colloidal gold nanoparticles after intravenous administration: effect of particle size. *Colloids and Surfaces B: Biointerfaces*, *66*(2). pp.274-280.

Song, S.H., Gao, Z.F., Guo, X. and Chen, G.H. 2019. Aptamer-based detection methodology studies in food safety. *Food Analytical Methods*. **12**(4), pp.966-990.

Songok, J. and Toivakka, M. 2016. Enhancing capillary-driven flow for paper-based microfluidic channels. *ACS applied materials & interfaces*. **8**(44), pp.30523-30530.

Sorlier, P., Denuzière, A., Viton, C. and Domard, A. 2001. Relation between the degree of acetylation and the electrostatic properties of chitin and chitosan. *Biomacromolecules*. **2**(3), pp.765-772.

Souto, P.C., Jager, A.V., Tonin, F.G., Petta, T., Di Gregório, M.C., Cossalter, A.M., Pinton, P., Oswald, I.P., Rottinghaus, G.E. and Oliveira, C.A. 2017. Determination of fumonisin B1 levels in body fluids and hair from piglets fed fumonisin B1-contaminated diets. *Food and chemical toxicology*. **108**, pp.1-9.

Sperling, R. A., Gil, P. R., Zhang, F., Zanella, M. and Parak, W. J. 2008. Biological applications of gold nanoparticles. *Chemical Society Reviews*. **37**(9), pp. 1896-1908.

Stetefeld, J., McKenna, S.A. and Patel, T.R. 2016. Dynamic light scattering: a practical guide and applications in biomedical sciences. *Biophysical reviews*. **8**(4), pp.409-427.

Sulyok, M., Krska, R. and Senyuva, H. 2020. Profiles of fungal metabolites including regulated mycotoxins in individual dried Turkish figs by LC-MS/MS. *Mycotoxin Research*. **36**(4), pp.381-387.

Sun, J., Li, W., Zhang, Y., Hu, X., Wu, L. and Wang, B. 2016. QuEChERS purification combined with ultrahigh-performance liquid chromatography tandem mass spectrometry for simultaneous quantification of 25 mycotoxins in cereals. *Toxins*. **8**(12), p.375.

Sun, Z., Xu, J., Wang, G., Song, A., Li, C. and Zheng, S. 2020. Hydrothermal fabrication of rectorite based biocomposite modified by chitosan derived carbon nanoparticles as efficient mycotoxins adsorbents. *Applied Clay Science*. **184**, p.105373.

Suo, S., Liu, M. and Gan, Y. 2019. Modelling imbibition processes in heterogeneous porous media. *Transport in Porous Media*. **126** (2019), pp.615-631.

Sydenham, E.W., Gelderblom, W.C., Thiel, P.G. and Marasas, W.F. 1990. Evidence for the natural occurrence of fumonisin B1, a mycotoxin produced by Fusarium moniliforme, in corn. *Journal of Agricultural and Food Chemistry*. **38**(1), pp.285-290.

Tamura, H., Furuike, T., Nair, S.V. and Jayakumar, R. 2011. Biomedical applications of chitin hydrogel membranes and scaffolds. *Carbohydrate Polymers*. **84**(2), pp.820-824.

Tang, D., Lin, Y., Zhou, Q., Lin, Y., Li, P., Niessner, R. and Knopp, D. 2014. Low-cost and highly sensitive immunosensing platform for aflatoxins using one-step competitive displacement reaction mode and portable glucometer-based detection. *Analytical Chemistry*. **86**(22), pp.11451-11458.

Tang, X., Li, P., Zhang, Z., Zhang, Q., Guo, J. and Zhang, W. 2017. An ultrasensitive gray-imaging-based quantitative immunochromatographic detection method for fumonisin B1 in agricultural products. *Food Control*. ***80***, pp.333-340.

Tansakul, N., Jala, P., Laopiem, S., Tangmunkhong, P. and Limsuwan, S. 2013. Co-occurrence of five Fusarium toxins in corn-dried distiller's grains with solubles in Thailand and comparison of ELISA and LC-MS/MS for fumonisin analysis. *Mycotoxin research*. **29**(4), pp.255-260.

Tao, Z., Zhou, Y., Li, X. and Wang, Z. 2020. Competitive HRP-linked colorimetric aptasensor for the detection of fumonisin B1 in food based on dual biotin-streptavidin interaction. *Biosensors*. **10**(4), p.31.

Thompson, V.S. and Maragos, C.M. 1996. Fiber-optic immunosensor for the detection of fumonisin B1. *Journal of Agricultural and Food Chemistry*. **44**(4), pp.1041-1046.

Tian, H., Sofer, Z., Pumera, M. and Bonanni, A. 2017. Investigation on the ability of heteroatom-doped graphene for biorecognition. *Nanoscale*. **9**(10), pp.3530-3536.

Tittlemier, S.A., Cramer, B., Dall'Asta, C., Iha, M.H., Lattanzio, V.M.T., Malone, R.J., Maragos, C., Solfrizzo, M., Stranska-Zachariasova, M. and Stroka, J. 2019. Developments in mycotoxin analysis: an update for 2017-2018. *World Mycotoxin Journa*l. **12**(1), pp.3-29.

Tittlemier, S.A., Cramer, B., Dall'Asta, C., Iha, M.H., Lattanzio, V.M.T., Maragos, C., Solfrizzo, M., Stranska, M., Stroka, J. and Sumarah, M. 2020. Developments in mycotoxin analysis: An update for 2018-19. *World Mycotoxin Journal*. **13**(1), pp.3-24.

Tittlemier, S.A., Brunkhorst, J., Cramer, B., DeRosa, M.C., Lattanzio, V.M.T., Malone, R., Maragos, C., Stranska, M. and Sumarah, M.W. 2021. Developments in mycotoxin analysis: an update for 2019-2020. *World Mycotoxin Journal*.**14**(1) pp.3-26.

Topgaard, D. and Söderman, O. 2001. Diffusion of water absorbed in cellulose fibers studied with 1H-NMR. *Langmuir*. **17**(9), pp.2694-2702.

Torres, O., Matute, J., Gelineau-van Waes, J., Maddox, J.R., Gregory, S.G., Ashley-Koch, A.E., Showker, J.L., Zitomer, N.C., Voss, K.A. and Riley, R.T. 2014. Urinary fumonisin B 1 and estimated fumonisin intake in women from high-and low-exposure communities in G uatemala. *Molecular nutrition & food research*. **58**(5), pp.973-983.

Udomkun, P., Wiredu, A.N., Nagle, M., Bandyopadhyay, R., Müller, J. and Vanlauwe, B. 2017. Mycotoxins in Sub-Saharan Africa: Present situation, socio-economic impact, awareness, and outlook. *Food Control*. **72**, pp.110-122.

Ueno, Y., Iijima, K., Wang, S.D., Sugiura, Y., Sekijima, M., Tanaka, T., Chen, C. and Yu, S.Z. 1997. Fumonisins as a possible contributory risk factor for primary liver cancer: a 3-year study of corn harvested in Haimen, China, by HPLC and ELISA. *Food and chemical toxicology*. **35**(12), pp.1143-1150.

Urusov, A.E., Petrakova, A.V., Gubaydullina, M.K., Zherdev, A.V., Eremin, S.A., Kong, D., Liu, L., Xu, C. and Dzantiev, B.B. 2017. High-sensitivity immunochromatographic assay for fumonisin B1 based on indirect antibody labeling. *Biotechnology letters*. **39**(5), pp.751-758.

Varga, J., Kocsubé, S., Suri, K., Szigeti, G.Y., Szekeres, A., Varga, M., Tóth, B. and Bartók, T. 2010. Fumonisin contamination and fumonisin producing black Aspergilli in dried vine fruits of different origin. *International journal of food microbiology*. **143**(3), pp.143-149.

Venkataramana, M., Navya, K., Chandranayaka, S., Priyanka, S.R., Murali, H.S. and Batra, H.V. 2014. Development and validation of an immunochromatographic assay for rapid detection of fumonisin B1 from cereal samples. *Journal of food science and technology*. **51**(9), pp.1920-1928.

Verma, H.N., Singh, P. and Chavan, R.M. 2014. Gold nanoparticle: synthesis and characterization. *Veterinary world*. **7**(2), p.72.

Vernon-Parry, K.D. 2000. Scanning electron microscopy: an introduction. *III-Vs Review*. **13**(4), pp.40-44.

Vosmanská, V., Kolářová, K., Rimpelová, S., Kolská, Z. and Švorčík, V. 2015. Antibacterial wound dressing: plasma treatment effect on chitosan impregnation and in situ synthesis of silver chloride on cellulose surface. *Rsc Advances*. **5**(23), pp.17690-17699.

Wall-Martínez, H. A., Pascari, X., Ramos, A. J., Marin, S. and Sanchis, V. 2019a. Frequency and levels of mycotoxins in beer from the Mexican market and exposure estimate for deoxynivalenol mycotoxins. *Mycotoxin Research*. **35**(2), pp. 207-216.

Wall-Martínez, H.A., Ramírez-Martínez, A., Wesolek, N., Brabet, C., Durand, N., Rodríguez-Jimenes, G.C., Garcia-Alvarado, M.A., Salgado-Cervantes, M.A., Robles-Olvera, V.J. and Roudot, A.C. 2019b. Risk assessment of exposure to mycotoxins (aflatoxins and fumonisins) through corn tortilla intake in Veracruz City (Mexico). *Food Additives & Contaminants: Part A*. **36**(6), pp.929-939.

Wang, C., Huang, X., Tian, X., Zhang, X., Yu, S., Chang, X., Ren, Y. and Qian, J. 2019. A multiplexed FRET aptasensor for the simultaneous detection of mycotoxins

with magnetically controlled graphene oxide/Fe 3 O 4 as a single energy acceptor. *Analyst*. **144**(20), pp.6004-6010.

Wang, C., Qian, J., An, K., Huang, X., Zhao, L., Liu, Q., Hao, N. and Wang, K. 2017. Magneto-controlled aptasensor for simultaneous electrochemical detection of dual mycotoxins in maize using metal sulfide quantum dots coated silica as labels. *Biosensors and Bioelectronics*. **89**, pp.802-809.

Wang, G., Xu, J., Sun, Z. and Zheng, S. 2020. Surface Functionalization of Montmorillonite with Chitosan and the Role of Surface Properties on Its Adsorptive Performance: A Comparative Study on Mycotoxins Adsorption. *Langmuir*. **36**(10), pp.2601-2611.

Wang, L., Ma, W., Chen, W., Liu, L., Ma, W., Zhu, Y., Xu, L., Kuang, H. and Xu, C. 2011a. An aptamer-based chromatographic strip assay for sensitive toxin semi-quantitative detection. *Biosensors and Bioelectronics*. **26**(6), pp.3059-3062.

Wang, L., Chen, W., Ma, W., Liu, L., Ma, W., Zhao, Y., Zhu, Y., Xu, L., Kuang, H. and Xu, C. 2011b. Fluorescent strip sensor for rapid determination of toxins. *Chemical Communications*. **47**(5), pp.1574-1576.

Wang, S., Ge, L., Song, X., Yu, J., Ge, S., Huang, J. and Zeng, F. 2012. Paper-based chemiluminescence ELISA: lab-on-paper based on chitosan modified paper device and wax-screen-printing. *Biosensors and bioelectronics*. **31**(1), pp.212-218.

Wang, W.F., Wu, S., Ma, X.Y., Xia, Y. and Wang, Z.P. 2013b. Novel methods for fumonisin B1 detection based on AuNPs labelling and aptamer recognition. *Journal of Food Science and Biotechnology.* **32***(5)*, pp.501-508.

Wang, X., Hagen, J.A. and Papautsky, I. 2013. Paper pump for passive and programmable transport. *Biomicrofluidics*. **7**(1), p.014107.

Wang, X., Park, S.G., Ko, J., Xiao, X., Giannini, V., Maier, S.A., Kim, D.H. and Choo, J. 2018. Sensitive and reproducible immunoassay of multiple mycotoxins using surface-enhanced Raman scattering mapping on 3D plasmonic nanopillar arrays. *Small*. **14**(39), p.1801623.

Wang, Y., Sun, J., Hou, Y., Zhang, C., Li, D., Li, H., Yang, M., Fan, C. and Sun, B. 2019. A SERS-based lateral flow assay biosensor for quantitative and ultrasensitive detection of interleukin-6 in unprocessed whole blood. *Biosensors & bioelectronics*. **141**, pp.111432-111432.

Wang, Y.K., Yan, Y.X., Ji, W.H., Wang, H.A., Li, S.Q., Zou, Q. and Sun, J.H. 2013a. Rapid simultaneous quantification of zearalenone and fumonisin B1 in corn and wheat by lateral flow dual immunoassay. *Journal of agricultural and food chemistry*. **61**(21), pp.5031-5036.

Wang, Z.J., Chen, E.N., Yang, G., Zhao, X.Y., Qu, F. 2020. Research advances of aptamers selection for small molecule targets. *Chinese Journal of Analytical Chemistry*. **48**(5), pp.573-582.

Wang, Z. and Wu, S. 2014. Oligonucleotides Aptamer Special for Distinguishing Fumonisin B1. Patent No. CN 103013999 B.

Wang, X., Zhang, H., Liu, H., He, C., Zhang, A., Ma, J., Ma, Y., Wu, W. and Zheng, H.A.O. 2011. An immunoarray for the simultaneous detection of two mycotoxins, Ochratoxin A and Fumonisin B1. *Journal of Food Safety.* **31**(3), pp.408-416.

Wangia, R.N., Githanga, D.P., Xue, K.S., Tang, L., Anzala, O.A. and Wang, J.S. 2019. Validation of urinary sphingolipid metabolites as biomarker of effect for fumonisins exposure in Kenyan children. *Biomarkers*. **24**(4), pp.379-388.

Wei, M., Xin, L., Feng, S. and Liu, Y. 2020. Simultaneous electrochemical determination of ochratoxin A and fumonisin B1 with an aptasensor based on the use of a Y-shaped DNA structure on gold nanorods. *Microchimica Acta*. **187**(2), pp.1-7.

Wei, M., Zhao, F., Feng, S. and Jin, H. 2019. A novel electrochemical aptasensor for fumonisin B 1 determination using DNA and exonuclease-I as signal amplification strategy. *BMC chemistry*. **13**(1), pp.1-6.

Wild, C.P., Miller, J.D. and Groopman, J.D. eds. 2015. Mycotoxin control in low-and middle-income countries.

Wrigglesworth, E. G. and Johnston, J. H. 2021. Mie theory and the dichroic effect for spherical gold nanoparticles: an experimental approach*. Nanoscale Advances*. **3**(12), pp. 3530-3536.

Wu, S., Duan, N., Li, X., Tan, G., Ma, X., Xia, Y., Wang, Z. and Wang, H. 2013. Homogenous detection of fumonisin B1 with a molecular beacon based on fluorescence resonance energy transfer between NaYF4: Yb, Ho upconversion nanoparticles and gold nanoparticles. *Talanta*. **116**, pp.611-618.

Wu, S., Duan, N., Ma, X., Xia, Y., Wang, H., Wang, Z. and Zhang, Q. 2012. Multiplexed fluorescence resonance energy transfer aptasensor between upconversion nanoparticles and graphene oxide for the simultaneous determination of mycotoxins. *Analytical chemistry*. **84**(14), pp.6263-6270.

Wu, Z., He, D., Cui, B., Jin, Z., Xu, E., Yuan, C., Liu, P., Fang, Y. and Chai, Q. 2020. Trimer-based aptasensor for simultaneous determination of multiple mycotoxins using SERS and fluorimetry. *Microchimica Acta*.**187**(9), pp.1-7.

Wulff, G., Gross, T. and Schönfeld, R. 1997. Enzyme models based on molecularly imprinted polymers with strong esterase activity. *Angewandte Chemie International Edition in English*. **36**(18), pp.1962-1964.

Xiao, J., Stone, H.A. and Attinger, D. 2012. Source-like solution for radial imbibition into a homogeneous semi-infinite porous medium. *Langmuir*. **28**(9), pp.4208-4212.

Xiao, L., Liu, X., Zhong, R., Zhang, K., Zhang, X., Zhou, X., Lin, B. and Du, Y. 2013. A rapid, straightforward, and print house compatible mass fabrication method for integrating 3D paper-based microfluidics. *Electrophoresis*. **34**(20-21), pp.3003-3007.

Xing, Y., Meng, W., Sun, W., Li, D., Yu, Z., Tong, L. and Zhao, Y. 2016. Simultaneous qualitative and quantitative analysis of 21 mycotoxins in Radix Paeoniae Alba by ultra-high performance liquid chromatography quadrupole linear ion trap mass spectrometry and QuEChERS for sample preparation. *Journal of Chromatography B*. **1031**, pp.202-213.

Xu, P. and Yu, B. 2008. Developing a new form of permeability and Kozeny–Carman constant for homogeneous porous media by means of fractal geometry. *Advances in water resources*. **31**(1), pp.74-81.

Yamagishi, D., Akamatsu, H., Otani, H. and Kodama, M. 2006. Pathological evaluation of host-specific AAL-toxins and fumonisin mycotoxins produced by Alternaria and Fusarium species. *Journal of General Plant Pathology*. **72**(5), pp.323-327.

Yang, C., Wang, Y., Marty, J.L. and Yang, X. 2011. Aptamer-based colorimetric biosensing of Ochratoxin A using unmodified gold nanoparticles indicator. *Biosensors and Bioelectronics*. **26**(5), pp.2724-2727.

Yang, H., Zhang, Q., Liu, X., Yang, Y., Yang, Y., Liu, M., Li, P. and Zhou, Y. 2020. Antibody-biotin-streptavidin-horseradish peroxidase (HRP) sensor for rapid and ultra-sensitive detection of fumonisins. *Food chemistry*. **316**, p.126356.

Yang, X., Zhou, X., Zhang, X., Qing, Y., Luo, M., Liu, X., Li, C., Li, Y., Xia, H. and Qiu, J. 2015. A highly sensitive electrochemical immunosensor for fumonisin B1 detection in corn using single-walled carbon nanotubes/chitosan. *Electroanalysis*. **27**(11), pp.2679-2687.

Yang, Y., Li, W., Shen, P., Liu, R., Li, Y., Xu, J., Zheng, Q., Zhang, Y., Li, J. and Zheng, T. 2017. Aptamer fluorescence signal recovery screening for multiplex mycotoxins in cereal samples based on photonic crystal microsphere suspension array. *Sensors and Actuators B: Chemical*. **248**, pp.351-358.

Yang, Z., Xu, G., Reboud, J., Ali, S.A., Kaur, G., McGiven, J., Boby, N., Gupta, P.K., Chaudhuri, P. and Cooper, J.M., 2018. Rapid veterinary diagnosis of bovine reproductive infectious diseases from semen using paper-origami DNA microfluidics. *ACS sensors*, ***3***(2), pp.403-409.

Yapo, A.E., Strub, C., Durand, N., Ahoua, A.R.C., Schorr-Galindo, S., Bonfoh, B., Fontana, A. and Koussémon, M. 2020. Mass spectrometry-based detection and risk assessment of mycotoxin contamination of ‘kankankan’used for roasted meat consumption in Abidjan, Côte d’Ivoire. *Food Additives & Contaminants: Part A*. **37**(9), pp.1564-1578.

Yetisen, A.K., Akram, M.S. and Lowe, C.R. 2013. based microfluidic point-of-care diagnostic devices. *Lab on a Chip*. **13**(12), pp.2210-2251.

Yoo, H., Jo, H. and Oh, S. S. 2020. Detection and beyond: challenges and advances in aptamer-based biosensors. *Materials Advances*. **1**(8), pp.2663-2687.

Yoon, J., Cai, S., Suo, Z. and Hayward, R.C. 2010. Poroelastic swelling kinetics of thin hydrogel layers: comparison of theory and experiment. *Soft Matter*. **6**(23), pp.6004-6012.

Yoshizawa, T., Yamashita, A. and Luo, Y. 1994. Fumonisin occurrence in corn from high-and low-risk areas for human esophageal cancer in China. *Applied and environmental microbiology*. **60**(5), pp.1626-1629.

Yu, S., He, L., Yu, F., Liu, L., Qu, C., Qu, L., Liu, J., Wu, Y. and Wu, Y. 2018. A lateral flow assay for simultaneous detection of deoxynivalenol, fumonisin B1 and aflatoxin B1. *Toxicon.* **156**, pp.23-27.

Yuan, Q., Jiang, Y., Fan, Y., Ma, Y., Lei, H. and Su, J. 2019. Fumonisin B1 induces oxidative stress and breaks barrier functions in pig iliac endothelium cells. *Toxins*.**11**(7), p.387.

Yüce, M., Ullah, N. and Budak, H. 2015. Trends in aptamer selection methods and applications. *Analyst*. **140**(16), pp.5379-5399.

Yue, S., Jie, X., Wei, L., Bin, C., Dou Dou, W., Yi, Y., QingXia, L., JianLin, L. and TieSong, Z. 2014. Simultaneous detection of Ochratoxin A and fumonisin B1 in cereal samples using an aptamer–photonic crystal encoded suspension Array. *Analytical chemistry*. **86**(23), pp.11797-11802.

Zangheri, M., Di Nardo, F., Anfossi, L., Giovannoli, C., Baggiani, C., Roda, A. and Mirasoli, M. 2015. A multiplex chemiluminescent biosensor for type B-fumonisins and aflatoxin B1 quantitative detection in maize flour. *Analyst*. **140**(1), pp.358-365.

Zhai, C., Sun, X., Zhao, W., Gong, Z. and Wang, X. 2013. Acetylcholinesterase biosensor based on chitosan/prussian blue/multiwall carbon nanotubes/hollow gold nanospheres nanocomposite film by one-stepelectrodeposition. *Biosensors and Bioelectronics*. **42**, pp.124-130.

Zhan, S., Zheng, L., Zhou, Y., Wu, K., Duan, H., Huang, X. and Xiong, Y. 2019. A gold growth-based plasmonic ELISA for the sensitive detection of fumonisin B1 in maize. *Toxins*. **11**(6), p.323

Zhang, B., Chen, X., Han, S.Y., Li, M., Ma, T.Z., Sheng, W.J. and Zhu, X. 2018a. Simultaneous analysis of 20 mycotoxins in grapes and wines from Hexi Corridor region (China): Based on a QuEChERS–UHPLC–MS/MS method. *Molecules.* **23**(8), p.1926.

Zhang, K., Li, H., Wang, W., Cao, J., Gan, N. and Han, H. 2020a. Application of Multiplexed Aptasensors in Food Contaminants Detection. *ACS sensors*. **5**(12), pp.3721-3738.

Zhang, L., Sun, Y., Liang, X., Yang, Y., Meng, X., Zhang, Q., Li, P. and Zhou, Y. 2020b. Cysteamine triggered “turn-on” fluorescence sensor for total detection of fumonisin B1, B2 and B3. *Food Chemistry*, *327*, p.127058.

Zhang, S., Lu, J., Wang, S., Mao, D., Miao, S. and Ji, S. 2016. Multi-mycotoxins analysis in Pheretima using ultra-high-performance liquid chromatography tandem

mass spectrometry based on a modified QuEChERS method. *Journal of Chromatography B*. **1035**, pp.31-41.

Zhang, W., Xiong, H., Chen, M., Zhang, X. and Wang, S. 2017. Surface-enhanced molecularly imprinted electrochemiluminescence sensor based on Ru@ SiO2 for ultrasensitive detection of fumonisin B1. *Biosensors and Bioelectronics*. **96**, pp.55-61.

Zhang, X., Wang, Z., Fang, Y., Sun, R., Cao, T., Paudyal, N., Fang, W. and Song, H. 2018b. Antibody microarray immunoassay for simultaneous quantification of multiple mycotoxins in corn samples. *Toxins*. **10**(10), p.415.

Zhao, P., Li, N. and Astruc, D. 2013. State of the art in gold nanoparticle synthesis. *Coordination Chemistry Reviews*. **257**(3-4), pp. 638-665.

Zhao, X.S., Kong, W.J., Wang, S., Wei, J.H. and Yang, M.H. 2017a. Simultaneous analysis of multiple mycotoxins in Alpinia oxyphylla by UPLC-MS/MS. *World Mycotoxin Journal*. **10**(1), pp.41-51.

Zhao, Y., Luo, Y., Li, T. and Song, Q. 2014. Au NPs driven electrochemiluminescence aptasensors for sensitive detection of fumonisin B1. *RSC Advances*. **4**(101), pp.57709-57714.

Zhao, Y., Wan, L.H., Bai, X.L., Liu, Y.M., Zhang, F.P., Liu, Y.M. and Liao, X. 2017b. Quantification of mycotoxins in vegetable oil by UPLC-MS/MS after magnetic solid-phase extraction. *Food Additives & Contaminants: Part A*. **34**(7), pp.1201-1210.

Zhao, Z., Liu, N., Yang, L., Wang, J., Song, S., Nie, D., Yang, X., Hou, J. and Wu, A. 2015. Cross-linked chitosan polymers as generic adsorbents for simultaneous adsorption of multiple mycotoxins. *Food Control*. **57**, pp.362-369.

Zheng, Y., Shi, Z., Wu, W., He, C. and Zhang, H. 2021. Label-Free DNA Electrochemical Aptasensor for Fumonisin B 1 Detection in Maize Based on Graphene and Gold Nanocomposite. *Journal of Analytical Chemistry*. **76**(2), pp. 252-257.

Zheng, Y.T., Zhao, B.S., Zhang, H.B., Jia, H. and Wu, M. 2020. Colorimetric aptasensor for fumonisin B1 detection by regulating the amount of bubbles in closed bipolar platform. *Journal of Electroanalytical Chemistry*. **877**, p.114584.

Zhou, W., Apkarian, R., Wang, Z.L. and Joy, D. 2006. Fundamentals of scanning electron microscopy (SEM). In *Scanning microscopy for nanotechnology* (pp. 1-40). Springer, New York, NY.

Zhou, Y., Huang, X., Zhang, W., Ji, Y., Chen, R. and Xiong, Y. 2018. Multi-branched gold nanoflower-embedded iron porphyrin for colorimetric immunosensor. *Biosensors and Bioelectronics*. **102**, pp.9-16.

Zhou, Q. and Tang, D. 2020. Recent advances in photoelectrochemical biosensors for analysis of mycotoxins in food. *TrAC Trends in Analytical Chemistry*. **124**, p.115814.

Zou, L., Xu, Y., Li, Y., He, Q., Chen, B. and Wang, D. 2014. Development of a single-chain variable fragment antibody-based enzyme-linked immunosorbent assay for determination of fumonisin B1 in corn samples. *Journal of the Science of Food and Agriculture*. **94**(9), pp.1865-1871.

Zuker, M. 2003. Mfold web server for nucleic acid folding and hybridization prediction. *Nucleic Acids Research*. **31**(13), pp.3406-3415.

吴淑庆, 杨在明 and 张良. 2012. Fumonisins B1 aptamer and applications thereof. Patent No. CN 102517291 A.

王红旗, **王俊**艳 and **洪慧杰**. 2017. **伏**马毒素 B1 **核酸适配体**链置换探针的筛选及应用. *农产品质量与安**全***. **1**, pp.44-48.

Appendix A
Supporting Information of Chapter 2

Table A1 References used for a general PCA analysis in Figure 2.5

Reference	#	Year	LOD	AT	AP	Type	General PCA		
							LODmax/LOD	Atmax/AT	Apmax/AP
Lattanzio et al., 2012	134	2012.1	3200	30	10	I	1.0	24.0	1290.0
Zou et al., 2013	154	2014.0	8.32	70	780	I	384.6	10.3	16.5
Peters et al., 2013	155	2013.5	170	50	3040	I	18.8	14.4	4.2
Tansakul et al., 2013	117	2013.6	200	20	3	I	16.0	36.0	4300.0
Tansakul et al., 2013	117	2013.6	9	15	730	C	355.6	48.0	17.7
Wang et al., 2013	135	2013.4	5.23	30	141	I	611.9	24.0	91.5
Petrarca et al., 2014	77	2014.2	50	13.5	-	C	64.0	53.3	#VALUE!
Venkataramana et al., 2014	65	2014.1	5	3	3010	I	640.0	240.0	4.3
Ezquerra et al., 2015	156	2015.2	0.58	40	12	I	5517.2	18.0	1075.0
Masikini et al., 2015a	60	2015.0	4.6E-07	-	1670	I	6956521739.1	#VALUE!	7.7
Bordin et al., 2015	84	2015.1	30	-	32	C	106.7	#VALUE!	403.1
Bordin et al., 2015	84	2015.1	3.3	6	915	C	969.7	120.0	14.1
Zangheri et al., 2015	136	2015.8	6	30	845	I	533.3	24.0	15.3
Yang et al., 2015	129	2015.8	0.002	180.11	1030	I	1600000.0	4.0	12.5
Jodra et al., 2015	157	2014.7	0.33	60	120	I	9697.0	12.0	107.5
Shu et al., 2015	158	2015.4	0.15	60	720	I	21333.3	12.0	17.9
Li et al., 2015	159	2015.4	157.4	30	16	I	20.3	24.0	806.3
Ren et al., 2015	66	2015.7	5	5	405	I	640.0	144.0	31.9
Ren et al., 2015	66	2015.7	20	5	385	I	160.0	144.0	33.5
Lee et al., 2016	56	2016.0	5000	1	60	O	0.6	720.0	215.0
Lu et al., 2016	160	2016.6	4.2	40	1170	I	761.9	18.0	11.0
Masikini et al.,2015b	61	2016.3	3.8E-06	-	1578	I	842105263.2	#VALUE!	8.2
Smolinska-Kempisty et al., 2016	177	2016.9	0.0044	70	1500	O	727272.7	10.3	8.6
Liu et al., 2016	85	2016.2	0.15	12	28.5	C	21333.3	60.0	452.6
Li et al., 2016	86	2016.3	0.05	12	32.25	C	64000.0	60.0	400.0
Xing et al., 2017	87	2016.6	0.32	12	11.5	C	10000.0	60.0	1121.7
Danezis et al., 2016	107	2016.7	0.3	23	757	C	10666.7	31.3	17.0
Zhang et al., 2016	114	2016.8	1	17	60	C	3200.0	42.4	215.0
Dagnac et al., 2016	88	2016.8	1.7	33	2971	C	1882.4	21.8	4.3
Sun et al., 2016	89	2017.0	15	30.3	38.5	C	213.3	23.8	335.1
Zhang et al., 2017	180	2017.3	0.00035	5	1586	O	9142857.1	144.0	8.1
Di Nardo et al., 2017	161	2017.2	1000	10	87	I	3.2	72.0	148.3
Urusov et al., 2017	162	2017.2	0.6	15	105	I	5333.3	48.0	122.9
Smith et al., 2017	82	2017.3	2.5	30	50.5	C	1280.0	24.0	255.4

Bánati et al., 2017	163	2017.2	116	45	22	I	27.6	16.0	586.4
Tang et al., 2017	137	2017.3	0.24	10	200	I	13333.3	72.0	64.5
Tang et al., 2017	137	2017.3	0.08	68	120	I	40000.0	10.6	107.5
Souto et al., 2017	63	2017.6	0.012	2	920	C	266666.7	360.0	14.0
Osteresch et al., 2017	90	2017.2	0.521	11.5	50	C	6142.0	62.6	258.0
Flores-Flores and González-Peñas, 2017	91	2017.7	10.14	30.1	47	C	315.6	23.9	274.5
Peltomaa et al., 2014	164	2017.4	11.1	210	4350	I	288.3	3.4	3.0
Zhao et al., 2017	92	2017.4	0.21	10	40.5	C	15238.1	72.0	318.5
Annunziata et al., 2017	93	2017.5	100	30	33	C	32.0	24.0	390.9
Miró-Abella et al., 2017	94	2017.2	0.04	14.5	11	C	80000.0	49.7	1172.7
Abia et al., 2017	111	2017.5	3.2	20.5	92	C	1000.0	35.1	140.2
Hamed et al., 2017	109	2017.7	9	11.25	8.16	C	355.6	64.0	1580.9
Zhao et al., 2017	95	2017.1	0.2	15	36	C	16000.0	48.0	358.3
Hao et al., 2018b	165	2018.3	25	10	120	I	128.0	72.0	107.5
Anfossi et al., 2018	138	2018.1	62.5	15	837	I	51.2	48.0	15.4
Zhou et al., 2018	166	2018.9	0.05	40	12620	I	64000.0	18.0	1.0
Munawar et al., 2018	128	2018.5	0.00137	5.16	5580	O	2335766.4	139.5	2.3
Du et al., 2018	96	2018.4	0.003	9	17	C	1066666.7	80.0	758.8
Huang et al,., 2018	97	2018.5	0.25	15	140	C	12800.0	48.0	92.1
Pagkali et al., 2018	167	2018.6	5.6	12	743	I	571.4	60.0	17.4
Peltomaa et al., 2018	168	2018.8	1.1	45	95	I	2909.1	16.0	135.8
Yu et al., 2018	139	2018.8	30	10	7835	I	106.7	72.0	1.6
Lu et al., 2018	169	2018.9	0.33	75	5435	I	9697.0	9.6	2.4
Jie et al., 2018	170	2018.2	0.027	150	855	I	118518.5	4.8	15.1
Li et al., 2018	171	2018.5	0.078	120	-	I	41025.6	6.0	#VALUE!
Chen et al., 2018	172	2018.3	12.5	120	5360	I	256.0	6.0	2.4
Sheng et al., 2018	173	2018.3	20	5.5	4910	I	160.0	130.9	2.6
Carballo et al., 2018	98	2018.7	1	12	12.5	C	3200.0	60.0	1032.0
Abdallah et al., 2018	110	2018.1	1	-	90	C	3200.0	#VALUE!	143.3
De Baere et al., 2018	118	2018.1	0.15	10	30	C	21333.3	72.0	430.0
Cladière et al., 2018	108	2018.7	0.5	26	65	C	6400.0	27.7	198.5
Carballo et al., 2018	99	2018.5	0.3	39	80.5	C	10666.7	18.5	160.2
Park et al., 2018	100	2018.7	2.4	26	60	C	1333.3	27.7	215.0
Šarkanj et al., 2018	101	2018.2	0.001	25	963	C	3200000.0	28.8	13.4
Wang et al., 2018	130	2018.1	0.00511	120	376	I	626223.1	6.0	34.3
Zhang et al., 2018	142	2018.8	0.24	45	120	I	13333.3	16.0	107.5
González-Jartín et al., 2019	102	2019.1	0.22	13	62	C	14545.5	55.4	208.1
Da Silva et al., 2019	64	2019.1	51.5	3.6	95	C	62.1	200.0	135.8
Bessaire et al., 2019	119	2019.1	8.3	25.5	44	C	385.5	28.2	293.2
Shu et al., 2019	126	2019.3	0.19	130	780	I	16842.1	5.5	16.5

Mao et al., 2019	181	2019.1	0.0047	15	480	O	680851.1	48.0	26.9
Lu et al., 2019	174	2019.1	0.097	50	1118.083	I	32989.7	14.4	11.5
Jedziniak et al., 2019	103	2019.1	0.5	16	75	C	6400.0	45.0	172.0
Nafuka et al., 2019	112	2019.2	2.4	-	90	C	1333.3	#VALUE!	143.3
Qu et al., 2019	127	2019.1	2.45	60	4410	I	1306.1	12.0	2.9
Duan et al., 2019	175	2019.3	20	10	1697	I	160.0	72.0	7.6
Cheng et al., 2019	176	2019.3	294	65	15	I	10.9	11.1	860.0
Zhan et al., 2019	123	2019.5	0.31	180	5359	I	10322.6	4.0	2.4
Shao et al., 2019	143	2019.6	1.58	18	270	I	2025.3	40.0	47.8
Munawar et al., 2019	178	2019.5	0.001	70	3952	O	3200000.0	10.3	3.3
Chotchuang et al., 2019	179	2019.7	0.9	65	96	O	3555.6	11.1	134.4
Abdallah et al., 2020	104	2020.1	1	28	161.16	C	3200.0	25.7	80.0
Hort et al., 2020	105	2020.1	0.3	8	105.5	C	10666.7	90.0	122.3
Huang et al., 2020	67	2020.1	5	5	455	I	640.0	144.0	28.4
Hou et al., 2020a	140	2020.1	60	-	350	I	53.3	#VALUE!	36.9
Yang et al., 2020	122	2020.2	0.21	22	523	I	15238.1	32.7	24.7
Ren et al., 2020	124	2020.2	2.5	10	4775	I	1280.0	72.0	2.7
Liu et al., 2020b	146	2020.2	0.59	8	858	I	5423.7	90.0	15.0
Liu et al.,2020b	146	2020.2	0.42	8	858	I	7619.0	90.0	15.0
Li et al., 2020	68	2020.1	0.119	4	160	O	26890.8	180.0	80.6
Gilbert-Sandoval et al., 2020	115	2020.8	20	11	41	C	160.0	65.5	314.6
Yapo et al., 2020	116	2020.4	0.03	11	30	C	106666.7	65.5	430.0
Sulyok et al., 2020	106	2020.6	2.39	18.5	90	C	1338.9	38.9	143.3
Zhang et al., 2020b	125	2020.4	0.23	46	368.75	I	320.5	15.7	35.0
Hou et al., 2020b	144	2020.3	60	25	1010	I	53.3	28.8	12.8
Guo et al., 2020	145	2020.8	8.26	7	3435	I	387.4	102.9	3.8
Munawar et al., 2020	62	2020.8	2.16E-08	5	4514	O	148148148148.1	144.0	2.9
Munawar et al., 2020	62	2020.8	5E-07	5	4514	O	6400000000.0	144.0	2.9
Kecskeméti et al., 2020	186	2020.6	156	40	130	O	20.5	18.0	99.2
Wu et al., 2012	53	2012.5	0.1	200	12900	A	32000.0	3.6	1.0
Wu et al., 2013	200	2013.6	0.01	100	6955	A	320000.0	7.2	1.9
Wang et al., 2013	209	2013.1	0.125	35	1495	A	25600.0	20.6	8.6
Yue et al., 2014	194	2014.9	0.00016	60	3390	A	20000000.0	12.0	3.8
Zhao et al., 2014	202	2014.8	0.27	120.41	2065	A	11851.9	6.0	6.2
Chen et al., 2015b	187	2015.4	0.0014	30	445.33	A	2285714.3	24.0	29.0
Chen et al., 2015a	205	2015.3	33	30	270.5	A	97.0	24.0	47.7
Shi et al., 2015	203	2015.2	0.001	25.11	3075	A	3200000.0	28.7	4.2
Gui et al., 2015	69	2015.7	0.1	25	15	A	32000.0	28.8	860.0
Ren et al., 2017	204	2017.4	0.0034	30	485	A	941176.5	24.0	26.6
Yang et al., 2017	201	2017.3	0.01104	90	3570	A	289855.1	8.0	3.6
Wang et al., 2017	206	2017.1	0.02	65	1290.5	A	160000.0	11.1	10.0
Molinero-Fernández et al., 2017b	198	2017.7	0.4	15	120	A	8000.0	48.0	107.5

Tian et al., 2017	188	2017.2	0.0123	30	7271	A	260162.6	24.0	1.8
王红旗 et al., 2017	207	2017.1	7.21	21	70	A	443.8	34.3	184.3
Liu et al., 2018	52	2018.3	0.00021	720	1068	A	15238095.2	1.0	12.1
Cheng and Bonanni, 2018	70	2018.2	10.82	65	20	A	295.7	11.1	645.0
Molinero-Fernández et al., 2017a	199	2018.3	0.7	17	75.51	A	4571.4	42.4	170.8
Hao et al., 2018a	210	2018.7	100	90	3420	A	32.0	8.0	3.8
Niazi et al., 2019	57	2019.2	0.000019	60	1927	A	168421052.6	12.0	6.7
Wang et al., 2019	215	2019.8	0.0162	60	2485	A	197530.9	12.0	5.2
Wei et al., 2019b	195	2019.9	0.00015	40	165	A	21333333.3	18.0	78.2
Han et al., 2020	196	2020.1	0.0005	15	1379.4	A	6400000.0	48.0	9.4
Wei et al., 2020a	197	2020.1	0.00026	10	1302.5	A	12307692.3	72.0	9.9
He et al., 2020b	189	2020.2	0.0003	45	795	A	10666666.7	16.0	16.2
He et al., 2020b	189	2020.2	0.0005	45	795	A	6400000.0	16.0	16.2
Tao et al., 2020	211	2020.2	0.3	73	1023	A	10666.7	9.9	12.6
He et al., 2020a	58	2020.3	0.000003	50	2650	A	1066666666.7	14.4	4.9
Jiang et al., 2020	208	2020.7	0.3	121	397	A	10666.7	6.0	32.5
Wu et al., 2020	190	2020.9	0.00002	120	2900	A	160000000.0	6.0	4.4
Zheng et al., 2020	212	2020.9	0.01	62	1260	A	320000.0	11.6	10.2
Mirón-Mérida et al., 2021	59	2020.9	0.000056	192.2	40	A	57142857.1	3.7	322.5

Table A2 References used for a general PCA analysis in Figure 2.8

Reference	#	Year	LOD	AT	AP	Type	LOD Max/LOD	AT Max/ AT	AP Max/AP
Wu et al., 2012	53	2012	0.1	200	12900	A	1000.0	3.6	1.0
Wu et al., 2013	200	2014	0.01	100	6955	A	10000.0	7.2	1.9
Wang et al., 2013	209	2013	0.125	35	1495	A	800.0	20.6	8.6
Yue et al., 2014	194	2015	0.000 16	60	3390	A	625000.0	12.0	3.8
Zhao et al., 2014	202	2015	0.27	120.4 1	2065	A	370.4	6.0	6.2
Chen et al., 2015b	187	2015	0.001 4	30	445.3 3	A	71428.6	24.0	29.0
Chen et al., 2015a	205	2015	33	30	270.5	A	3.0	24.0	47.7
Shi et al., 2015	203	2015	0.001	25.11	3075	A	100000.0	28.7	4.2
Gui et al., 2015	69	2016	0.1	25	15	A	1000.0	28.8	860.0
Ren et al., 2017	204	2017	0.003 4	30	485	A	29411.8	24.0	26.6
Yang et al., 2017	201	2017	0.011 04	90	3570	A	9058.0	8.0	3.6
Wang et al., 2017	206	2017	0.02	65	1290. 5	A	5000.0	11.1	10.0
Molinero-Fernández et al., 2017b	198	2018	0.4	15	120	A	250.0	48.0	107.5
Tian et al., 2017	188	2017	0.012 3	30	7271	A	8130.1	24.0	1.8
王红旗 et al., 2017	207	2017	7.21	21	70	A	13.9	34.3	184.3
Liu et al., 2018	52	2018	0.000 21	720	1068	A	476190.5	1.0	12.1
Cheng and Bonanni, 2018	70	2018	10.82	65	20	A	9.2	11.1	645.0
Molinero-Fernández et al., 2017a	199	2018	0.7	17	75.51	A	142.9	42.4	170.8
Hao et al., 2018a	210	2019	100	90	3420	A	1.0	8.0	3.8
Niazi et al., 2019	57	2019	0.000 019	60	1927	A	5263157.9	12.0	6.7
Wang et al., 2019	215	2020	0.016 2	60	2485	A	6172.8	12.0	5.2
Wei et al., 2019b	195	2020	0.000 15	40	165	A	666666.7	18.0	78.2
Han et al., 2020	196	2020	0.000 5	15	1379. 4	A	200000.0	48.0	9.4
Wei et al., 2020a	197	2020	0.000 26	10	1302. 5	A	384615.4	72.0	9.9
He et al., 2020b	189	2020	0.000 3	45	795	A	333333.3	16.0	16.2
He et al., 2020b	189	2020	0.000 5	45	795	A	200000.0	16.0	16.2
Tao et al., 2020	211	2020	0.3	73	1023	A	333.3	9.9	12.6
He et al., 2020a	58	2020	0.000 003	50	2650	A	33333333.3	14.4	4.9
Jiang et al., 2020	208	2021	0.3	121	397	A	333.3	6.0	32.5
Wu et al., 2020	190	2021	0.000 02	120	2900	A	5000000.0	6.0	4.4
Zheng et al., 2020	212	2021	0.01	62	1260	A	10000.0	11.6	10.2
Mirón-Mérida et al., 2021	59	2021	0.000 056	192.2	40	A	1785714.3	3.7	322.5

Appendix B
Supporting Information of Chapter 3

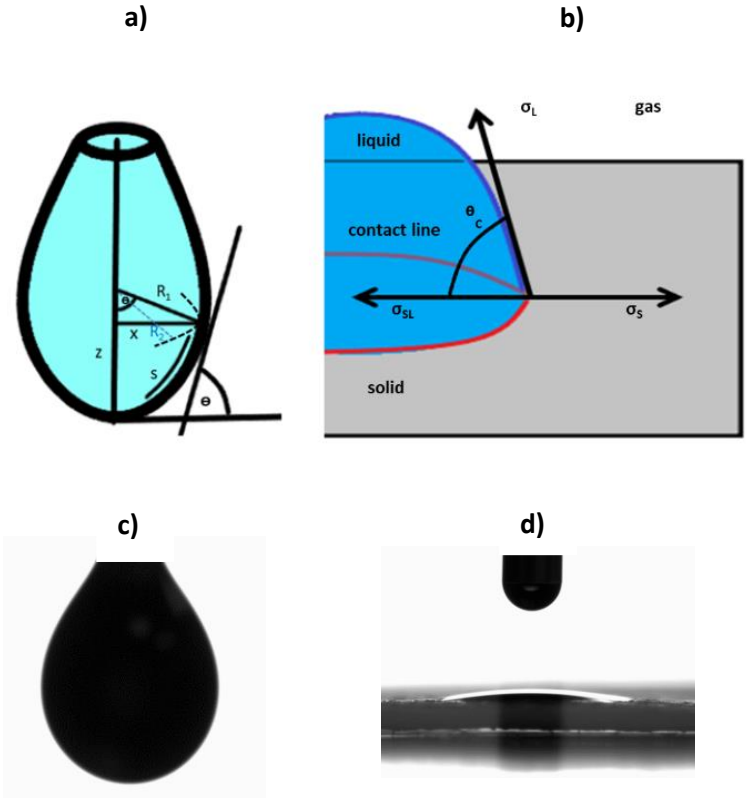

Figure B1 SCA 20 software processing parameters for interfacial tension (**a**) and contact angle (**b**) calculations in OCA 25 tensiometer, (d) interfacial surface tension image an ink drop, (e) ink drop deposited on 3MM Chr paper for contact angle measurement

Construction of µPADs

Cellulose chromatography paper was cut into squares (4.5 cm × 4.5 cm), where hydrophobic boundaries were drawn with a permanent marker using a 3-D printed template in a 'flower' shape, as shown in Fig B2.

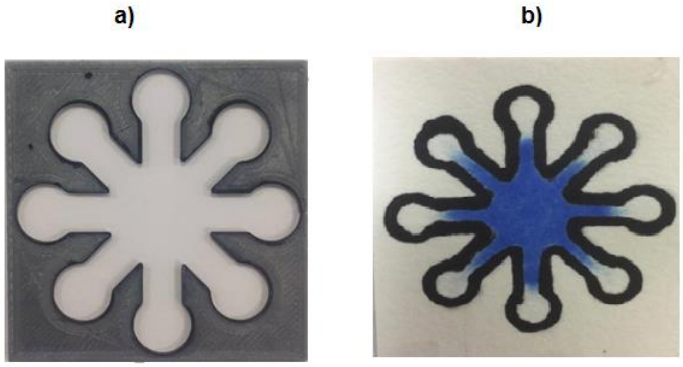

Figure B2 (**a**) 3D-printed template stamp used for the delimitation of hydrophobic zones in (**b**) a flower-shape paper with a Stabilo® marker (mobile phone image showing the diffusion a blue ink aliquot applied at the center of the design)

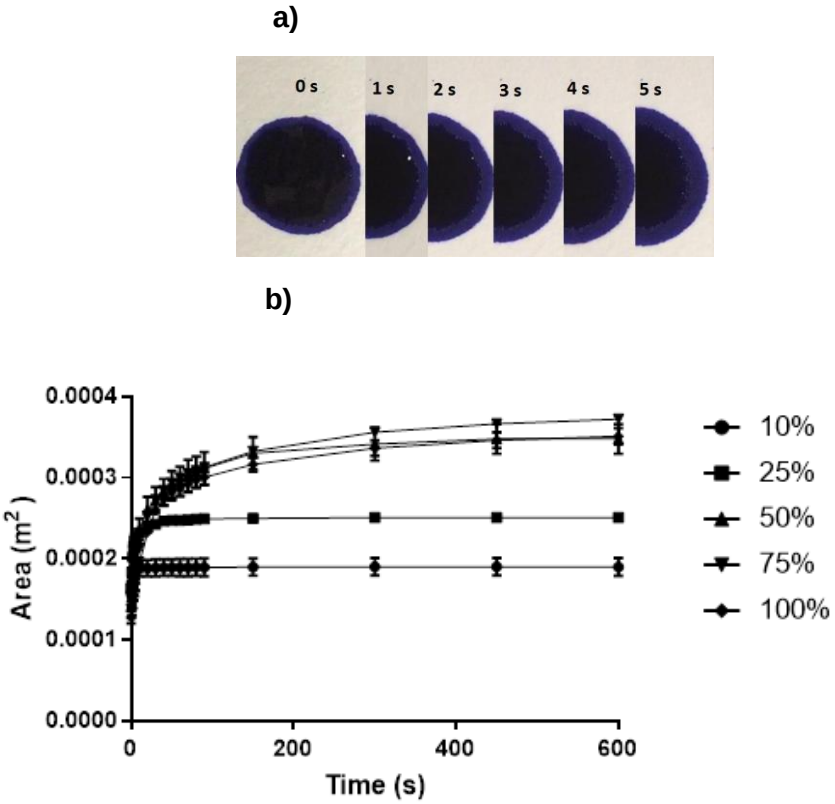

Figure B3 (**a**) Diffusion of an ink model during 5 s, (**b**) ink front area at different concentrations (% v/v dilution in water, as shown in label) on 3MM chromatography paper

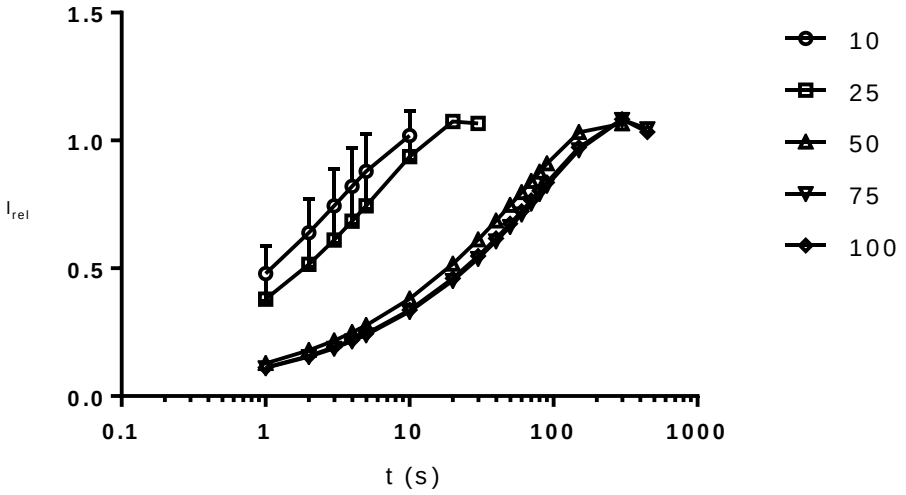

Figure B4 Relative distance (l_{rel}) of the ink models until steady state time for varying ink concentrations (% v/v dilution in water, as shown in label)

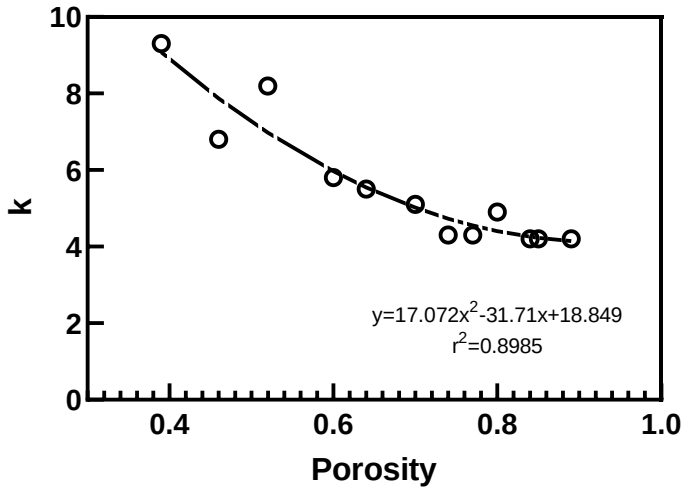

Figure B5 Dependence of the Kozeny-Karman constant (k) to the porosity value as reported by Rahli and collaborators (Rahli et al., 1997) and its mathematical expression (Inset)

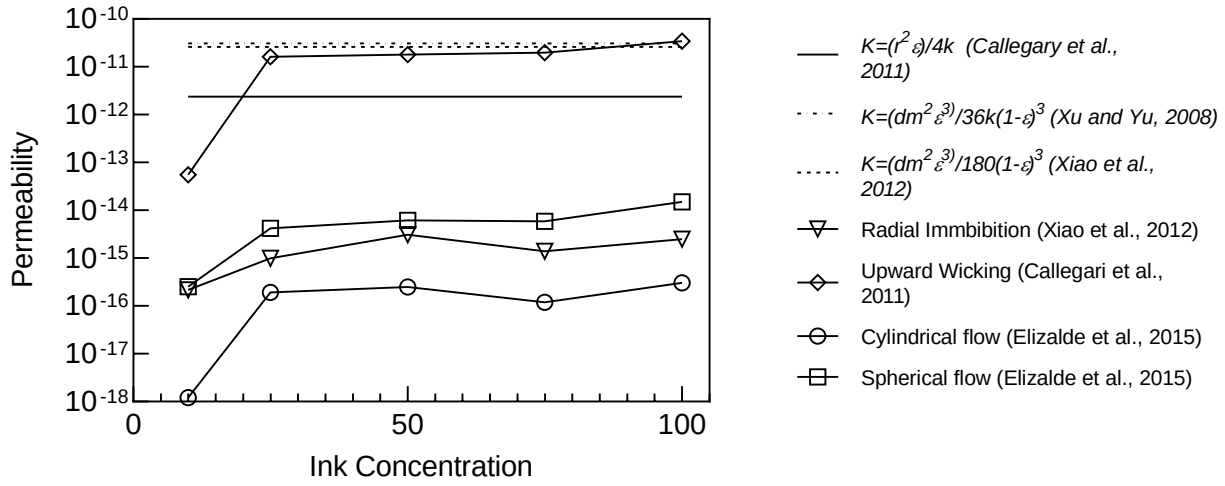

Figure B6 Graphical comparison between the experimental and theoretical permeability values at different ink concentrations. (The numbers in brackets indicate the corresponding reference for each model)

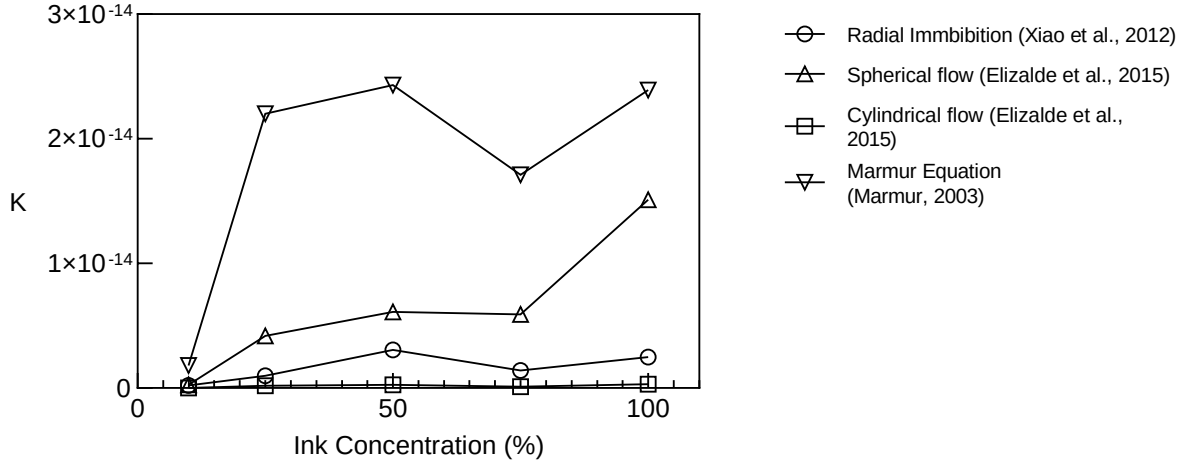

Figure B7 Graphical comparison between the experimental permeability (K) and Marmur's determination at different ink concentrations. (The numbers in brackets indicate the corresponding reference for each model)

Appendix C
Supporting Information of Chapter 4

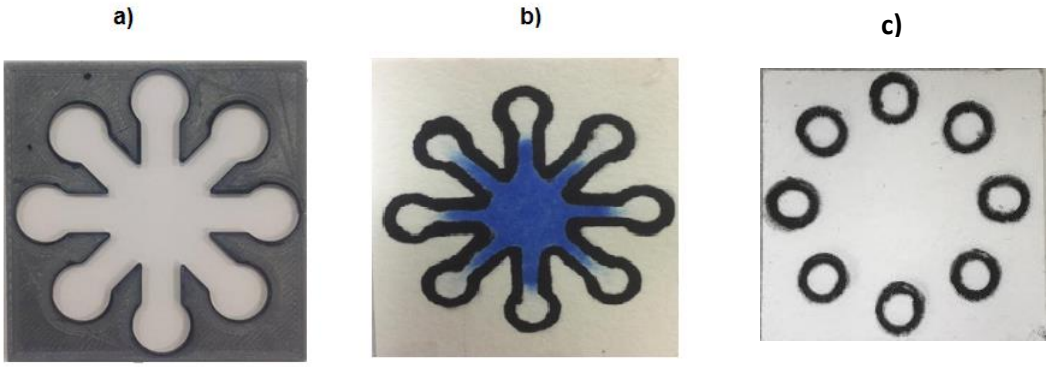

Figure C1 (**a**) 3D-printed template stamp used for the delimitation of hydrophobic zones in (**b**)a flower-shape paper with a Stabilo® marker (mobile phone image showing the diffusion a blue ink aliquot applied at the center of the design) and (**c**) a 8 circular spots arrangement (scanned image)

Ellman's Colorimetric Method

The principle of this work was based Ellman's colorimetric assay (Figure S5). In this reaction, aflatoxin B_1 acts as an inhibitor of the activity of acetylcholinesterase (AChE), which reduced the final intensity of the yellow colouration.

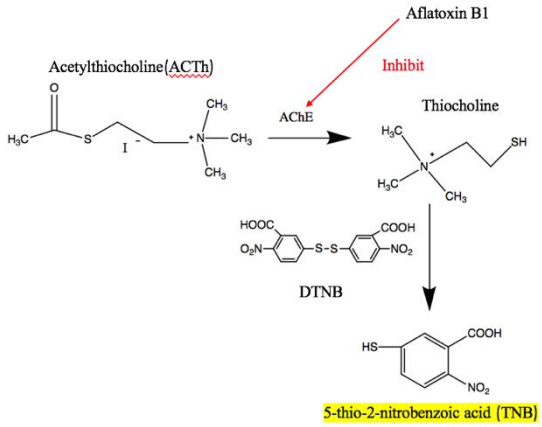

Figure C2 Ellman's assay (Ellman et al. 1961)

First, acetylthiocholine (ATCh) was hydrolised by acetylcholinesterase (AChE) to generate thiocholine. Then thiocholine reacted with DTNB to generate the yellow compound 5-thio-2-nitrobenzoic acid (TNB). In this reaction, aflatoxin B1 acted as a revisible inhibitor for AChE. Thus, under the presence of aflatoxin B1, the colour intensity of the reaction system exhibited a reduction.

AChE activity in bulk assay.

The activity of AChE was monitored by a microplate assay (Multimode microplate reader Spark, TECAN), where the optimum concentration was also determined. First, 80 µL of AChE solution (concentration ranging from 0 to 200 Unit/mL) was applied to each well. Then 20 µL of mixture of DTNB (final concentration 100 µM) and ATCh (final concentration 60 µM) were added to each well. The microplate was incubated for 5 min and the absorbance was measured at 412 nm.

The effects of aflatoxin B1, ochratoxin A and fumonisin B1 by microplate assay.

First, 5 µL of aflatoxin B_1 solution were applied at different concentrations (0 to 20 µM) to each well. Then 80 µL of AChE (50 U/mL) were added to each well, followed by 10 µL of DTNB (final concentration 500 µM). The plate was incubated for 10 min, of 10 µL of ATCh (final concentration 300 µM) were added in a final step. After 5 min incubation, the absorbance was measured in TECAN microplate reader at 412 nm. The same procedure was employed for ochratoxin A and fumonisin B1.

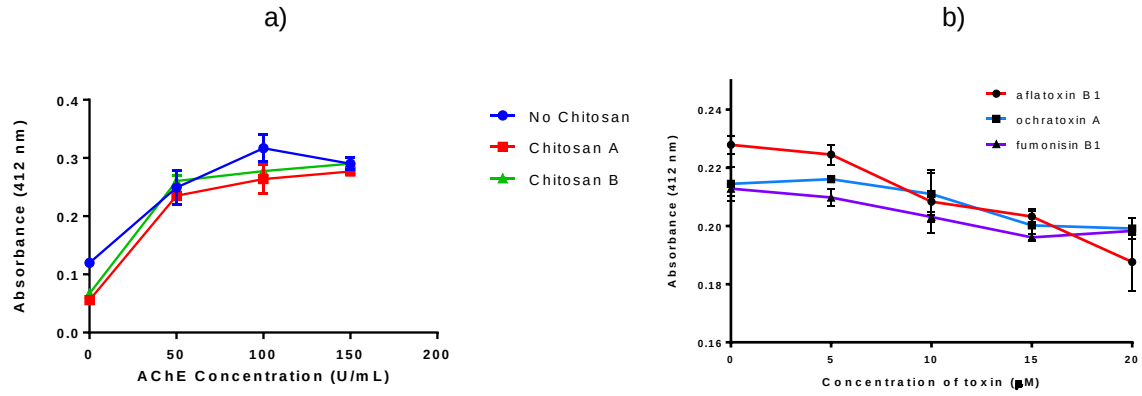

Figure C3 (**a**) Effect of chitosan (0.2% w/w) in the synthesis of TNB, (**b**) inhibitory effects of corn-related mycotoxins on the activity of AChE

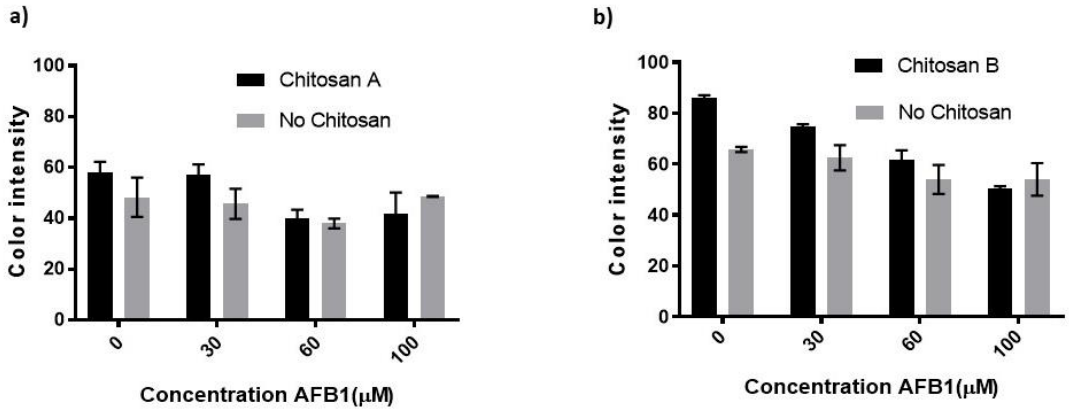

Figure C4 Inhibition effect at different concentrations of AFB1 on the activity of free (no chitosan) and immobilized AChE (50 U/mL) with (**a**) chitosan A and (**b**) chitosan B

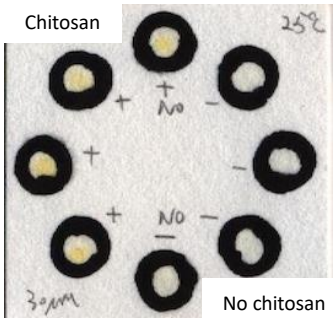

Figure C5 The effect of cross-linked chitosan B immobilization of AChE (50 u/mL) in a paper-based determination. Concentration AFB1 standard: 30 μM, total volume: 10 μL

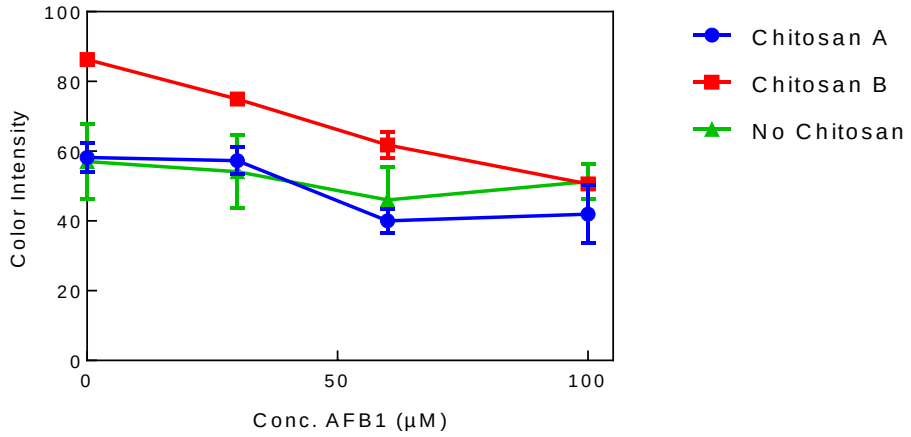

Figure C6 Color intensity at different concentrations of AFB1 on a free (No chitosan) and immobilized (chitosan A and B) AChE (50 U/mL) colorimetric assay. The displayed No chitosan values are an average from the corresponding samples in Fig C4a and C4b

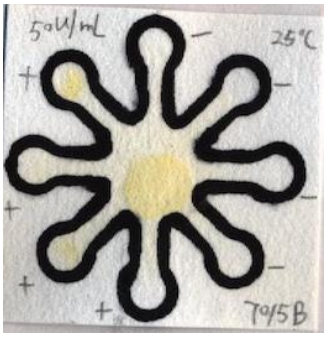

Figure C7 Determination of AFB1 in corn samples with chitosan A (+) immobilized AChE (50 u/mL) on a flower shaped paper-based µPAD. Concentration AFB1 in corn extract: 50 µM, total volume: 40 µL

Appendix D
Supporting Information of Chapter 5

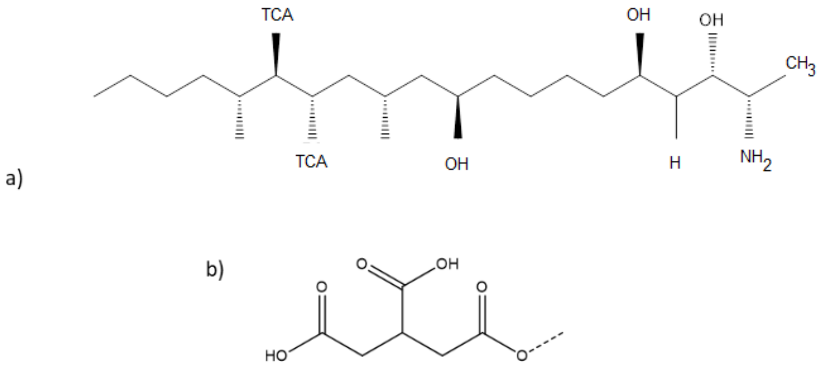

Figure D1 Structure representation of (**a**) FB1 and (**b**) tricarballylic acid (TCA)

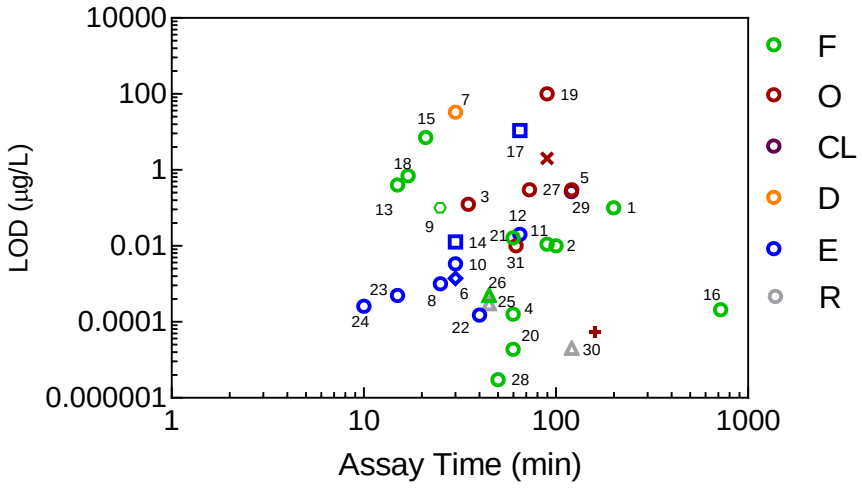

Figure D2 Comparison of the assays from this work with aptamer 96 nt for the analysis of the $A_{650/520}$ ratio (**X**) and the AF4 peak 2 area at 600 nm (**+**) with other aptamer-based biosensors with fluorescent (green), optical (red), chemiluminescent (purple), deflection (yellow), electrochemical (blue) and Raman (grey) determinations with a 96 nt (circle), 80 nt (rhombus), 60 nt (hexagon), 40 nt (square) and not specified (triangle) sequence. Each labelled number represents a reference listed at the end of the supplementary materials

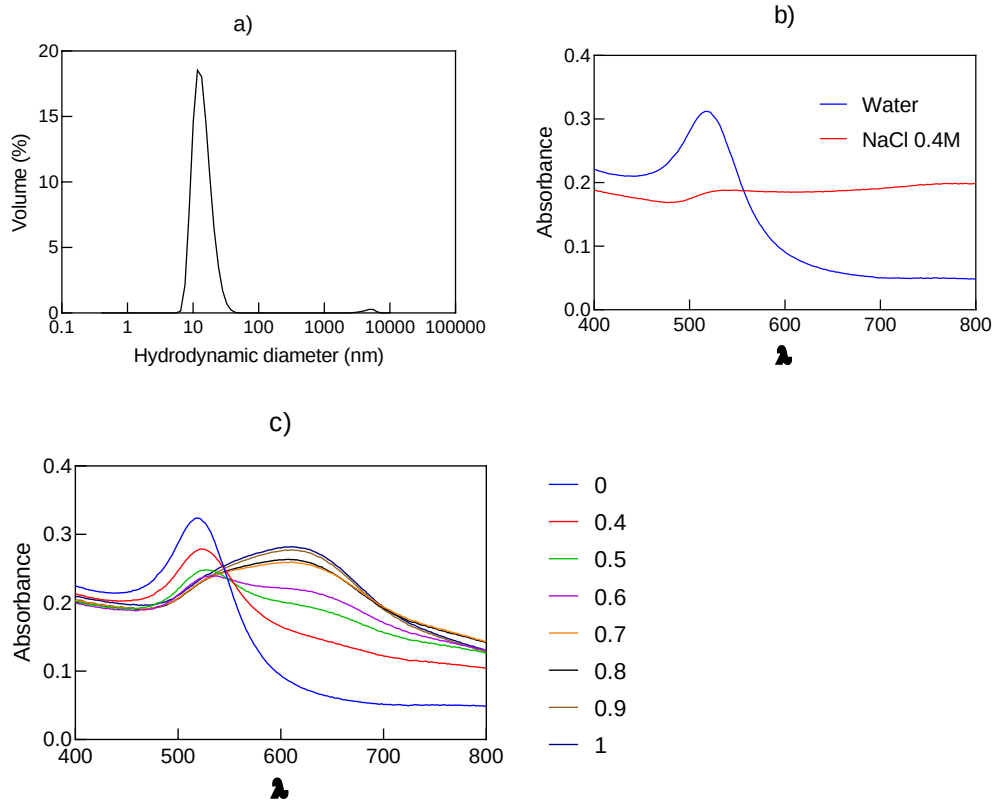

Figure D3 (**a**) Particle size distribution of AuNPs in Stock 1, (**b**) spectrophotometric scan (λ = 400-800 nm) upon addition of water or NaCl 1:1 (v/v), and (**c**) aggregation profile of aptamer 40 nt-functionalized AuNPs (117:1 molar ratio) at different NaCl concentrations (0-1M)

Table D1 ANOVA for the incubation of FB1 with Aptamer 40 nt in three buffers

		One-Way ANOVA (*p*)		
Sample		**Tris**	**PBS**	**Mix**
Tris	T0		vsP0 (<0.05)	vsM0 (<0.05)
	T10		vsP10 (<0.05)	vsM10 (<0.05)
	T100		vsP100(<0.05)	vsM100(<0.05)
PBS	P0	vsT0 (<0.05)		vsM0 (<0.05)
	P10	vsT10 (<0.05)		vsM10 (<0.05)
	P100	vsT100(<0.05)		vsM100(<0.05)
Mix	M0	vsT0 (<0.05)	vsP0 (<0.05)	
	M10	vsT10 (<0.05)	vsP10 (<0.05)	
	M100	vsT100 (**0.33**)	vsP100(<0.05)	

Incubation: Aptamer 40 nt: AuNP molar ratio (117:1), FB1-aptamer incubation (60 min, 37 °C), AuNP incubation (120 min, 37 °C). Tris-HCl buffer: 31.1 mM, PBS: 12.79 mM, Mix: Tris-HCl buffer 31.1 mM + PBS 12.79 mM (NaCl yield).

a)

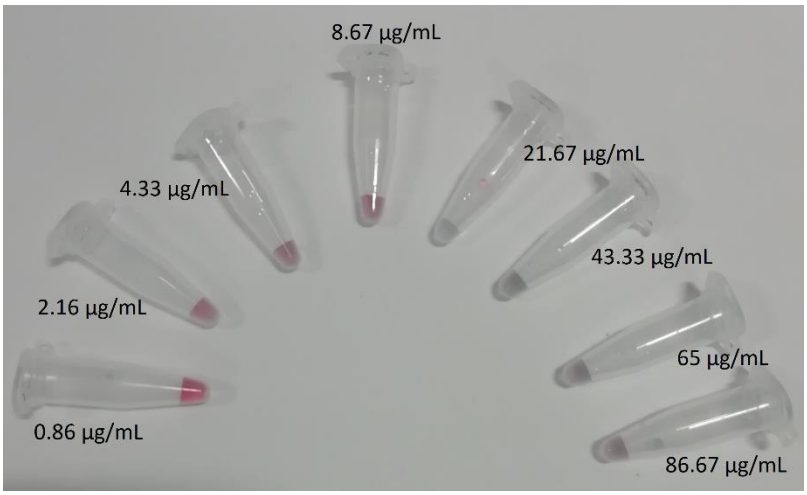

b)

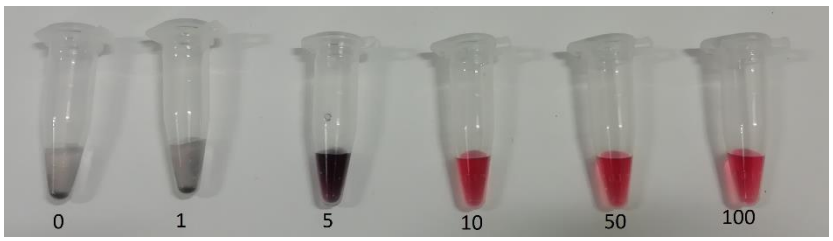

Figure D4 (**a**) Colorimetric effect from the incubation of aptamer 40 nt and FB1 (0.86-86.67 µg/mL, 60 min, 37 °C) with Stock 1 (117:1 Aptamer:AuNP molar ratio, 120 min, 37 °C) after the addition of NaCl (0.4 M, 1:1 v:v) and (**b**) the incubation of FB1(0-100 µg/mL) with Stock 1 (117:1 aptamer:AuNP molar ratio, 120 min, 37 °C) Note: FB1 was dissolved in a mixture of Tris-HCl (31.1 mM) and PBS (NaCl 12.79 mM yield) buffers

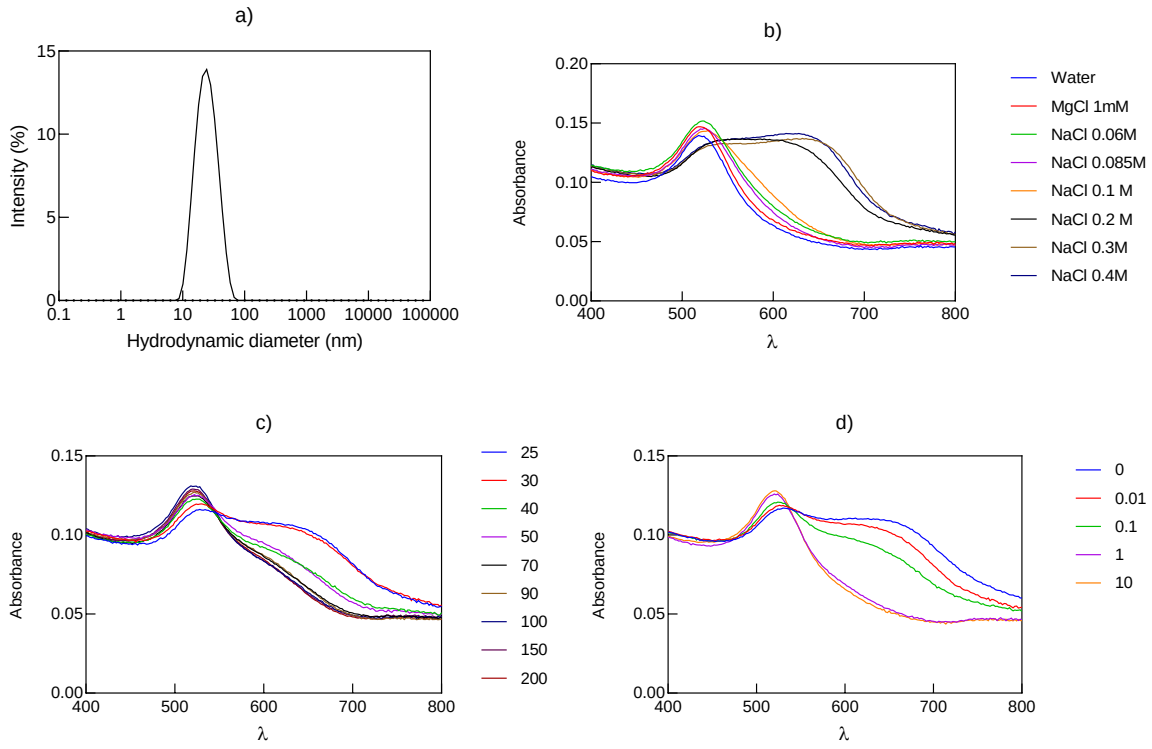

Figure D5 (**a**) Particle size distribution of AuNP in Stock 2, (**b**) Wavelength (λ= 400-800 nm) scan of AuNP upon addition of water, $MgCl_2$ and NaCl (1:1 v/v) , (**c**) Wavelength (λ = 400-800 nm) scan of AuNP functionalized with different molar ratios of aptamer 96 nt after the addition of NaCl (0.2 M), (**d**) aggregation profile of functionalized AuNP with aptamer 96 nt (30:1 molar ratio) and different concentrations of FB1 after the addition of NaCl 0.2 M

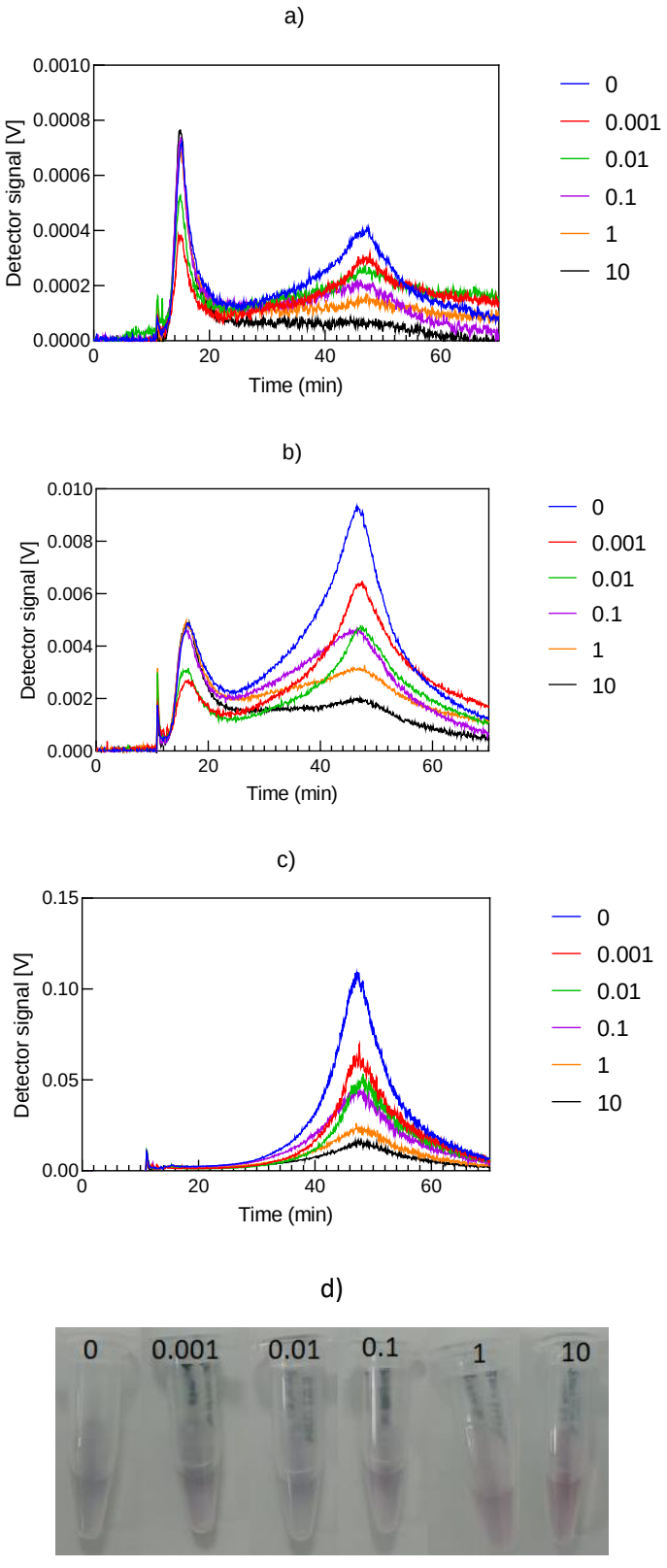

Figure D6 Fractograms of the FB1-Aptamer 96 nt-AuNP conjugates at different FB1 concentrations (0-10 µg/mL) after the addition of NaCl 0.2 M detected by AF4 through UV/Vis, λ =520 nm (**a**), l = 600 nm (**b**), MALS 28° (**c**) signals, and (**d**) their colorimetric aggregation profile

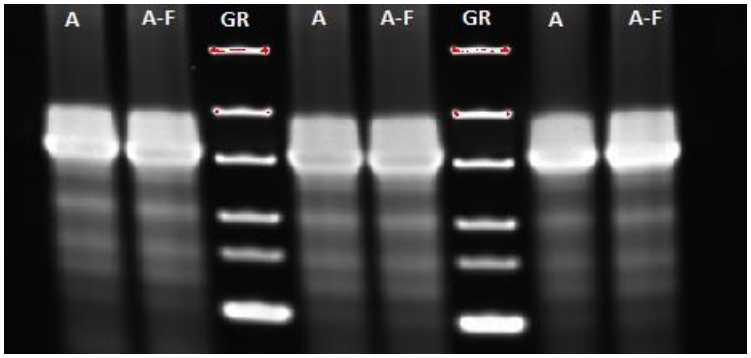

Figure D7 Characterization of aptamer 96 nt (A) and aptamer 96 nt-FB1 (A-F) in 14% polyacrylamide gel revealed in ChemiDocTm (Bio Rad) and analyzed in ImageJ. GR: Gene ruler ultra low range DNA Ladder, ready-to-use (SM1213, Thermofisher); Total volume per well 6 µL: 5 µL of aptamer 96 nt (9.3874 µM) or its combination with FB1 (340.11 µM) in $MgCl_2$ 1 mM + 1 µL DNA loading dye. FB1/Aptamer 96 nt molar ratio=36.2305 (equivalent to incubating with 10.02 µg/mL). Electrophoresis at 120 V for 3 h 30 min in TAE buffer, followed by 1 h fixation (10 % acetic acid,40% methanol, 50% water), and 1 h in SYBR gold 1X

a)

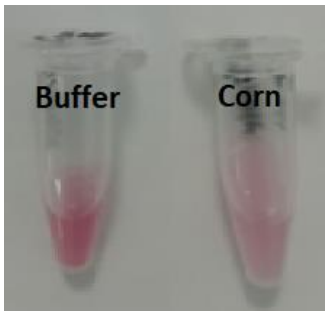

b)

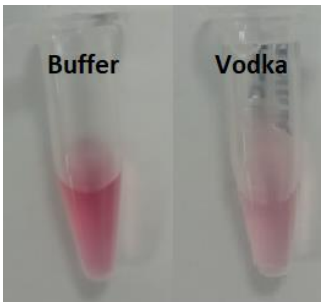

c)

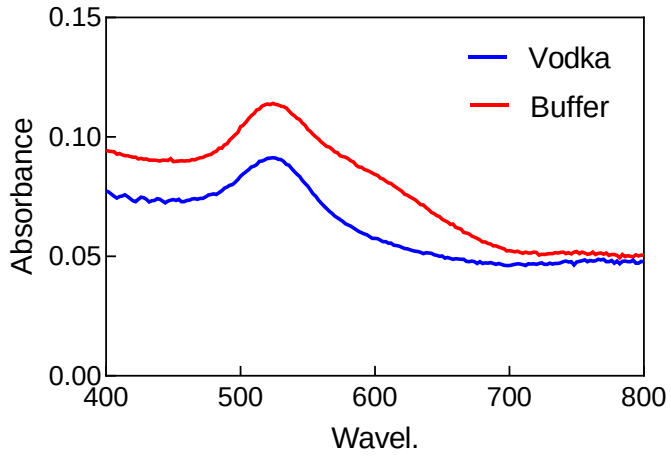

Figure D8 Aptamer 96 nt-FB1-AuNP conjugates from the incubation with FB1 (**a**) 10 µg/mL in buffer and corn extracted with 5% methanol, and (**b**) 1 µg/mL in buffer and vodka. (**c**) Wavelength (λ = 400-800 nm) scan of the conjugates in buffer and vodka (NB: Aptamer 96 nt: AuNP molar ratio 30:1, Aptamer-FB1 incubation: 37 °C for 30 min, Incubation with Stock 2: 1 h at RT. Binding buffer: $MgCl_2$ 1 mM)

Table D2 References from Figure D2

1 Wu, S., Duan, N., Ma, X., Xia, Y., Wang, H., Wang, Z. and Zhang, Q. 2012. Multiplexed fluorescence resonance energy transfer aptasensor between upconversion nanoparticles and graphene oxide for the simultaneous determination of mycotoxins. Analytical Chemistry. 84(14), pp.6263-6270.

2 Wu, S., Duan, N., Li X., Tan, G., Ma, X., Xia, Y., Wang, Z. and Wang, H. 2013. Homogenous detection of fumonisin B1 with a molecular beacon based on fluorescence energy transfer between NaYF4:YB, Ho upconversion nanoparticles and gold nanoparticles. Talanta. 116(15), pp.611-618.

3 Wang, W., Wu, S., Ma, X., Xia, Y., Wang, Z. 2013. Novel methods for fumonisin B1 detection based on AuNPs labelling and aptamer recognition. Journal of Food Science and Biotechnology. 32(5).

4 Yue, S., Jie, X., Wei, L., Bin, C., Dou, W.D., Yi, Y., QingXia, L., JianLin, L. and TieSong, Z. 2014. Simultaneous detection of ochratoxin A and fumonisin B1 in cereal samples using an aptamer-photonic crystal encoded suspension array. Analytical Chemistry. 86(23), pp.11797-11802.

5 Zhao, Y., Luo, Y., Li, T. and Song, Q. 2014. Au NPs driven electrochemiluminescence aptasensors for sensitive detection of fumonisin B1. RSC Advances, 4, pp.57709-57714.

6 Chen, X., Huang, Y., Ma, X., Jia, F., Guo, X. and Wang, Z. 2015.Impedimetric aptamer-based determination of the mold toxin fumonisin B1. Microchimica Acta. 182(9-10), pp.1709-1714.

7 Chen, X., Bai, X., Li, H. and Zhang, B. 2015. Aptamer-based microcantilever array biosensor for detection of fumonisin B1. RSC Advances. 5, pp.35448-35452.

8 Shi, Z.-Y., Zheng Y.-T., Zhang, H.-B., He, C.-H., Wu, W.-D. and Zhang, H.-B. 2015. DNA electrochemical aptasensor for detecting fumonisin B1 based on graphene and thionine nanocomposite. Electroanalysis. 27(5), pp.1097-1103.

9 Gui H, Jin Q, Zhang Y, Wang X, Yang Y, Shao C, Cheng C, Wei F, Yang Y, Yang M, Song H (2015) Development of an aptamer/ fluorescence dye PicoGreen-based method for detection of fumonisin B1. Sheng Wu Gong Cheng Xue Bao. 31(9), pp.1393–1400.

10 Ren, C., Li, H., Lu, X., Quian, J., Zhu, M., Chen, W., Liu, Q., Hao, N. Li, H. and Wang, K. 2017. A disposable aptasensing device for label-free detection of fumonisin B1 by integrating PDMS film-based micro-cell and screen-printed carbon electrode. Sensors and actuators B: Chemical. 251, pp.192-199.

11 Yang, Y., Li, W., Shen, P. Liu, R., Li., Y., Xu, J., Zheng, Q., Zhang, Y., Li, J. and Zheng. T. 2017. Aptamer fluorescence signal recovery screening for multiplex mycotoxins in cereal samples based on photonic crystal microsphere suspension array. Sensors and Actuators B: Chemical. 248, pp.351.358.

12 Wang, C., Qian, J., An, K., Huang, X., Zhao, L., Liu, Q., Hao, N., Wang, K. 2017 Magneto-controlled aptasensor for simultaneous electrochemical detection of dual mycotoxins in maize using metal sulfide quantum dots coated silica as labels. *Biosensors and Bioelectronics.* **89**, pp.802-809.

13 Molinero-Fernández, A., Moreno-Guzmán, M., Ángel López, M., Escarpa, A. 2017. Biosensing strategy for simultaneous and accurate quantitative analysis of mycotoxins in food samples using unmodified graphene micromotors. Analytical Chemistry.89, pp.10850-10857.

14 Tian, H., Sofer, Z., Pumera, M., Bonanni, A. 2017. Investigation on the ability of heteroatom-doped graphen for biorecognition. Nanoscale. 9, pp.3530-3536.

15 王红旗, 王俊艳, 洪慧杰, 尹海燕, Maragos, C., 张 玲, 刘继红. 2017. 伏马毒素 B1 核酸适配体链置换探针的筛选及应用. 农产品质量与安全. 1, pp.44-48.

16 Liu, R., Li, W., Cai, T., Deng, Y., Ding, Z., Liu, Y., Zhu, X., Wang, X., Liu, J., Liang, B., Zheng, T., LI, J. 2018. TiO2 nanolayer-enhanced fluorescence for simultaneous multiplex mycotoxin detection by aptamer microarrays on a porous silicon surface. Applied Materials and Interfaces. 10, pp.14447-14453.

17 Cheng, Z., Bonanni, A. 2018. All-in-One: Electroactive nanocarbon as simultaneous platform and label for single-step biosensing. Nanomaterials. 24, pp.6380-6385.

18 Molinero-Fernández, A., Jodra, A., Moreno-Guzmán, M., López, M.A., Escarpa, A. 2018. Magnetic reduced graphene oxide/nickel/platinum nanoparticles micromotors for mycotoxin analysis. Chemistry A European Journal. 24, pp.7172-7176.

19 Hao, N., Lu, J., Zhou, Z., Hua, R., Wang, K. 2018. A pH-resolved colorimetric biosensor for simultaneous multiple target detection. ACS Sensors. 3, pp.2159-2165.
20 Niazi, S., Khan, I.M., Yan, L., Khan, M.I., Mohsin, A., Duan, N., Wu, S., Wang, Z. 2019. Simultaneous detection of fumonisin B1 and ochratoxin A using dual-color, time-resolved luminescent nanoparticles (NaYF4: Ce, Tb and NH2-Eu/DPA@SiO2) as labels. Analytical and Bioanalytical Chemistry. 411, pp.1453-1465.
21 Wang, C., Huang, X., Tian, X., Zhang, X., Yu, S., Chang, X., Ren, Y., Qian, J. 2019. A multiplexed FRET aptasensor for the simultaneous detection of mycotoxins with magnetically controlled graphene oxide/Fe3O4 as a single energy acceptor. Analyst, 144(20), 6004-6010. https://doi.org/10.1039/C9AN01593K
22 Wei, M., Zhao, F., Feng, S., Jin, H. 2019. A novel electrochemical aptasensor for fumonisin B 1 determination using DNA and exonuclease-I as signal amplification strategy. BMC chemistry, 13(1), 1-6. https://doi.org/10.1186/s13065-019-0646-z
23 Han, Z., Tang, Z., Jiang, K., Huang, Q., Meng, J., Nie, D., Zhao, Z. 2020. Dual-target electrochemical aptasensor based on co-reduced molybdenum disulfide and Au NPs (rMoS2-Au) for multiplex detection of mycotoxins. Biosensors and Bioelectronics, 150, 111894. https://doi.org/10.1016/j.bios.2019.111894
24 Wei, M., Xin, L., Feng, S., Liu, Y. 2020. Simultaneous electrochemical determination of ochratoxin A and fumonisin B1 with an aptasensor based on the use of a Y-shaped DNA structure on gold nanorods. Microchimica Acta, 187(2), 1-7. https://doi.org/10.1007/s00604-019-4089-y
25 He, D., Wu, Z., Cui, B., Xu, E. 2020. Aptamer and gold nanorod–based fumonisin B1 assay using both fluorometry and SERS. Microchimica Acta, 187(4), 1-8. https://doi.org/10.1007/s00604-020-4192-0
26 He, D., Wu, Z., Cui, B., Xu, E. 2020. Aptamer and gold nanorod–based fumonisin B1 assay using both fluorometry and SERS. Microchimica Acta, 187(4), 1-8. https://doi.org/10.1007/s00604-020-4192-0
27 Tao, Z., Zhou, Y., Li, X., & Wang, Z. (2020). Competitive HRP-Linked Colorimetric Aptasensor for the Detection of Fumonisin B1 in Food based on Dual Biotin-Streptavidin Interaction. Biosensors, 10(4), 31. https://doi.org/10.3390/bios10040031
28 He, D., Wu, Z., Cui, B., Jin, Z., Xu, E. 2020. A fluorometric method for aptamer-based simultaneous determination of two kinds of the fusarium mycotoxins zearalenone and fumonisin B1 making use of gold nanorods and upconversion nanoparticles. Microchimica Acta, 187, 254. https://doi.org/10.1007/s00604-020-04236-4
29 Jiang, D., Huang, C., Shao, L., Wang, X., Jiao, Y., Li, W., Chen, J. and Xu, X., 2020. Magneto-controlled aptasensor for simultaneous detection of ochratoxin A and fumonisin B1 using inductively coupled plasma mass spectrometry with multiple metal nanoparticles as element labels. Analytica Chimica Acta, 1127, pp.182-189.
30 Wu, Y., Yu, J., Li, F., Li, J. and Shen, Z., 2020. A Calibration Curve Implanted Enzyme-Linked Immunosorbent Assay for Simultaneously Quantitative Determination of Multiplex Mycotoxins in Cereal Samples, Soybean and Peanut. *Toxins*, *12*(11), p.718.
31 Zheng, Y.T., Zhao, B.S., Zhang, H.B., Jia, H. and Wu, M., 2020. Colorimetric aptasensor for fumonisin B1 detection by regulating the amount of bubbles in closed bipolar platform. *Journal of Electroanalytical Chemistry*, *877*, p.114584.

Appendix E
Supporting Information of Chapter 6

a)

b)

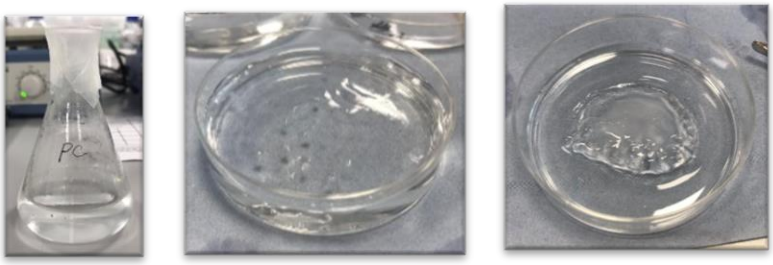

c)

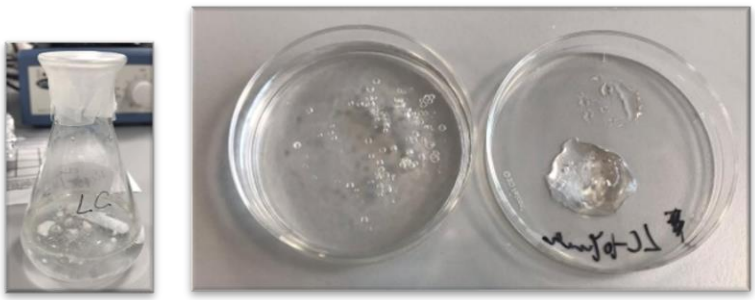

Figure E1 (**a**) β-chitin dispersion by ultrasound and its resulting chitin scaffold; (**b**) chitosan solution (chitosan I, 6 g/L, D.A. 14 %, M.W. 228 000 g/mol) with NIBC hydrogel formation, (**c**) and chitosan solution (chitosan III, 3 g/L, D.A. 28.8 %, M.W. 1 460 000 g/mol) without NIBC hydrogel formation

a) b)

Figure E2 (**a**) Conventionally and (**b**) liquid N_2 produced β-Chitin scaffolds incubated in PBS at room temperature for 40 min

a) b)

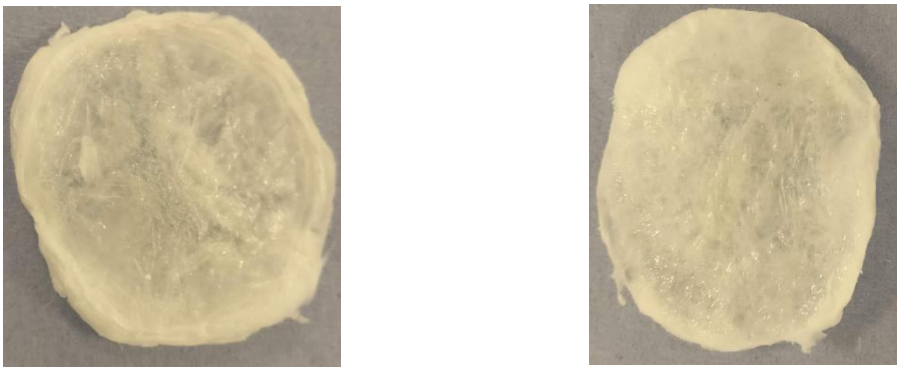

Figure E3 Freeze dried control NIBC chitosan hydrogels (non-imprinted) produced with (**a**) chitosan I (**b**) and chitosan II

a) b)

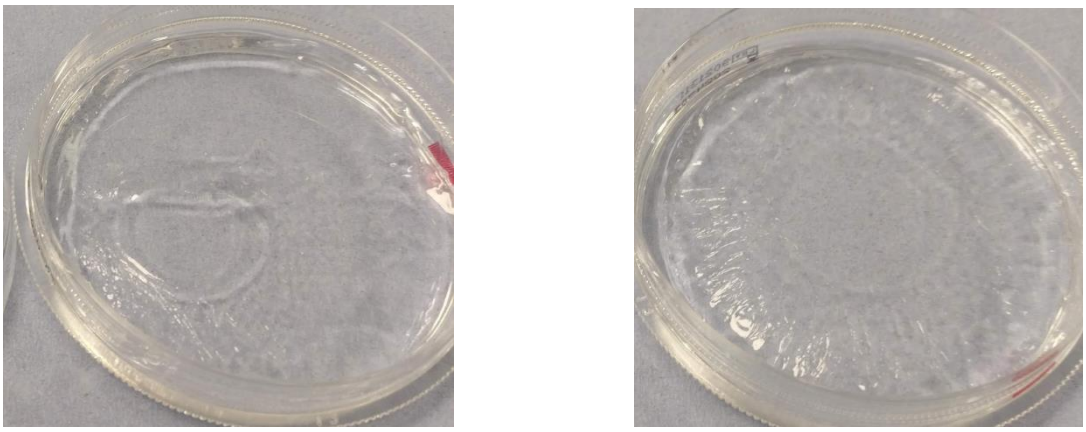

Figure E4 Molecularly imprinted NIBC-L-phe hydrogels produced with (**a**) chitosan I (**b**) and chitosan II

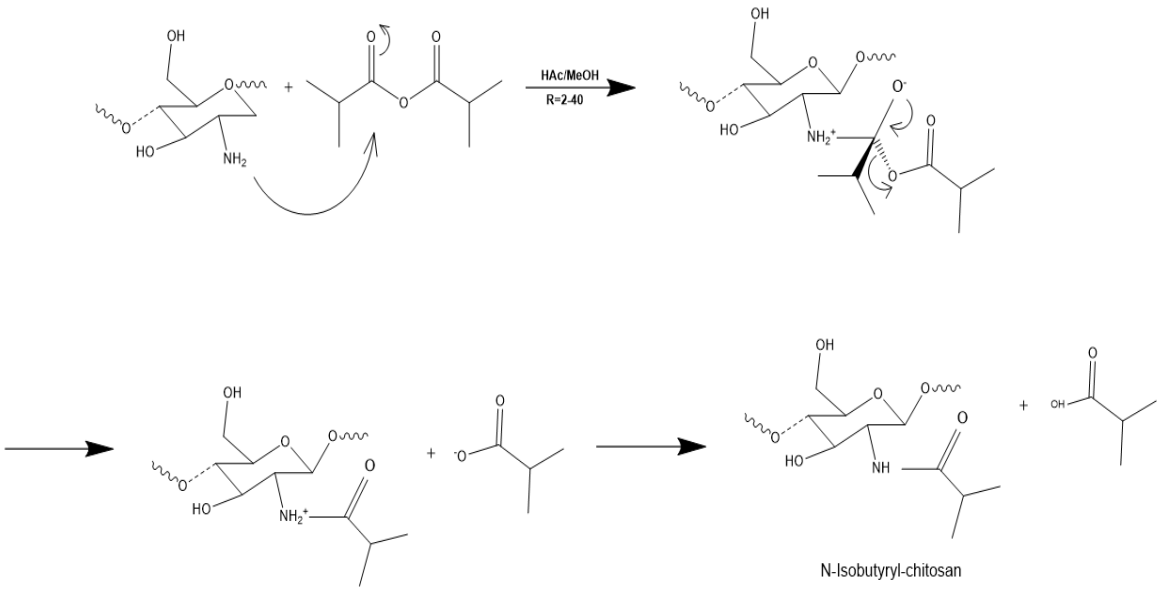

Figure E5 Mechanism of the N-acylation of chitosan

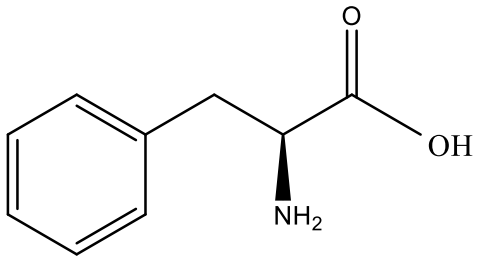

Figure E6 Chemical structure of Phenylalanine